CL11993

3

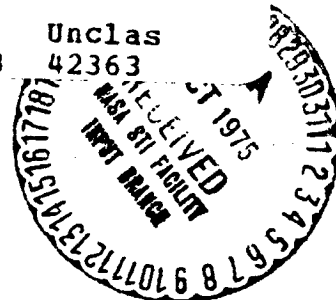(NASA-CR-111993) HYPERSONIC RESEARCH ENGINE
PROJECT. PHASE 2: STRUCTURES ASSEMBLY
MODEL (SAM), TEST REPORT, DATA ITEM NO.
63.05 (AiResearch Mfg. Co., Los Angeles,
Calif.) 277 p

N76-70988

00/98   Unclas   42363

AIRESEARCH MANUFACTURING COMPANY
A DIVISION OF THE GARRETT CORPORATION
9851-9951 SEPULVEDA BLVD. • LOS ANGELES, CALIFORNIA 90009
TELEPHONE: SPRING 6-1010, ORCHARD 0-0131 • CABLE: GARRETTAIR LOS ANGELES

GARRETT

AIRESEARCH MANUFACTURING COMPANY
Los Angeles, California

HYPERSONIC RESEARCH ENGINE PROJECT - PHASE II
STRUCTURES ASSEMBLY MODEL (SAM)
TEST REPORT (U)

DATA ITEM NO. 63.05
NASA CONTRACT NO. NASI-6666

Document No. AP-71-7702

Number of pages _____ 277 _____

Original date _____ 22 September 1971 _____

Prepared by _____ Engineering Staff _____

Edited by _____ L. F. Jilly _____

Approved by _____ Edward N. Harris
HRE Program Manager

FORM 2377, A 70

ACKNOWLEDGEMENTS

Acknowledgements for assistance in the completion of this document are extended to the following contributors:

O. Buchmann	Testing and Technical Supervision
W. Flieder E. Katinszky	Structural Analysis
M. Horner A. Vuigner	Heat Transfer Analysis

In addition, acknowledgements are extended to A. Watts and A. Wieting of the NASA-Langley 8-Foot High Temperature Structures Tunnel for their considerable efforts in setting up, reviewing, and controlling the computer processing of the large amounts of data.

AIRESEARCH MANUFACTURING COMPANY
Los Angeles, California

UNCLASSIFIED

Preceding page blank

71-7702

Page ii

CONTENTS

UNCLASSIFIED

CONTENTS (Continued)

UNCLASSIFIED

ILLUSTRATIONS

UNCLASSIFIED

ILLUSTRATIONS (Continued)

ILLUSTRATIONS (Continued)

UNCLASSIFIED

ILLUSTRATIONS (Continued)

ILLUSTRATIONS (Continued)

UNCLASSIFIED

ILLUSTRATIONS (Continued)

TABLES

TABLES (Continued)

I. INTRODUCTION

This report describes the wind tunnel testing performed on the Structures Assembly Model (SAM), in the 8-ft High Temperature Structures Tunnel (HTST) at the NASA-Langley Research Center, Hampton, Virginia. The data obtained from the tests was analyzed to determine the aerodynamic heating conditions, the cooling performance of the structure, and the applied structural loads. The results of these analyses are presented in this report. Where appropriate, comparison of the test results with the predicted performance of the cooled structure is made. A total of 47 wind tunnel runs involving 60 loading cycles was performed. The accumulated time in the wind tunnel stream was 30.7 min.

Test data, as such, is not presented in this report. Very extensive data was obtained during the tests and is on file at NASA-Langley and identifiable by the test and run numbers assigned by the 8-ft HTST. The complete test series consisted of Test No. 41, Runs 1 through 53, and Test No. 42, Runs 1 through 47. Run numbers are assigned whenever data is recorded on the data system during a tunnel run. For cases when the SAM was not inserted into the tunnel stream during a run, no data is on file. Section 5 of this report enumerates all of the tunnel runs during which data was obtained on the model.

1.1 PURPOSE AND SCOPE

The general approach to the SAM tests, as reflected in the specific test conditions, was based on not exceeding the basic HRE structural design capability. This capability is considered to be as follows:

Cross section, ΔT = $800^\circ F$ (cooled shells)

Hot surface, T = $1600^\circ F$ (maximum steady-state)

Hot surface, T = $1700^\circ F$ (maximum transient)

Cold structure, T = $1140^\circ F$ (maximum)

Design life = 10 hr at the above condition

Cycle life = 100 cycles at the above condition

Coolant pressure = 700 psia

At the same time, however, parameters were adjusted in such a way as to produce significant loading in the structure. Reflecting actual operating conditions, for example, cross-section ΔT's as high as $1400^\circ F$ were imposed, offsetting hot surface temperatures that were lower than design maximums.

UNCLASSIFIED

The specific objectives of the program fall into two broad categories
involving heat transfer and structural performance. Each of these is dis-
cussed in the following sections. The approach used to obtain and evaluate the
data is indicated.

I.I.I Heat Transfer

The main objectives of the test program relative to heat transfer were to
demonstrate the adequacy of the cooling system design, to verify the analytic
procedures used, and to compare the test results with analytic predictions.
Specific heat transfer test objectives can be divided into three main areas,
(I) aerodynamic heating, (2) cooling performance, and (3) transient response.

I.I.I.I Aerodynamic Heating

SAM aerodynamic heat loads were determined from test measurements of sur-
face metal temperatures, pressures, and tunnel conditions. The experimentally
determined heat loads are compared with the analytically predicted aerodynamic
heating. Since the analytic procedures used for calculating aerodynamic heat-
ing have little or no data available for correlation, a secondary objective was
to determine which analytic procedures correlate best with experimental data.

I.I.I.2 Cooling Performance

The SAM cooling system was evaluated from measurements of the hydrogen
flow rate, and the inlet and outlet conditions. The temperature and flow data
were used to establish the energy absorbed by the hydrogen. The experimental
cooling performance is compared with theoretical predictions. Pressure drop
characteristics of the flow routes were evaluated as was the ability of each
flow circuit to maintain surface metal temperatures at the analytically pre-
dicted values. The energy absorbed by the hydrogen fuel is compared with the
aerodynamic heat load in an energy balance on the engine.

I.I.I.3 Transient Response

From the surface and hydrogen temperature data, time constants were estab-
lished for the engine surfaces and hydrogen system. The experimental metal
temperatures and temperature gradients are compared with the theoretical tran-
sient temperature histories. Transient hydrogen temperature response is also
compared to analytic predictions.

I.I.2 Structural Evaluation

The principal objectives of the test program as related to structures were
to evaluate structural loading due to aerodynamic effects, structural capability
to withstand the applied loads, thermal fatigue performance of the engine, and
internal pressure-containment capability.

I.I.2.I Aerodynamic Loads

Loads caused by aerodynamic effects were monitored and evaluated by a com-
bination of accelerometer and strain gage data.

1.1.2.2 Dynamic Response

Accelerometers mounted at various locations in the engine were used to evaluate dynamic loads due to engine insertion and retraction as well as tunnel unstarts. The data was also used in the evaluation of possible engine resonant frequencies. The accelerometer data combined with the strain gage information was capable of indicating the duration and intensities of the various short-duration and highly impulsive transient loads.

1.1.2.3 Pressure-Containment Loads

The engine coolant was supplied at an inlet pressure of 600-700 psia with 500-550 psia pressure in the dump plenum. This pressurized all of the coolant passages to levels that would be imposed at Mach 8 flight conditions.

1.1.2.4 Thermal Fatigue

Thermal fatigue damage accumulated in selected areas during the entire test program was evaluated. The data used for this was obtained from the various thermocouple measurements and the heat transfer analysis. Temperature-time histories at the critical engine locations were used to determine the ΔT effect due to the startup and shutdown sequences. The specific locations were determined by the operating conditions and the configuration of the re-straining structure. In the case of the fuel injectors located in the spike and outer shell, localized cycling of the structure was accomplished by in-jecting hot hydrogen.

1.1.2.5 Assembly Interaction

Inherent to the test is the evaluation of structural loads due to the interaction of the components as a basic engine assembly. One of the design objectives was to limit interaction loads by suitable devices; e.g., flow routing for minimum ΔT at flow route interfaces and temperature-matching at structural interfaces. Similarly, the load path to the mounts is through the actuator, struts, and outer shell. The assumptions regarding load flow were evaluated by the tests on a gross basis. The high temperatures in many of the critical areas limited the use of gaging and the possibility of detail measure-ments.

1.2 APPLICABLE DOCUMENTS

The following reports served as the basis for the wind tunnel testing of the SAM:

NASA Statement of Work L-4947-B (Revised), 3 September 1968

SAM Test Plan, Data Item 64.01, AiResearch Report AP-70-6120,
11 March 1970

SAM Test Procedure, Data Item 65.01, AiResearch Report AP-70-6302,
23 June 1970

2. DESCRIPTION OF SAM

The test item as furnished to the test facility, consisted of the SAM and its associated manifolding and valves, and of support equipment necessary to control the SAM subsystems. The configuration and functions of the various components and subsystems are discussed in the following paragraphs.

2.1 FLIGHT-DESIGNED COOLED STRUCTURE

The basic configuration of the SAM is shown in AiResearch Drawing 980800, Sheets 1 and 2 (attached at end of this report). Sheet 2 shows the external water and hydrogen manifolding for the SAM and defines the SAM/wind-tunnel interfaces. Figure 2.1-1 shows the nomenclature and overall dimensions of the SAM. The SAM and its manifolding systems were delivered as separate items and assembled at the facility. Instrumentation and electrical lines on the assembly were terminated at connectors compatible with the facility interface.

Figure 2.1-2 shows the SAM hydrogen system schematically. The internal flow routing for the cooled structure is shown in Figure 2.1-3. All of the plumbing and valves shown in the figures form a part of the SAM, as shown on either sheet of Drawing 980800. The system has a single inlet connection and a single outlet connection. At the inlet to the SAM system, the facility provides hydrogen at ambient or at $160°R$, and at 900 to 1100 psia. The exhaust from the SAM system is to the facility vent line.

The basic system consists of the valves, designated PCV (pressure control valve), CRV (coolant regulating valve), FDV (fuel dump valve), and ICV (injection control valves). Valve operation is as follows:

PCV--This is a pressure regulator, sensing the pressure in the SAM dump plenum, which is to be controlled at 500 to 550 psia. A drop in plenum pressure causes the PCV to open in response to an electrical signal. The PCV is a ball-type valve, electrically actuated.

CRV--These valves are located at the inlet to each of the five engine flow routes. CRV's 1 through 4 are ball-type valves, pneumatically actuated, using solenoid control and position feedback by means of a potentiometer, while CRV 5 is a manually operated needle valve. These valves are set prior to testing to provide the correct coolant flow in each of the routes for the test condition planned for the specific test. The presetting is done using room temperature nitrogen and is based on analytical and experimental predictions of flow requirements. During the test itself,

OUTER SHELL

STRUTS

NOZZLE
ACTUATOR

WATER-COOLED
SUPPORT
STRUCTURE

86-91 IN.

WATER-COOLED COWL-PYLON

SPIKE

INNER SHELL

LEADING EDGE

9 IN.

50 IN.
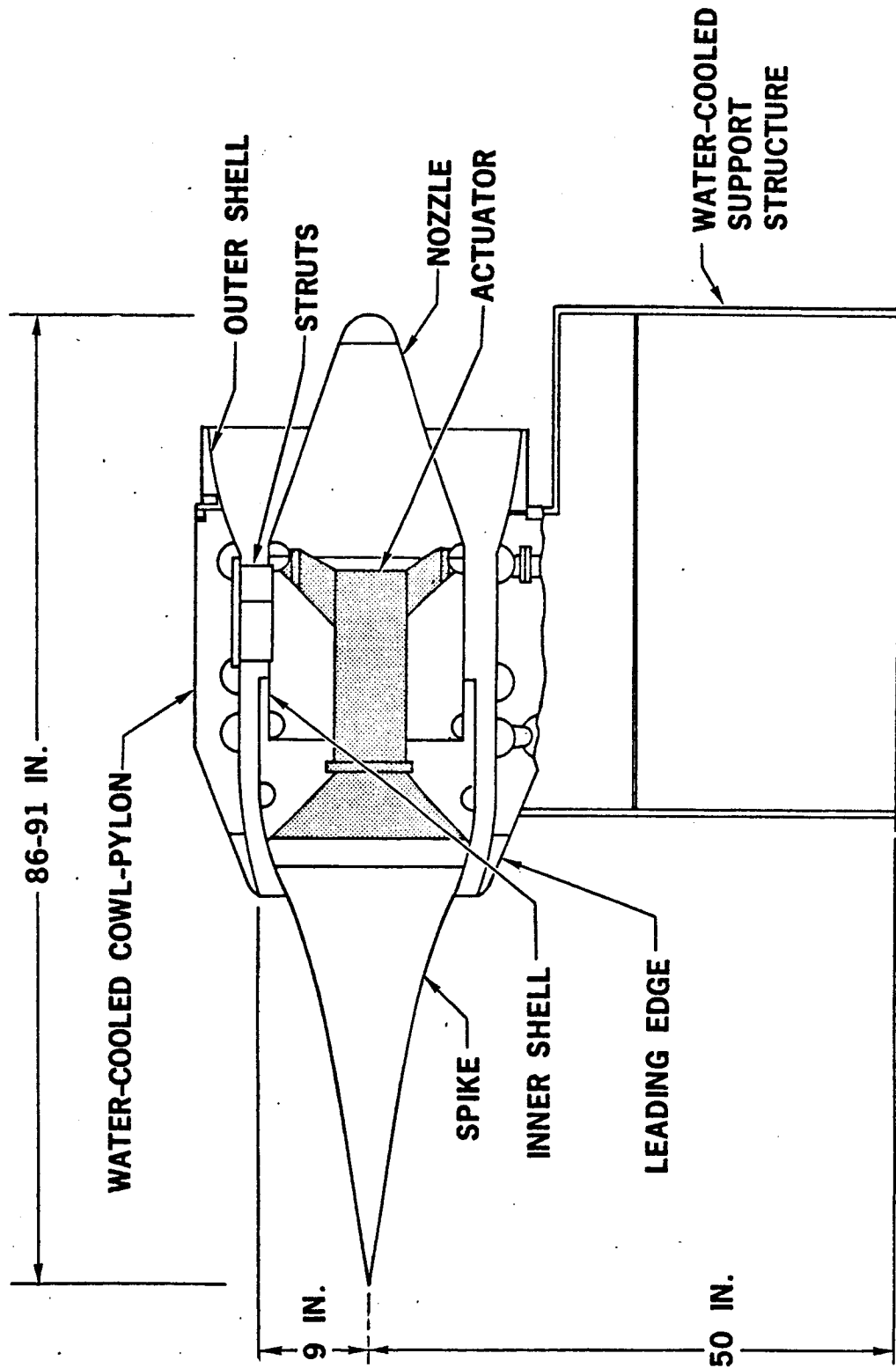
Figure 2.1-1. Structures Assembly Model (SAM)
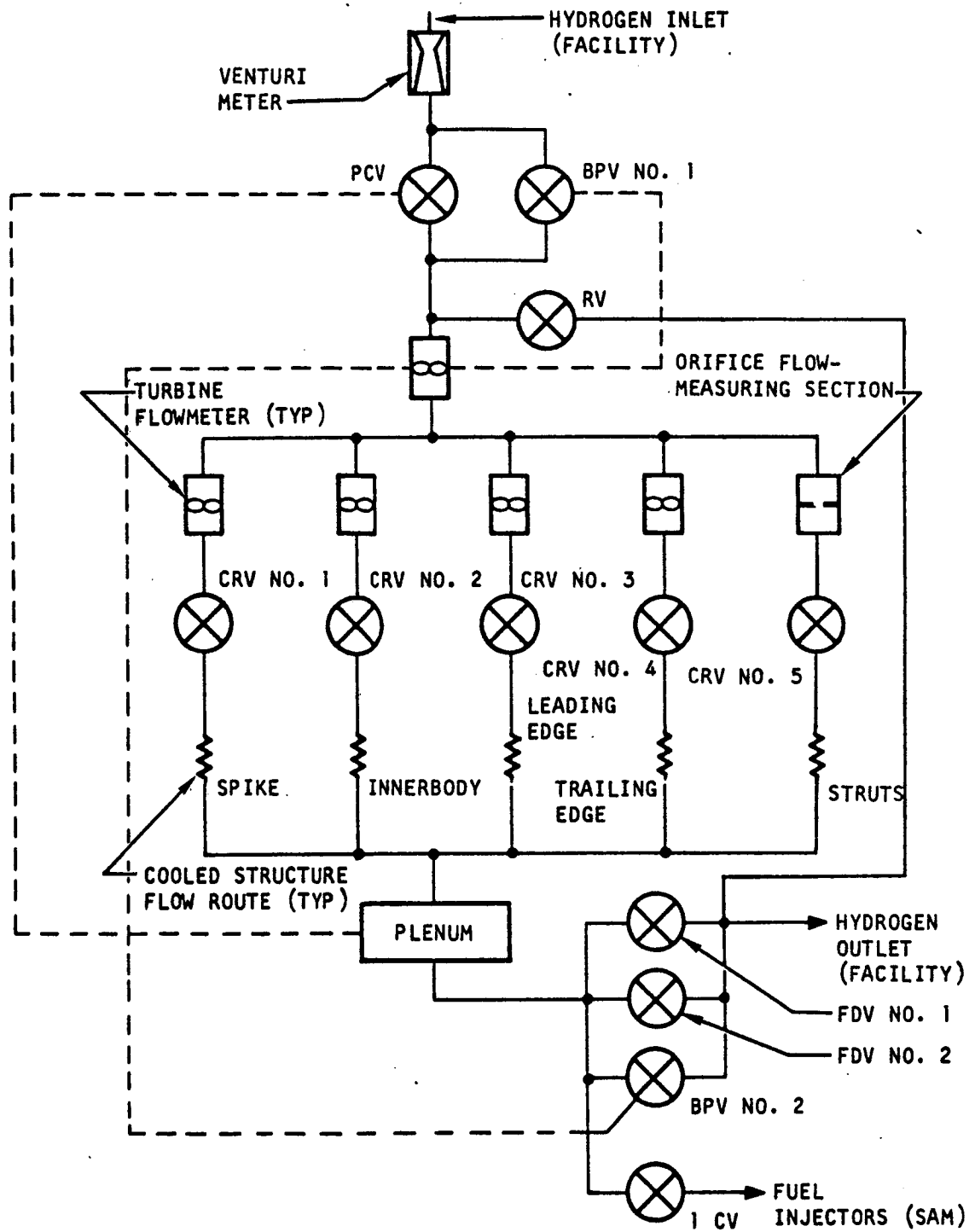
Figure 2.1-2. HRE/SAM Hydrogen System

S-53586
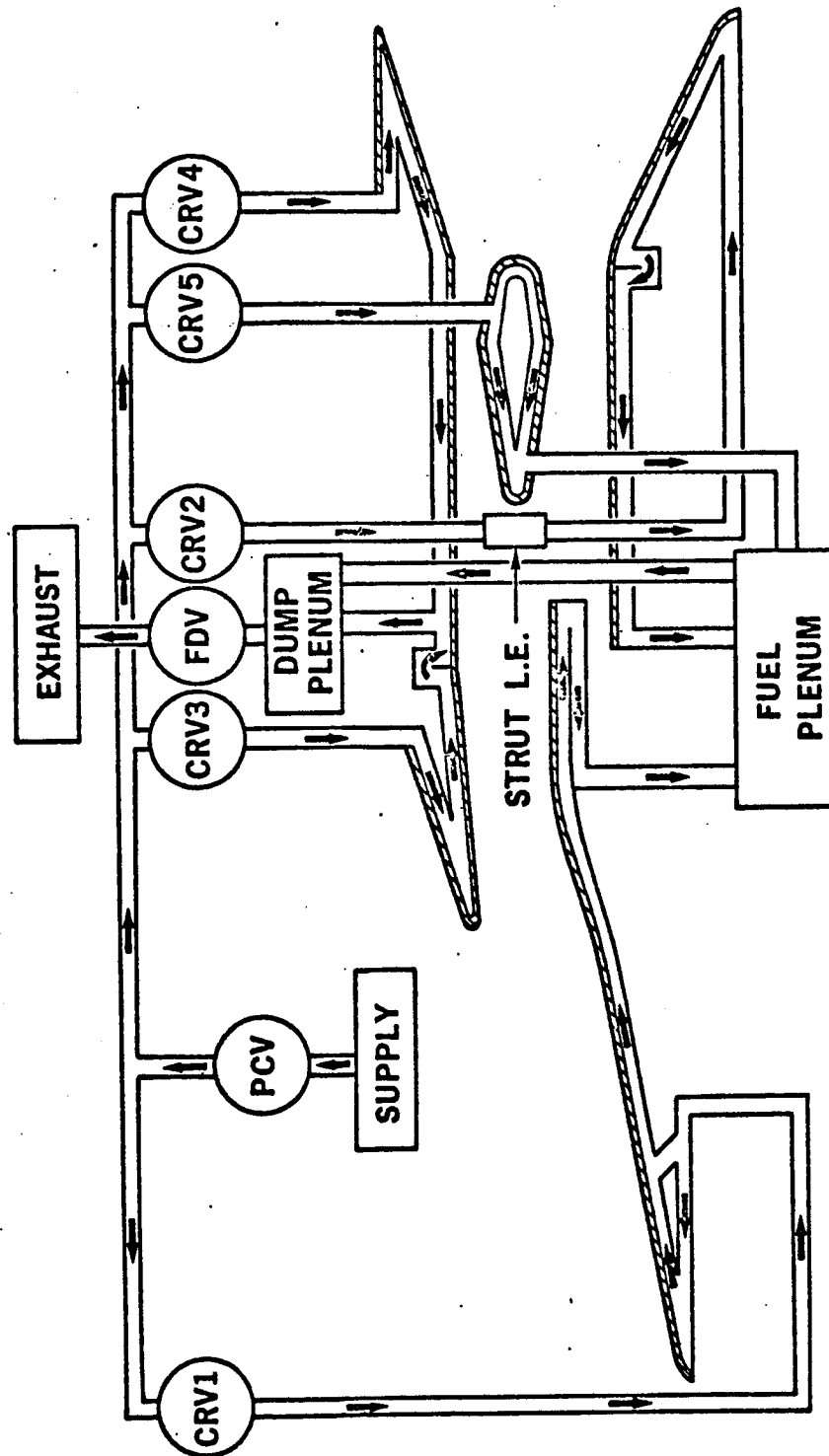
Figure 2.1-3. SAM Flow Routing

these valves are not adjusted, although the capability exists for CRV's I through 4.

FDV--Two valves are used to serve the dump-valve function. They are controlled by the temperature-control system to maintain the maximum coolant operating temperature from any of the flow routes below a preset maximum. Excess temperature in any of the flow routes causes the FDV's to open, plenum pressure to decrease, and the PCV to open and restore plenum pressure to the set range. Positioning of the FDV's is in parallel.

ICV--This valve is opened to provide for discharge of the coolant to the inner and outerbody fuel injectors. Initiation of valve opening is manual. The FDV's and ICV are programmed to operate in push-pull fashion to minimize perturbations to the system during the switchover from dump to injection flow, and conversely. Following the switchover, the control system retains active control over the FDV's and will open these valves if an overtemperature condition develops. The open position of the ICV, on the other hand, is fixed at a preselected value for a particular test.

In addition to the basic system valves, the system includes three failure-protection valves. These are:

BPV I and BPV 2 (Bypass Valve)--These are solenoid-operated, pneumatically driven valves which open when the system flow, as sensed by the total-flowmeter, decreases to an unacceptable level. The system does not discriminate between failure of the PCV and of the FDV but will open the BPV's as though both had failed in the closed position.

RV (Relief Valve)--This valve is a conventional, spring-loaded relief valve used to limit upstream system pressure. Flow through this valve is directed into the vent line.

Failure mode of the bypass valves is the open position for either electrical or pneumatic failures.

System valves were not required to provide zero-leakage shutoff for the selected plumbing configuration. This is particularly important for the hot valves, where the occurrence of minor leakage did not require their refurbishment.

2.2 WATER SYSTEMS

Figure 2.2-1 shows the two SAM water systems. The model facility interface is indicated. The facility provides a single inlet to each of the two systems. Each of the five flow routes has a manual valve at the outlet which is used to adjust flow rate through the routes. The flow rate in each individual route is determined from a pressure-drop-versus-flow-rate calibration prior to test.
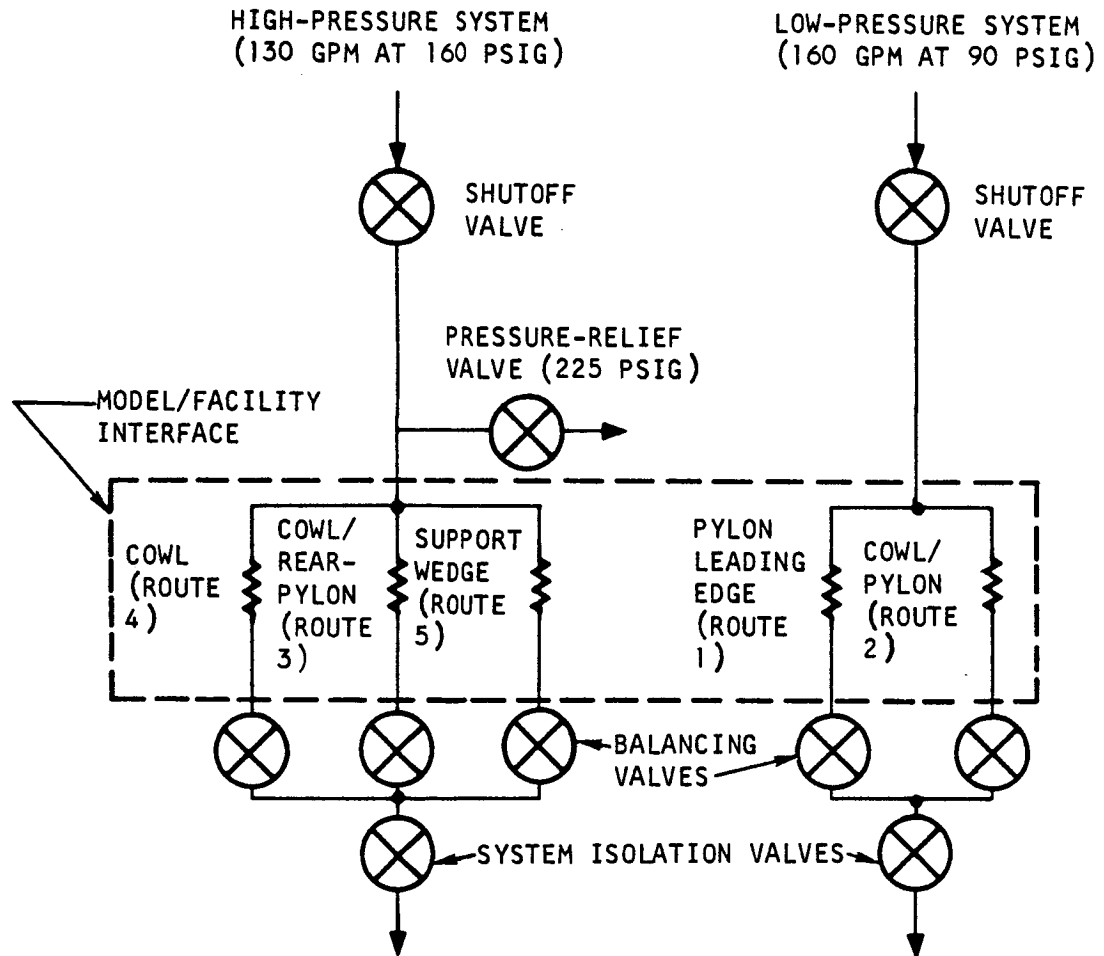
Figure 2.2-1. HRE/SAM Water Systems

AIRESEARCH MANUFACTURING COMPANY
Los Angeles, California

2.3 SUPPORT EQUIPMENT

The support equipment required for testing of the model includes the temperature-control system, the pressure-control system, and the inlet spike actuation-control system.

2.3.1 Temperature-Control System (TCS)

The TCS provides for control of all hydrogen system valves, for hydrogen system flow rate monitoring and flowmeter signal conditioning, and for inter-locks with the facility. The system is shown schematically in Figures 2.3-1 and 2.3-2. The functions of the temperature-control system are as follows:

(a) Automatic control of hydrogen coolant system flow by modu-lating the fuel dump valve (FDV) as a function of individ-ual flow route temperature. An auctioneering circuit selects the highest temperature in any flow route and adjusts flow to maintain this temperature within a preset maximum. When the FDV reaches a predetermined opening approaching 100 per-cent of system flow capacity, the TCS commands a system shutdown.

(b) Provisions for opening the injection flow-control valve and closing the fuel dump valve in such a way as to maintain approximately constant flow during the transition. Initiation of ICV opening occurs manually.

(c) Provisions for monitoring total-flow rate and, in each of the four main flow routes, percentage of total-flow rate on the face of the panel. Closed-loop adjustment of the coolant regulating valves (CRV's) is also provided for on the panel.

(d) Capability of opening the ICV, FDV, and BPV in response to a facility signal preceding system purge.

(e) Ability to issue shutdown commands based on water flow (as determined with pressure-differential switches), a manual shutdown trip, a low-hydrogen-flow alarm from the total-flowmeter, and a signal from the facility. Any shutdown signal also results in a command to the inlet spike actu-ation control system for closing of the inlet.

2.3.2 Inlet Spike Actuation Control System (ISACS)

The functions of the ISACS include the following:

(a) Spike position control. This is accomplished by presetting the desired spike position and commanding a retraction by means of manual switching. Adjustment of the pre-selected position is possible,as is extension and retraction by manual ramping.

Figure 2.3-I. Functional Diagram of Temperature-Control System
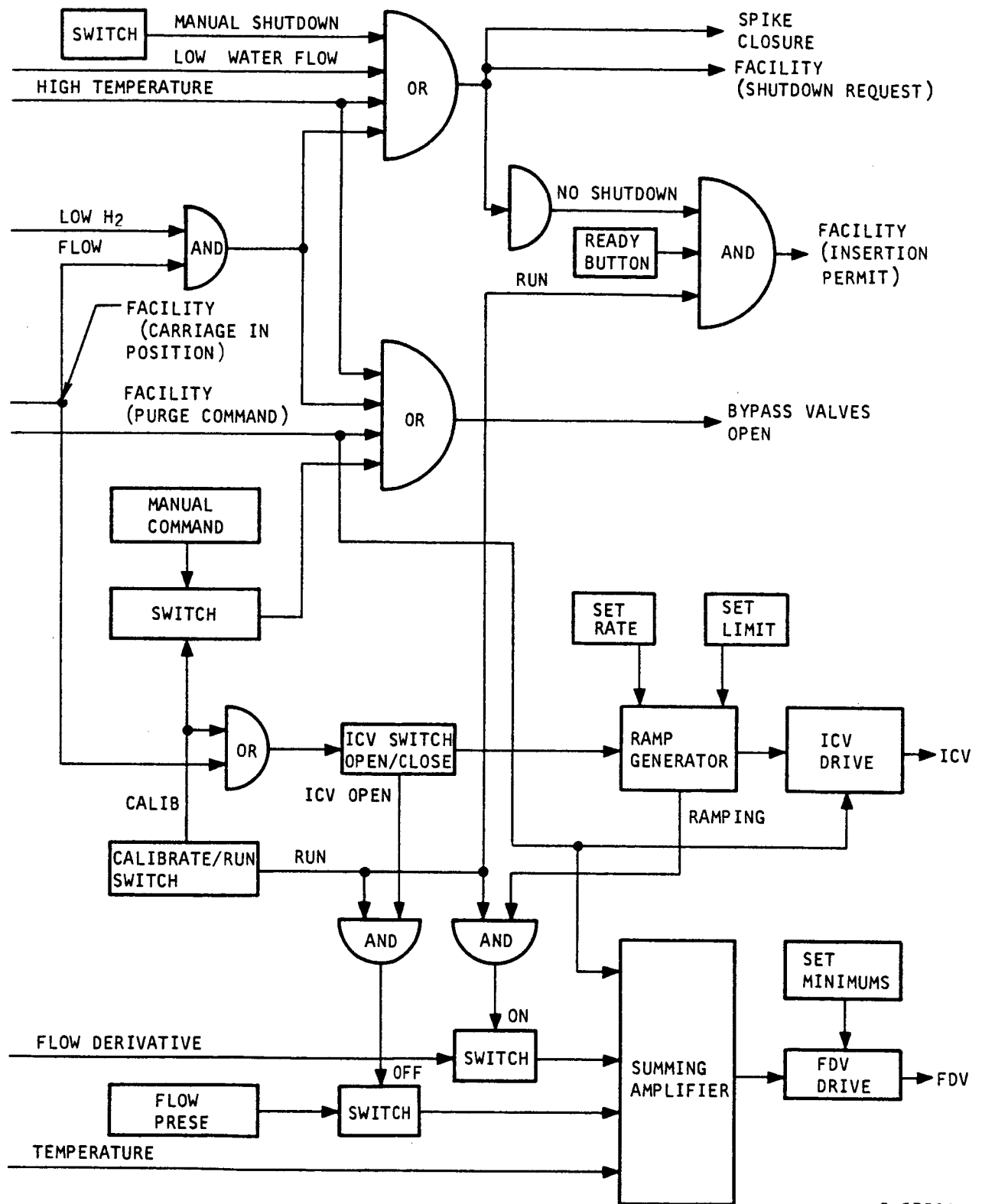
S-53589

Figure 2.3-2. Logic Diagram for SAM Temperature-Control System

S-53588

(b) Output of signals proportional to spike position and position error to the data acquisition system.

(c) Automatic command of spike closing on signal from the temperature control system.

2.4 INSTRUMENTATION

Much of the instrumentation (hydrogen thermocouples, hot skin thermocouples, and static pressure taps) associated with the basic flightweight components is installed as part of the manufacturing process. This portion of the instrumentation was defined at a very early stage. Accelerometers, strain gages, and cold-wall thermocouples were installed as required, as were thermocouples and pressure taps in the hydrogen lines.

The instrumentation of the coolant water systems was aimed at permitting verification of operating conditions (flow rates, pressure drop, and water temperatures). Performance data (aerodynamic heating and metal temperatures) on the water-cooled cowl/pylon and support wedge were not obtained, in keeping with the test objectives.

Tables 2.4-1 through 2.4-6 contain a complete listing of instrumentation installed on SAM. The tables are arranged by basic component and by assembly. The status at the start of the testing is indicated. Although some switching was done from time to time, the tables reflect the hookup for most of the tests. As the tests progressed, also, additional instrumentation became defective. In no case was the loss serious enough to affect data analysis, either because of redundancy or because the loss occurred late enough in the test series for data to have been obtained.

The assignment of instrumentation to specific recording devices reflects availability as follows:

Data Acquisition System	Channels
Beckman B-210	99
SEL	90
Total	189
Less facility requirements	20
Total available	169
FM tape	26
CEC recorders	60

The Beckman B-210 has a 2-Hz response and the SEL has a 20-Hz response. This response difference was not a primary consideration and, in general, the two

TABLE 2.4-1

INLET SPIKE (980770/980803)

Description	No.	CW Aft θ Degree	Range (psia, °R, mv)			Recording DAS		Recording CEC		Monitor			Test Group			Remarks
			Design	Maximum	Transducer	B-210	SEL	100~	500~	FM	B-210	Strip Chart	1	2	3	
Hydrogen																
Inlet	P71	0	15-650	1065	1000		X						X	X		
Injector	P85	93	0-400	600	500		X							X		
~~Injector~~	~~P84~~	~~17~~	~~0-400~~	~~600~~	~~500~~		~~X~~						~~X~~	~~X~~		Grounded
Outlet	P87	70	15-550	1065	1000		X						X	X		
Outlet	P88	154	15-550	1065	1000		X						X	X		
Gas																
Station 0.59	P70	-	7-25	25	25	X							X	X		
24.00	P72	0	0.5-2.0	15	5	X							X	X		
24.00	P73	90	0.5-2.0	15	5	X							X	X		
24.00	P74	180	0.5-2.0	15	5	X							X	X		
24.00	P75	270	0.5-2.0	15	5	X							X			
35.70	P76	0	2.0-10	15	10	X							X	X		
35.70	P77	90	2.0-10	15	10	X							X			
35.70	P78	180	2.0-10	15	10	X							X	X		
35.70	P79	270	2.0-10	15	10	X							X	X		
42.00	P80	0	10-52	108	50	X							X	X		
42.00	P81	90	10-52	108	50	X							X	X		
42.00	P82	180	10-52	108	50	X							X	X		
42.00	P83	270	10-52	108	50											Spare
44.30	P86	0	8-42	84	50	X							X	X		
Pressure Channels	18					13	4	-	-	-	-	-	16	14		
Hydrogen																
Inlet	T13	90	200-560				X						X	X		
Injector	T22	225	500-1600				X							X		
Outlet	T25	28	200-1600			X					X		X	X		
Outlet	T26	334	200-1600				X						X	X		
Control	T28	30	800-1500				X						X	X		
Control	T29	90	800-1500				X							X		
Control	T30	150	800-1500				X						X	X		
Control	T31	210	800-1500				X						X	X		
Control	T32	270	800-1500				X						X	X		
Control	T33	330	800-1500				X						X	X		
Metal																
Station 21.00	T14	5	200-600			X							X	X		
~~21.00~~	~~T15~~	~~355~~	~~200-600~~													
35.70	T16	5	200-800			X							X	X		
35.70	T17	355	200-600			X							X	X		
40.50	T18	5	200-800			X							X	X		
~~40.50~~	~~T19~~	~~355~~	~~200-600~~			~~X~~							~~X~~	~~X~~		Open
Injector	T20	12	400-1600				X						X	X		
Injector	T21	102	400-1600					X					X	X		
44.30	T23	5	200-1100				X						X	X		
44.30	T24	355	200-1400				X						X	X		
Cone	T27	5	500-700			X							X	X		
Temperature channels	19					6	12	1	-	-	1	-	17	19		
Strain																
Station 44.50	S1	30	0-2.5	3						P*	X			X	X	
44.50	S2	90	0-1.3	2						P	X			X	X	
44.50	S3	0/180	0-0.5	1						P	X			X	X	
~~44.50~~	~~S4~~	~~90/270~~	~~0-30~~								~~X~~					

*P designates requirements for playback after test

TABLE 2.4.-I (Continued)

Description	No.	CW Aft θ Degree	Range (psia, °R, mv) Design	Range (psia, °R, mv) Maximum	Range (psia, °R, mv) Transducer	Recording DAS B-210	Recording DAS SEL	Recording CEC 100~	Recording CEC 500~	Recording FM	Monitor B-210	Monitor Strip Chart	Test Group 1	Test Group 2	Test Group 3	Remarks
Strain (cont)																
Strain channels	3					-	-	-	-	3	-	-	3	3		
Accelerometer**																
Cone	A4(U)	120	25-1000	1250						X			X	X		
Cone	A5(U)	90	25-1000	1250						X			X	X		
Accelerometer channels	2									2			2	2		
Totals	42					19	16	-	-	5	-	-	36	36		

**(U) is uniaxial accelerometer

TABLE 2.4-2
INNER SHELL (980750/980802)

Description	No.	CW Aft θ Degree	Range (psia, °R, mv) Design	Maximum	Transducer	Recording DAS B-210	SEL	CEC 100~	500~	Monitor FM	B-210	Strip Chart	Test Group 1	2	3	Remarks
Hydrogen																
Inlet	P68	174	15-650	1065	-											
Inlet	P69	240	15-650	1065	1000		X							X		
Outlet	P58	5	15-550	1065	1000											Spare
Outlet	P59	185	15-550	1065	1000		X						X	X		
ΔP*	ΔP4	-	0-5	10	5		X						X	X		
Gas																
Station 58.75	P60	0	1.5-6	17	10	X							X	X		
58.75	P61	80	1.5-6	17	10	X							X	X		
58.75	P62	180	1.5-6	17	10	X							X	X		
62.00	P63	0	1-4	16	5	X							X	X		
62.00	P64	80	1-4	16	5	X							X			Slow
62.00	P65	180	1-4	16	5	X							X	X		
~~62.00~~	~~P66~~	~~280~~	~~1-4~~	~~16~~	~~5~~	~~X~~							~~X~~			Plugged
64.00	P67	0	1-4	16	5	X							X	X		
Bellows	P105	180	3-12	35	50				X				X	X		
Pressure channels	13					7	3	-	1	-	-	-	10	10		
Hydrogen																
Inlet	T53	354	200-560				X						X	X		
Outlet	T34	175	200-1700			X					X		X	X		
Outlet	T35	355	200-1700				X						X	X		
Control	T36	30	800-1600				X						X	X		
Control	T38	150	800-1600				X						X	X		Grounded
Control	T40	270	800-1600				X						X	X		
Control	T41	330	800-1600				X						X	X		
Metal																
Station 54.00	T42	0	200-2000				X						X	X		
54.00	T43	5	200-1700				X						X	X		
Injector	T44	0	500-1200				X						X	X		
Injector	T45	0	500-1200			X							X	X		
Socket	T46	32	500-1200				X						X	X		
~~58.25~~	~~T47~~	~~0~~	~~200-1800~~			~~X~~							~~X~~	~~X~~		
58.25	T48	5	200-1600			X							X	X		
Injector	T49	0	400-1200			X								X		
62.30	T50	5	200-1500			X							X	X		
62.30	T51	0	200-1300			X							X	X		
Actuator mounting	T52	30	450-700			X								X		No Ground (Gas Temp.)
Temperature channels	17					7	10	-	-	-	1	-	15	17		
Totals	30					14	13	-	1	-	1	-	25	27		

*ΔP4 = P68-P59

TABLE 2.4-3

NOZZLE (980740/980801)

Description	No.	CW Aft θ Degree	Design	Maximum	Transducer	DAS B-210	DAS SEL	CEC 100~	CEC 500~	FM	Monitor B-210	Monitor Strip Chart	TG 1	TG 2	TG 3	Remarks
Hydrogen																
Inlet	P96	-	15-650	1065	1000	X					X		X	X		
Outlet	P89	24	15-650	1065	1000		X						X	X		
Spare	~~P104~~															
Gas																
Station 76.50	P90	90	0.5-4.0	15	5	X							X			
76.50	P91	175	0.5-4.0	15	5	X							X	X		
76.50	P92	270	0.5-4.0	15	5	X							X			
76.50	P93	355	0.5-4.0	15	5	X							X	X		
81.40	P94	175	0.5-4.0	15	5	X							X			
81.40	P95	355	0.5-4.0	15	5	X							X	X		
Pressure channels	8					7	1	-	-	-	-	-	8	5		
Hydrogen																
Inlet	T59	-	200-560				X						X	X		
Outlet	T54	132	200-800				X						X	X		
Metal																
~~Station 68.60~~	~~T55~~	~~345~~	~~200-900~~													
68.60	T56	350	200-800			X							X	X		
75.60	T57	345	200-600			X							X	X		
75.60	T58	350	200-600			X								X		
Temperature channels	5					3	2	-	-	-	-	-	4	5		
Totals	13					10	3	-	-	-	1	-	12	10		

TABLE 2.4-4
LEADING EDGE (980820/980801)

Description	No.	CW Aft θ Degree	Range (psia, °R, mv) Design	Maximum	Transducer	DAS B-210	SEL	CEC 100~	500~	FM	Monitor B-210	Strip Chart	Test Group 1	2	3	Remarks
Hydrogen																
Inlet	P13	0	15-700	1065	1000		X				X		X	X		
~~Inlet~~	~~P14~~	~~180~~	~~15-700~~	~~1065~~	~~1000~~		~~X~~						~~X~~	~~X~~		Plugged
Outlet	P28	5	15-650	1065	1000		X						X	X		
Outlet	P29	185	15-650	1065	1000			X					X	X		
ΔP*	ΔP9						X						X	X		
Gas																
O.D. Station																
~~37.45~~	~~P1~~	~~5~~	~~1.5-5.5~~	~~15~~	~~10~~	~~X~~							~~X~~	~~X~~		Plugged
37.45	P2	95	1.5-5.5	15	10	X							X			
37.45	P3	185	1.5-5.5	15	10	X							X	X		
37.45	P4	275	1.5-5.5	15	10	X							X			
39.10	P5	5	2-7	15	10	X							X	X		
39.10	P6	95	1-3	15	5											Spare
39.10	P7	185	1-3	15	5	X							X	X		
39.10	P8	275	1-3	15	5											Spare
40.25	P9	5	2-7	15	10	X							X	X		
40.25	P10	95	1-3	15	5	X							X	X		
40.25	P11	185	1-3	15	5	X							X	X		
40.25	P12	275	1-3	15	5											Spare
I.D. Station																
37.45	P15	0	4-16	152	50	X							X	X		
37.45	P16	180	4-16	152	50	X							X	X		
38.20	P17	0	5-20	144	50	X					X		X	X		
38.20	P18	90	5-20	144	50	X							X	X		
~~38.20~~	~~P19~~	~~180~~	~~5-20~~	~~144~~	~~50~~	~~X~~					~~X~~					
38.20	P20	270	5-20	144	50	X							X			
39.20	P21	0	6-24	137	50	X							X	X		
39.20	P22	180	6-24	137	50	X							X	X		
40.00	P23	0	9-35	125	50	X							X	X		
41.65	P24	0	12-48	112	50	X							X	X		
41.65	P25	90	12-48	112	50	X							X	X		
41.65	P26	180	12-48	112	50	X							X	X		
41.65	P27	270	12-48	112	50	X							X	X		
Pressure channels	27					20	3	1	-	-	2	-	24	21		
Hydrogen																
Outlet	T5	168	200-1200				X						X			
Inlet	T6	185	200-560				X						X	X		
Outlet	T10	0	200-1200			X					X		X	X		
~~Outlet~~	~~T11~~	~~183~~	~~200-1200~~				~~X~~						~~X~~	~~X~~		
Inlet	T63	20	200-560													Spare
Metal																
O.D. Station																
38.20	T1	5	200-600			X							X	X		
38.40	T3	0	200-600			X							X	X		
40.25	T2	0	200-600			X							X	X		
40.20	T4	5	200-600			X							X	X		
I.D. Station																
~~37.60~~	~~T8~~	~~0~~	~~200-600~~				~~X~~									
~~40.40~~	~~T7~~	~~0~~	~~200-1200~~			~~X~~										
40.40	T9	5	200-800			X							X	X		
Manifold	T12	0	200-1200			X								X		
Temperature channels	10					7	2	-	-	-	1	-	7	9		
Totals	37					27	5	1	-	-	3	-	31	30		

*ΔP9 = P13-P28

TABLE 2.4-5
OUTER SHELL (980768/980802)

Description	No.	CW Aft θ Degree	Range (psia, °R, mv) Design	Maximum	Transducer	Recording DAS B-210	SEL	CEC 100~	500~	FM	Monitor B-210	Strip Chart	Test Group 1	2	3	Remarks
Hydrogen																
~~Inlet (LE)~~	P30	20	15-650	1065	-	X										
Inlet (LE)	P31	202	15-650	1065	-											
~~Inlet (TE)~~	P56	5	15-650	1065	1000		X						X	X		Plugged
Outlet	P40	0	15-550	1065	1000		X						X	X		
Outlet	P41	180	15-550	1065	1000		X							X		
Injector	P34	30	0-400	600	500		X							X		
Injector	P35	190	0-400	600	500		X							X		
Plenum	P97	90	15-550	1065	1000	X					X		X	X		
Aft support	P107	180	15-650	1065	-											
ΔP*	ΔP5	-	0-5	10	5		X						X	X		
~~ΔP*~~	~~ΔP6~~	-	0-5	10	5		X						X	X		P56
ΔP*	ΔP7	-	0-5	10	5		X						X	X		
Gas																
Station 46.00	P32	5	7-27	75	50	X							X	X		
46.00	P33**	189	7-27	75	50											Spare
~~50.40~~	P36	0	3.5-14	55	15	X							X	X		Plugged
~~50.40~~	P37	95	3.5-14	55	15	X							X			Slow
~~50.40~~	P38	185	3.5-14	55	15	X							X	X		Slow
50.40	P39**	275	3.5-14	55	15											Spare
54.13	P42	145	3-12	25	15	X							X	X		
54.13	P43**	215	3-12	25	15											Spare
56.70	P44	0	2-7	17	10	X							X	X		
56.70	P45**	80	2-7	17	10										r	Spare
56.70	P46	180	2-7	17	10	X							X	X		
56.70	P47	260	2-7	17	10	X							X			
60.40	P48	0	1.5-5	16	5	X							X	X		
60.40	P49	80	1.5-5	16	5	X							X			
60.40	P50**	180	1.5-5	16	5											Spare
60.40	P51	260	1.5-5	16	5	X							X	X		
68.75	P52	10	1-3	15	5	X							X	X		
~~68.75~~	P53	185	1-3	15	5	X							X	X		Slow
71.50	P54	10	0.5-2	15	5	X							X	X		
71.50	P55**	185	0.5-2	15	5											Spare
Pressure channels	25					11	6	-	-	-	1	-	14	16		
Hydrogen																
Inlet (LE)	T60	354	200-1200				X						X	X		
Inlet (TE)	T98	45	200-560				X						X	X		
Injector	T64	50	500-1600				X							X		
Injector	T65	330	500-1600				X							X		
Outlet	T77	90	200-1700				X						X	X		
Outlet	T78	270	200-1700			X					X		X	X		
Plenum	T101	240	200-1700				X						X	X		
Aft support	T96	40	200-800													Spare
Aft support	T97	140	200-800													Spare
LE cont	T70	35	800-1600				X						X	X		
~~LE cont~~	T71	90	800-1600													Open
LE cont	T72	150	800-1600				X						X	X		
~~LE cont~~	T73	210	800-1600				X						X	X		Short
LE cont	T74	270	800-1600				X							X		
LE cont	T75	330	800-1600				X						X	X		
TE cont	T80	35	800-1600				X						X	X		
TE cont	T81	90	800-1600				X						X	X		
TE cont	T82	150	800-1600				X						X	X		

*ΔP5 = P31 - P40
ΔP6 = P56 - P107
ΔP7 = P107 - P40

**These pressure lines respond slowly

AIRESEARCH MANUFACTURING COMPANY
Los Angeles, California

TABLE 2.4-5 (Continued)

Description	No.	CW Aft θ Degree	Range (psia, °R, mv) Design	Maximum	Transducer	Recording DAS B-210	SEL	CEC 100~	500~	Monitor FM	B-210	Strip Chart	Test Group 1	2	3	Remarks
Hydrogen (cont)																
TE cont	T83	207	800-1600				X						X	X		
TE cont	T84	270	800-1600				X							X		
TE cont	T85	330	800-1600				X						X	X		
Metal																
Station 46.00	T61	358	200-1500				X						X	X		
46.00	T62	354	200-1200				X						X	X		
Injector	T66	40	500-1600			X								X		
50.40	T67	5	200-1800				X						X	X		
50.40	T68	10	200-1600				X						X	X		
50.40	T69	180	200-1600				X							X		
Outlet	T76	45	300-1600			X							X	X		
Outlet	T79	45	300-1600				X						X	X		
54.13	T86	180	200-1800				X						X	X		
53.88	T87	8	200-1600			X							X	X		
54.13	T88	210	200-1600				X						X	X		
54.13	T131	182	200-1600			X							X	X		
54.13	T132	187.5	200-1600			X								X		
54.13	T133	195	200-1600			X								X		
54.13	T134	202.5	200-1600			X								X		
Injector	T89	45	500-1200			X								X		
Injector	T90	45	500-1200				X						X	X		
Injector	T91	45	500-1200			X								X		
62.30	T92	0	200-1300				X						X	X		
62.30	T93	5	200-1100				X						X	X		
62.30	T135	22	200-1300			X								X		
Aft support	T94	180	300-700			X								X		
Aft Support	T95	180	300-700			X								X		
70.10	T99	5	200-700			X							X	X		
70.10	T100	185	200-600			X							X	X		
Temperature channels	44					15	27	-	-	-	1	-	28	42		
Totals	69					26	33	-	-	-	2	-	42	58		

TABLE 2.4-6
ASSEMBLIES (980802, 980801, 980800)

Description	No.	CW Aft θ Degree	Range Design	Maximum	Transducer	DAS B-210	SEL	CEC 100~	500~	FM	B-210	Strip Chart	Test Grp 1	2	3	Remarks
980802 **Hydrogen**																
~~Plenum~~	P98	345	15-550	1065	1000		X						X	X		Plugged
~~Plenum~~	P99	15	15-550	1065	1000											
Pressure channels	-					-	-	-	-	-	-	-				
Plenum	T105A	345	200-1700				X						X	X		
Plenum	T105B	15	200-1700													Spare
~~Strut. Cont.~~	T102	30	700-1600			X							X	X		
Strut. Cont.	T103	150	700-1600				X						X	X		
~~Strut. Cont.~~	T104	270	700-1600				X						X	X		Grounded
Strut. Cont.	T106B	210	700-1600		-		X						X	X		
Metal																
Heater	T107	-	500-2000													
Heater	T109	-	500-2000													} Control Only
Heater	T111	-	500-2000													
~~Strut~~	T115	150	300-1400				X						X	X		
~~Strut~~	T116	150	300-1200			X								X		} Not Installed
~~Strut~~	T117	150	300-1200			X								X		
Temperature channels	7					-	3	-	-	-	-	-				
Totals	7					-	3	-	-	-	-	-	3	3		
980801 **Strain**																
Act. Hsg.	S5	0/180	0-5.0	7.5					P*	X			X	X		
Act. Leg	S6	330	0-3.0	3.5					P	X			X	X		
Act. Leg	S7	90	0-0.8	1.0						X			X	X		
~~Strut~~	S8	90	0-30						X							
~~Strut~~	S9	330	0-30						X							
~~Mount pad~~	S10	Left	0-30							X						
~~Mount pad~~	S11	Right	0-30							X						
Block	S12	-	0-1.5	2.0						X			X	X		
Block	S13	-	0-15.0	20.0					P	X			X	X		
Flexure	S16	Left	0-4.0	5.0						X			X	X		
Flexure	S17	Right	0-4.0	5.0						X			X	X		
Act. clevis	S18	-	0-6.0	7.5					P	X			X	X		
Act. clevis	S19	-	0-6.0	7.5						X			X	X		
Strain channels	9					-	-	-	-	9	-	-	9	9		
Metal																
Bellows	T106A	0	500-1200			X								X		
~~Thrust Block~~	T118		500-800			X								X		
Accelerometer **																
Act. leg	A1(U)	30	25-1000	1250						X			X	X		
Act. leg	A2(U)	210	25-1000	1250						X			X	X		
Act. leg	A3(T)	90	10-250	300						X			X	X		
Block	A6(T)	-	10-250	300						X			X	X		
Accelerometer channels	8					-	-	-	-	8	-	-	8	8		
Totals	18					1	-	-	-	17	-	-	17	18		

*P designates requirement for playback after test

**(U) is uniaxial
(T) is triaxial

TABLE 2.4-6 (Continued)

Description	No.	CW Aft θ Degree	Range (psia, °R, mv) Design	Maximum	Transducer	DAS B-210	SEL	CEC 100~	500~	FM	Monitor B-210	Strip Chart	1	2	3	Remarks
980800																
Hydrogen																
Main	P121	-	15-800	1065	1000											Spare
Main	P110	-	15-800	1065	1000	X					X		X	X		
Spike	P111	-	15-800	1065	1000		X						X	X		
L.E.	P112	-	15-800	1065	1000		X						X	X		
Venturi	P113	-	15-1000	1500	1000		X						X	X		
Venturi	ΔP1	-	0-150	1500	250		X						X	X		
Strut orif.	P108	-	15-800	1065	1000		X						X	X		
Strut orif.	ΔP8	-					X						X	X		
Injector inlet	P134	-	0-400	600	500		X							X		
Dump line	P132	-	15-550	1065	1000		X						X	X		
Gas (Cowl)																
Station 45.35	P103	180	1-3	15	5	X							X			
50.31	P102	180	1-3	15	5	X							X			
57.71	P101	180	0.3-1.0	15	5	X							X			
70.67	P100	180	0.3-1.0	15	5	X							X			
Water																
Inlet	P114	-	15-195	285	250							X	X	X		
Inlet	P115	-	15-105	135	250							X	X	X		
Route 1	P116	-	15-35	135	50							X	X	X		
Route 2	P117	-	15-25	135	25							X	X	X		
Route 3	P118	-	15-35	285	50							X	X	X		
Route 4	P119	-	15-55	285	50							X	X	X		
Route 5	P120	-	15-35	285	100							X	X	X		
Orifice	ΔP2	-		285								X	X	X		
Orifice	ΔP3	-		135								X	X	X		
Nitrogen																
Cavity	P106	-	0-25	25	25	X					X		X	X		
Pressure channels	24					6	7	-	-	-	2	9	22		19	
Hydrogen																
Main*	T119	-	0-100				X						X	X		
Spike*	T120	-	0-100													Spare
L.E.*	T121	-	0-100				X						X	X		
Venturi*	T122	-	0-100				X						X	X		
Main*	T123	-	0-100													Spare
Water																
Inlet	T124	-	520-550									X	X	X		
Inlet	T125	-	520-550									X	X	X		
Route 1	T126	-	520-660									X	X	X		
Route 2	T127	-	520-660									X	X	X		
Route 2	T140	-	520-660									X	X	X		
Route 3	T128	-	520-660									X	X	X		
Route 4	T129	-	520-660									X	X	X		
Route 5	T130	-	520-660									X	X	X		
Temperature channels	13						3	-	-	-	-	8	11	11		

*Resistance thermometers

TABLE 2.4-6 (Continued)

Description	No.	EW Aft θ Degree	Range (psia, °R, mv) Design	Range Maximum	Transducer	Recording DAS B-210	Recording DAS SEL	Recording CEC 100~	Recording CEC 500~	Monitor FM	Monitor B-210	Monitor Strip Chart	Test Group 1	Test Group 2	Test Group 3	Remarks
Frequency																
Inlet	H5	-	0-100				X						X	X		
Spike	HI	-	0-100				X						X	X		
Innerbody	H2	-	0-100				X						X	X		
L.E.	H3	-	0-100				X						X	X		
T.E.	H4	-	0-100				X						X	X		
Frequency channels	5						5	-	-	-	-	-	5	5		
Accelerometer																
Carriage	A7(T)**	-	10-200	250					P***	X			X	X		
Accelerometer channels	3						-	-	-	3	-	-	3	3		
Actuator																
Position	LI	-	-2500 +2500			X					X		X	X		
Error	L2	-	0-6000						X				X	X		
Channels	2					-		-	-	-	-	-	2	2		
Totals	47					7	15	-	1	3	3	17	43	40		

**(T) is triaxial

***P designates requirement for playback after test

systems were used interchangeably. In assigning measurements of aerodynamic static pressure, preference was given to the Beckman System because the SEL might have produced unwanted hash.

A summary of the assignments is shown in Table 2.4-7. To minimize manual handling of data, the DAS and FM tape were considered primary devices. CEC recording channels were used to record strains and accelerations in parallel with the FM tapes, as well as for post-run playback, as indicated in the tables (two records were obtained in this way as a convenience). Additional CEC channels were used to monitor parameters for the various system valves.

Monitoring of data on the Beckman B-210 occurs on a bargraph (98 channels) or on a Sanborn recorder (8 channels). The number of monitored quantities was minimized. Run times were relatively short; consequently, the capability for reaction was limited, and monitoring was confined to the critical parameters. Reliance was generally placed on the temperature-control system to ensure fail-safe operation of the model. Monitoring of data on the strip chart recorders served two purposes; (1) pretest setup of coolant water flows, and (2) recording of water flows and pressures during test to verify adequacy of operation and permit failure analysis as required.

Test groups are noted in Tables 2.4-1 to 2.4-7 for data recording purposes. Each group reflects a single run or group of runs during which a specific number of parameters were recorded. The changeover from one test group to the other was accomplished with electrical patch boards. Test Group I constitutes runs during which aerodynamic data (pressures) were measured. Test Group 2 was aimed at obtaining thermal performance data (temperatures) at the cost of aerodynamic data. Strain gages and accelerometers were recorded during all runs, since (1) they did not infringe on available DAS channels, and (2) these data would be of particular interest during abnormal tunnel or model operation. The differences in instrumentation hookups between Test Groups I and 2 are reflected in Table 2.4-7.

TABLE 2.4-7
SAM TEST INSTRUMENTATION SUMMARY

Description	Installed Channels	Recording Channels Per Test						Monitoring Channels Per Test	
		Test Group 1		Test Group 2		CEC	FM	B-210	Strip Chart
		B-210	SEL	B-210	SEL				
H$_2$ Pressure	28	3	13	3	19	1		4	
H$_2$ ΔP	6		6	45	6	1		1	
Hot Gas Pressure	71	60							7
H$_2$0 Pressure	7								2
H$_2$0 ΔP	2								
N$_2$ Cavity Pressure	1	1		1				1	
H$_2$ Thermocouple	51	4	30	4	37			4	
H$_2$ Resistance Thermometer	5		3		3				
Metal Thermocouple	57	21	17	35	18	1			3
H$_2$0 Thermocouple	8								8
Frequency	5		5		5				
Actuator	2	1		1		1		1	
Strain	12						12		
Acceleration	13						13		
Totals	268	80	74	89	88	4	25	11	20
Total 4-Wire	134	65	22	50	28	3	12	7	9
Total 2-Wire	134	15	52	39	60	1	13	4	11

3. TEST SETUP

3.1 WIND TUNNEL FACILITY

The basic 8-ft High Temperature Structures Tunnel (HTST) was modified to permit testing of the hydrogen-cooled SAM. The hot gas system constitutes the basic facility. A hydrogen system was added to this facility.

3.1.1 Hot Gas System

The 8-ft HTST is a blowdown facility, shown schematically in Figure 3.1-1. Methane is burned with air in the combustor and discharged into the test section through the supersonic nozzle. The nominal Mach number in the test section is 7; the nozzle diameter is 8 ft. An air-driven ejector is used in the diffuser. Tunnel run times are a function of total conditions in the combustor and of the air requirements in the ejector. During the SAM tests, the total pressures in the combustor ranged from 920 to 3370 psia, and the total temperatures in the combustor ranged from 2500° to 3500°R. For the low pressure runs, run times (i.e., SAM in the stream) were in the range of 40 to 50 sec; the run times reach a maximum near 2200 psia. At this condition, a run duration of 116 sec was achieved. At maximum tunnel conditions (3300 psia), run times were between 35 and 40 sec.

The SAM was installed on an elevator with a travel of 7 ft. The elevator inserted the model into the gas stream at the beginning of the test in 1.4 sec; at the conclusion of the run, the elevator retracted the model from the gas stream. Insertion and retraction occurred with the tunnel flow established at supersonic conditions. In this way, shock loadings on the SAM associated with tunnel starting and flow breakdown were avoided.

3.1.2 Hydrogen System

The hydrogen used in the tests was obtained by the blowdown of bottle cascades. The nominal flow capability of the system was 1.25 lb per sec at 1000 psia SAM inlet pressure. The flow was plumbed through a liquid nitrogen heat exchanger to provide the cooling for runs requiring cryogenic hydrogen. This heat exchanger was capable of furnishing hydrogen at approximately 160°R and 1 lb per sec. It was possible to achieve essentially steady-state outlet temperatures from the heat exchanger in most of the runs. For runs at tunnel conditions not requiring cryogenic hydrogen, the liquid nitrogen heat exchanger was drained. Ambient temperature hydrogen was used to facilitate control for runs requiring relatively low hydrogen flow rates. The hot hydrogen exhausted from the model was ducted to five vent stacks for direct discharge to the atmosphere. Gaseous nitrogen purges were provided at the beginning and at the end of the test runs.
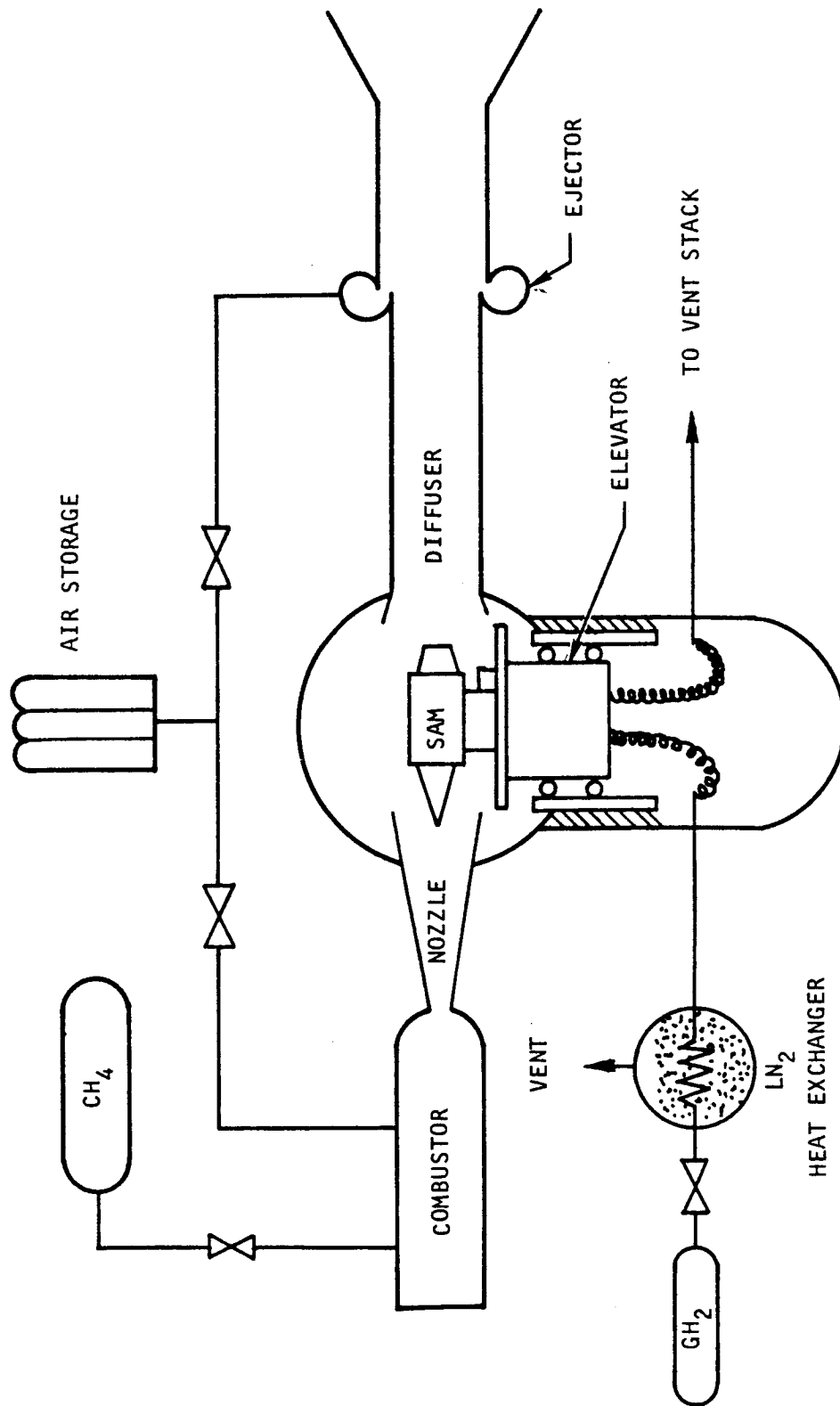
Figure 3.1-1. NASA-Langley 8-Foot High Temperature Structures Tunnel – SAM Tests

S-67780

UNCLASSIFIED

The hydrogen system was interlocked with the other tunnel systems in such a way that hydrogen flow could only be initiated after supersonic flow was established in the test section. This was a safety precaution to prevent accumulation of hydrogen in the test section.

3.1.3 Water Systems

Two separate water systems were available to supply the five water flow routes in the SAM test adapters. They were continuous-operating and were turned on prior to start of tunnel flow, and turned off after tunnel flow had stopped.

The low pressure system, supplying Routes 1 and 2, operated at 163 gpm and 96 psig inlet pressure. This essentially corresponded to the design flow rates and inlet pressure. The high pressure system supplied 118 gpm at an inlet pressure of 205 psig. This compared to a design flow rate of 130 gpm at 180 psig. This system supplied Routes 3, 4, and 5. Visual inspection of the test adapters showed that the flow rates obtained were entirely adequate, i.e., there was no evidence of overheating. No effort was made to modify the system (reduce back pressure) to obtain design values.
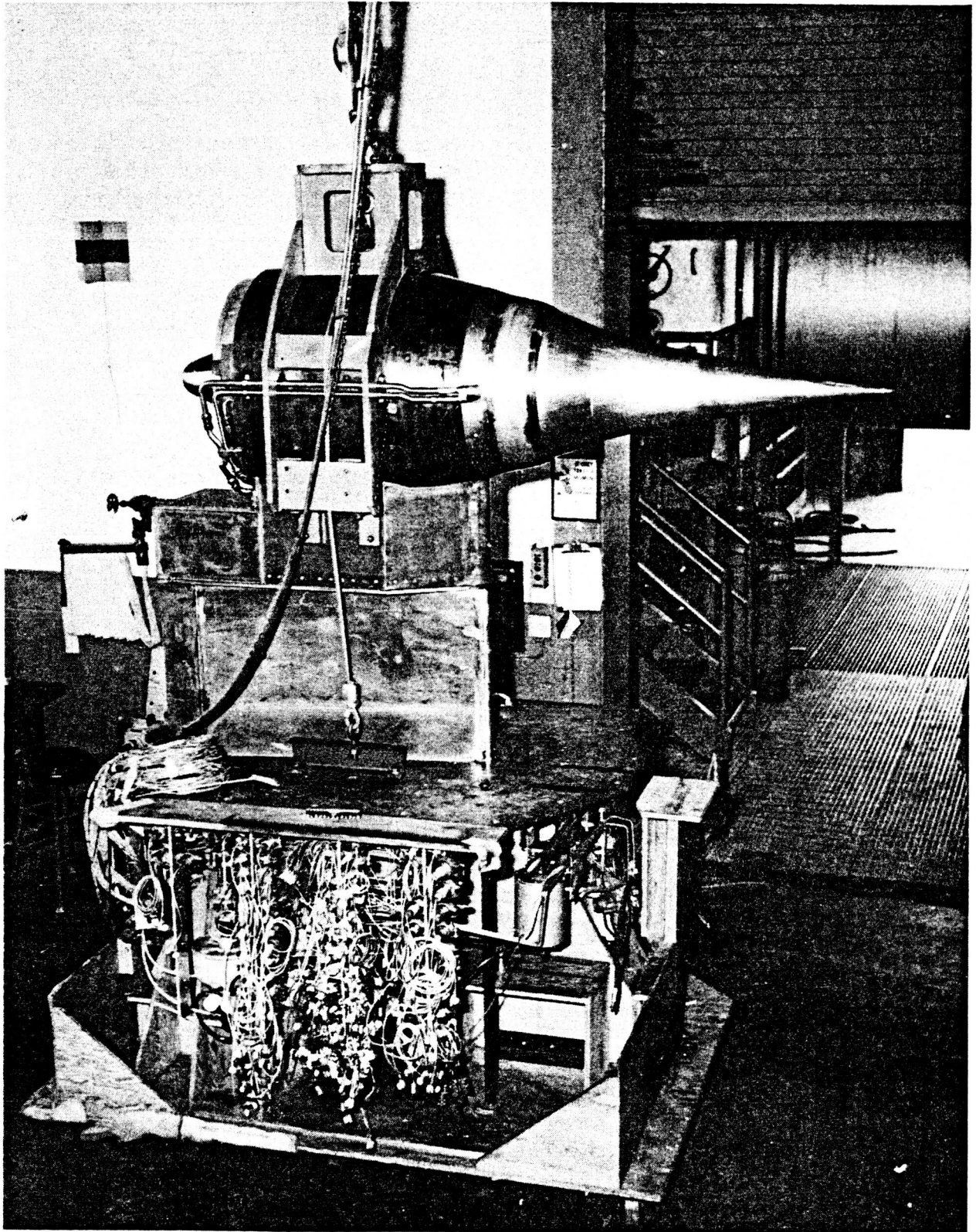
3.2 SAM INSTALLATION

A photo of the SAM at the wind tunnel, prior to installation in the wind tunnel test section, is shown in Figure 3.2-1. The assembly is mounted on a mockup of the elevator carriage. The tight fits involved in the installation were checked in this way. The particular view in the figure also shows the array of pressure transducers as mounted to the SAM baseplate. To minimize vibratory inputs to the transducers, they were all mounted in rubber cushions. Rubber dampers were used at the frame mounting points.

Figures 3.2-2 and 3.2-3 show the SAM installed in the test section at zero angle of attack, with the elevator in the raised, or running position. Attachment to the elevator carriage was by a series of bolts on either side of the support wedge. Figure 3.2-3 shows cameras installed in protective housings on either side of the diffuser inlet; one of the forward cameras is visible in Figure 3.2-2. Up to eight cameras were used during a test run. Schlieren photography was made by means of a setup mounted outside of the test section and operating through the windows shown in Figure 3.2-2.

The final sections of plumbing were fitted with the model in place. In this way, a relatively strain-free installation was obtained. In addition, the lines on the SAM side of the interface were solidly anchored to avoid introduction of loads into the SAM plumbing during operation. Hydrogen connections were limited to a single inlet and outlet. Each of the water systems had a single inlet. To allow adjustment of flow splits among the routes, however, each of the outlets from the five water flow routes was separately plumbed into a manual valve.

UNCLASSIFIED

F-13830

Figure 3.2-1. SAM at Wind Tunnel, on Mockup of Elevator Carriage

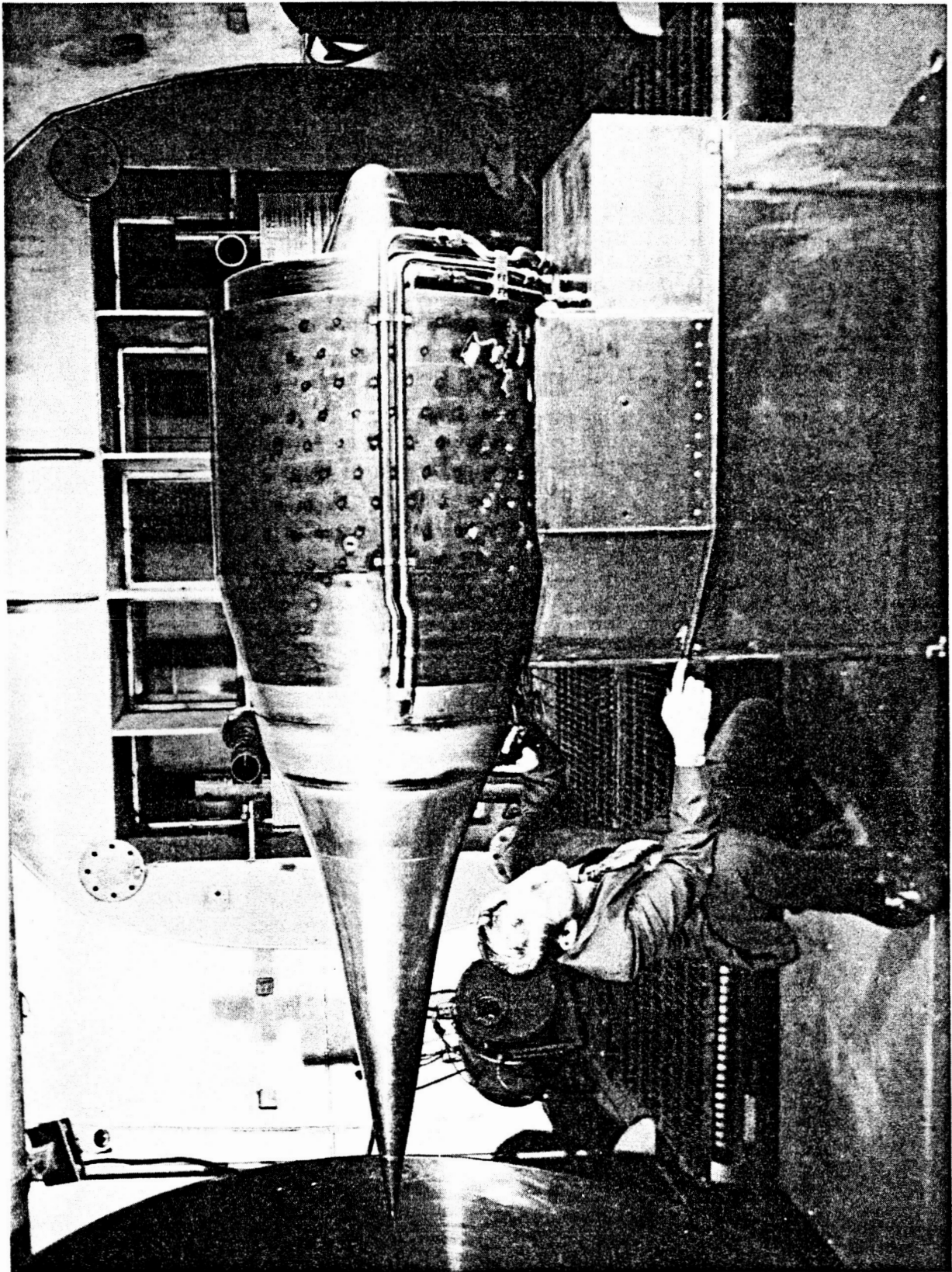GARRETT | AIRESEARCH MANUFACTURING COMPANY
Los Angeles, California

UNCLASSIFIED

71-7702
Page 3-4

F-13826
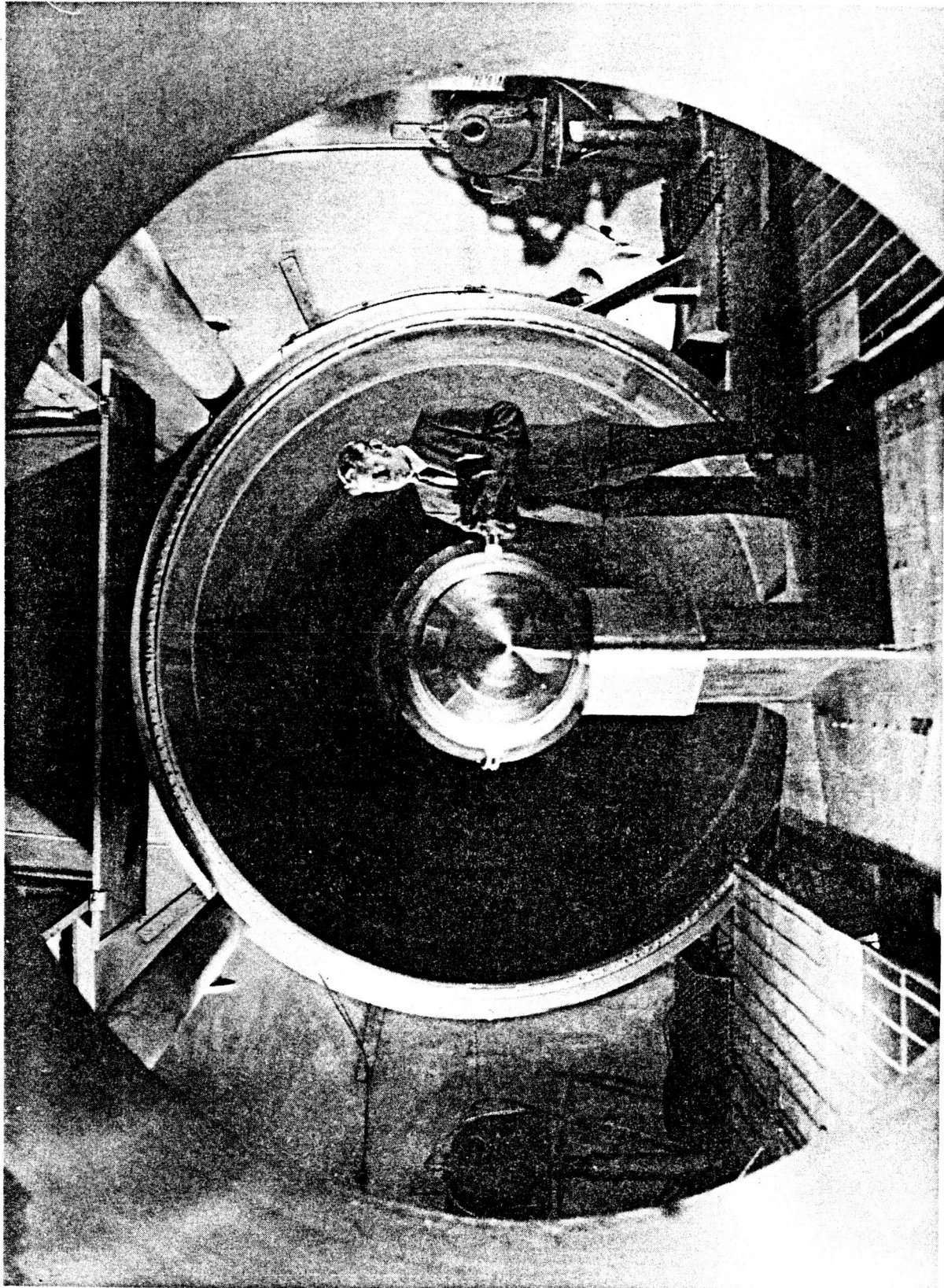

Figure 3.2-2. SAM Installed in Wind Tunnel Test Section

UNCLASSIFIED

Figure 3.2-3. SAM Installed in Wind Tunnel Test Section

F-13828

GARRETT AIRESEARCH MANUFACTURING COMPANY
Los Angeles, California

UNCLASSIFIED

71-7702
Page 3-6

4. TEST PROCEDURE

This section outlines the sequencing of various test operations, inspections performed before and after tests, and the integration of the SAM and the wind tunnel operations. The numerous detail checks performed on both the wind tunnel and SAM systems prior to and between tests are not discussed. All systems were elaborately interlocked to prevent damage to both the facility and the SAM as a result of malfunction of components or subsystems.

4.1 WIND TUNNEL SYSTEMS

The limiting wind tunnel function was air storage. Frequency and length of the test runs were determined by the air-storage pressure.

With all systems ready prior to a test, the hydrogen system was purged with nitrogen gas. After this, the airflow was started and the pilot burner lit. With everything satisfactory, the main burner was lit. At this point the hydrogen flow to the model was started. The SAM could now be inserted at the discretion of the model controller. Only minor adjustments to the wind tunnel systems were generally required in the course of a run.

When the available air supply was depleted to within approximately 95 percent of the setpoint pressure, the model was retracted on a verbal command. Hydrogen flow through the model was stopped as soon as the model hit the bottom of the test section pod. On some runs, this interlock was manually overridden to permit controlled cooldown of the model or two insertions during a single run.

All data systems were started at 10 sec before burner lightoff. They were shut down at the discretion of the operator, at the end of the run, as a function of the SAM temperature history wanted during the cooldown cycle. Motion picture and Schlieren cameras were started with the data system. For some of the runs, the test section was left dark to give improved Schlieren photography and the monitoring cameras turned on at some preselected point during the run.

An emergency shutdown of the tunnel resulted in retraction of the model from the wind stream and shutoff of hydrogen supply to the model. On several occasions on which this occurred, no significant increase in loading on the model could be observed from the test data.

4.2 SAM SYSTEMS

The following discussion deals with the highlights of the procedures used to operate the SAM systems before, during, and after tests. All operations were performed against checklists.

4.2.1 Pretest

The most significant pretest activities involved setup and calibration of various control functions. These included the following:

(a) Presetting of the coolant regulating valves to give the flow split desired for the upcoming test conditions. This was done with nitrogen at approximately 100 psi. Except for the manual needle valve in the strut flow route, all other adjustments were made from the control room.

(b) Adjustments of the control temperature set points for each of the flow routes.

(c) Calibration of spike position vs LVDT output. This calibration was performed only periodically as opposed to on a run-by-run basis. The position calibration was accomplished with a fixture using dial indicators.

(d) Verification of water flows in each of the five water flow routes on the basis of pressure drops in the flow routes. This was generally accomplished immediately preceding the test, once the valves had been set, since experience indicated little tendency for drift.

(e) Instrumentation zeros and spans. This was a facility function performed on a daily basis. Data from previous runs were also reviewed for indications of defects in the instrumentation. Where possible, repairs were performed.

4.2.2 Test

Functions of the model operator during the test were limited because of the generally short run times. Figure 4.2-1 shows a typical test cycle involving the following events:

(a) Two insertions and retractions during the run for the purpose of thermally cycling the SAM. This was accomplished manually and also required manual reset of the tunnel hydraulics. During the performance runs, the intermediate retraction of the SAM from the wind tunnel gas stream was omitted.

(b) Hydrogen injection through SAM fuel injectors using the ICV, when required. Opening and closing of the ICV was again a manual function of the model operator. The flow opening was preset and not adjustable when the valve was open.

(c) Hydrogen flow with the model out of the stream and at the bottom of the test section pod for various lengths of time. At the conclusion of the run, the duration of hydrogen flow was limited by the requirement that the tunnel be supersonic whenever hydrogen was flowing.
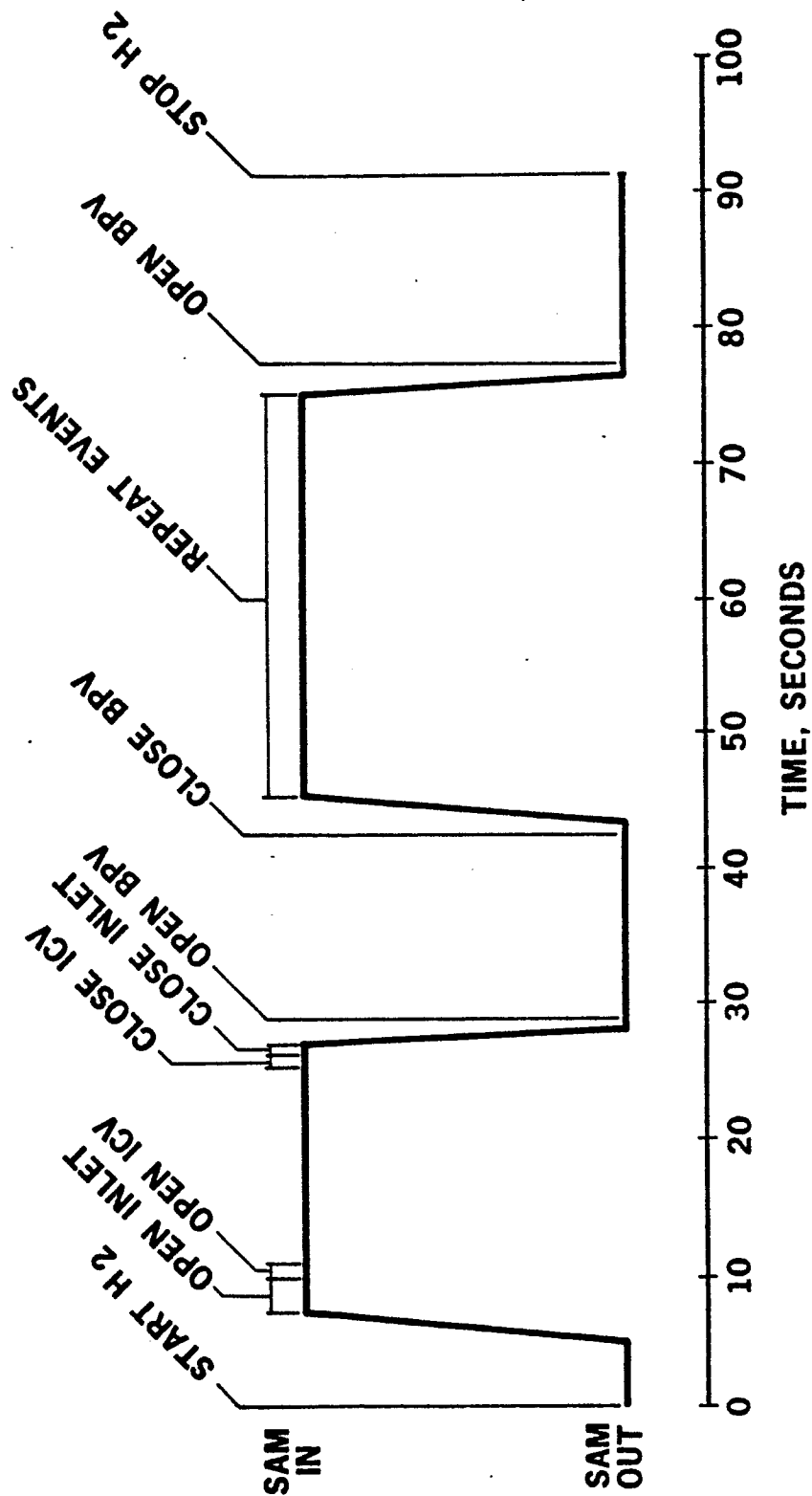
Figure 4.2-I. Wind Tunnel Test Cycle

(d) Opening and closing of the inlet spike, manually, by the model operator. Because of the pressure load exerted by the purge gas in the engine cavity, opening of the inlet was relatively slow, extending over approximately 3 sec. During the closing stroke of the inlet, the cavity purge gas pressure aids the actuator and results in closing of the inlet in approximately 1/2 sec. (At the flight design condition, the closing loads are much higher than the opening loads and the actuator piston areas have been proportioned accordingly. This makes them the opposite of what would be desired of a design intended for this test only. There was, however, no difficulty in spike positioning.)

(e) For the cycling runs, the bypass valves were opened to provide a high rate of cold hydrogen flow through the engine and rapidly reduce metal temperatures when the model is out of the stream. For cryogenic hydrogen runs, the bypass valves were not opened. Also, the hydrogen flow was stopped earlier, after retraction of the SAM, to control the reverse temperature differences possible with cryogenic hydrogen.

In addition to the above, selected channels of data were monitored to assure satisfactory operation of critical functions. Among these were:

(a) Dump plenum pressure. Where required, setpoint of the pressure-control system was adjusted to provide the correct outlet operating pressure.

(b) Inlet spike retraction. The amount of retraction was preset.

(c) Operation of the FDV. A Sanborn recorder showed valve position and electrical command signal.

(d) Percentage of flow rates in the flow routes, as indicated by panel meters in the TCS.

(e) The sequence of temperature control as indicated by lights representing each of the control thermocouples on the face of the TCS panel.

4.2.3 Posttest

Following a test, the SAM was visually inspected for areas of high heating and for foreign object damage. Leak tests were run on both a pressure-decay basis and using soap solution. Selected data was played back on the SEL system, on paper tape. Using this data, run conditions could be reviewed and adjusted prior to the next run. Some of the data channels were assigned to the PCM based on the need to have data immediately available after the run. On an overnight basis, also, test results were available in the form of engineering units from the data acquisition systems. This more complete listing was again reviewed, where possible, to check conditions for the run and establish the need for modification to settings for the upcoming run.

5. TEST RESULTS

A total of 47 thermal performance and cycling test runs were performed for the SAM test program (Test 41, Run 5, through Test 41, Run 53; the SAM was not inserted into the gas stream for Test 41, Run 30). The runs were divided into two test groups: the first group, designated as Test 41, emphasized the collection of aerodynamic and thermal performance data. The second group, designated as Test 42, was aimed at the accumulation of thermal-structural data. Twenty-seven runs were performed in this latter test group, twenty-three of them using hydrogen injection. Instrumentation hookups for the two test groups differed to reflect the test emphasis. The SAM was subjected to 60 thermal/structural loading cycles with an accumulated time in the hot gas stream of 30.7 min (1843 sec). Individual run times were from 6 to 115 sec.

5.1 TEST RUN SUMMARY

A summary of the test conditions and operating parameters is presented in Table 5.1-1, in chronological sequence. Corresponding AiResearch run numbers, as defined in Reference 5-1, are included in this table. Tunnel reservoir total pressures and temperatures ranged from 920 to 3370 psia and 2500^0 to 3500^0R, respectively. These reservoir conditions produced test section Mach numbers from 6.3 to 6.8 and total pressures from 300 to 2300 psia. Engine times in the gas stream were from 6 to 115 sec.

Most test runs were performed with a spike retraction (from the fully closed, latched position) of approximately 2.9 in. This retraction gave a spike-shock position outside the leading edge lip. For the remainder of the runs, the spike retractions were from 1.70 to 4.34 in. This range of spike positions gave inlet mass flow ratios from 0.78 to 1.0. The shock-on-lip spike retraction was approximately 3.9 in. at 1380 psia, 2700^0R tunnel reservoir total conditions. Operation with spike shock-on-lip was attempted at 1380, 2290, and 3300 psia reservoir total pressures.

The engine was cooled with room temperature inlet hydrogen for the first 34 runs (through Test 42, Run 43) where tunnel reservoir pressures were up to 2200 psia. For the remainder of runs, cryogenic hydrogen (approximately 160^0R) was used to cool the engine (reservoir pressures of 2200 psia and above). Of the 47 test runs, 23 were performed with partial or full coolant-jacket hydrogen flow injected into the hot gas stream.

Most of the thermal cycling runs (Test 42, Runs 17 to 38) were achieved by inserting the engine into the tunnel gas stream twice during a test run, with an intermediate withdrawal into the tunnel pod. Three thermal cycles were performed for Test 42, Run 21. Three angle-of-attack runs (Test 41, Runs 51, 52, and 53) were performed at the maximum reservoir pressure of 3370 psia, with the engine centerline pitched 3-deg downward. All other runs were at zero angle of attack.

AIRESEARCH MANUFACTURING COMPANY
Los Angeles, California

TABLE 5.1-1

SUMMARY OF HRE SAM STRUCTURAL AND COOLING TESTS (U)

LRC Test No.	LRC Run No.	LRC Cycle No.	AiResearch Run No.	Tunnel Total Pressure, psia	Tunnel Total Temp, °R	Time In Tunnel, sec	Spike Retraction, in.	H_2 Injection	Nom. Venturi H_2 Flow Rate, lb/sec	Max Outlet H_2 Temp, T101, °R	Max H_2 Heat Load, Btu/sec	Outerbody Outlet Manifold $\Sigma\Delta T$, °R	Max Hot Wall Temp, °R	$\Delta(\alpha\Delta T)$	Damage Fraction	Accum. Damage	Remarks
41	5	1	2	975	2600	46	2.34	No	0.38	1025	650	660	1260	0.00535	0.0013	0.0013	Automatic shutdown due to SAM over-temperature.
41	7	1	2	960	2600	32	2.30	No	0.19	1210	497	680	1680	0.00620	0.0031	0.0044	
41	12	1	3	950	2500	15	2.88	No	0.29	850	337	661	1110	0.00520	0.0010	0.0054	Foreign object damage (FOD) in 13 areas of leading edge.
41	13	1	3	920	2500	42	2.89	No	0.23	1160	508	845	1370	0.00710	0.0041	0.0085	
41	16	1	5	1300	2600	42	2.89	No	0.35	1180	770	805	1360	0.00674	0.0034	0.0129	Dent and leak at leading edge stagnation line due to FOD.
41	17	1	5	1290	2700	49	2.89	No	0.35	1220	820	840	1420	0.00700	0.0040	0.0169	
41	20	1	7	1540	2700	45	2.86	No	0.31 - 0.44	1291	911	1122	1565	0.00952	0.0114	0.0283	0.045 x 0.065-in. hole in side of leading edge tip due to FOD.
42	3	1	4	950	2600	39	2.85	Yes	0.24 - 0.33	1210	480	819	1380	0.00680	0.0035	0.0318	
42	11	1	6	1275	2700	44	2.89	Yes	0.25 - 0.47	1290	830	1207	1555	0.01020	0.0138	0.0456	
42	12	1	8	1510	2800	41	2.89	Yes	0.25 - 0.40	1310	1100	1035	1510	0.00875	0.0086	0.0542	Automatic shutdown caused by electrical noise.
41	26	1	30	2200	3100	16	1.70	No	0.31 - 0.47	1205	770	1215	1675	0.01037	0.0158	0.0700	
41	27	1	30, 31	2200	3000	40	0.0	No	0.34 - 0.41	682	190	---	---	---	0	0.0700	No spike retraction. Control error. 0.010-in. dia hole in side of leading edge.
41	28	1	30, 31	2200	3000	22/8	2.33/2.87	No	0.37 - 0.51	1350	1380	1265	1550	0.01055	0.0151	0.0851	Two spike positions. Automatic shutdown due to methane alarm. Leak at nozzle-inner shell port seals; replaced these.
41	29	1	9	1380	2700	50	2.86	No	0.20 - 0.50	1310	690	1215	1570	0.01027	0.0142	0.0993	Leak at aft end of strut No. 5.
42	14	1	8	1530	2700	52	2.89	Yes	0.25 - 0.35	1410	800	1300	1637	0.01093	0.0177	0.1170	
42	16	1	10	1375	2700	7/6/6	0.0	No	0.38 - 0.42	680	---	130	708	---	0	0.1170	Four model insertions. No spike retraction. Determine minimum ejector pressure.
42	17	1	10	1360	2700	68	2.89	Yes	0.16 - 0.35	1320	690	1050	1384	0.00813	0.0079	0.1249	Leak at nozzle-inner shell port seals; replaced these with rubber O-rings.
42	19	1	11	1380	2700	21	2.89	Yes	0.24 - 0.31	1100	480	770	1390	0.00648	0.0030	0.1279	

TABLE 5.1-1 (Continued) (U)

Test No.	Run No.	Cycle No.	AiResearch Run No.	Pressure, psia	Temp, °R	Time in Tunnel, sec	Spike Retraction, in.	H_2 Injection	Nom. Venturi H_2 Flow Rate, lb/sec	Max Outlet H_2 Temp, T101, °R	Max H_2 Heat Load, Btu/sec	$\Sigma\Delta T$, °R	Max Hot Wall Temp, °R	$\Delta(\propto\Delta T)$	Damage Fraction	Accum. Damage	Remarks
42	38	1	24	1370	2700	18	2.90	Yes	0.13-0.44	1210	450	970	1599	0.00830	0.0081	0.2857	Shock-on-lip calibration. No Schlieren obtained.
42	38	2	24	1370	2700	31	2.89	Yes	0.15-0.30	1340	630	955	1550	0.00814	0.0066	0.2923	
42	41	1	25	1380	2700	8	3.68	No	0.21	830	210	620	1083	0.00488	0.0007	0.2930	Shock-on-lip calibration. No Schlieren obtained.
42	41	2	25	1380	2700	9	4.00	No	0.21	930	270	656	1182	0.00537	0.0012	0.2942	
42	41	3	25	1380	2700	8	4.34	No	0.21	940	300	650	1186	0.00524	0.0011	0.2953	
42	42	1	25	1390	2700	8	3.56	No	0.23	750	85	530	1054	0.00420	0.0003	0.2956	Shock-on-lip calibration. Hole and leak in leading edge due to foreign object damage.
42	42	2	25	1390	2700	8	3.86	No	0.21	970	200	743	1304	0.00761	0.0048	0.3004	Automatic shutdown due to faulty SAM thermocouple.
42	43	1	26	1370	2700	62	3.85	No	0.21-0.30	1190	630	1078	1414	0.00883	0.0084	0.3088	Shock-on-lip. Spike coolant outlet bellows leak. Replaced nozzle seals; adjusted nozzle fit.
41	30	1	---	---	---	---	---	---	0.50-1.0	---	---	4.60	RT	0.00343	0.0001	0.3089	Cryogenic H_2 calibration run.
41	37	1	27	2835	3300	57	2.90	No	0.60-0.94	1170	2775	1224	1435	0.00999	0.0119	0.3208	Shutdown due to high tunnel nozzle throat temp
41	38	1	32	3330	3500	18	2.91	No	0.75-0.87	1240	3200	1410	1561	0.01159	0.0195	0.3403	
41	39	1	33	3320	3400	32	2.89	No	0.62-0.77	1330	2840	1390	1535	0.01140	0.0183	0.3586	
42	44	1	34	2220	3000	34	2.89	Yes	0.15-0.45	1360	1500	1452	1675	0.01215	0.0240	0.3826	Tunnel flow breakdown during SAM refraction.
42	45	1	34	2250	3000	115	2.89	Yes	0.30-0.67	1180	2050	1128	1511	0.00950	0.0109	0.3935	
42	46	1	28	3330	3400	36	2.90	Yes	0.60-0.90	1260	3030	1326	1458	0.01084	0.0154	0.4089	Hole and leak in leading edge due to foreign object damage.
42	47	1	35	3350	3200	31	2.90	Yes	0.58-0.80	1415	2350	1327	1570	0.01093	0.0168	0.4258	
41	40	1	29	2290	3000	64	3.43	No	0.23-0.54	1280	1910	1373	1544	0.01127	0.0178	0.4436	Shock-on-lip. Automatic shutdown due to SAM overtemperature (trailing edge route).
41	42	1	37	3300	3200	40	3.12	No	0.57-0.85	1290	2620	1297	1488	0.01059	0.0145	0.4581	Shock-on-lip.

TABLE 5.1-1 (Continued) (U)

LRC Test No.	LRC Run No.	LRC Cycle No.	AiResearch Run No.	Tunnel Total Pressure, psia	Tunnel Total Temp, °R	Time in Tunnel, sec	Spike Retraction, in.	H_2 Injection	Nom. Venturi H_2 Flow Rate, lb/sec	Max Outlet H_2 Temp, T101, °R	Max H_2 Heat Load, Btu/sec	$\Sigma\Delta T$, °R	Outerbody Outlet Manifold Max Hot Wall Temp, °R	$\Delta(c\Delta T)$	Damage Fraction	Accum. Damage	Remarks
42	19	2	11	1380	2700	22	2.89	Yes	0.24 – 0.31	1200	560	715	1430	0.00627	0.0028	0.1307	
42	21	1	12	1380	2800	14	2.90	Yes	0.18 – 0.27	1080	300	1017	1500	0.00856	0.0080	0.1387	
42	21	2	12	1380	2800	14	2.89	Yes	0.18 – 0.27	1120	410	723	1364	0.00605	0.0022	0.1409	
42	21	3	12	1380	2800	15	2.89	Yes	0.18 – 0.27	1130	380	735	1378	0.00612	0.0024	0.1433	
42	22	1	13	1370	2700	19	2.89	Yes	0.25 – 0.43	1220	380	945	1636	0.00817	0.0077	0.1510	
42	22	2	13	1370	2700	20	2.88	Yes	0.20-0.22	1280	540	610	1506	0.00528	0.0015	0.1525	
42	24	1	14	1370	2700	24	2.89	Yes	0.19 – 0.22	1080	460	1010	1480	0.00842	0.0075	0.1600	Automatic shutdown due to methane alarm after one cycle.
42	25	1	15	1380	2700	14	2.90	Yes	0.13 – 0.18	1080	460	1020	1500	0.00850	0.0078	0.1678	Leak at forward end of strut No. 5
42	25	2	15	1380	2700	13	2.89	Yes	0.14 – 0.17	1090	270	820	1370	0.00682	0.0036	0.1714	
42	28	1	16	1370	2700	18	2.89	Yes	0.19 – 0.33	1216	450	1139	1576	0.00965	0.0120	0.1834	
42	28	2	16	1370	2700	15	2.89	Yes	0.16 – 0.21	1260	420	724	1490	0.00620	0.0027	0.1861	
42	29	1	17	1380	2700	19	2.89	Yes	0.20 – 0.30	1220	400	1122	1563	0.00940	0.0110	0.1971	
42	29	2	17	1380	2700	17	2.88	Yes	0.16 – 0.20	1290	410	810	1518	0.00720	0.0042	0.2013	
42	30	1	18	1380	2700	31	2.89	Yes	0.15 – 0.23	1320	510	1147	1560	0.00955	0.0115	0.2128	Leak at forward end of strut No. 2.
42	31	1	19	1380	2750	22	2.90	Yes	0.18 – 0.21	1160	360	935	1452	0.00760	0.0053	0.2181	
42	31	2	19	1380	2750	34	2.90	Yes	0.16 – 0.20	1320	400	841	1516	0.00710	0.0045	0.2236	
42	32	1	20	1380	2700	19	2.89	Yes	0.08 – 0.20	1150	360	1064	1498	0.00877	0.0086	0.2322	Leak at forward end of strut No. 3.
42	32	2	20	1380	2700	31	2.89	Yes	0.08 – 0.20	1310	450	870	1547	0.00636	0.0031	0.2353	
42	33	1	21	1380	2700	20	2.89	Yes	0.09 – 0.21	1150	400	905	1429	0.00713	0.0043	0.2396	
42	33	2	21	1380	2700	31	2.90	Yes	0.09 – 0.21	1310	460	921	1536	0.00768	0.0058	0.2454	
42	34	1	22	1390	2700	67	2.90	No	0.19 – 0.41	1300	720	1388	1573	0.01155	0.0198	0.2652	
42	36	1	23	1390	2700	59	2.89	Yes	0.14 – 0.23	1360	660	1183	1570	0.00980	0.0124	0.2776	Leak at aft end of inner shell.
41	51	1		3370	2700	12	4.24	No	0.47	1250	2300	1140	1489	0.00926	0.0100	0.4670	Automatic shutdown due to methane alarm. Large dent in spike, with small leak.
41	52	1		3350	2700	6	4.24	No	0.56	1225	-	1112	1658	0.00956	0.0122	0.4792	Automatic shutdown due to SAM over-temperature. Low flow in L.E. and T.E. routes.
41	53	1		3370	2900	19	4.22	No	0.56	1350	2600	1199	1351	0.00989	0.0108	0.4900	Bolt damage at outerbody flange; leading edge separated from outer shell by 0.2 in. and held in place by connecting tubes. No new hydrogen leaks.

UNCLASSIFIED

In addition to the test conditions and operating parameters, Table 5.1-1 contains the significant data affecting thermal fatigue of the hot skin at the outerbody outlet manifold, Station 51.4 in. The summed ΔT's represent the absolute sum of positive and negative ΔT's of the hot skin with respect to the manifold. Δ is the differential growth, and the damage fraction is the fraction of the estimated cycle life expended at the conditions listed. At the conclusion of the tests, 49 percent of the cycle life available in the structure at this location is estimated to have been expended in the course of the tests. A detailed discussion of this data and its interpretation appears in Section 5.5.

5.1.1 Measured Data

Thermal performance tests were run for the purpose of collecting steady-state aerodynamic and thermal data on the hydrogen-cooled plate-fin surfaces of the model. The test procedure was to insert the engine into the operating tunnel and retract the spike--insertion and retraction taking 4 to 5 sec. Steady-state aerodynamic conditions, as determined by wall-static pressure measurement, were achieved in less than 5 sec of run time for most locations (partial plugging of some of the static lines appreciably increased the response time). Steady-state thermal conditions, as determined by coolant outlet temperature histories, were achieved in 10 to 30 sec for the spike and leading edge flow routes. Steady-state thermal conditions were not achieved for the innerbody, trailing edge, and strut flow routes for almost all thermal performance runs up to 68 sec test time where tunnel reservoir pressures were 2200 psia or less and the hydrogen flow requirements were low. Measured metal temperatures on the spike and leading edge reached steady-state as soon as the coolant temperatures reached steady-state. Metal temperatures on the innerbody and trailing edge responded to the hot gas heating as quickly as those on the spike and leading edge, but after the initial response, tracked the adjacent transient coolant temperature. At the higher tunnel reservoir pressures (2200 to 3320 psia) where the hydrogen flow requirements were higher, steady-states were achieved on the innerbody, trailing edge, and strut flow routes after about 40 sec of run time.

Thermal-cycling runs (Test 42, Runs 11 to 38) were performed for the purpose of accumulating low-cycle thermal fatigue performance data for the engines. The engine was inserted into the tunnel for 15 to 30 sec and then withdrawn. For several tests the engine was reinserted into the tunnel for an additional 15 to 30 sec, after a 10- to 15-sec dwell time in the pod. Hydrogen flow was maintained in the routes for this dwell period. The absolute sum of the maximum-positive and maximum-negative wall-to-structural ΔT for the outerbody outlet manifold for each test run is indicated in Table 5.1-1. The calculation of the low-cycle fatigue damage fraction (indicated in Table 5.1-1) is discussed in Section 5.5.

5.1.2 Observed Data

5.1.2.1 Metal Discoloration

Both Hastelloy X (used as face sheets for the regeneratively cooled shells) and nickel (used as the hot skin for the leading edge tip) show distinct surface

discolorations as a function of temperature. In addition, surface preparation immediately prior to exposure strongly affects the appearance of the oxide films in certain temperature ranges. These phenomena were used to obtain estimates of hot skin temperatures in areas of high local heating where thermocouple instrumentation was lacking.

To aid in the temperature estimates based on surface discoloration, five sets of calibration specimens were prepared as follows:

(a) <u>Hastelloy X (0.008 in. Thick)</u>

   Temperatures: 1000^0, 1100^0, 1200^0, 1300^0, 1400^0, 1500^0, and 1600^0F

   Exposure time: 2 minutes

   Surface preparation prior to exposure: None (as-received mill finish)

   Cleaning prior to exposure: Freon

(b) <u>Hastelloy X (0.008 in. Thick)</u>

   Temperatures: 1000^0, 1100^0, 1200^0, 1300^0, 1400^0, 1500^0, and 1600^0F

   Exposure time: 2 minutes

   Surface preparation prior to exposure: Polished with "Crocus" cloth

   Cleaning prior to exposure: Freon

(c) <u>Hastelloy X (0.008 in. Thick)</u>

   Temperatures: 1000^0, 1100^0, 1200^0, 1300^0, 1400^0, 1500^0, and 1600^0F

   Exposure time: 10 minutes

   Surface preparation prior to exposure: None (as-received mill finish); however, the area for the thermocouple attachment had been polished and thus, provided a calibration for this condition.

   Cleaning prior to exposure: Freon

(d) Nickel Ni-200 (0.040 in. Thick)

      Temperatures: 1000°, 1100°, 1200°, 1300°, 1400°, 1500°, and $1600^\circ F$

      Exposure time: 2 minutes

      Surface preparation prior to exposure: None (as-received mill finish)

      Cleaning prior to exposure: Freon

(e) Nickel Ni-200 (0.040 in. Thick)

      Temperatures: 1000°, 1100°, 1200°, 1300°, 1400°, 1500°, and $1600^\circ F$

      Exposure time: 2 minutes

      Surface preparation prior to exposure: Polished with "Crocus" cloth

      Cleaning prior to exposure: Freon

(f) All Two-Minute Specimens

      Specimens were placed in the furnace and an inert (nitrogen) atmosphere maintained until the desired exposure temperature was reached. At that point, oxygen, corresponding to that present in methane combustion products for equivalence ratio of 0.5, was introduced into the furnace with the nitrogen (90 percent nitrogen, 10 percent oxygen). Following the specified exposure time, oxygen flow was stopped and nitrogen flow maintained while the specimen cooled.

(g) Ten-Minute Specimens

      Atmosphere was 90 percent nitrogen and 10 percent oxygen during heating and 10-minute exposure time. During cooldown time, a pure nitrogen atmosphere was used. The heating time was 10 minutes for all 10-minute exposures.

(h) All Specimens

      Specimen temperatures were monitored by means of thermocouples welded to each of the specimens. Temperatures were recorded and monitored.

      Figures 5.1-1 through 5.1-12 and Table 5.1-2 describe the discolorations observed on the SAM. The color descriptions are subjective and for reference only. The temperatures shown in the diagrams are the best estimates based on color comparisons of these temperatures and at bracketing temperatures.

S-63673

STA 57.76   50   40.0   30   20   10   0

3/4 IN.

1000°F (10 MIN SPECIMEN, UNPOLISHED)
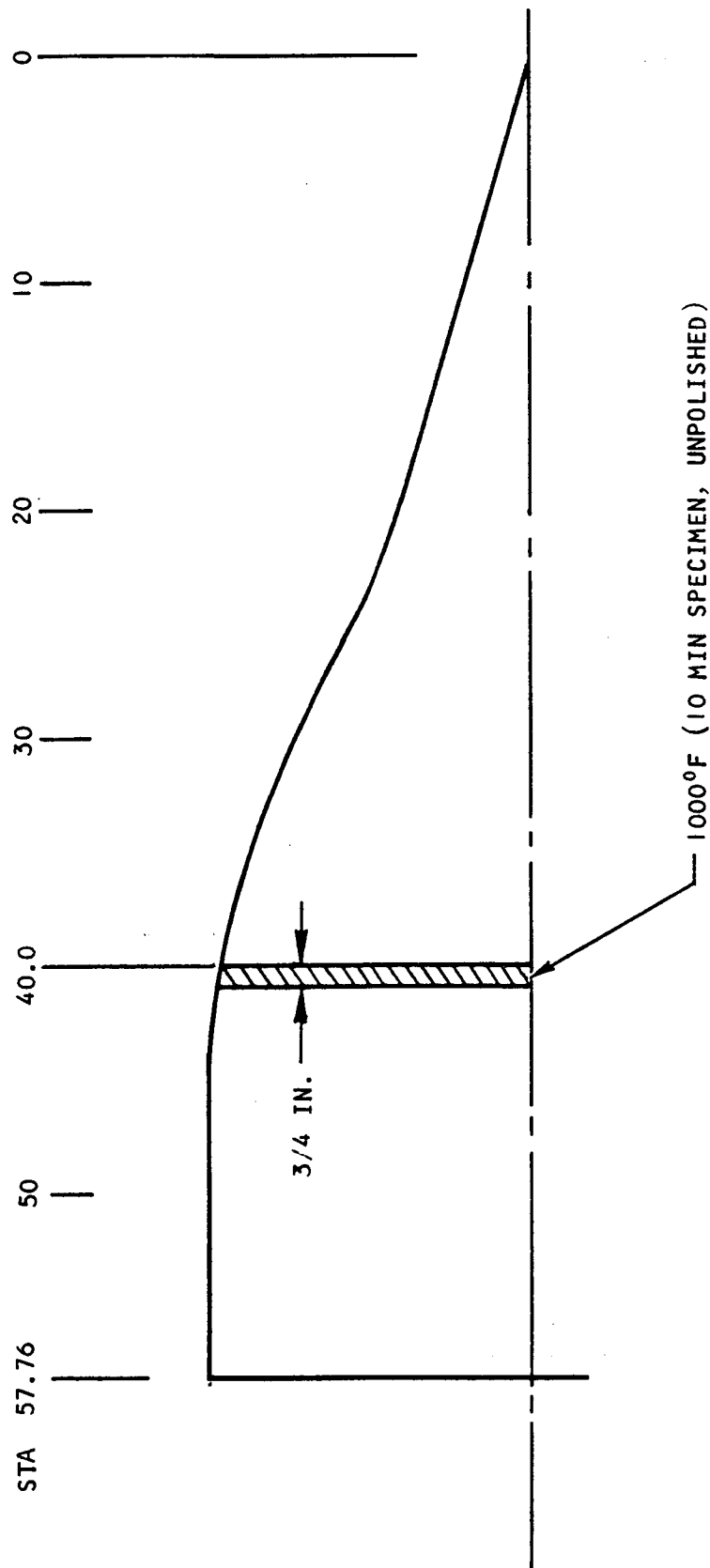
NOTES: 1. AREAS AFT OF STA 40 ARE NOT SUFFICIENTLY VISIBLE
TO PERMIT INTERPRETATION OF COLORS
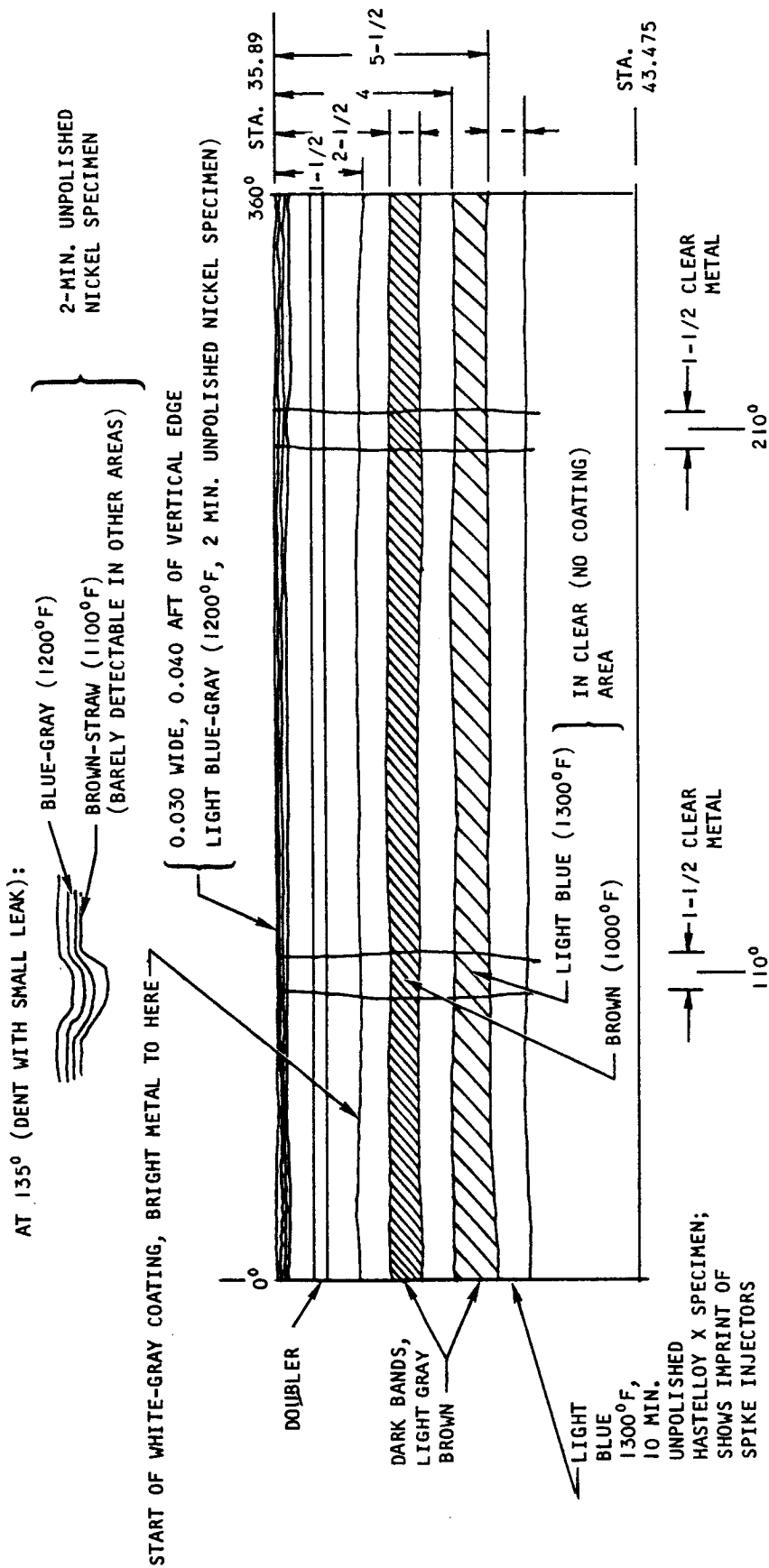2. COMPARED POST-TEST 42, RUN 36

Figure 5.1-1.   Spike Color Markings (U)

DOUBLER

180°

90°

LINE INDICATES A LINE OF BLUE
COLOR APPROX. 0.030 IN. WIDE
(1000°F OR 1200°F) ~ 0.070 AFT
OF VERTICAL EDGE

LIGHT STRAW COLOR - (APPROX.
1100°F) - BORDERING BLUE LINE
AFT, TRANSITION TO AS-RECEIVED
COLOR IN 0.070 TO 0.100 IN.

0°

DOUBLER

180°

270°

0°
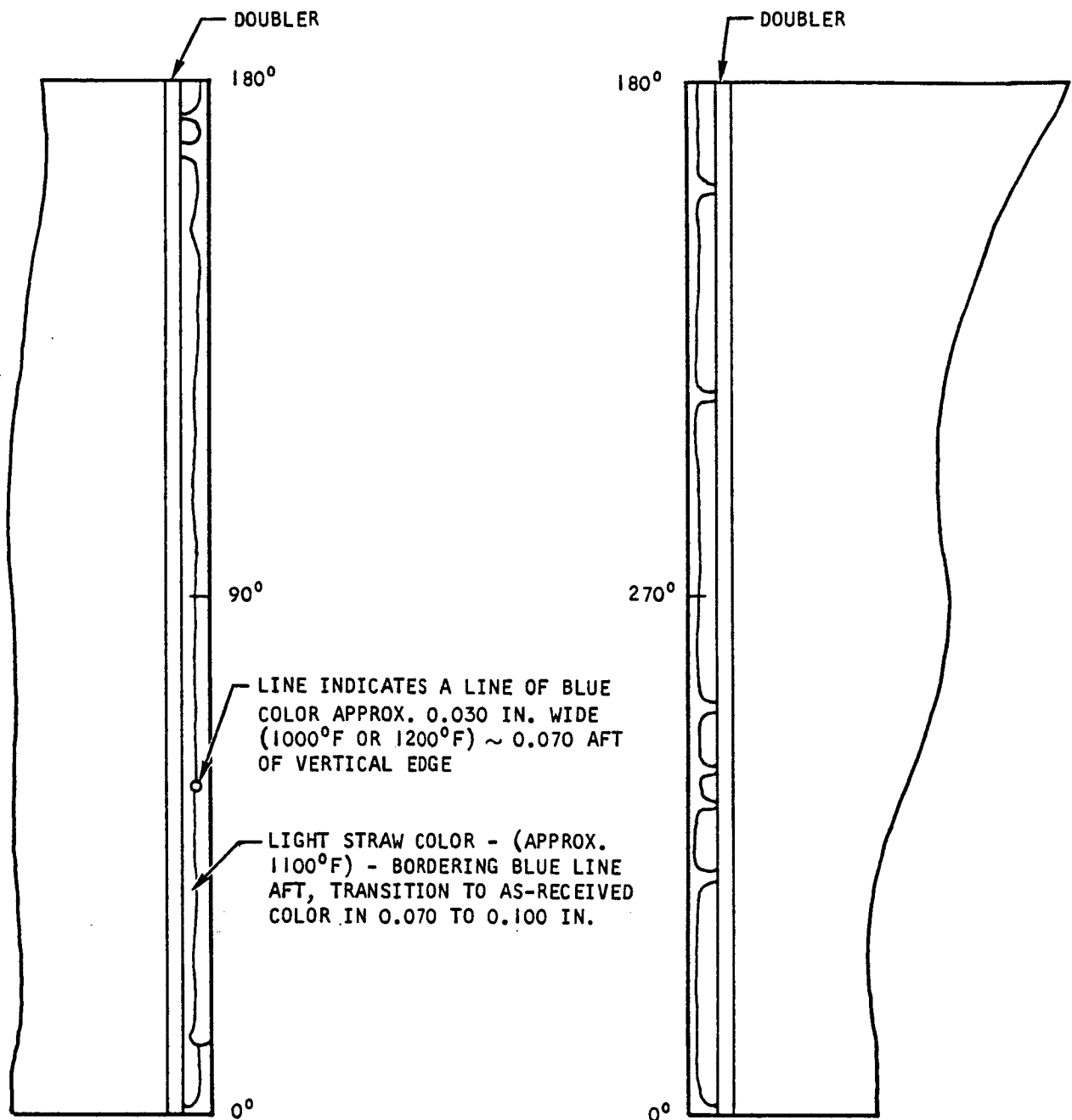
NOTES: 1. COMPARED POSTTEST 42, RUN 36

2. ALL DISCOLORATION (BLUE)
OCCURRED DURING TEST 41, RUN 26

3. INTERPRETATION BASED ON 2-MIN
POLISHED AND UNPOLISHED NICKEL
SPECIMENS

S-63675

Figure 5.1-2.   Leading Edge External Surface Color Markings (U)

AT 135° (DENT WITH SMALL LEAK):

BLUE-GRAY (1200°F)

BROWN-STRAW (1100°F)
(BARELY DETECTABLE IN OTHER AREAS)

2-MIN. UNPOLISHED
NICKEL SPECIMEN

START OF WHITE-GRAY COATING, BRIGHT METAL TO HERE

0.030 WIDE, 0.040 AFT OF VERTICAL EDGE
LIGHT BLUE-GRAY (1200°F, 2 MIN. UNPOLISHED NICKEL SPECIMEN)

STA. 35.89

360°

1-1/2

2-1/2

4

5-1/2

STA.
43.475

S-63679

DOUBLER

DARK BANDS,
LIGHT GRAY
BROWN

LIGHT
BLUE
1300°F,
10 MIN.

UNPOLISHED
HASTELLOY X SPECIMEN;
SHOWS IMPRINT OF
SPIKE INJECTORS

0°

LIGHT BLUE (1300°F)

BROWN (1000°F)

IN CLEAR (NO COATING)
AREA

1-1/2 CLEAR
METAL

110°

1-1/2 CLEAR
METAL

210°

1-1/2 CLEAR
METAL

NOTES: 1. COMPARED POSTTEST 42, RUN 36
2. ALL DIMENSIONS IN INCHES

Figure 5.1-3.   Leading Edge Internal Surface Color Markings (U)

Figure 5.1-4. Outer Shell Color Markings (U)

BOTTOM AS INSTALLED

180° 210° 270° 330° 0° 30° 90° 150° 180°

32.7 IN.

8.6 IN.

NOTE

1-1/2 IN.

3-1/2 IN.

2 IN.

BLUE WITH BROWN RIM (1300°F BLUE); BROWN TRANSITIONS QUICKLY TO AS-RECEIVED COLOR TOWARD STRUTS

STRUTS:

FIRST BREAK

FLOW

1/2 IN.

BLUE-BROWN BAND (1200°F, 10 MIN., UNPOLISHED SPECIMEN)

S-63680

NOTES:
1. DISCOLORED AREA SPACED OFF SIDES OF STRUTS, WITH BORDER THAT IS PARALLEL TO SIDES OF SECOND WEDGE ON STRUTS

2. INTERPRETATION BASED ON 10-MIN. EXPOSURE SPECIMENS

3. SCALE: APPROXIMATELY 1/8 IN. = 1 IN.

4. COMPARED POSTTEST 42, RUN 36.

GARRETT AIRESEARCH MANUFACTURING COMPANY
Los Angeles, California

TOP
180°

STRUT NO. 6   NO. 5   NO. 4   NO. 3   NO. 2   NO. 1

INNER
SHELL

15.6 IN.

1/2 IN.

BLUE WITH BROWN RIM (1200°F)

LIGHT BROWN (1000°F, PREDOMINANT)
AND BLUE (1100°F)

21.6 IN.

NOZZLE

NOTES: 1.   INTERPRETATION BASED ON 10-MIN UNPOLISHED SPECIMENS

2.   SCALE: APPROXIMATELY 1/8 IN. = 1 IN.

3.   COMPARED POSTTEST 41, RUN 36

S-63677

Figure 5.1-5. Innerbody Color Markings - Inner Shell (U)

Figure 5.1-6. Innerbody Discoloration - Nozzle (U)
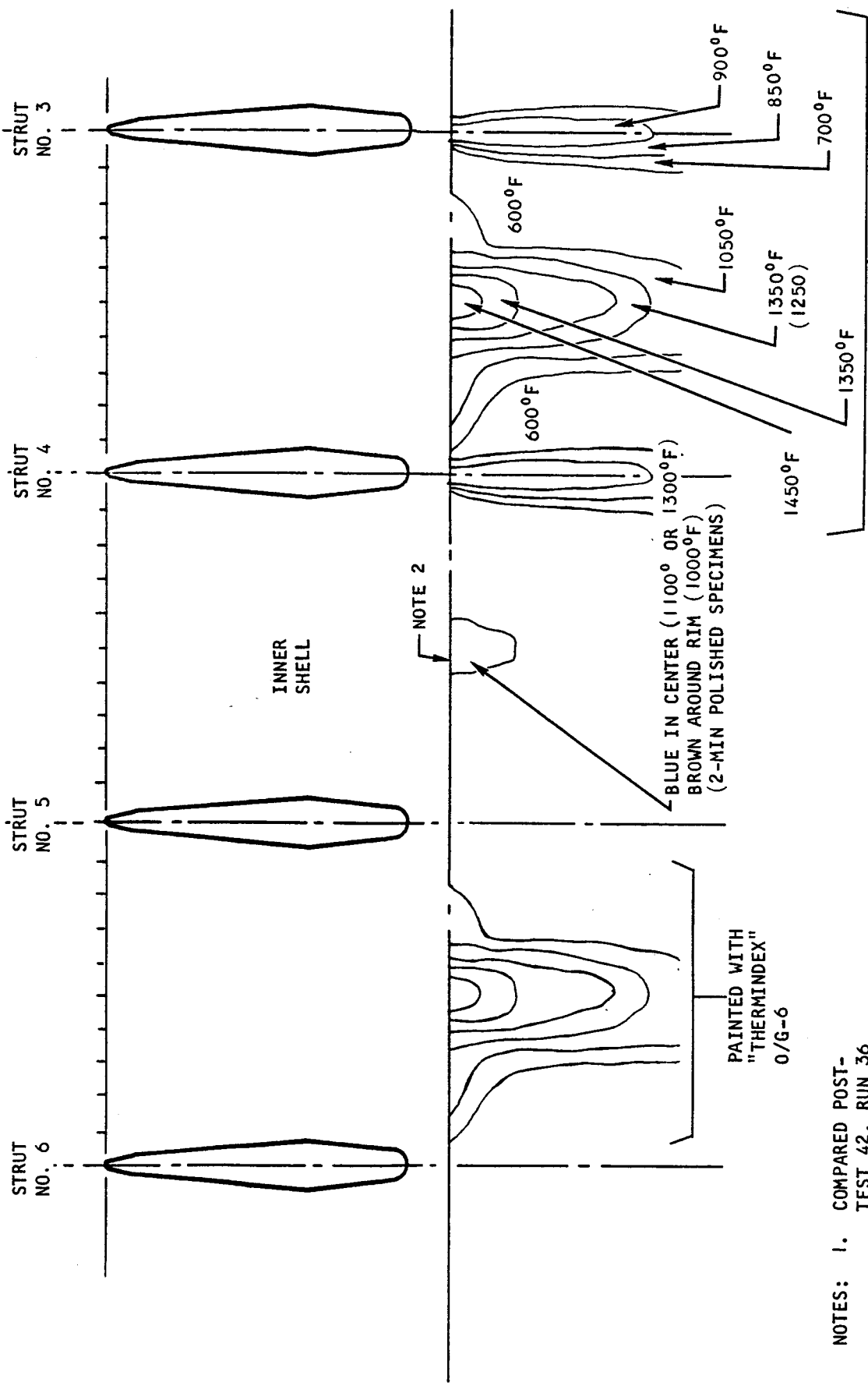
Figure 5.1-7. Color Pattern on Nozzle (U)

STRUT NO. 3

STRUT NO. 4

STRUT NO. 5

STRUT NO. 6

INNER SHELL

900°F
850°F
700°F
600°F
1050°F
1350°F (1250)
1350°F
1450°F
600°F

NOTE 2

BLUE IN CENTER (1100° OR 1300°F)
BROWN AROUND RIM (1000°F)
(2-MIN POLISHED SPECIMENS)

PAINTED WITH "THERMINDEX" 0/G-6

PAINTED WITH "THERMINDEX" 0/G-6

S-63676

NOTES: 1. COMPARED POST-
         TEST 42, RUN 36
       2. THIS AREA POLISHED WITH
          "CROCUS" CLOTH TO REMOVE
          OXIDES PRIOR TO RUN 36

STRUT
NO. 5

STRUT
NO. 4

STRUT
NO. 3

1-1/2 IN.

YELLOW

2 IN.

NOTE 1

BLUE (1100°F)
IN CENTER
BROWN (1000°F)
AROUND RIM

PAINTED WITH
THERMINDEX
O/G-6

NOTE 3
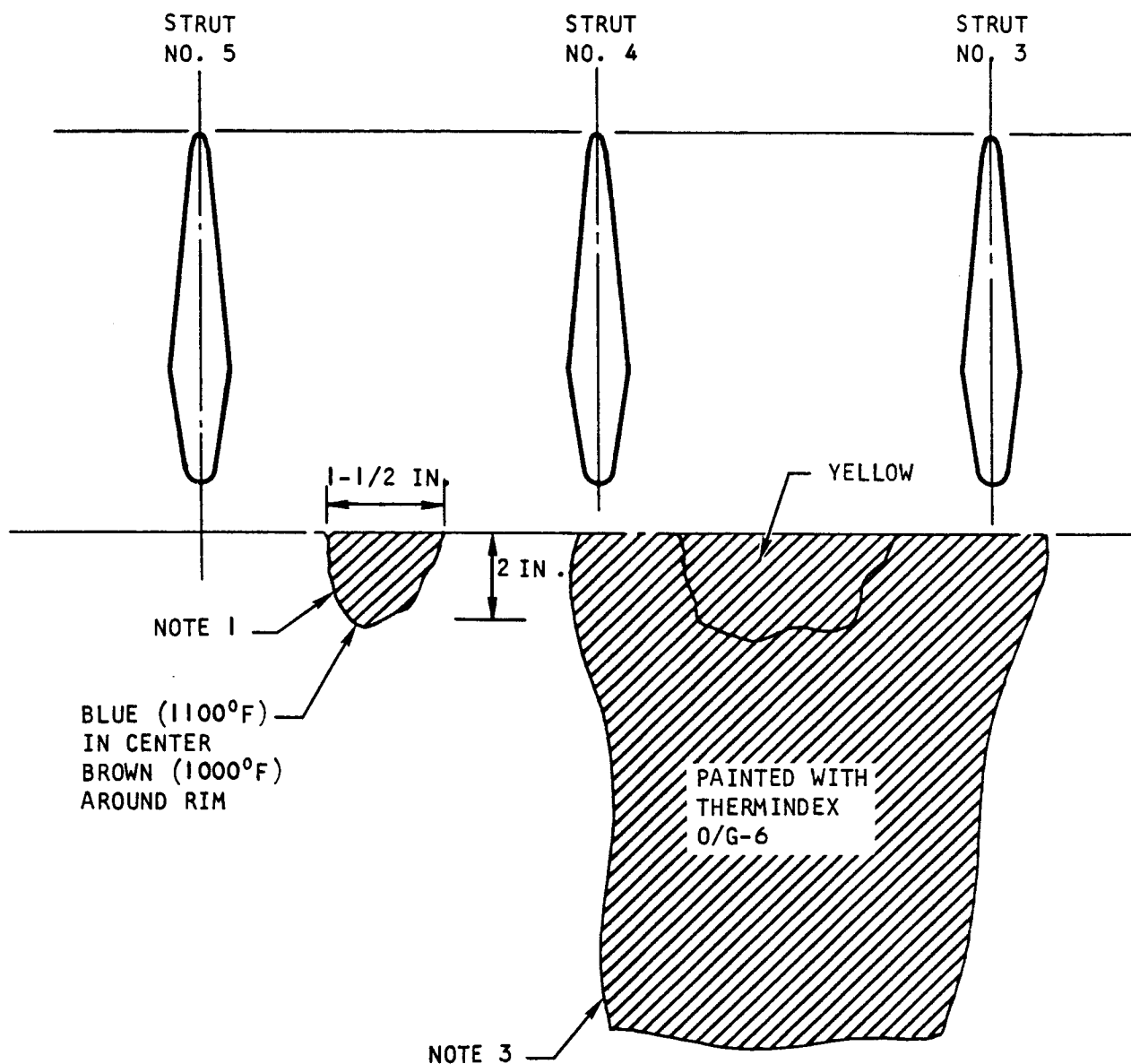
NOTES: 1. AREA POLISHED WITH CROCUS CLOTH BEFORE RUN; COMPARED
            WITH 2-MINUTE POLISHED SPECIMENS

        2. POSTTEST 42, RUN 38

        3. COLOR PATTERNS SAME AS TEST 42, RUN 36; CANNOT
            INTERPRET TEMPERATURES; BRUSHED SURFACE AND
            OBTAINED YELLOW AREA, WITH ALL ELSE REDDISH

S-67771

Figure 5.1-8. Nozzle Color Patterns (U)
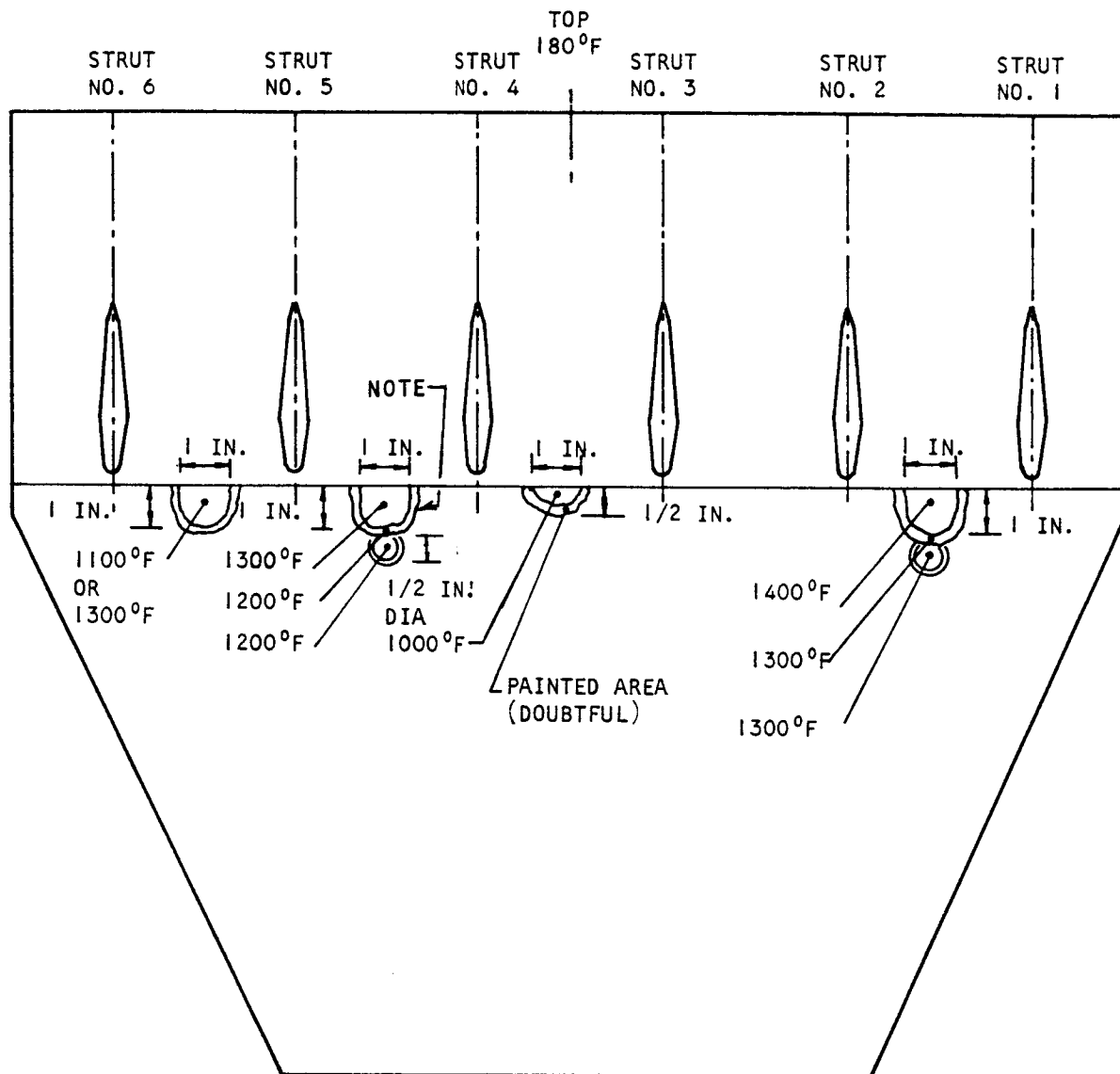
Figure 5.1-9. Nozzle Color Markings (U)

S-67805
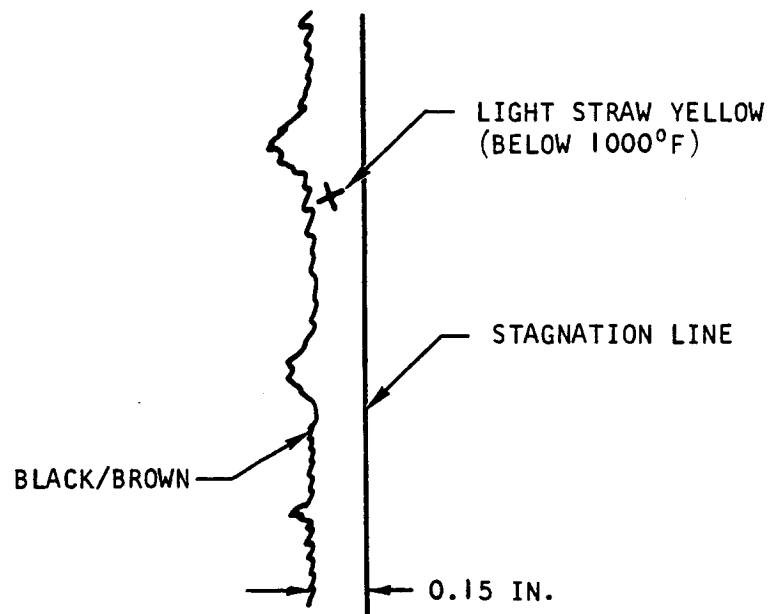
(a) Posttest 42, Run 38
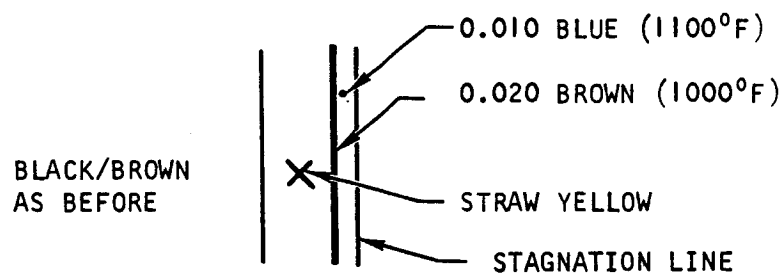
(b) Posttest 41, Run 39

S-67782

Figure 5.1-10. Leading Edge Discoloration Pattern (U)

BETWEEN STRUTS, IN 5 PLACES
(BOTTOM OBSCURED)

LOCATION OF AFT END OF SPIKE (EXTENDED)
(OUTER SHELL FORWARD OF THIS LINE
APPEARS UNIFORMLY BROWN (1400°F))

1 IN.

1400°F
BROWN,
IN BLUE
FIELD
(1300°F)

2 IN.
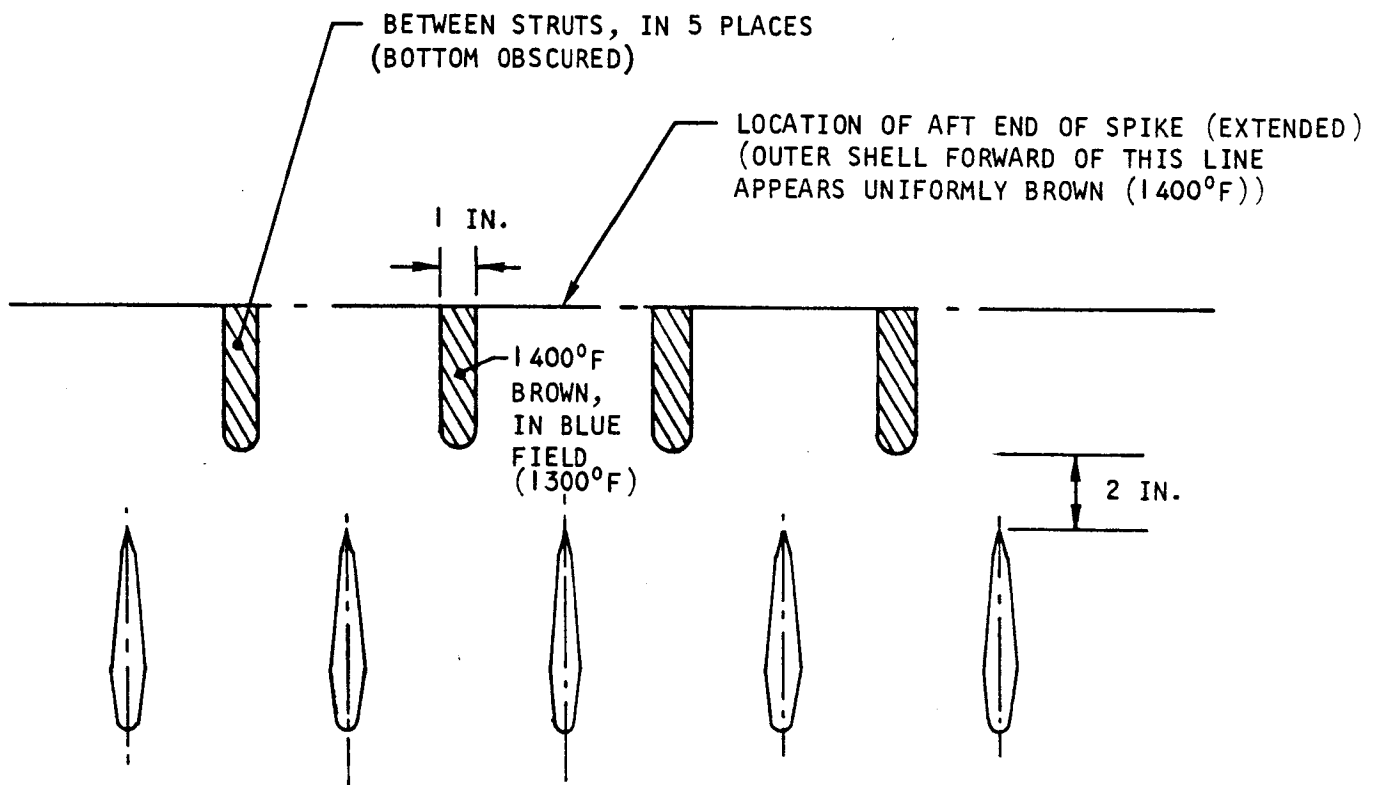
NOTES: 1. NOTED AFTER TEST 41, RUN 40; INTERPRETED AFTER
            TEST 41, RUN 42

        2. INNER SHELL SHOWS NO COMPARABLE MARKINGS   S-67784

Figure 5.1-11. Outer Shell Color Markings (U)

Figure 5.1-12. Spike and Leading Edge Discolorations After Angle-of-Attack Test Runs (U)
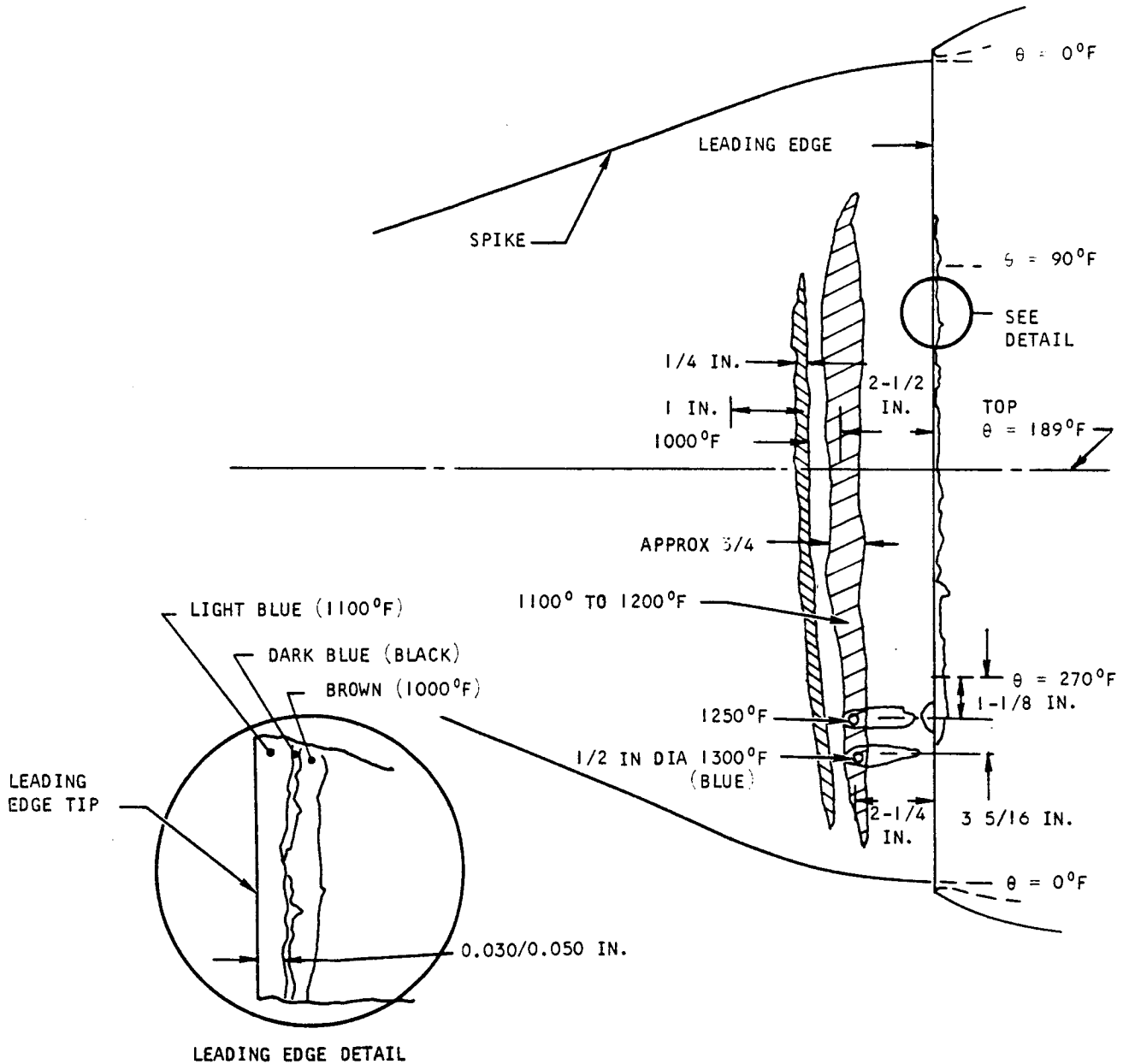
NOTES: 1. POSTTEST 41, RUN 52 OBSERVATIONS

S-67806

TABLE 5.1-2

LEADING EDGE DISCOLORATION PATTERNS (U)

Test/Run	Color Pattern on Leading Edge
42/38	(1) Brass at leading edge radius (to about 0.050 in. back from tip.
	(2) 1200°F. Purple at joints of segments, approximately 1/8 in. circumferentially, tip only.
42/41	Polished leading edge area shows no color at all.
42/42	Polished leading edge area shows brass color on tip only; does not extend back beyond tangency point of radius.
41/43	No significant change from previous run, except dulling of coloring noted in Run 42.
41/38	Light straw yellow (below 1000°F) from leading edge stagnation line to approximately 0.015 in. aft. Black/brown line at approximately 0.015 in. from stagnation line (ascribed to soot deposition but will not clean with solvent). See Figure 5.1-10(a).
41/39	Leading edge discoloration same as Test 41, Run 38, except 210-250 deg clockwise looking aft, shows blue (1100°F) to about 0.01 in. behind stagnation line, bordered brown (1000°F). Does not appear in other polished quadrant or in all of this quadrant. See Figure 5.1-10(b).

The calibration specimens used as the basis for the estimates are noted in the diagrams. Figure 5.1-6 also shows an area of localized deformation noted after Test 42, Run 26, but not present after Test 42, Run 19, when the nozzle was removed for seal replacement. Figure 5.1-12 shows the unsymmetrical discoloration pattern on the spike and leading edge after the 3-deg angle-of-attack test runs. All angular locations are based on 0 deg at the bottom of the SAM, as installed, and are viewed clockwise looking aft (CWLA).

5.1.2.2 Temperature-Indicating Paint

For two of the test runs, selected areas on the nozzle were polished with No. 400 grit paper, and temperature-indicating paint applied. Results are shown diagrammatically in Figures 5.1-6, 5.1-7, and 5.1-8.

The low-temperature-range paint ("Thermindex" 0/E-94) was overheated and did not provide meaningful data, as shown in Figure 5.1-6. The high temperature paint ("Thermindex" 0/G-6) gave results which agreed reasonably well with observed metal discoloration for this run. On the subsequent run, however, the paint gave results which are not quantitatively valid, as shown in Figure 5.1-7, although distinct color patterns were obtained. This may be due to a peculiarity of application or the effects of hydrogen injection during this run (no hydrogen was injected during the run for which results are shown in Figure 5.1-6. It is known that these paints are pressure sensitive and can yield erratic indications as a result of such sensitivity.

5.1.2.3 Inlet Schlieren Photographs

The shock-on-lip spike position was found by inspection of engine inlet Schlieren photographs which showed the spike bow shock wave in relation to the cowl leading edge lip. The progression of the shock as the spike was retracted for Test 42, Run 43 (1380 psia, 2700°R tunnel reservoir conditions) is shown in Figures 5.1-13 to 5.1-17. In Figure 5.1-13, the engine is in the tunnel without hot gas flow and the spike is in the fully closed, latched position. The intersection of the cross hairs locates the cowl leading edge. As the spike was retracted from the latched position in Figure 5.1-14 with hot gas flow, the shock can be seen moving to the lip in the succeeding figures. The approximate shock-on-lip condition can be seen in Figure 5.1-17 where the spike retraction was 3.85 in. This shock-on-lip-position condition was not steady for Test 42, Run 43 due to pressure fluctuations in the freestream. In addition, the shock-on-lip position changed at the higher tunnel reservoir pressures due to changing gas properties.

5.1.3 Wind Tunnel Aerodynamic Conditions

The data and procedures used to determine the SAM aerodynamic conditions in the NASA Langley 8-Foot High Temperature Structures Tunnel are presented. The tunnel parameters selected for calculation were freestream Mach number, static pressure, and total temperature at the tunnel test section and the hot gas flow rate captured by the engine inlet. Figures 5.1-18 to 5.1-26 present the aerodynamic data for the methane combustion-products gas as determined from tunnel survey tests and analysis. The calculation procedure is presented in
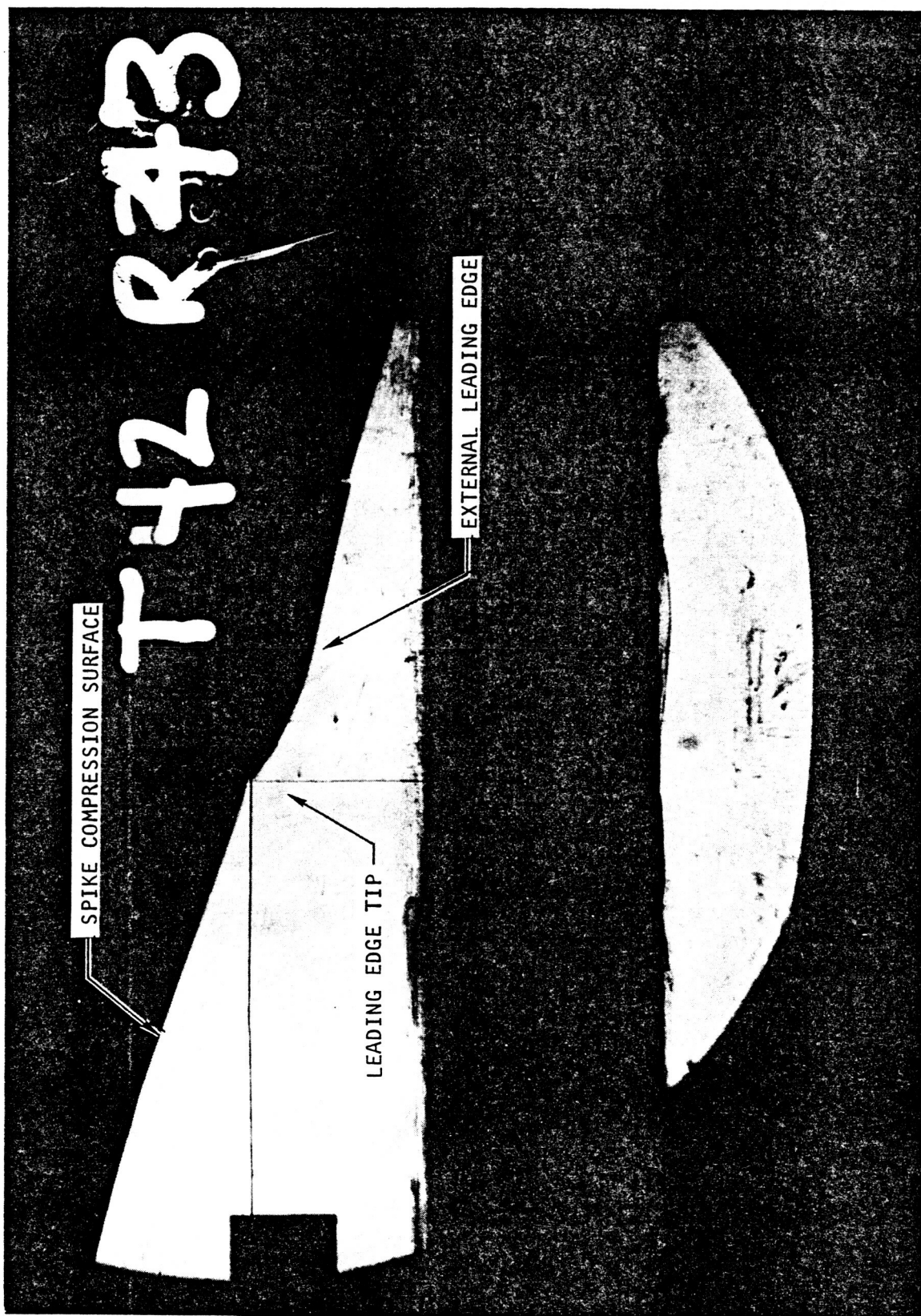
F-13836

Figure 5.1-13. Inlet Schlieren Photograph for Test 42, Run 43 - Inlet Closed, No Gas Flow

Figure 5.1-14. Inlet Schlieren Photograph for Test 42, Run 43 - Inlet Closed
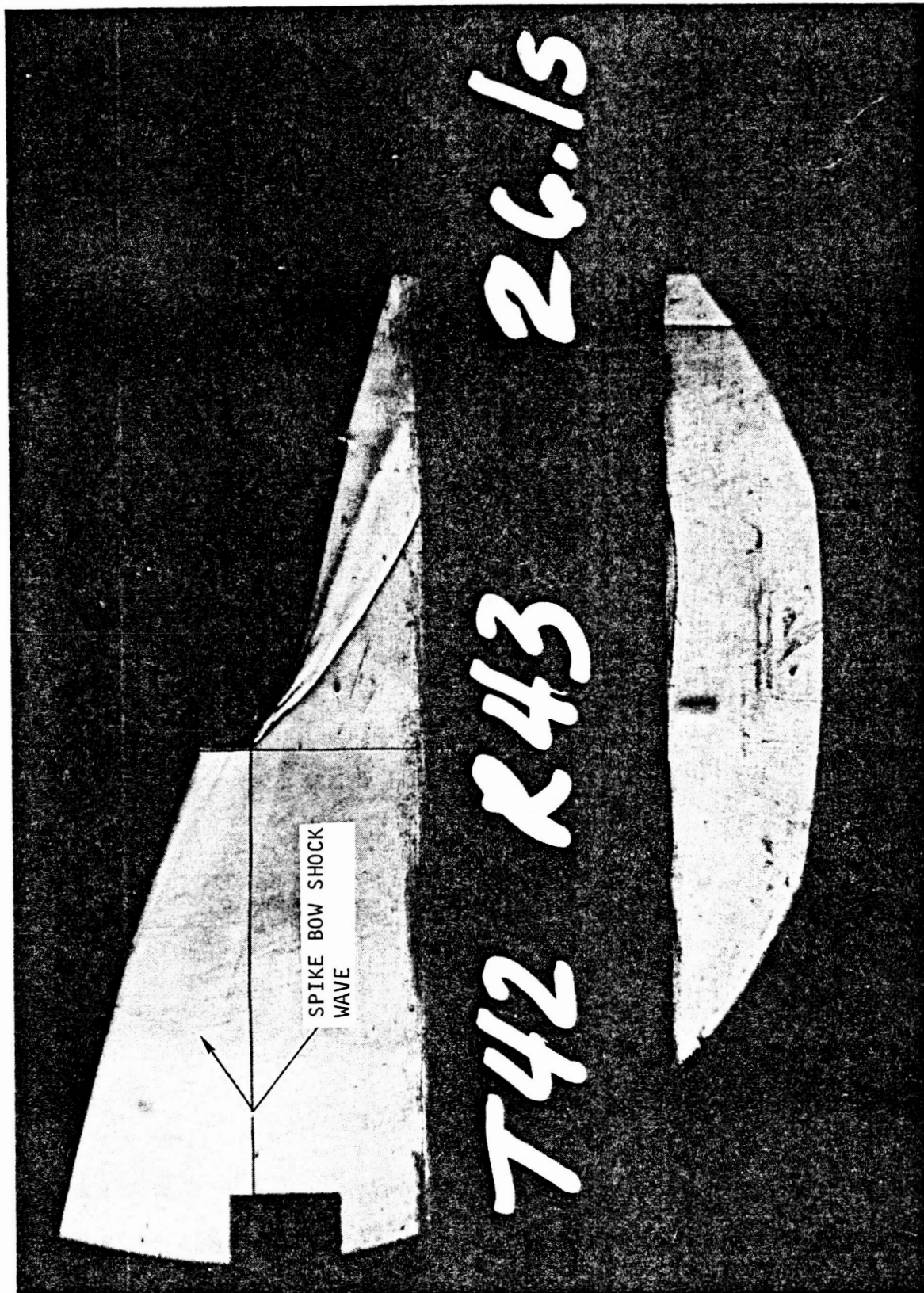
Figure 5.1.15. Inlet Schlieren Photograph for Test 42, Run 43 - Spike Retraction = 2.58 In.

AIRESEARCH MANUFACTURING COMPANY
Los Angeles, California

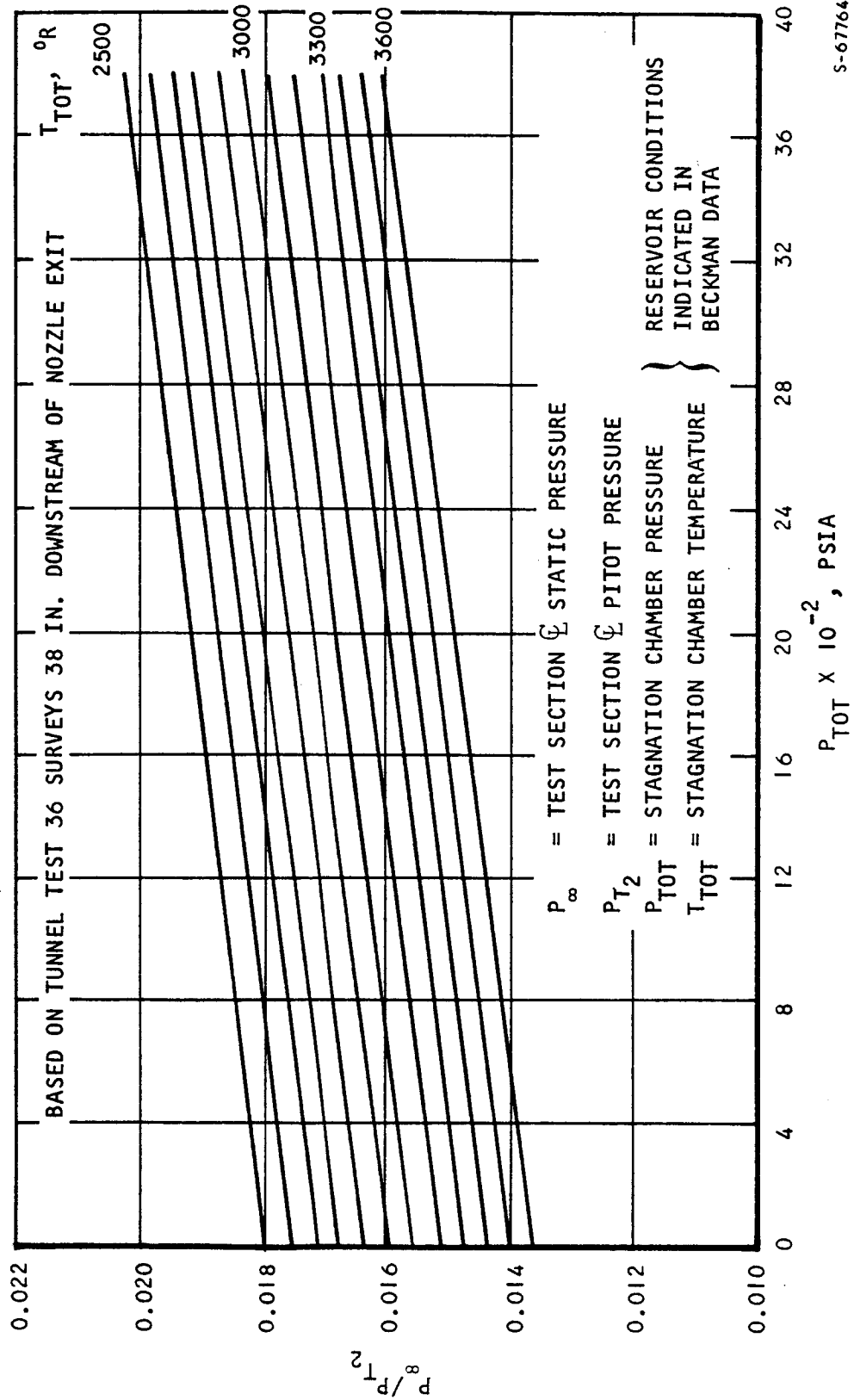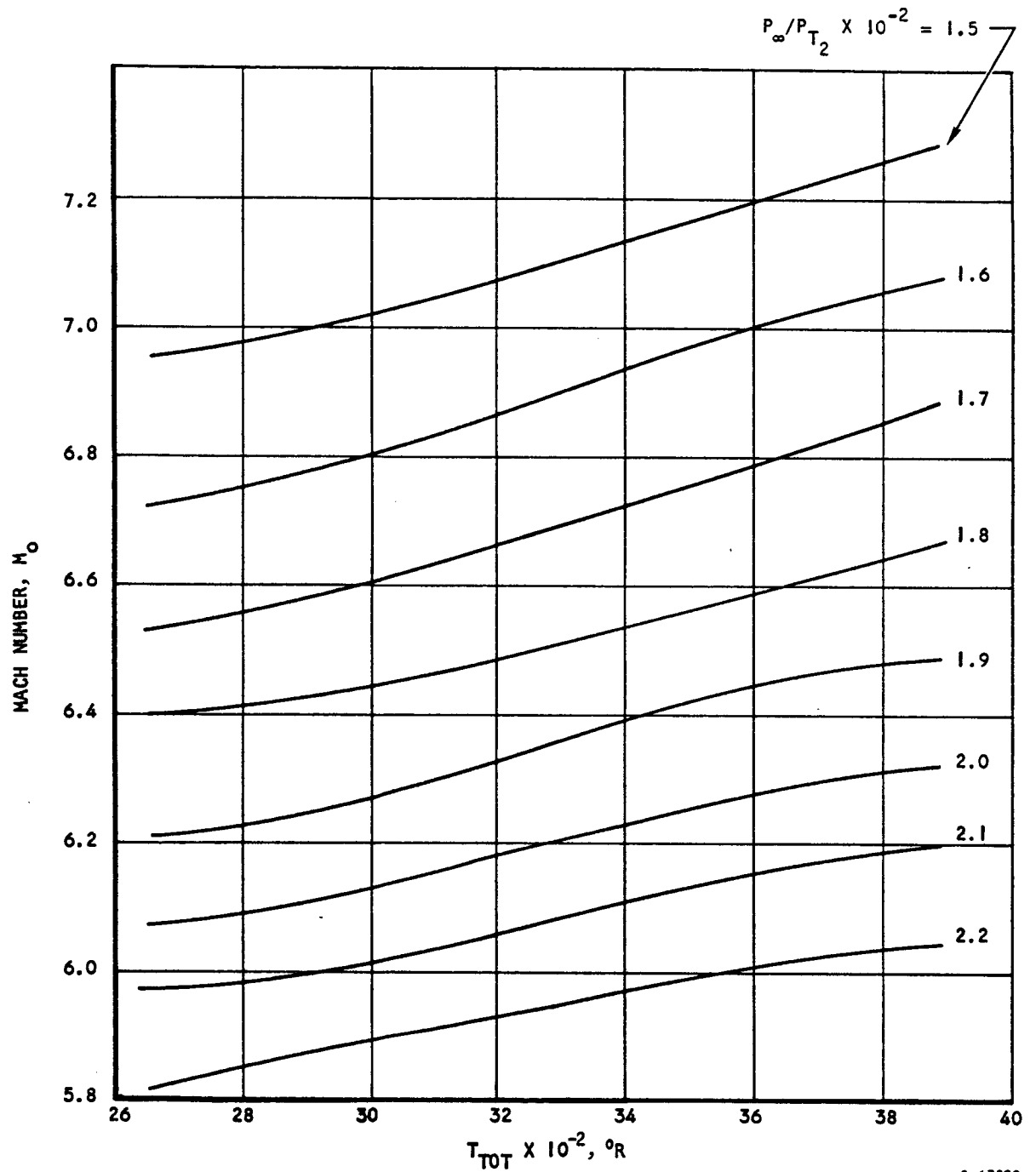Figure 5.1-16. Inlet Schlieren Photograph for Test 42, Run 43 - Spike Retraction = 3.88 in.

F-13835

T42 R43 38.75

APPROXIMATE
SHOCK-ON-LIP
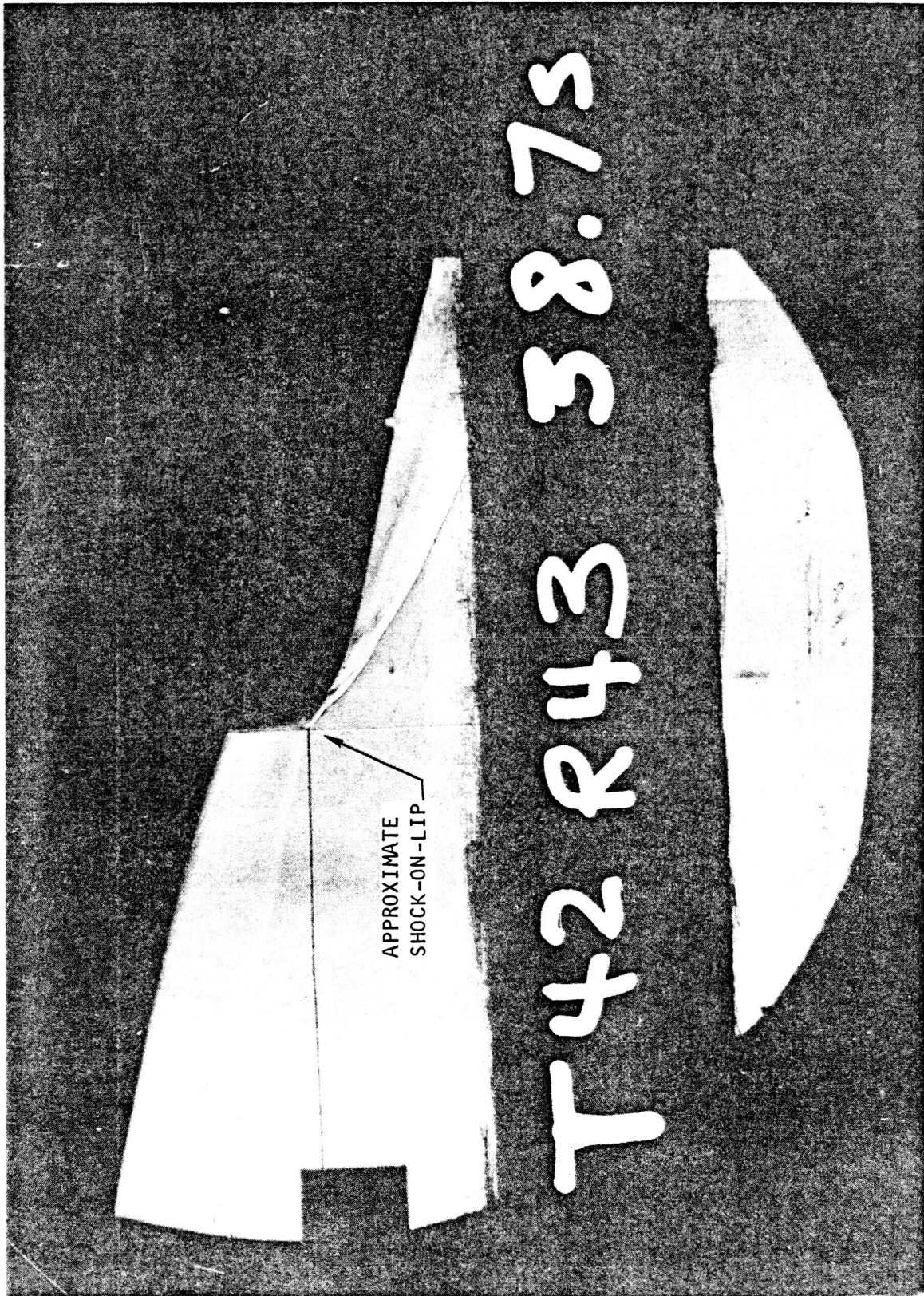
Figure 5.1-17. Inlet Schlieren Photograph for Test 42, Run 43 - Spike Retraction = 3.85 in.

UNCLASSIFIED

Figure 5.1-18. P_∞/P_{T_2} Versus P_{TOT} and T_{TOT}

UNCLASSIFIED

AIRESEARCH MANUFACTURING COMPANY
Los Angeles, California

71-7702
Page 5-27

Figure 5.1-19. Test Section Average M_o Versus T_{TOT} and P_∞/P_{T_2}

S-67809

GARRETT AIRESEARCH MANUFACTURING COMPANY
Los Angeles, California
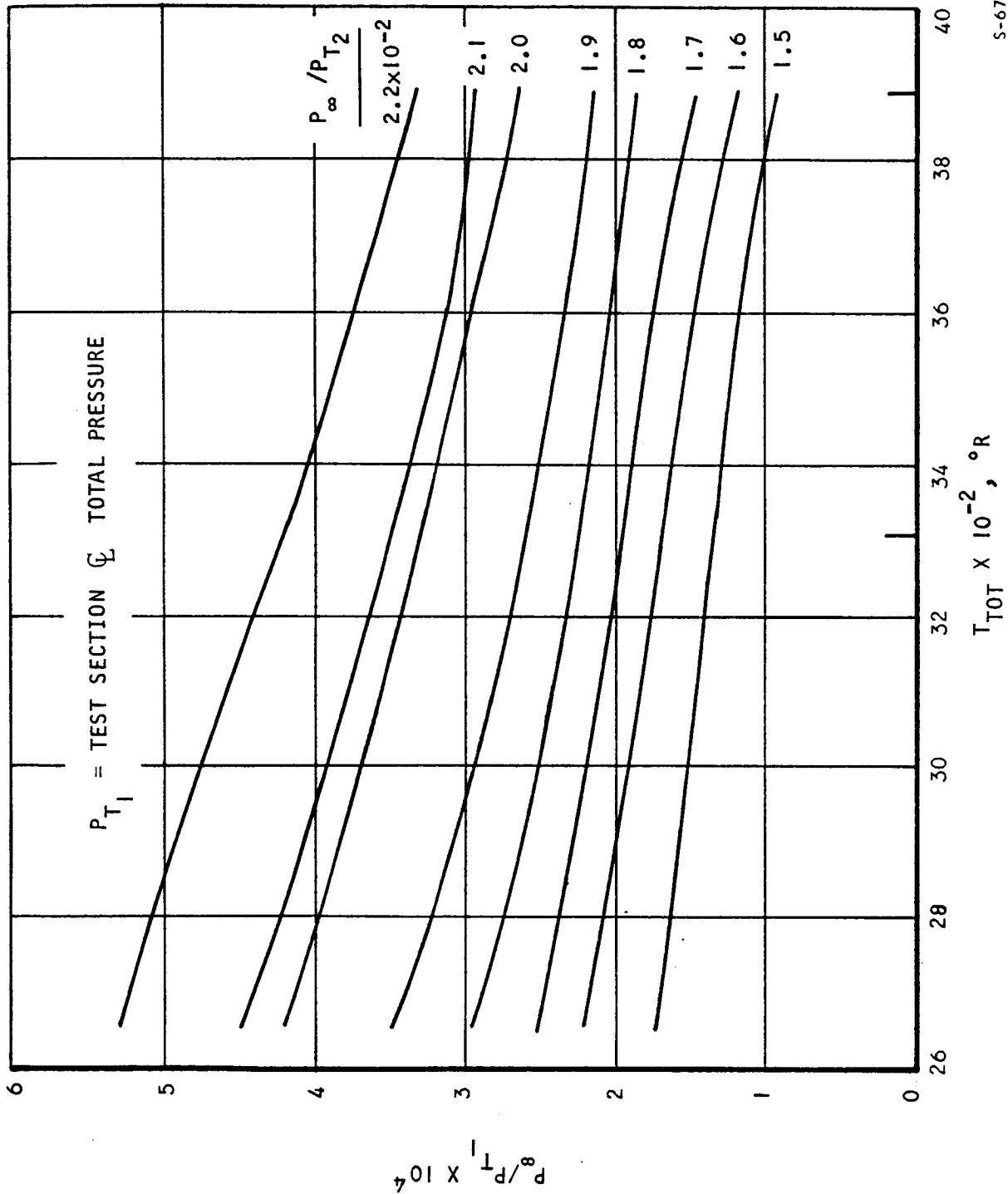
Figure 5.1-20. P_∞ and P_{T_1} Versus T_{TOT} and P_∞/P_{T_2}

S-67768

AIRESEARCH MANUFACTURING COMPANY
Los Angeles, California

P_{70} = SAM SPIKE TIP PITOT PRESSURE
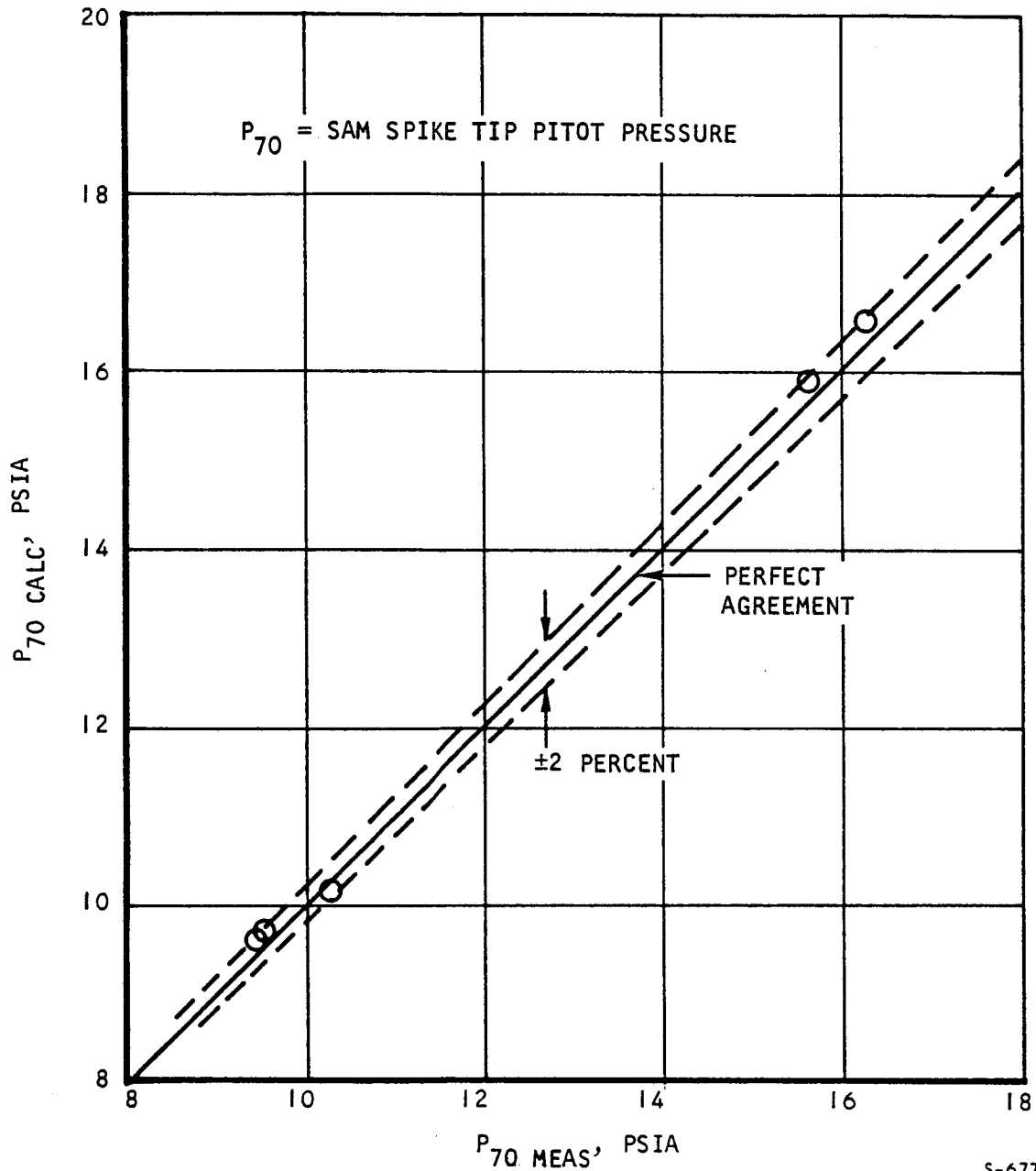
Figure 5.1-21. Calculated P_{70} Versus Measured P_{70}

S-67773
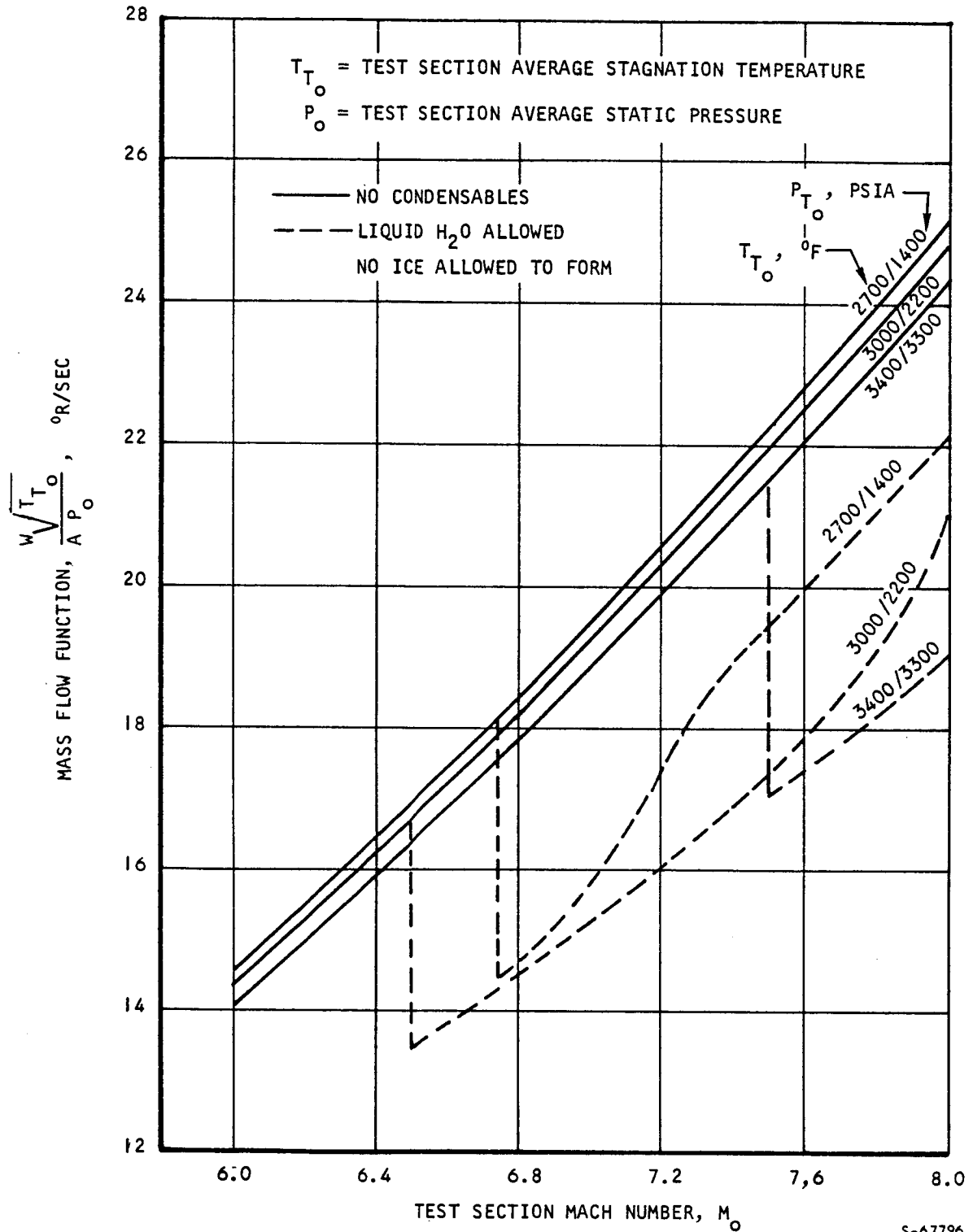
UNCLASSIFIED

Figure 5.1-22. Equilibrium Methane/Air Combustion Mass-Flow Function

UNCLASSIFIED

AIRESEARCH MANUFACTURING COMPANY
Los Angeles, California

71-7702
Page 5-31
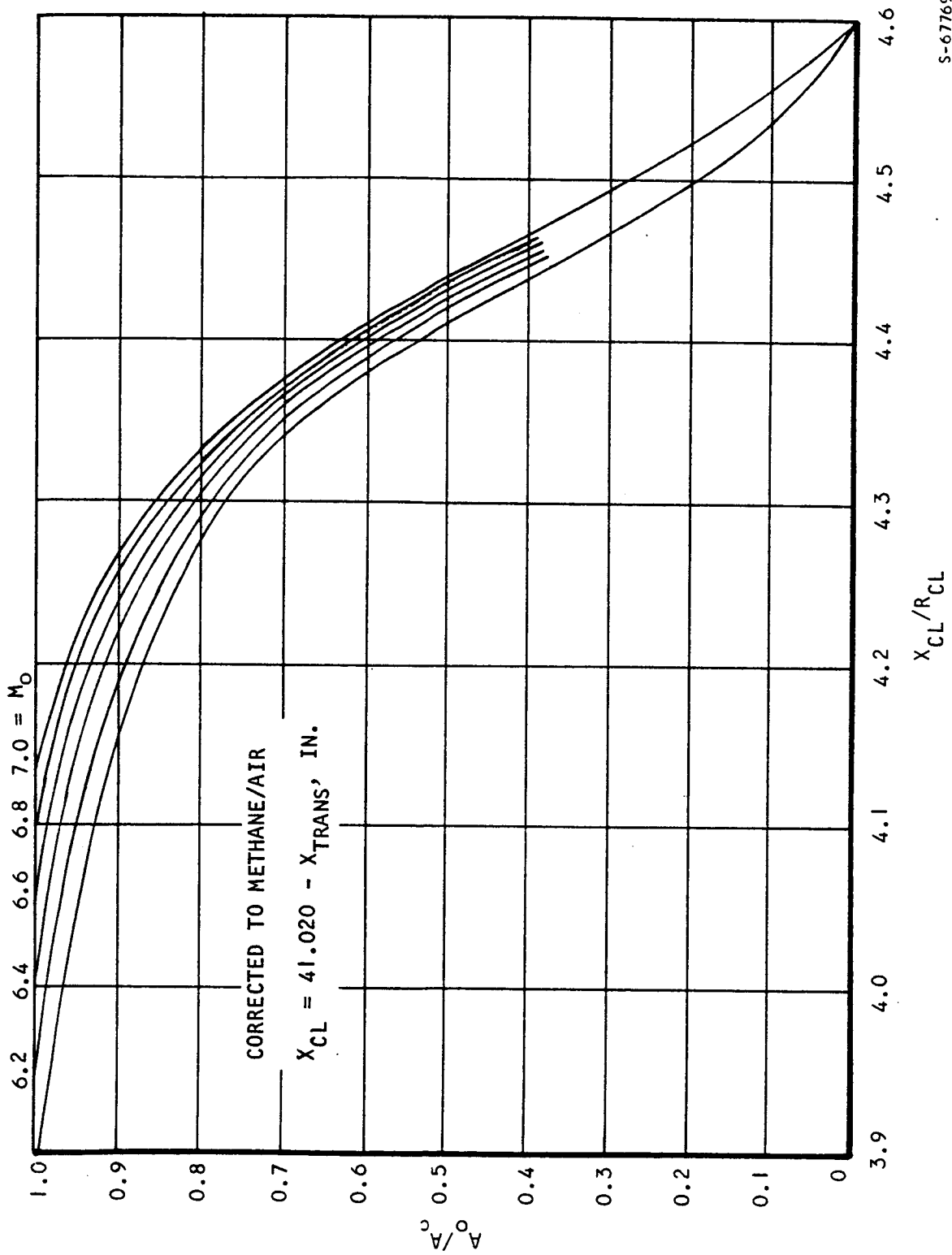
UNCLASSIFIED

Figure 5.1-23. SAM Inlet Mass Flow Ratio, A_o/A_c, Versus Spike Position

S-67769

CORRECTED TO METHANE/AIR

$X_{CL} = 41.020 - X_{TRANS}$, IN.

GARRETT AIRESEARCH MANUFACTURING COMPANY
Los Angeles, California

UNCLASSIFIED

71-7702
Page 5-32

LIP DETAIL

$r_c = 0.030$

$\delta = 11.5$ DEG

X'

X_{CL}
0.036

$R_{CL} = 9.000$

X'
= "TIP-TO-TIP"
DISTANCE,
MEASURED PARALLEL
TO ENGINE ℄.

0.595

SPIKE VERTEX

10 DEG

$r_s = 0.125$

X_{CL}
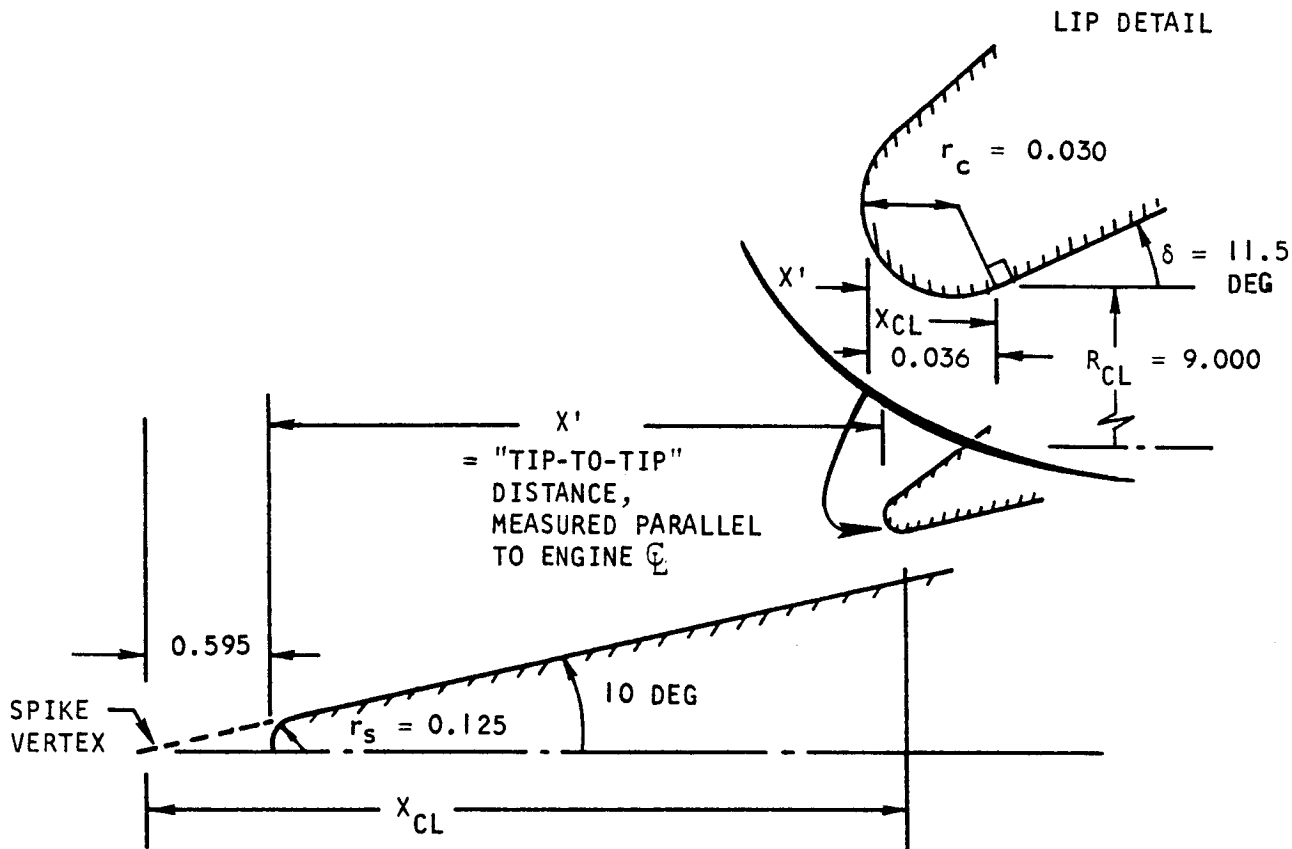
NOTE: ALL DIMENSIONS ARE IN INCHES   S-67777

IN GENERAL,

$$X_{CL} = X' + C_1, \quad C_1 \equiv 0.595 + 0.036 \approx 0.63$$

ALSO,

$$X' = X'_{LATCH} - X_{TRANS}, \quad X'_{LATCH} = 40.39 \text{ (AT } X_{TRANS} = 0)$$

$$\therefore X_{CL} = 40.39 - X_{TRANS} + 0.63$$

OR, $X_{CL} = 41.02 - X_{TRANS}$

X_{TRANS} = SAM SPIKE RETRACTION DISTANCE FROM FULLY CLOSED, LATCHED POSITION

= 0.0, CLOSED

= 5.09, FULLY RETRACTED

Figure 5.1-24. SAM Inlet Schematic and Nomenclature
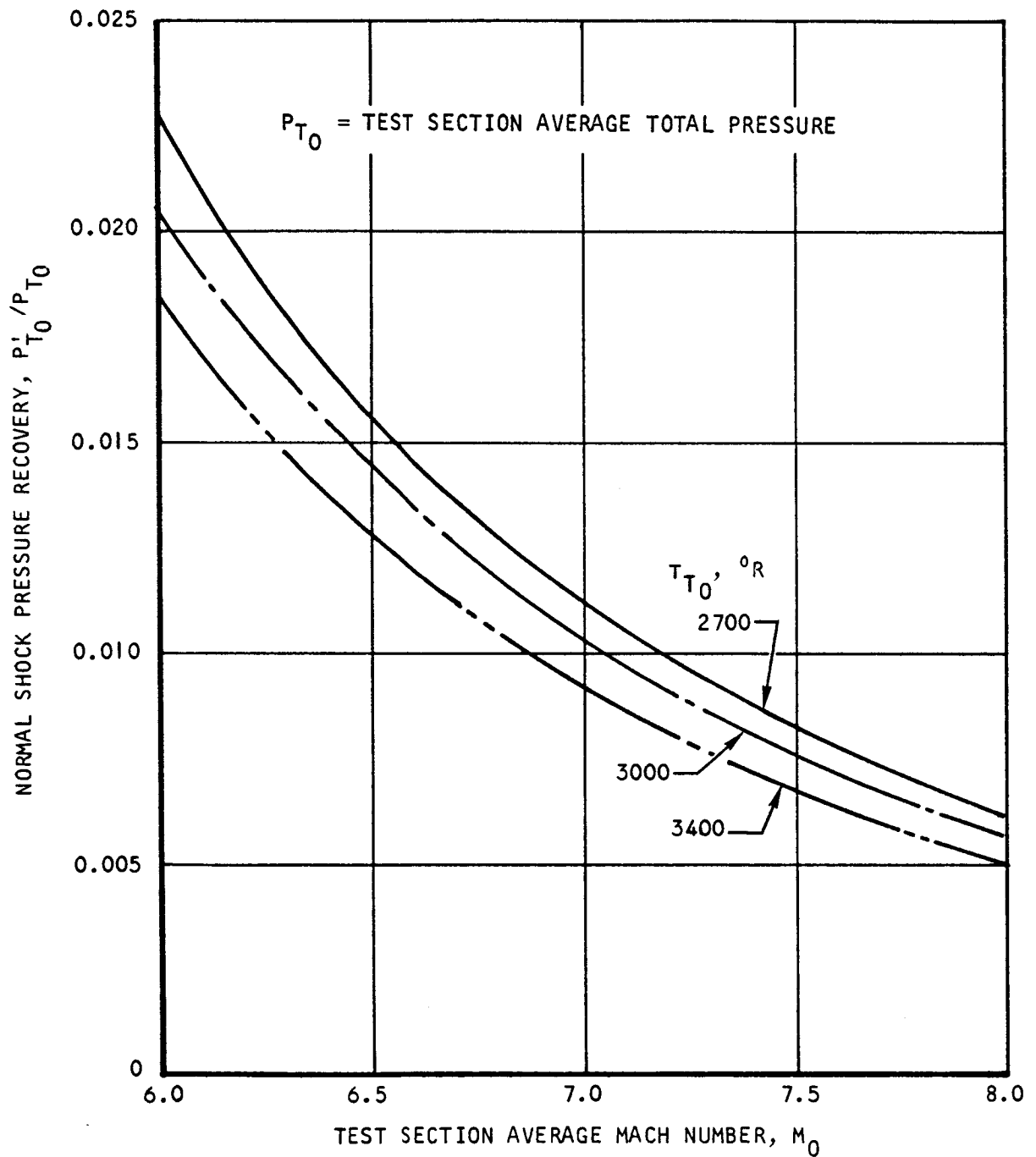
Figure 5.1-25. Normal Shock Pressure Recovery Versus Mach No. for Methane/Air Combustion Products

S-67785
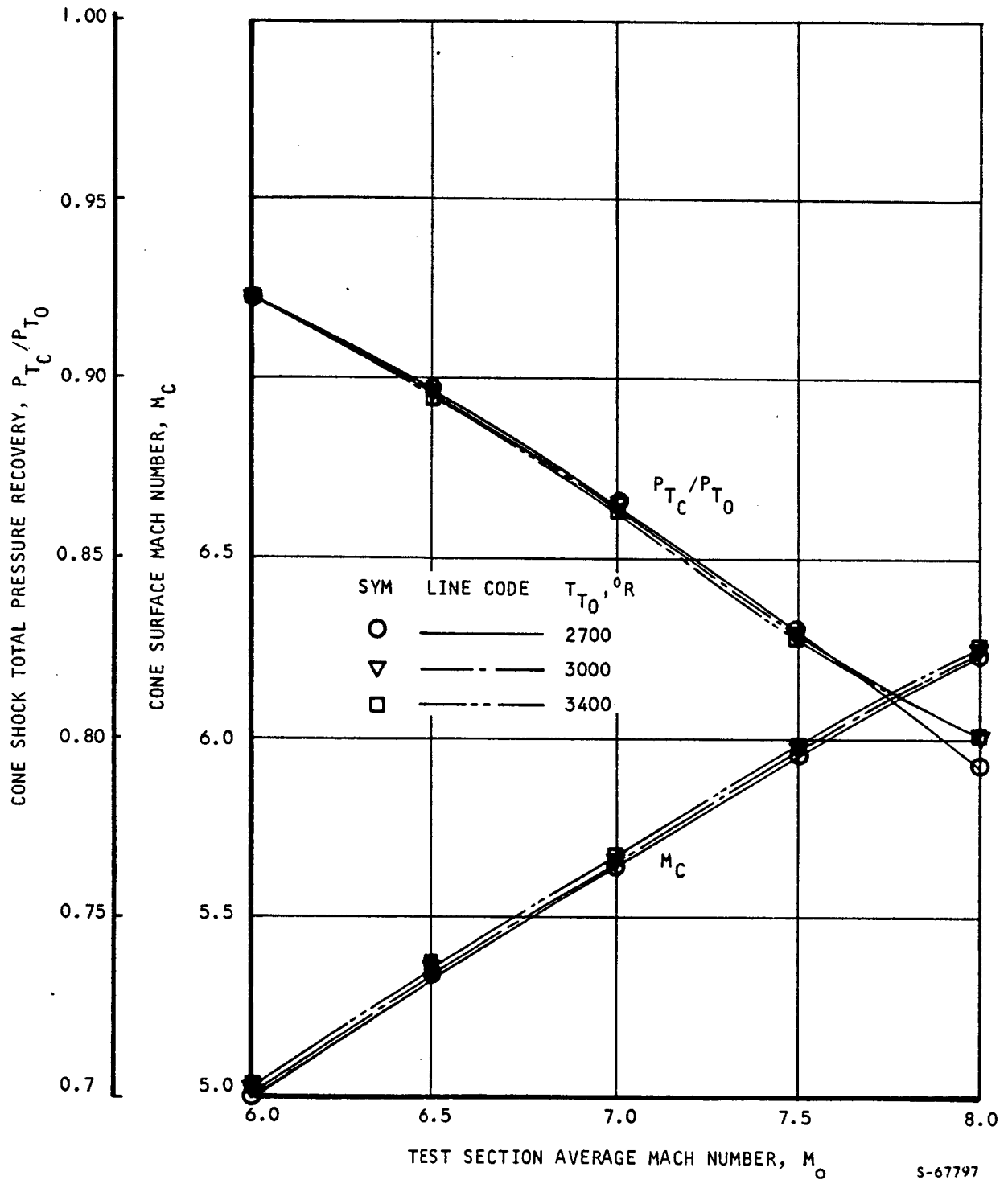
Figure 5.1-26.   Flow Variables on a 10-deg Cone for Methane/Air Combustion
Products

GARRETT AIRESEARCH MANUFACTURING COMPANY
Los Angeles, California

UNCLASSIFIED

Table 5.1-3 and some results of the calculation procedure as used in the data reduction are presented in Table 5.1-4.

5.2 AERODYNAMIC HEATING

5.2.1 Summary of Results

One of the SAM test objectives was to verify or update the methods previously used to predict design flight heat loads and fluxes (Mach 8 freestream and local, 88,000-ft altitude, zero-deg angle of attack). Test heat loads and average heat fluxes were obtained from measurement of the heat input to the hydrogen coolant in the flow routes at steady state. Analytic heat loads and fluxes were obtained from measured tunnel freestream conditions, SAM hot gas surface pressure and temperature distributions, and the design prediction methods. Test and analytic average heat fluxes agree within ±20 percent over most surfaces of the engine.

Hot coolant hydrogen from the outlet of the SAM flow routes was injected into the captured hot gas stream for most of Test 42 runs. The effect of hydrogen injection was detected as higher hot gas static pressures downstream of the injectors than for runs (Test 41) without injection. The effect of injection was not detected in the hydrogen heat loads or measured surface temperatures on the aft flow routes.

Locally highly heated areas were detected from posttest observations of surface metal discolorations. The highly heated zones were traced to shock wave-boundary layer interactions. The heating rates relative to unaffected adjacent areas were estimated from a layout of the aerodynamic flow field.

5.2.2 Test Data

5.2.2.1 Tunnel Conditions

Heat loads on the spike flow route and the total SAM are shown in Figure 5.2-1 as a function of tunnel reservoir total pressure. These heat loads are maximum loads during thermal performance runs as measured from the hydrogen coolant heat absorption. The range of tunnel reservoir total pressure was from 900 psia to 3330 psia for the tests shown. Tunnel total temperature increased from 2500° to 3400°R with increasing tunnel total pressure in the following manner:

Total Pressure, psia	Total Temperature, °R
900	2500
1400	2700
2200	3000
3300	3400

TABLE 5.1-3

PROCEDURES FOR CALCULATING SAM TEST CONDITIONS

| Step	Definition	Enter Figure No.	With	To Obtain	Equation	Comment
1	Parameter	5-70	P_{TOT}, T_{TOT}	P_∞/P_{T_2}		Use average values of P_{TOT}, T_{TOT} from Beckman data
2	M_0 = Test Mach No.	5-71	$T_{TOT}, P_\infty/P_{T_2}$	M_0		$T_{TOT}, P_\infty/P_{T_2}$ from Step 1
3	Parameter	5-72	$T_{TOT}, P_\infty/P_{T_2}$	P_∞/P_{T_1}		$T_{TOT}, P_\infty/P_{T_2}$ from Step 1
*4	Parameter			β	$\beta = \left[0.896 + (2.4468E-0.05)(2560-T_{TOT})\right]\left(\dfrac{P}{W_{612}}\right)$	*If cryogenic H_2, complete Step 4; If room temp H_2, go to Step 5
5	Spike pitot pressure			P_{70}	$*P_{70} = \dfrac{\beta}{P_\infty/P_{T_2}}$, *If room temp H_2, obtain P_{70} from Beckman data	P_∞/P_{T_2} from Step 1. Accuracy of this step shown in Figure 5.1-21
6	Test section average pitot pressure = P_{T_2}			$\bar{P}_{T_2}$	$\bar{P}_{T_2} = (0.8524)P_{70} + (1.146E - 0.03) P_{TOT}$	P_{70} from Step 5; P_{TOT} from Step 1
7	Test Section average static pressure = P_0			P_0	$P_0 = \bar{P}_{T_2}\left(P_\infty/P_{T_2}\right)$	$\bar{P}_{T_2}, P_\infty/P_{T_2}$; Steps 6 and 1, respectively
8	Test stagnation temp			T_{T_0}	$T_{T_0} \equiv T_{TOT}$	T_{TOT} from Step 1
9	Airflow parameter	5-74	T_{TOT}, M_0	$\dfrac{W\sqrt{T_{T_0}}}{A P_0}$		
10	Airflow per unit area			W/A	$W/A = \left(\dfrac{W\sqrt{T_{T_0}}}{A P_0}\right) P_0/\sqrt{T_{T_0}}$	P_0, T_{T_0}; Steps 7 and 8, respectively
11	Spike position	5-75		x_{CL}/R_{CL}	$x_{CL}/R_{CL} = (41.02 - x_{TRANS})/9.000$	x_{TRANS} from Beckman data
12	Mass flow ratio	5-75	$x_{CL}/R_{CL}, M_0$	A_0/A_c		
13	Captured airflow			W	$W = 81\pi\left(\dfrac{W}{A}\right)\left(\dfrac{A_0}{A_c}\right)$, lb/sec	
14	Test section average total pressure			P_{T_0}	$P_{T_0} = P_0/\left(P_\infty/P_{T_1}\right)$	
15	Oblique shock recovery	5-78	T_{TOT}, M_0	P_{T_c}/P_{T_0}		
16	10-deg cone surface total pressure			P_{T_c}	$P_{T_c} = P_{T_0}\left(P_{T_c}/P_{T_0}\right)$	P_{T_0} from Step 14
17	10-deg cone surface Mach No.	5-78	T_{TOT}, M_0	M_c		

TABLE 5.1-4

MEASURED AND CALCULATED AERODYNAMIC CONDITIONS FOR SELECTED SAM TEST RUNS (U)

Test No.	Run No.	Data Averaging Times, sec	Average Measured				M_o	X_{CL}/R_{CL}	A_o/A_c	Captured Mass Flow, lb/sec
			P_{TOT}, psia	T_{TOT}, °R	P_{70}, psia	X_{TRANS}, in.				
42	34	81.2-91.2	1390	2742	9.42	2.8977	6.43	4.2358	0.887	12.4
42	36	73.8-83.8	1388	2752	9.51	2.8960	6.43	4.2360	0.888	12.5
41	20	73.2-83.2	1504	2685	10.25	2.8631	6.36	4.23966	0.875	13.1
42	45	129.2-139.2	2244	3022	-*	2.8924	6.53	4.2364	0.898	20.2
41	40	75.0-85.0	2286	2961	-*	3.4244	6.51	4.1773	0.912	20.2
41	37	75.5-85.5	2832	3321	-*	2.8985	6.80	4.2357	0.923	25.5
41	39	48.3-58.3	3323	3385	-*	2.8923	6.81	4.2364	0.923	29.4
42	46	48.7-58.7	3318	3245	-*	2.9016	6.67	4.2354	0.915	28.9
41	42	52.3-62.3	3323	3088	-*	3.1174	6.52	4.2114	0.920	29.2

*Frost formation for these cryogenic hydrogen-cooled test runs plugged P_{70}.
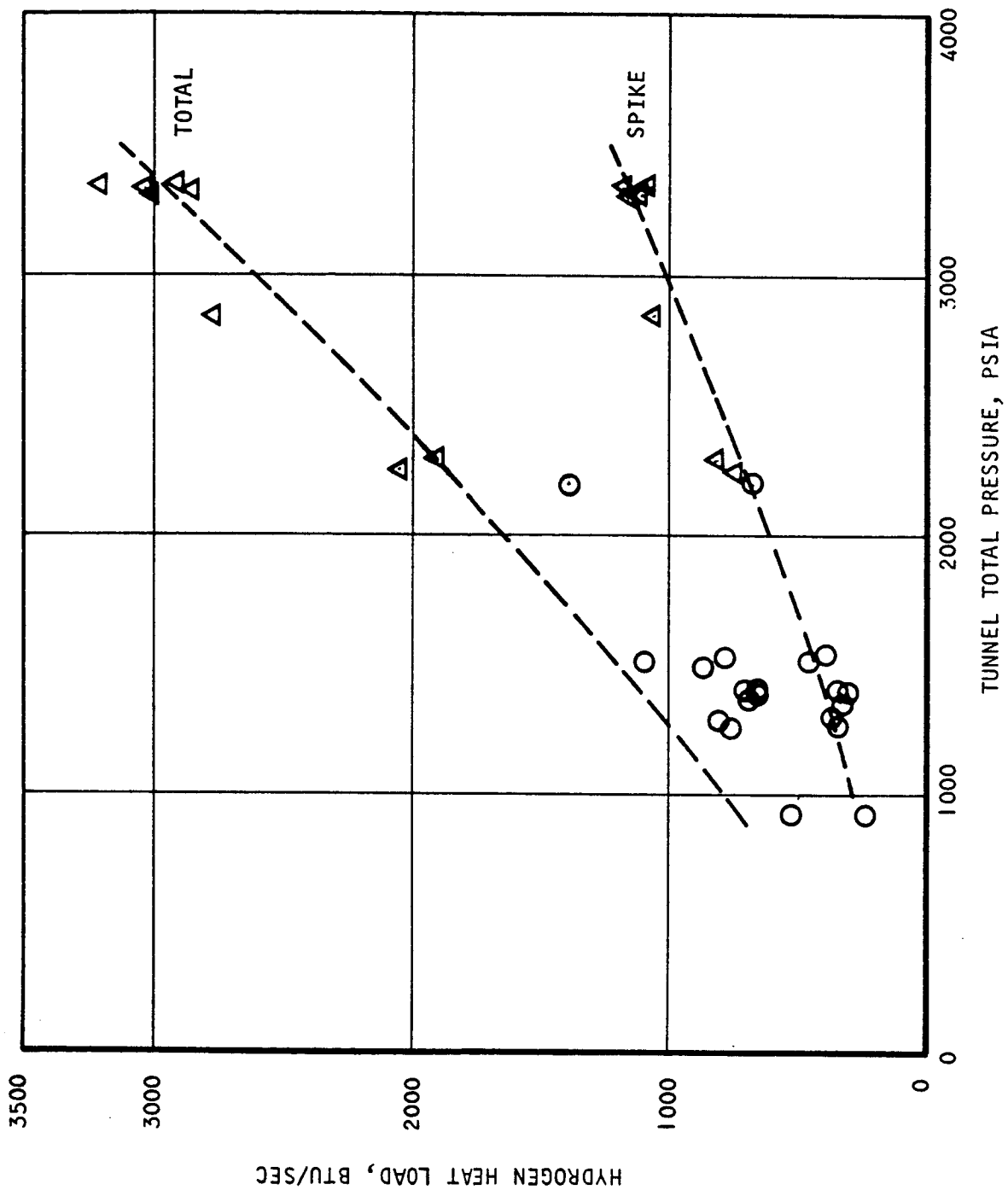
Figure 5.2-1. Test Hydrogen Heat Loads (U)

S-67774

UNCLASSIFIED

Circular data points represent test runs with room temperature inlet hydrogen; triangular data points represent test runs with cryogenic inlet hydrogen ($150°$ to $200°R$). Room temperature inlet hydrogen was used for tunnel total pressures up to 2200 psia, and cryogenic hydrogen was used at and above 2200 psia. Though the inlet lines were sized for cryogenic hydrogen, room temperature inlet hydrogen was permissible from the standpoint of inlet line pressure drop below 2200 psia because the lower flow rates required at or below 2200 psia (0.15 to 0.50 lb/sec model total) more than offset the threefold reduction in hydrogen density. Cryogenic inlet hydrogen flow rates of up to 0.90 lb/sec were used for test runs up to 3330 psia tunnel total pressure.

The dashed lines represent steady-state analytical predictions of spike and total heat loads. These predictions were based on a detailed analysis at 3300 psia tunnel reservoir total pressure. Predictions at lower pressures were calculated by ratioing the detailed prediction by the total-pressure ratio (to the eight-tenths power) and the total-to-average wall-temperature-difference ratio.

Agreement between the data and prediction is good (±20 percent or less) for the spike at all total pressures, and for the total model at pressures of 2200 psia and above. At total pressures at and below 2200 psia with room temperature inlet hydrogen, the total heat loads are consistently lower than the prediction by as much as 43 percent. These lower-than-predicted test loads result from non-attainment of steady-state thermal conditions on the aft routes (innerbody, trailing edge, strut sides) during exposure times of up to 68 sec to the hot gas. The spike and leading edge flow routes reached steady state (as determined by hydrogen coolant outlet temperatures) in 10 to 30 sec for all thermal performance runs. At the higher coolant flow rates used with tunnel reservoir total pressures above $2200°R$, steady state on the aft routes was achieved in 40 sec or less.
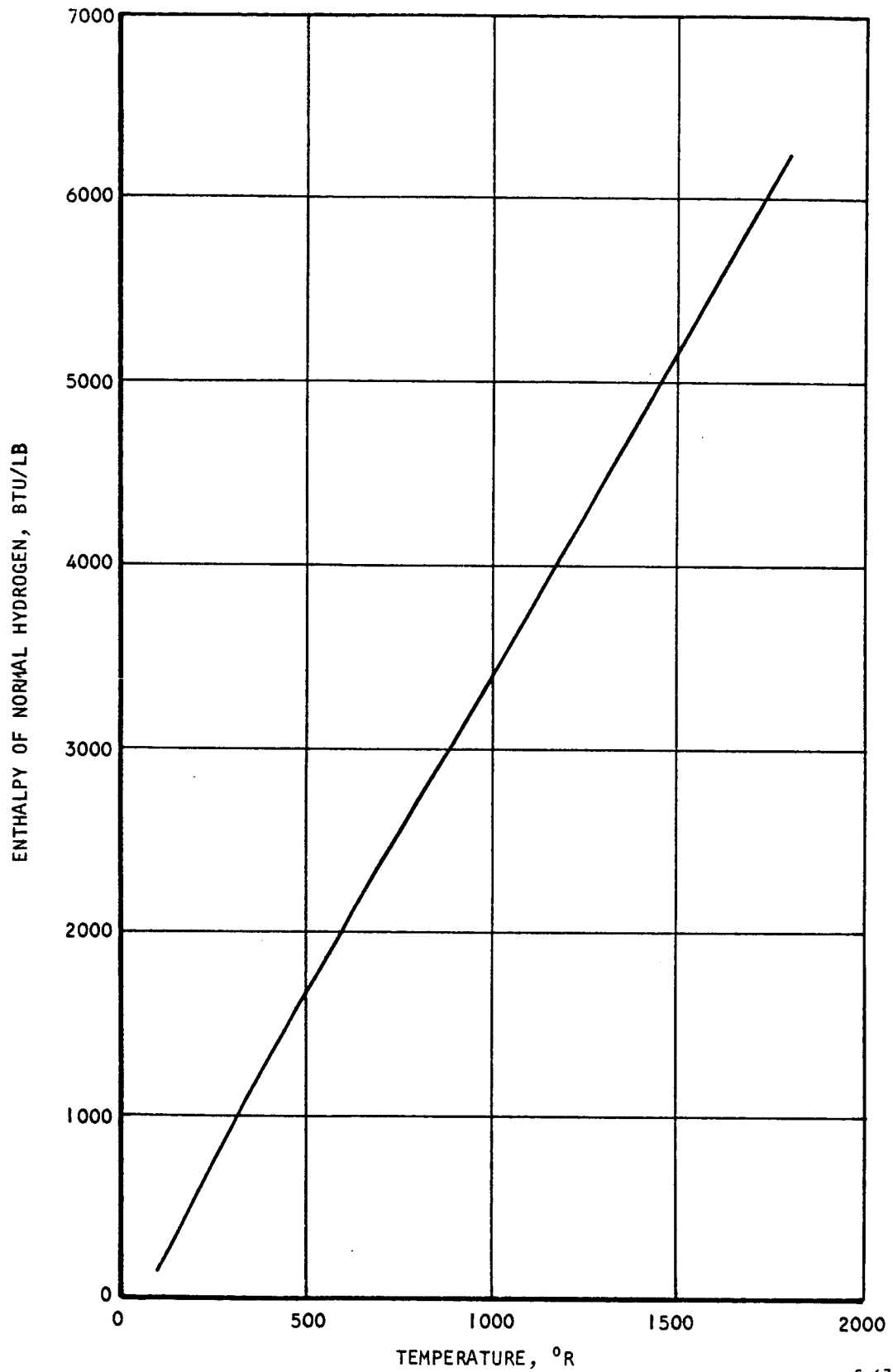
5.2.2.2 Heat Load Distribution

Flow route heat loads and average heat fluxes were based on test hydrogen flow rates and inlet and outlet hydrogen temperatures at steady state. At intermediate locations along the flow routes, cold wall thermocouple measurements were used interchangeably with hydrogen temperatures. Enthalpy differences, derived from hydrogen (or cold wall) temperatures, were multiplied by hydrogen flow rate to obtain heat load. The enthalpy-temperature curve for normal hydrogen is shown in Figure 5.2-2. This curve applies to all test runs, since the hydrogen for the cryogenic runs was obtained from ambient temperature storage and no ortho-para conversion is expected for the conditions encountered.

A tabulation of the heat loads and average heat fluxes for Test 41, Run 39 is presented in Table 5.2-1. This test run was performed at the tunnel reservoir total conditions of 3320 psia and $3400°R$. The spike retraction was 2.89 in. relative to the fully extended position; the coolant hydrogen inlet temperature was approximately $150°R$; and all outlet coolant was exhausted out the vent line (no hydrogen injection). The run time in the tunnel was 32 sec and the flow rate and temperature data indicated in Table 5.2-1 are averages over the last 10 sec prior to engine withdrawal from the tunnel. All flow

AIRESEARCH MANUFACTURING COMPANY
Los Angeles, California   UNCLASSIFIED

71-7702
Page 5-40

Figure 5.2-2.   Enthalpy of Normal Hydrogen

TABLE 5.2-1

HYDROGEN HEAT LOAD DISTRIBUTION FOR TEST 41, RUN 39 (U)

Flow Route	Axial Location X_1, in. (ref. coord)	Axial Location X_2, in. (ref. coord)	H_2 Flow Rate, lb/sec	H_2 Temp at X_1, °R	H_2 Temp at X_2, °R	H_2 Heat Load X_1 to X_2, Btu/sec	Surface Area X_1 to X_2, ft²	Avg Heat Flux X_1 to X_2, Btu/sec-ft²
Spike →	Inlet	35.70	0.279 →	154	388	251	5.10	49.2
	35.70	44.30		388	821	430	3.30	130.3
	44.30	55.76		821	1237	408	4.87	83.8
Innerbody →	55.76	65.60	0.078 →	1160	555	166	4.80	34.6
	65.60	75.60		544	316	68	3.50	19.42
	75.60	Inlet		316	212	31	2.00	15.5
Leading Edge →	Inlet (external surface)	LE Tip	0.269 →	151	343**	200*	1.30	168.4
	LE Tip	43.45		343	921	546	3.15	173.0
	43.45	46.00		921	1065	136	1.13	120.2
	46.00	50.40		1065	1212	140	1.97	71.0
Outerbody Outlet Manifold (OBOM) →	50.40	54.13		1212 (1255***)	1140	88	1.70	51.7
Trailing Edge →	54.13	TE Tip	0.166 →	1140	210	389	10.75	36.2
	TE Tip (external surface)	Inlet		210·*	148	27*	2.11	12.8
Strut Sides	Inlet	Outlet	0.0163	154	1116	58	0.87	60.0
Strut Leading Edges	Inlet	Outlet	(0.078)	154	212	18	0.0213	845.0
Totals			0.754	154 (inlet temp to engine)	1260 (average)	2956	46.67	63.4

Test 41 Run 33
5320 psia, 3400°R reservoir total conditions
2.89 in. spike retraction
No H_2 injection

NOTES
* Estimated heat load, see text
** Calculated from estimated heat load
*** H_2 temp in OBOM, equals average of T77 and T78

routes were at approximately steady-state thermal conditions during this period.

The total engine heat load is 2956 Btu/sec and compares with a pretest analytical prediction of 2890 Btu/sec reported in Reference 5-3 for approximately the same tunnel reservoir total conditions (3300 psia, 3600°R). The heat loads on the external surfaces of the leading and trailing edge flow routes in Table 5.2-I are estimated values. There are no hydrogen thermocouples directly at the leading and trailing edges, so discrete heat load values on these external surfaces could not be obtained. The heat flux distribution on the external leading edge was estimated by calculating the local heat fluxes at 2.30 in. and 4.35 in. aft of the leading edge tip based on hot and cold wall thermocouple pairs T1, T3, and T2, T4, respectively. A flat-plate heat flux distribution passing through the two calculated heat flux points was extrapolated up to the leading edge tip. The local heat flux calculation procedure based on hot and cold wall thermocouple readings is described in Appendix A. The analytical value reported in Reference 5-3 was used as the external trailing edge heat load in Table 5.2-I since there is no hot gas pressure or thermocouple instrumentation in this region. These external surface heat load estimates do not affect the total engine heat load since the inlet and outlet hydrogen temperatures of all routes are experimentally measured. These estimates do, however, affect the heat load distribution within the leading and trailing edge flow routes.

For purposes of data reduction, the locations of coolant control thermocouples at axial Station 50.40 (T70 through T75) and at Station 54.13 (T80 through T85) on the outer shell were defined as the outlets of the leading and trailing edge flow routes, respectively. The average thermocouple readings of T70, T72, and T75 were used as the leading edge coolant outlet temperature. The value of T80 only was used as the average trailing edge outlet temperature. Coolant and/or heating maldistribution in the trailing edge route and in the vicinity of the struts biased the other coolant control thermocouples by about 100°R on the low side

The region between the leading and trailing edge coolant control thermocouples at axial Stations 50.40 and 54.13 is identified as "Outerbody Outlet Manifold" in Table 5.2-I and includes the common outlet orifices leading into the outerbody outlet manifold at axial Station 51.40. The mixed mean temperature of the leading and trailing edge outlet hydrogen is measured by thermocouples T77 and T78 in the outerbody outlet manifold. The heat load for this region is calculated from

$$Q_{OBOM} = (W_{LE} + W_{TE}) H_{OBOM} - (W_{LE} H_{LE} + W_{TE} H_{TE}), \frac{Btu}{sec}$$

where

W_{LE} = leading edge H_2 flow rate, lb/sec

W_{TE} = trailing edge H_2 flow rate, lb/sec

H_{LE} = enthalpy of leading edge outlet H_2
based on (T70 +T72 +T75)/3, Btu/lbm

$$H_{TE} = \text{enthalpy of trailing edge outlet } H_2$$

based on T80, Btu/lbm

$$H_{OBOM} = \text{enthalpy of } H_2 \text{ in outerbody outlet manifold based}$$

(T77 + T78)/2, Btu/lbm

The heat load on the six strut leading edges is based on the hydrogen inlet temperature to the engine, 154°R, and the inlet temperature to the nozzle (T59), 212°R. These temperatures produced a heat load of 18 Btu/sec and an average heat flux of 845 Btu/sec-ft^2. An average heat flux as high as 450 Btu/sec-ft^2 was expected for these tunnel conditions. The prediction is reported in Reference 5-3 and was based on a turbulence factor of 2-times the Fay and Ridell heat flux, and Lee's distribution. The high test value resulted from non-attainment of steady-state of T59. During Test 41, Run 30 (cryogenic hydrogen calibration run with no insertion into the hot gas stream), the cooldown of T59 lagged behind the engine inlet temperature for all of the 60-sec calibration. This lag is sufficient to account for the difference between test and predicted values. This difference is so large, however, that detailed comparisons would not be meaningful and were not attempted.

5.2.2.3 Effect of Hydrogen Injection

Some or all of the outlet coolant hydrogen from the engine flow routes was injected into the captured hot gas stream for most of Test 42 runs. The injection ports are located at Station 43.00 on the spike and at Station 43.84 (ref. coord.) on the forward outer shell. The purpose of injection was to thermally cycle the structure in the vicinity of the injection ports, since the injected hydrogen temperature was expected to be several hundred degrees higher than the local coolant temperature. The effects of the hydrogen injection were detected in the hot gas surface pressure measurements downstream of the injectors. It is unlikely that overall combustion occurred, since the hydrogen heat loads on the aft routes were no higher than without hydrogen injection.

Hot gas surface pressure measurements (expressed in terms of a pressure coefficient) are presented in Figure 5.2-3 for a test run with hydrogen injection (Test 42, Run 46) and a test run without hydrogen injection (Test 41, Run 39). Both test runs were at the maximum tested tunnel reservoir total conditions of 3320 psia and 3400°R. The spike retraction was 2.89 in. relative to the fully latched position. The circular data points are centerbody measurements and triangular data points are outerbody (internal surface) pressure measurements. Flagged data points indicate pressure measurements of the hydrogen injection test run. The injection rate was 0.35 lb/sec relative to a captured methane combustion products (equivalence ratio of 0.74) flow rate of 28.9 lb/sec. The curve is the analytical prediction without hydrogen injection.

Static pressure measurements with injection are generally higher than without injection, particularly near the injector locations, as indicated in Figure 5.2-3; however, the increase in static pressures near the injectors with hydrogen injection falls within the data scatter of equivalent static pressure
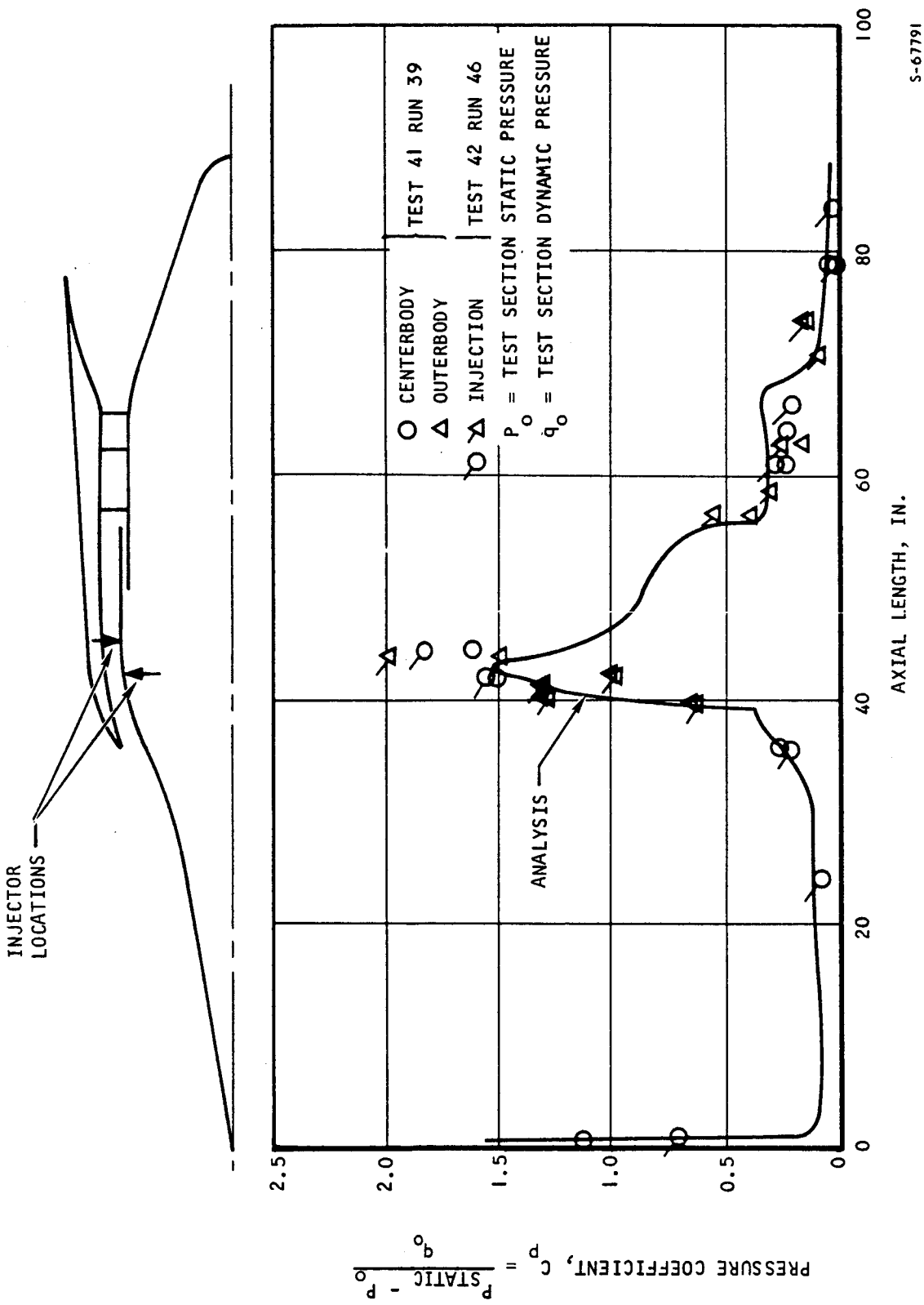
Figure 5.2-3. Aerodynamic Static Pressure Distributions (U)

increases recorded during 2/3-scale inlet model testing with helium injection.
Similar static pressure results were obtained when two test runs at 1380 psia,
2700°R tunnel reservoir total conditions were compared (Test 42, Run 34 without
hydrogen injection, and Test 42, Run 36 with hydrogen injection). At these
tunnel conditions, the freestream oxygen content of the methane combustion
products (equivalence ratio of 0.45) is higher than for the comparison in
Figure 5.2-3 but the total temperature is lower.

Heat loads on the trailing edge flow route were calculated for Test 42,
Run 34 (without hydrogen injection) and Run 36 (with hydrogen injection).
Since the trailing edge flow route (as well as the strut sides and innerbody
flow routes) did not reach thermal steady-state conditions after test run times
of 67 and 59 sec, respectively, the heat-sink rate into the flow route struc-
ture was added to the hydrogen heat load to obtain an estimate of the aero-
dynamic heat load. The average trailing edge structural temperatures and
hydrogen heat loads for both test runs are shown in Figure 5.2-4. The data
acquisition time periods shown are the last 32 and 22 sec of Runs 34 and 36,
respectively, prior to test shutdown. The average structural temperature is
formed by the arithmetic average of thermocouple readings T88, T93, and T100,
at reference coordinate axial Stations 54.13, 62.30, and 70.10, respectively.
For both runs, the rate of structural temperature increases and the hydrogen
heat loads are approximately equal over the time periods shown. A summary
of the hot gas and coolant conditions and the parameters that contributed to
the aerodynamic heat load estimate for both runs is shown in Table 5.2-2. The
estimated aerodynamic heat load without hydrogen injection (Run 34) is 45.0
Btu/sec, and 42.5 Btu/sec with hydrogen injection (Run 36). The 6-percent
difference between these heat loads is within the estimated ±11.2-percent band
of uncertainty in trailing edge heat load reported in Reference 5-2.

5.2.3 Data Analysis and Discussion

5.2.3.1 Comparison of Experimental and Analytical Results

One of the SAM test objectives was to evaluate the methods used to predict
the design heat loads and fluxes (Mach 8 freestream, 88,000 ft altitude, local
dynamic pressure of 1800 psf) reported in Reference 5-4. To accomplish this
objective, an aerodynamic heat transfer analysis was performed on the surfaces
of the SAM similar to that reported in Reference 5-4 except that all aero-
dynamic inputs to the analysis were either measured test data or data derived
directly from test data. Aerodynamic inputs to the design analysis reported in
the stated reference were based on analytical considerations. Heat load and
average heat flux results from the data analysis were compared with experi-
mental heat loads and average heat fluxes obtained from measured hydrogen
flow rates and temperatures. Local heat fluxes from the data analysis were
compared with local heat fluxes calculated from measured data of hot and
cold wall thermocouple pairs. The thermocouple pairs are located in the plate-
fin coolant passages of the flow routes and the calculation procedure is des-
cribed in Appendix A.
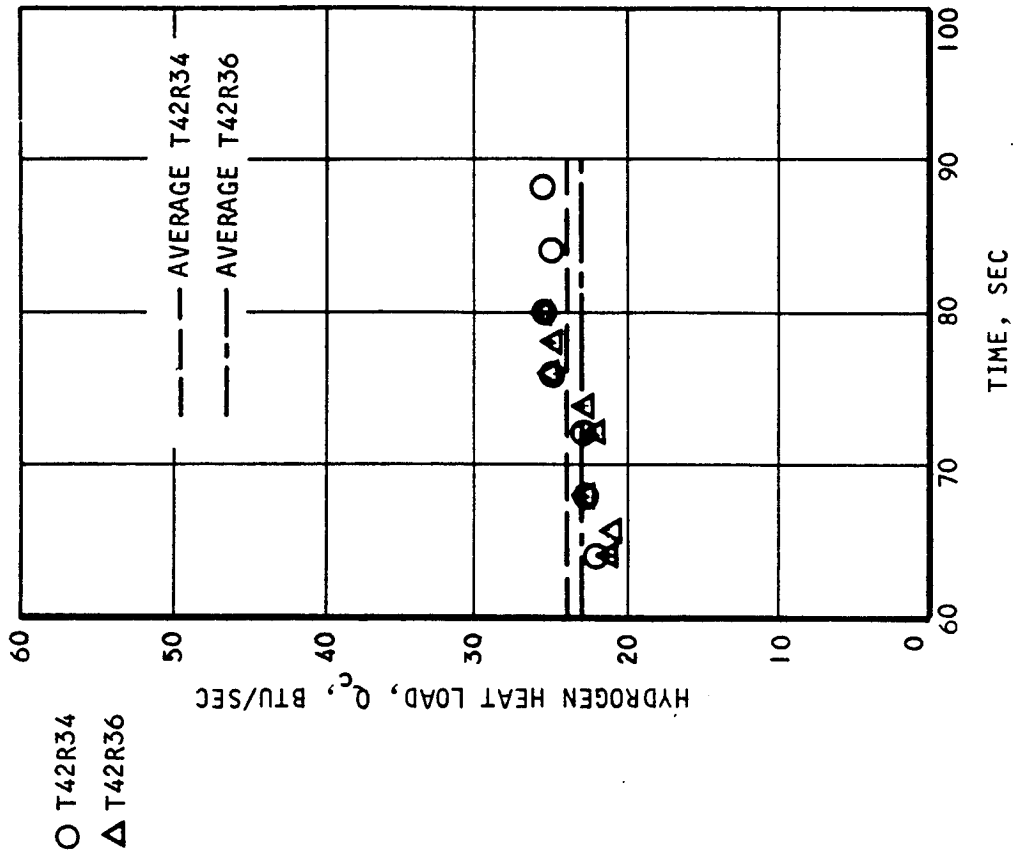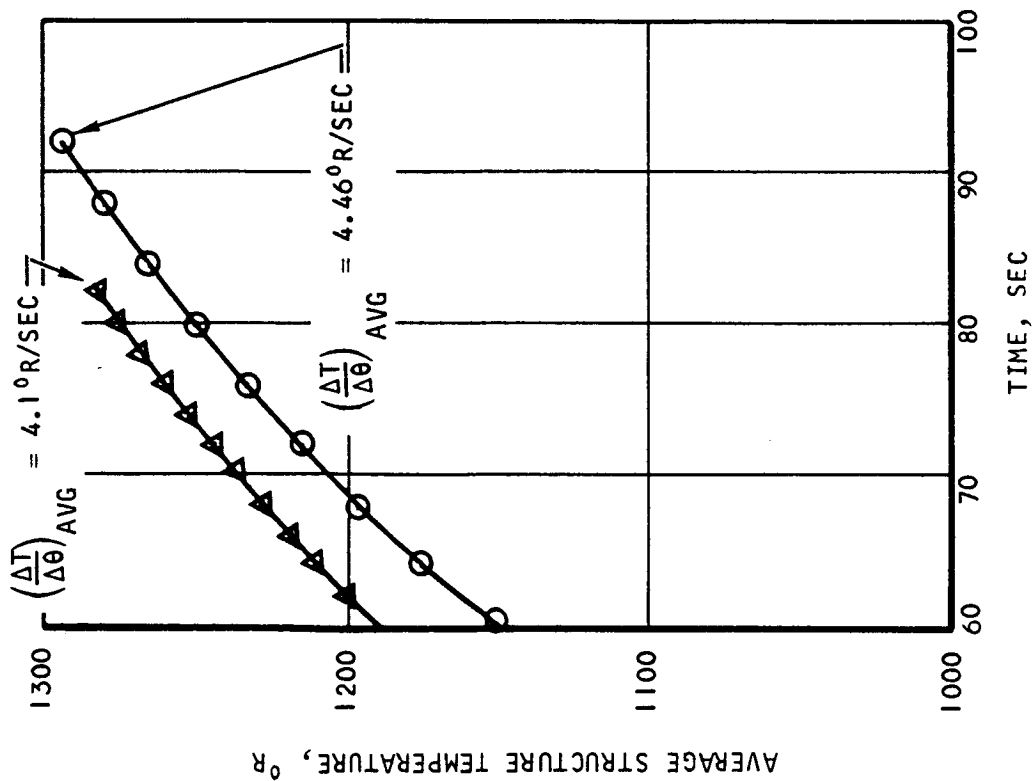
Figure 5.2-4. Trailing Edge Average Structure Temperature and Hydrogen Heat Load (U)

S-67760

TABLE 5.2-2

TRAILING EDGE FLOW ROUTE HEAT LOADS (TEST 42)* (U)

		Run 34	Run 36
Spike retraction from latched position, in.		2.90	2.89
Captured hot gas flow rate, lb/sec		12.4	12.5
W_{H_2}TOTAL,	lb/sec	0.257 ±0.016	0.223 ±0.009
W_{H_2}TRAILING EDGE,	lb/sec	0.0089 ±0.0005	0.0087 ±0.0004
W_{H_2}INJECTION,	lb/sec	None	0.143 ±0.005
$\left(\Delta T_m/\Delta\theta\right)_{AVG}$,	°R/sec	4.46	4.10
$M \times C_m \times \left(\dfrac{\Delta T_m}{\Delta\theta}\right)_{AVG} = Q_{SINK}$,	Btu/sec	21.1	19.4
$W_{H_2} \times C_P \times (\Delta T_{H_2}) = Q_c$,	Btu/sec	23.9	23.1
Q_{AERO},	Btu/sec	45.0	42.5

*Nominal tunnel reservoir total conditions, 1380 psia, 2700°R

$$Q_{AERO} = Q_c + Q_{SINK}$$

$$= W_{H_2} \times C_P \times (\Delta T_{H_2}) + MC_m \left(\frac{\Delta T_m}{\Delta\theta}\right)_{AVG}$$

where   M = estimated trailing edge structural mass = 45 lb

      C_m = metal specific heat = 0.105 Btu/lb-°R

      C_P = hydrogen specific heat = 3.5 Btu/lb-°R

The inputs to the data analysis are itemized as follows:

(a) Measured hot gas static pressure distribution

(b) Measured engine hot surface temperature distribution

(c) Mach number, total temperature, total pressure, and equivalence
     ratio of the methane combustion products hot gas upstream of the
     engine

(d) The hot gas flow rate captured by the engine inlet

The data analysis calculations were performed on a computer program written
to accept the above input data from the SAM tests data listings. Test 41,
Run 39 was selected for data analysis because it was performed at the maximum
tunnel conditions for the test program (3320 psia, 3400°R reservoir total con-
ditions) and it was one of the few test runs where thermal steady-state con-
ditions were reached simultaneously on all engine coolant flow routes. A
tabulation of the steady-state hydrogen heat loads for this test run is pre-
sented in Table 5.2-1 of Section 5.2.2.2. The hot gas static pressure distri-
bution is shown in Figure 5.2-5 and was constructed from the measured pressures
shown in Figure 5.2-3 of Section 5.2.2.3. It is noted in Figure 5.2-3 that
there are no data points between axial Stations 43 and 56. The folded-flow
section of the spike coolant flow route is located in this region and in-
stallation of static pressure taps was not feasible. Static pressure taps
were located on the outer shell in this region but they became inoperative
in the test program prior to Test 41, Run 39. To fill the void in this region,
the analytical distribution shown in Figure 5.2-3 was used. This was done with
reasonable confidence, since the measured data for Test 41, Run 39 is in good
agreement at most other locations. In general, the good agreement of static
pressure measurements with the pretest analysis indicates that the degree of
analytical pressure accuracy should be similar for flight conditions. The
aerodynamic heating estimates will correspondingly be subject to the same
accuracy since aerodynamic heating is highly dependent on surface pressure dis-
tribution.

The hot surface temperature distribution used for the data analysis for
Test 41, Run 39 is also shown in Figure 5.2-5. This distribution was construc-
ted from hot wall insert thermocouple readings along the surfaces of the engine
and corrected to indicate hot surface temperature as described in Appendix A.
The surface temperature distributions between insert thermocouple readings was
obtained from a preliminary data analysis of the hot gas heating and hydrogen
cooling of the engine surfaces. A detailed discussion of surface temperature
distributions is presented in Section 5.3.3.

Local aerodynamic conditions along the engine surfaces (velocity, Mach
number, static temperature, total pressure, etc.) were calculated on a one-
dimensional basis from the pressure distribution and the time-averaged upstream
Mach number (6.81), total temperature (3385°R), reservoir pressure (3320 psia),
equivalence ratio (0.74), and hot gas captured flow rate (29.4 lb/sec) for the
last 10 sec of Test 41, Run 39. The engine was divided into three sections for
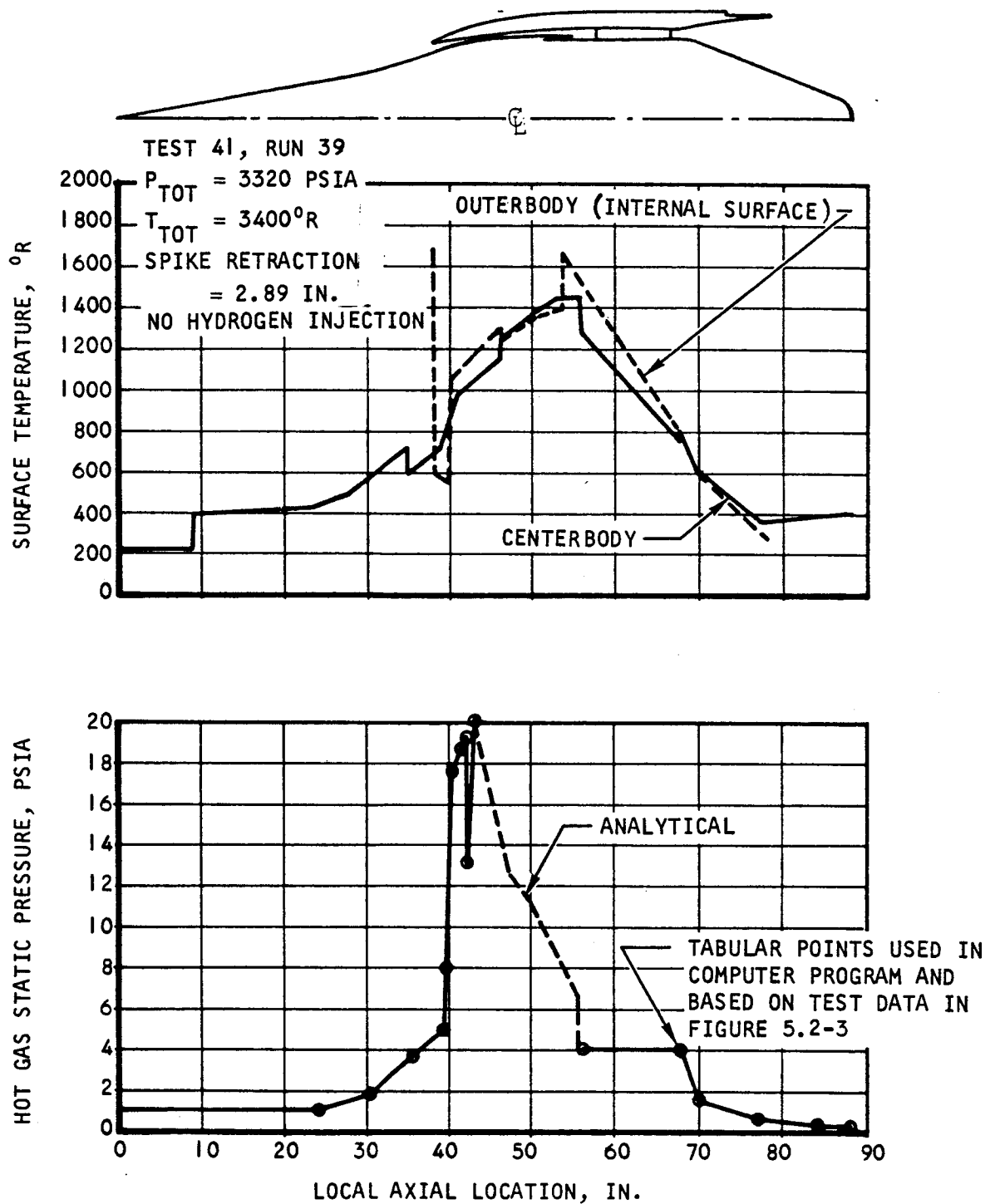
Figure 5.2-5. Static Pressure and Surface Temperature Distribution
Inputs to Aerodynamic Heating Data Analysis (U)

S-67715

the one-dimensional analysis. From the spike tip to the cowl lip, the hot gas
flow was considered isentropic (constant total pressure). The cowl lip was
at an axial distance of 38.09 in. from the spike apex (35.90 in. for reference
drawing coordinates) during Test 41, Run 39 for a spike retraction of 2.89 in.
relative to the fully latched position. The spike shock was outside the cowl
lip. From the cowl lip to the outerbody trailing edge the flow equations for
a duct with known flow rate and static pressure distribution were used. From
the trailing edge to the nozzle cap the flow was again considered isentropic.

As indicated above, the data analysis was performed with the same heat
transfer methods as used for the design heat transfer analysis reported in
Reference 5-4. Local heat fluxes were calculated from the flat-plate reference-
enthalpy method (FPRE) on all surfaces with the virtual origin of the center-
body and outerbody boundary layers at the spike tip and cowl lip, respectively.
The hot gas transport properties were evaluated at a temperature given by
Eckert's reference enthalpy of

$$H^* = H_\infty + 0.50 (H_W - H_\infty) + 0.22 (H_r - H_\infty)$$

where H_∞ = enthalpy at static conditions

H_W = enthalpy at wall conditions

H_r = recovery enthalpy

$= H_\infty + Pr^{*n} (H_T - H_\infty)$

H_T = enthalpy at total conditions

Pr^* = Prandtl number at reference conditions

n = 1/2 for laminar flow

$= 1/3$ for turbulent flow

and H and Pr are given functions of temperature for the methane combustion
products hot gas. The laminar and turbulent heat fluxes on the spike sur-
face up to the cowl lip were multiplied by $\sqrt{3}$ and $5\sqrt{2}$, respectively, to modify
the flat-plate solution for flow over a cone.

The resulting heat flux distributions for the centerbody and internal
outerbody surfaces are presented in Figure 5.2-6. The dashed curves are
calculated local heat fluxes from the data analysis, and the dashed horizontal
lines are area-weighted average heat fluxes of the dashed curves over the
indicated axial lengths. These calculated average heat fluxes offer a direct
comparison with the solid horizontal line averages which are hydrogen test
data from Table 5.2-1. The triangular points are calculated local heat fluxes
based on measurements of hot and cold thermocouple pairs in the plate-fin
coolant passages (Appendix A). These local heat fluxes are, in effect, con-
sidered as data analysis also, except that the calculation is based entirely
on internal cooling-side measurements and conditions. The dashed-curve data

TEST 41, RUN 39
$T_{TOT} = 3400^\circ R$
$P_{TOT} = 3320$ PSIA
SPIKE RETRACTION = 2.89 IN.
NO HYDROGEN INJECTION

$Q_{TOT} = 2650$ BTU/SEC (EXPERIMENTAL)
$Q_{TOT} = 2670$ BTU/SEC (DATA ANALYSIS)
(EXCLUDING LEADING AND TRAILING
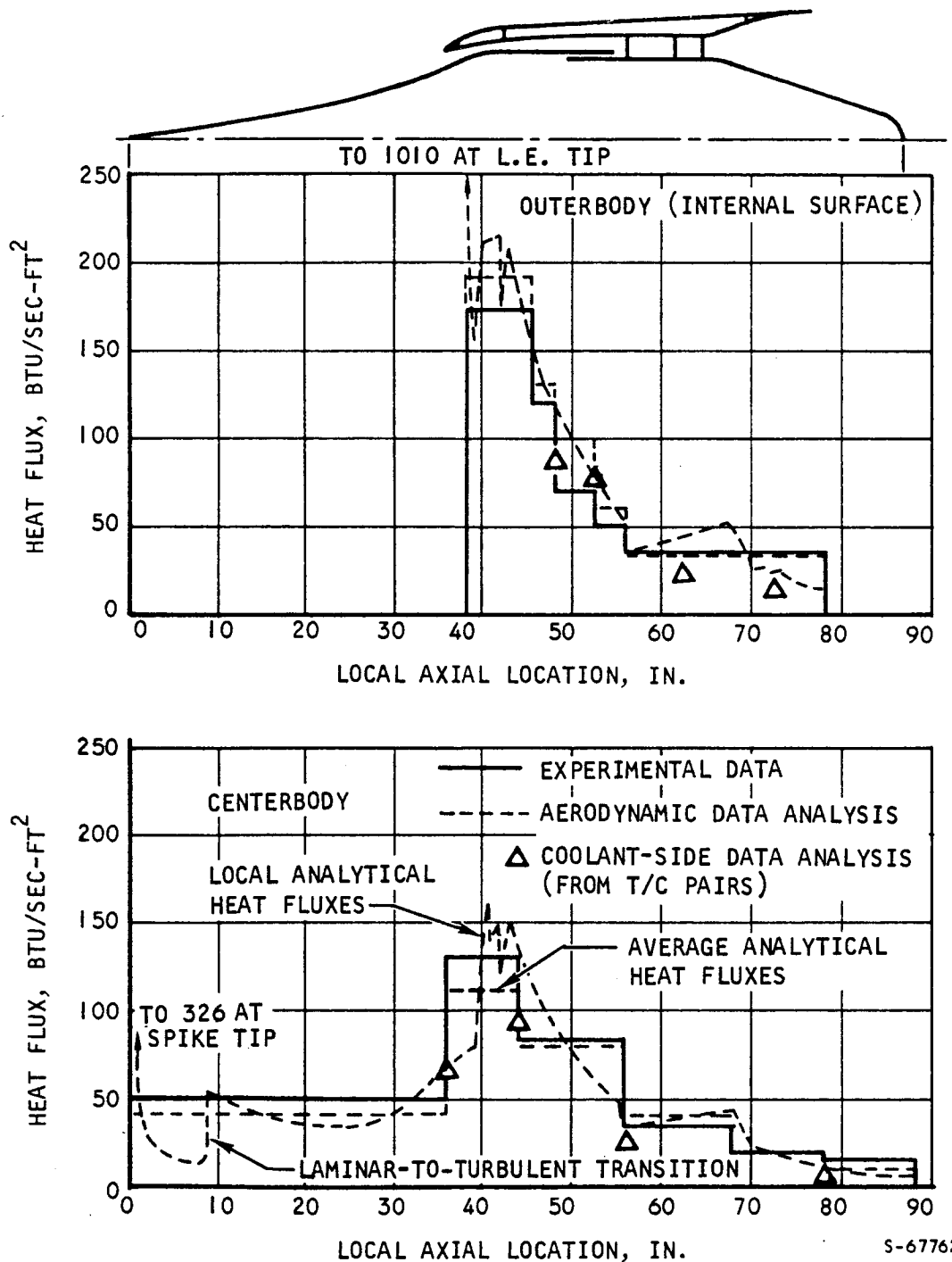EDGE EXTERNAL SURFACES AND STRUTS)

Figure 5.2-6.   Experimental and Data Analysis Heat
Flux Distributions (U)

S-67762

analysis results, on the other hand, are based on hot-gas-side measurements and conditions only.

Average heat fluxes from the data analysis (dashed lines in Figure 5.2-6) compare favorably (within ±20 percent) with the experimental average heat fluxes (solid lines) except on the outer shell at axial Station 50 (43 percent) and on the aft part of the nozzle (33 percent). The total data analysis heat load is 2670 Btu/sec while the total experimental heat load is 2650 Btu/sec. These total heat loads do not include the leading and trailing edge external surface heat loads, or the struts (leading edge or sides) heat load. The close agreement in total-heat load was produced by a combination of underpredictions and overpredictions in the data analysis. For example, the data analysis heat load for the centerbody was 8 percent lower than the experimental value (1250 Btu/sec versus 1350 Btu/sec), while the data analysis heat load for the outerbody was 9.5 percent higher than the experimental value (1420 Btu/sec versus 1300 Btu/sec).

The local heat fluxes calculated from coolant-side thermocouple measurements (triangular data points in Figure 5.2-6) are in fair agreement with the data analysis local heat fluxes (dashed curves) and the experimental average heat fluxes. In general, these calculated local fluxes are lower than experimental average values, particularly on the aft surfaces of the engine (aft of axial Station 55).

All of the thermocouple pairs used to calculate local heat flux are installed in the flow routes at zero deg (CWLA) circumferentially, which corresponds to a location midway between the struts. The presence of the struts produces localized heating patterns on the aft surfaces of the engine, with the least amount of heating occurring midway between the struts (except at the nozzle/inner shell joint as discussed in Section 5.2.3.2). Since the experimental average heat flux is based on the mixed-mean hydrogen outlet temperature, the local calculated heat fluxes on the aft sections can be lower than experimental averages. The calculated local heat fluxes on the spike at axial Station 40.0 and on the outer shell at axial Stations 48 and 52 are in acceptable agreement with experiment (within the calculation uncertainty of ±13 percent indicated in Appendix A). The calculated local heat flux of 92 Btu/sec ft^2 at axial Station 44.30 on the spike, appears to be substantially on the low side.

In the data analysis, a laminar-to-turbulent boundary layer transition Reynolds number of 2×10^6 was used on the spike. This transition occurred at approximately 9 in. aft of the spike tip. This compares with a value of 10^7 (20 in.) for Mach 8 flight predictions. A transition Reynolds number of 2×10^6 was used for Test 41, Run 39 because (1) the test heat load on the forward spike (to axial Station 35.7) is correlated best with this transition Reynolds number, and (2) observations of ice formation on the cryogenic hydrogen-cooled surface (a white frost changing to a gray frost corresponding to a Reynolds number of 2×10^6) also suggests transition here. The boundary layer

on the inside surface of the leading edge was considered fully turbulent,since there is a sharp increase in static surface pressure just downstream of the leading edge tip. A transition Reynolds number of 7.5×10^4 was used for Mach 8 flight conditions (0.40 in. from the cowl lip). The estimated external leading edge heat load indicates fully turbulent flow for SAM test conditions. For Mach 8 flight predictions with spike bow shock-on-cowl lip,the flow was assumed fully laminar. Test thermocouple measurements on the external leading edge indicated a heat load much higher (a factor of about 3) than could be calculated for laminar flow conditions at these test conditions. Premature transition on the external leading edge was probably caused by interaction of the spike shock wave and cowl shock wave (shock-outside-cowl lip) in this region.

In summary, the flight heat transfer calculation procedure (flat-plate method with Eckert's reference enthalpy technique for hot gas property evalua-tion), when used in conjunction with the test hot-gas static pressure distri-bution and the one-dimensional flow solution, predicted average test heat fluxes to within ±20 percent over most surfaces of the engine. Based on this close agreement, the predicted Mach 8 heat load level of 10,800 Btu/sec should be realistic. The calculated and test heat loads did not include the effect of combustion on the flow routes, and, if the effect is significantly differ-ent than predicted for Mach 8 flight, the predicted heat load will be affected.

5.2.3.2 Localized Heating

Metal discolorations were observed at several locations during posttest inspection of twenty thermal performance and thermal cycle runs (Test 41, Run 26 through Test 42, Run 36). The observed discolorations occurred on the inlet sections of the spike and leading edge, the strut sides, the inner and outer shells between the struts, and at the nozzle-inner shell joint between the struts. A detailed description of the three areas and interpretations of dis-colored metal temperatures are presented in Section 5.1.2.1. The thermal per-formance runs (4 runs) were at 2200 psia, 3000°R (tunnel reservoir total con-ditions), and the thermal cycling runs were at 1380 psia, 2700°R. Room tem-perature inlet hydrogen coolant was used for these test runs and, in general, the flow routes were undercooled relative to the flow rates required for steady-state operation with 1600°R maximum structural temperature. In all locations, the discoloration patterns were traced to locally highly heated areas caused by shock wave-boundary layer interactions. Local heat transfer increases have been estimated for these areas. Propogation of these dis-colorations was not observed for test runs at higher tunnel total pressures and temperatures with adequate hydrogen cooling.

The one-dimensional flow solution used in the data analysis described in Section 5.2.3.1 is not accurate enough for localized heating calculations. The presence of shock interference patterns in the inlet and combustor sections produced non-uniform flow conditions between the centerbody and outerbody sur-faces. Because of this, the hot gas pressure distribution is not linear be-tween pressure tap locations as used in the data analysis (Figure 5.2-5). The existence of shock waves in the inlet is shown in the Schlieren photograph, Figure 5.2-7, which shows an oblique shock inclined at approximately 24 deg
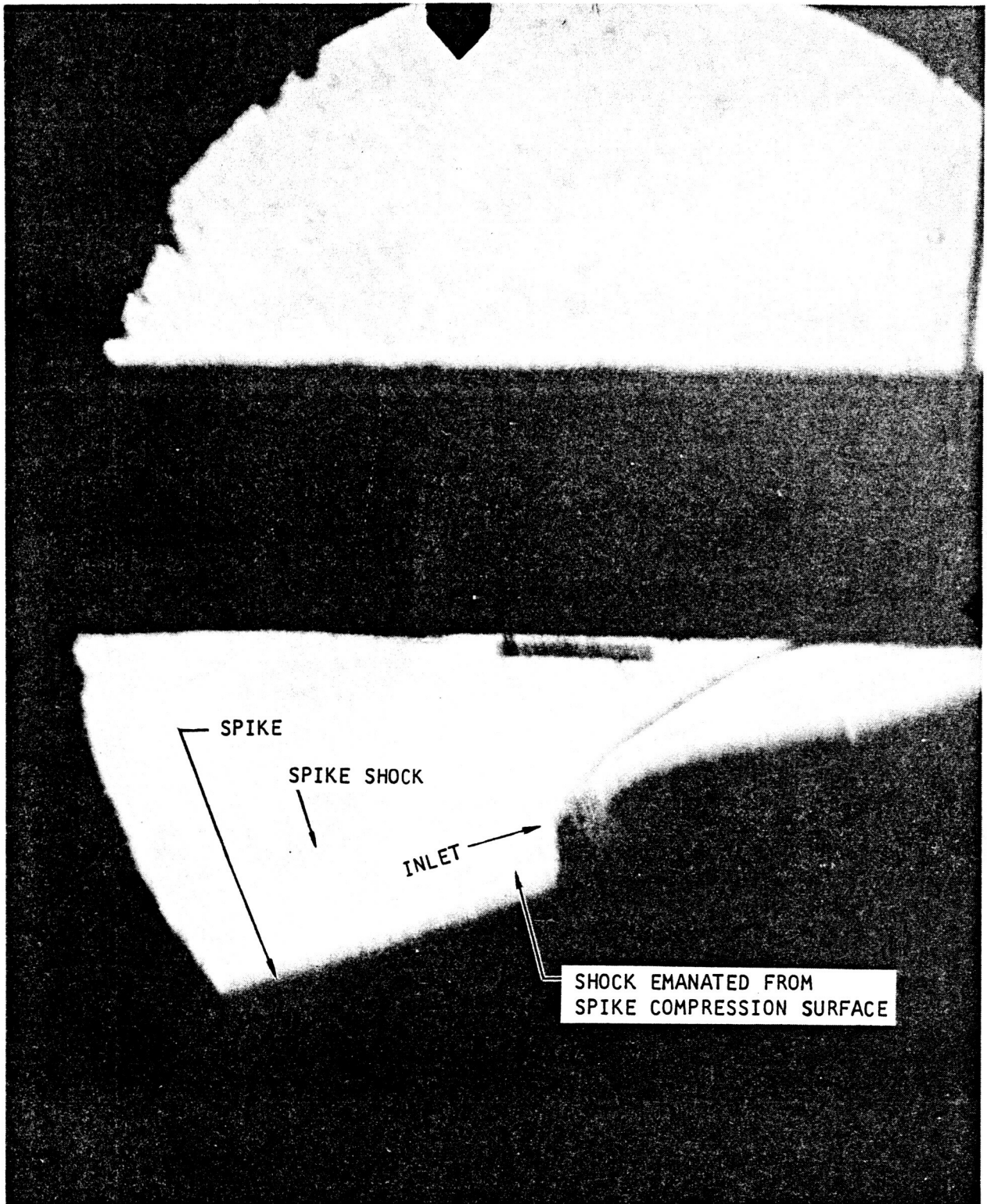
F-13201

Figure 5.2-7. Typical Schlieren Photograph of Cowl Leading Edge Region

AIRESEARCH MANUFACTURING COMPANY
Los Angeles, California

71-7702
Page 5-55

relative to the engine centerline. In addition, a moderately strong shock emanates from the cowl lip due to its finite bluntness. The evidence of the strong shocks persisting into the duct to the vicinity of axial Station 44.0 is shown in Figure 5.2-8, in which the local outer shell and spike pressures, and the spike retraction distance (from the fully extended position) are plotted versus time for Test 41, Run 7 at 65 sec (Data Acquisition System time). When the spike retraction is 2.2 in. from the fully extended position, the outer shell pressure P25 (44.54 in. axial distance from the spike apex at 2.20 in. spike retraction) reads 3.4 psia, while the spike surface pressure P86 (44.30 in.) reads 5.7 psia. When the spike is retracted an additional half-inch to 2.70 in., two pressure taps P25 (44.04 in. at 2.7 in. spike retraction) and P86 (still at 44.30 in.) interchange pressure levels. This pressure level interchange and the observed metal discolorations can be attributed to the presence of strong shocks in this region. Based on the shock emanating from the spike 1 compression surface shown in Figure 5.2-7 and the internal cowl-lip shock, the inlet-zone flow field was constructed by the method of characteristics. The angle of the cowl-lip shock was determined at 17-1/2 deg relative th the ap- oach-proaching flow. Results of the flow-field estimation for Test 41, Run 20 are shown in Figure 5.2-9. The observed metal discolorations on the spike and internal leading edge surfaces are included in Figure 5.2-9 and indicate that they occur in the areas where the shock waves interact with the surface boundary layers.

The areas of localized high heating in the vicinity of the struts are shown in Figure 5.2-10 and were constructed from the observed metal discoloration patterns after Test 42, Run 36. The observed metal discolorations are shown by the shaded areas in Figure 5.2-10 and are typical of the discolorations between each of the six struts. The high heating in these areas is caused by either shock impingement or by flow interference. Each of the six struts and the rearward-facing step at the end of the spike produce shock waves. Some of the high-heating areas are caused by the intersection of more than one of these shocks. An approximate solution of the flow field by the method of characteristics is shown in Figure 5.2-11. The estimated Mach number at axial Station 50.0 is about 3.3. Rarefaction waves emanate from the spike at axial Station 50.0 and from the rearward-facing step at the end of the spike. Compression waves emanate from the inner shell immediately downstream of the reattachment point of the separated base flow. Compression waves are indicated by the solid lines in Figure 5.2-11 and the rarefaction (or expansion) waves are indicated by the dashed lines. These wave constructions are for a two-dimensional channel without the presence of the strut and without fuel injection.

The flow-field pattern due to the presence of the strut alone (without other shocks) is shown in Figure 5.2-12 for a local Mach number of 4. Some areas of the inner and outer shell surfaces were subjected to this strut shock intersection with the boundary layer alone. At other areas, the surfaces were subjected to the multiple intersection of both the base recompression shock and the strut-shock waves. At these areas, higher localized heating occurred than when just the strut shock intersected with the surfaces. In Figure 5.2-10, the areas marked A_i and B_o received the recompression shock from the base flow only. Area A_o, in addition to receiving the recompression shock, also received
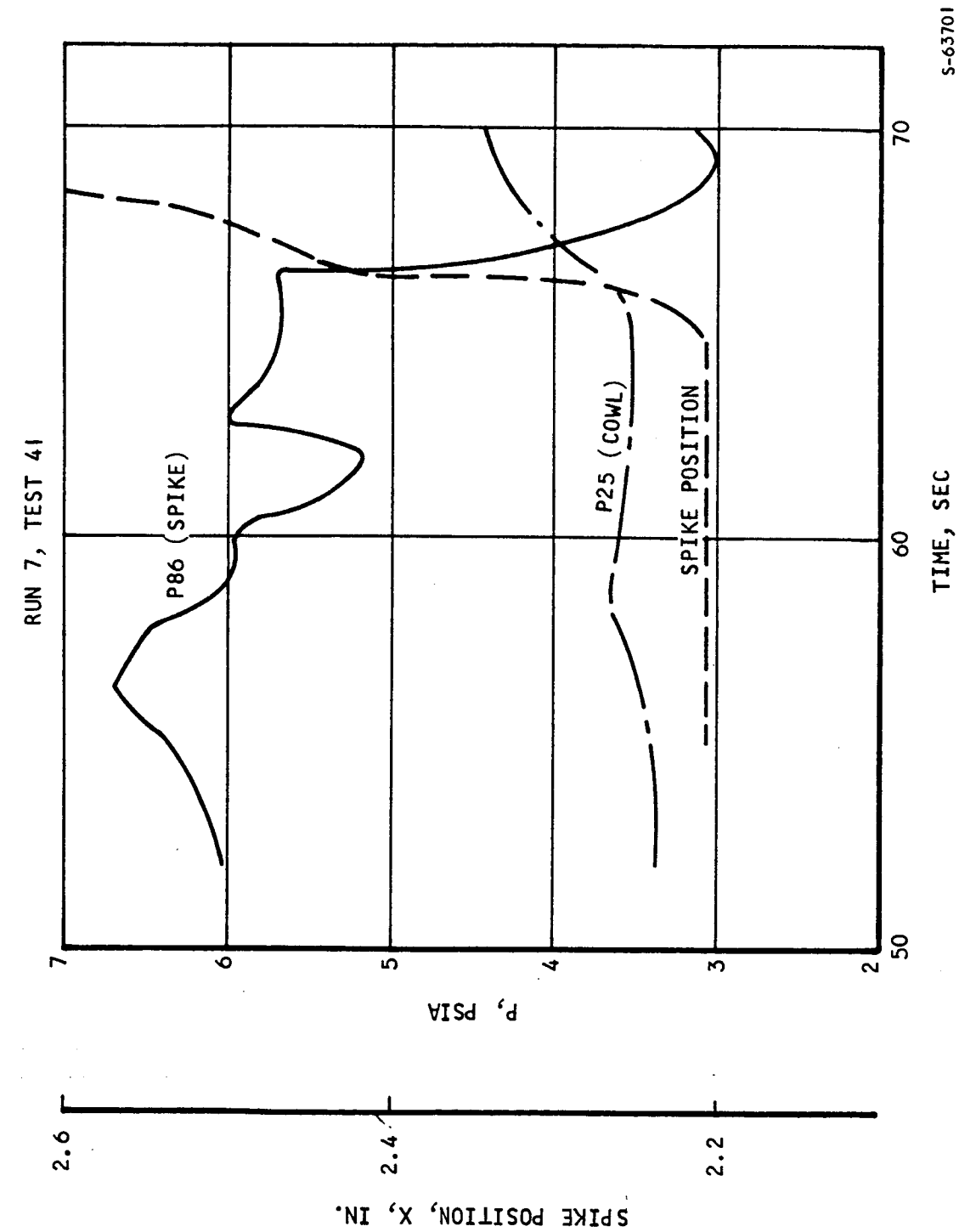
Figure 5.2-8. Pressure at Station 44 vs Spike Position (U)

S-63701

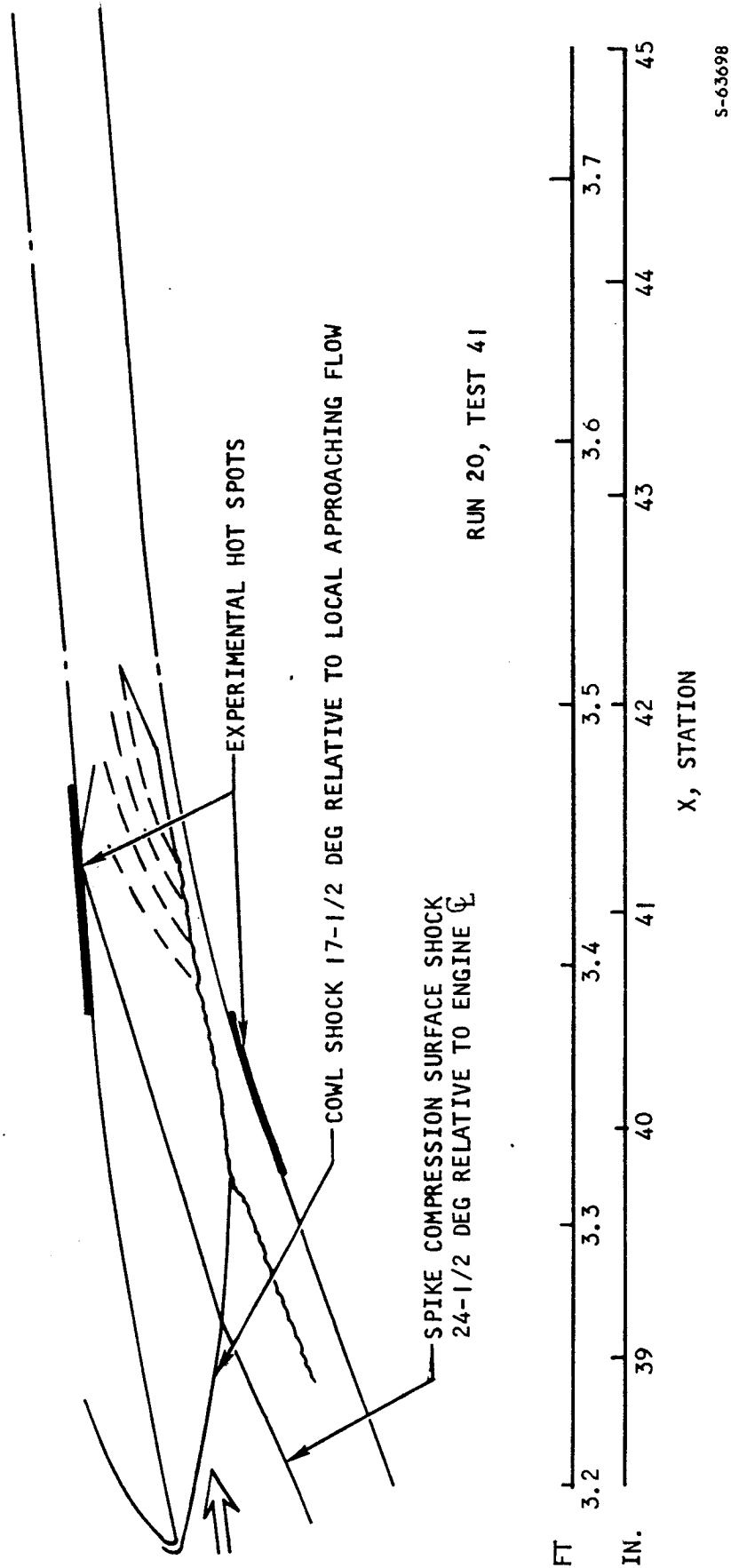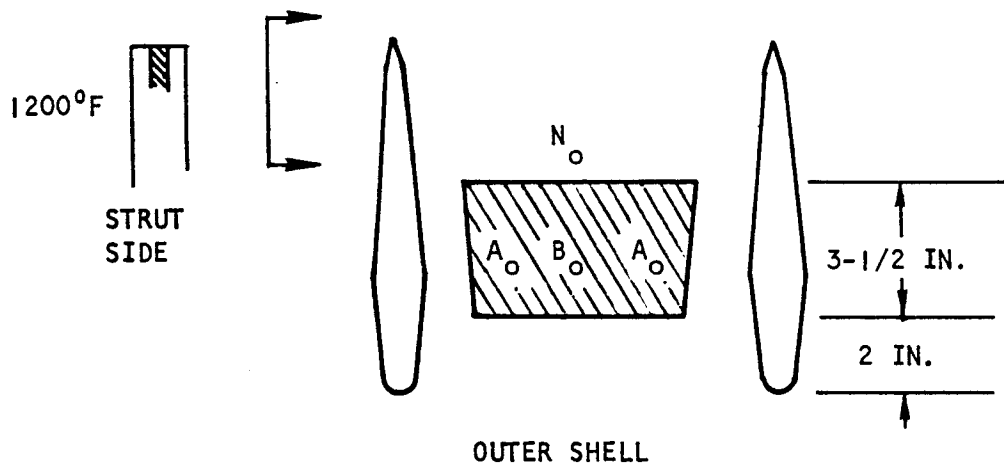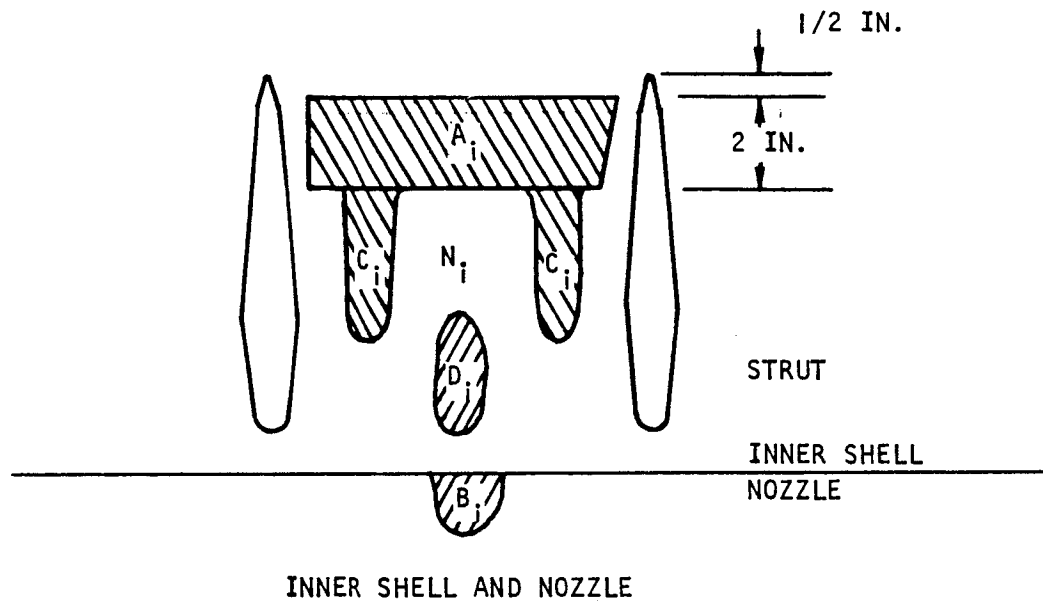AIRESEARCH MANUFACTURING COMPANY
Los Angeles, California

EXPERIMENTAL HOT SPOTS

COWL SHOCK 17-1/2 DEG RELATIVE TO LOCAL APPROACHING FLOW

SPIKE COMPRESSION SURFACE SHOCK
24-1/2 DEG RELATIVE TO ENGINE ℄

RUN 20, TEST 41

S-63698

FT 3.2
IN.

3.3   3.4   3.5   3.6   3.7

39   40   41   42   43   44   45

X, STATION

Figure 5.2-9. Approximate Flow Field at the Inlet Section

Figure 5.2-10. Some Discolored Areas As Observed After
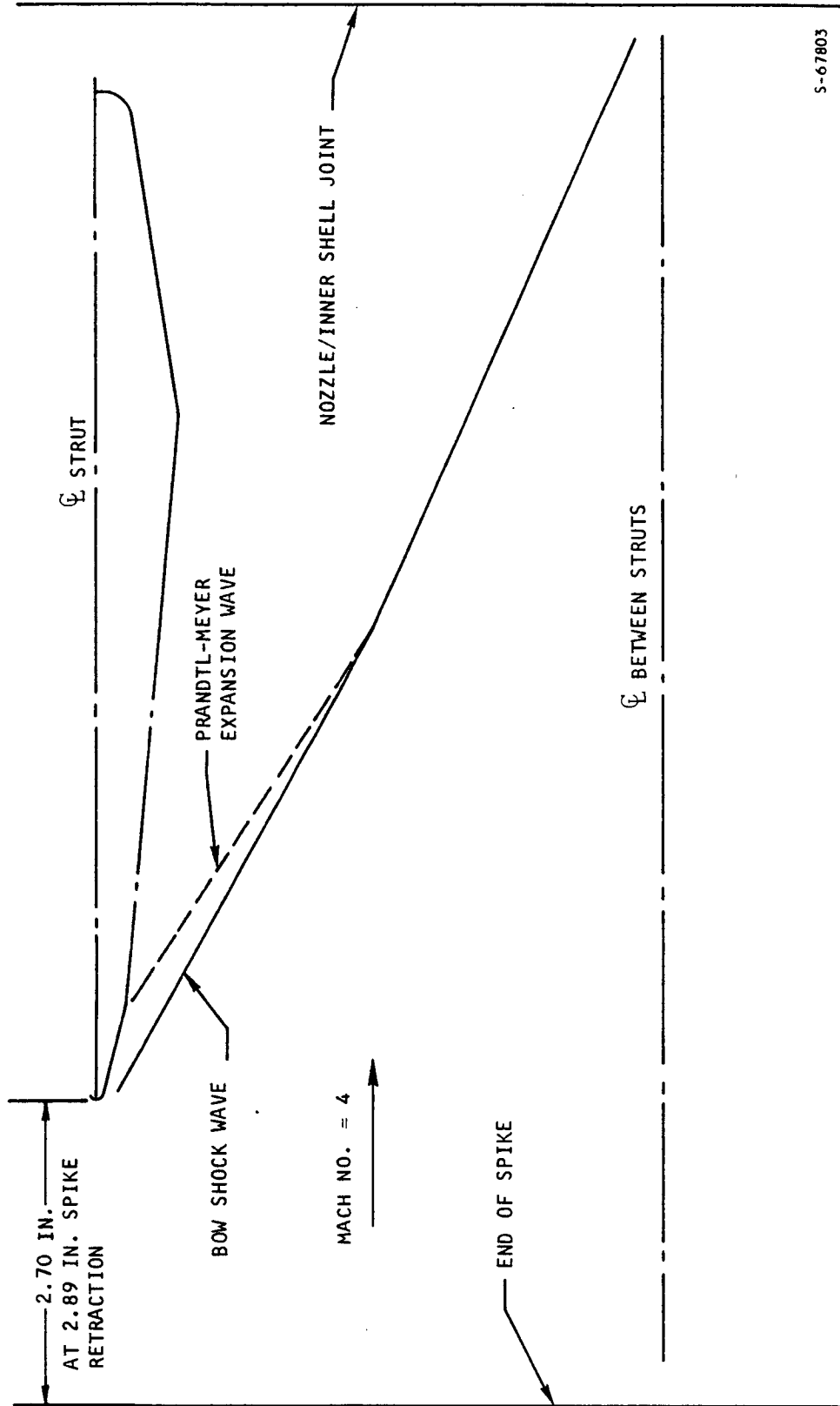Run 36, Test 42
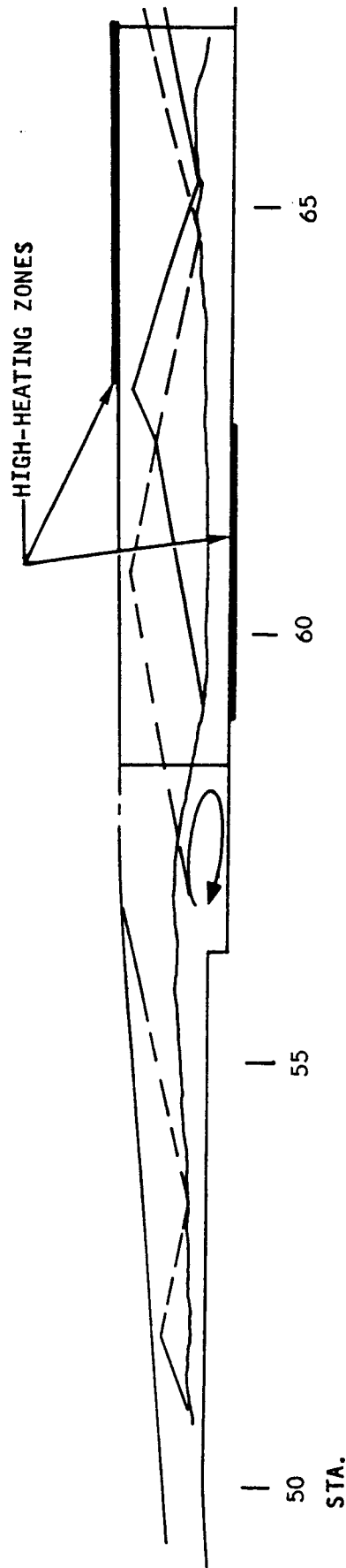
UNCLASSIFIED

Figure 5.2-11. Estimated Flow Fields Produced by the Aft-Facing Step, Test 41, Run 20

S-63697

UNCLASSIFIED

AIRESEARCH MANUFACTURING COMPANY
Los Angeles, California

71-7702
Page 5-60

S-67803

‖ STRUT

NOZZLE/INNER SHELL JOINT

PRANDTL-MEYER
EXPANSION WAVE

‖ BETWEEN STRUTS

2.70 IN.

AT 2.89 IN. SPIKE
RETRACTION

BOW SHOCK WAVE

MACH NO. = 4

END OF SPIKE

Figure 5.2-12. Flow Patterns Produced by the Strut

GARRETT | AIRESEARCH MANUFACTURING COMPANY
Los Angeles, California

71-7702
Page 5-61

the wedge shock wave from the struts. The area marked B_i appears to have been the intersection point of the shock waves from two adjacent struts, and of the recompression-base shock wave which was reflected from the outer shell. Areas N_i and N_o are unaffected by shock impingement.

Estimates of the increased heating in the described areas are presented in Table 5.2-3. On the spike and leading edge surfaces, flow separation did not occur upstream of the impingement points. Because of this, the relative local peak-heating was calculated (for the spike only, in Table 5.2-3) by inclusion of the local pressure gradient term in the boundary-layer equations. The pressure gradient was obtained from an approximate two-dimensional flow solution. Except for the spike compression shock wave, which was not expected to exist, the effect of the pressure-gradient-producing shock waves in the inlet section was included in the Mach 8 and SAM pretest heat transfer predictions. These predictions were based on two-dimensional flow solutions.

The local heating zone on the inner shell (zone A_i in Figure 5.2-10) was anticipated in the Mach 8 flight heat transfer design analysis and its effect was estimated at two-times the heat flux level just upstream of the spike rearward-facing step (as in Table 5.2-3). However, it was predicted for flight that the local peak-heating would occur just upstream of the strut leading edge rather than just downstream as in Figure 5.2-10. The location of this heating is still expected to occur just upstream for Mach 8 flight. First, the Mach 8 flight spike-retraction distance (from the closed position) of 1.78 in. will produce a 3.8-in. clearance between the end of the spike and the strut leading edges, as compared to 2.7 in. for most of the SAM tests (2.90 in. spike retraction). Second, for Mach 8 flight the local Mach number in this region will be less than during SAM test, since combustion will be present. This lower Mach number will produce a reattachment point (of the rarefaction wave from the spike rearward-facing step, and therefore, a local heating zone) further upstream than during SAM testing.

The other localized heating areas in the vicinity of struts (zones C_i, D_i, B_i, A_o, B_o in Figure 5.2-10) were not included in the Mach 8 flight heat transfer design analysis. It was not anticipated that a compression wave would (1) emanate from inner shell downstream of the base flow reattachment point, (2) impinge on the outer shell, (3) reflect off the outer shell, and (4) impinge on the nozzle while simultaneously interacting with the strut wedge shock waves. The effect of the strut wedge shock waves intersecting the inner and outer shell surfaces only was included in the Mach 8 predictions. However, the effect was thought to diminish to a negligible value at the nozzle/inner shell joint (zone B_i in Figure 5.2-10). For Mach 8 flight, the local heating strength on these zones (relative to adjacent average fluxes) is not expected to be as high as calculated in Table 5.2-3, since local Mach numbers with combustion at Mach 8 flight conditions will be lower. The resulting lower shock strengths (as measured by overall pressure rise in Table 5.2-3) in the combustion zone will give lower relative local heating values.

TABLE 5.2-3

SUMMARY OF LOCAL HEATING EFFECTS DUE TO SHOCK IMPINGEMENT (U)

Location	Mach No. Upstream of Shock Wave	Mach No. Downstream of Shock Wave	Pressure Ratio Across Shock Wave	Type of Flow	Heat Transfer Coefficient Increase
Spike, axial location 40 in. in Figure 5.2-9	4.8	3.9	2.9	Shock impingement with no separation	1.7-times upstream value
Inner shell at A_i, Figure 5.2-10	4.5	4.1	1.6	Base flow with separation	2.0-times the value upstream of spike rearward facing step
Nozzle at B_i, Figure 5.2-10	4.5	-	5.0	Shock impingement with separation	3.0-times the value at N_i, Figure 5.2-10
Outer shell at A_o, Figure 5.2-10	4.8	-	4.0	Shock impingement with separation	2.5-times the value at N_o, Figure 5.2-10
Outer shell at B_o, Figure 5.2-10	4.8	3.8	3.0	Shock impingement with no separation	1.8-times the value at N_o, Figure 5.2-10
Strut side area in Figure 5.2-10	4.0	-	-	3-dimensional shock	1.5-times the value for 2-dimensional flow shown in Figure 5.2-12

5.3 COOLING PERFORMANCE

5.3.1 Summary of Results

The basic objective of the SAM test program was to verify the design of the hydrogen-cooled engine structure in a severe wind tunnel environment. Since the engine design is dependent on the cooling system, a specific objective was to evaluate the cooling performance. The steady-state cooling performance was evaluated (Section 5.3.3.1.1) by comparing measurements of hot wall, cold wall and hydrogen temperatures in the engine coolant routes with results of heat transfer analyses for the specific test measurement conditions.

The heating distribution for the analyses was obtained from the test results and data analyses in Section 5.2.3.1. The coolant-side analyses were performed with the analytical methods used for the Mach 8 flight design analysis. However, the heat transfer characteristics for the 20- and 28-fin-per-inch coolant passages (Colburn heat transfer factor (j)) were updated from the Mach 8 design analysis by inclusion of the recent (j) vs Reynolds number test data for these fins reported in Reference 5-5. The j-factor data in Reference 5-5 are equal to (28 fins per inch) and greater than (20 fins per inch) the Mach 8 design data. As a result, revised Mach 8 surface temperature predictions based on Reference 5-5 data will be equal to or slightly less than the values reported in Reference 5-4.

The coolant-side data analyses gave hot and cold wall temperatures at each axial location based on average circumferential conditions. When the test hot and cold wall temperature measurements were adjusted for circumferential heating and coolant flow maldistribution, test and data analysis values agreed within 50°R. For this comparison, the hot wall insert-thermocouple data was corrected to account for the insert thermocouple bead location in relation to the hot wall outer surface.

During the thermal cycle tests, the engine structure was subjected to a thermal environment (combination of hot wall temperatures and hot wall-to-structure temperature differences) as severe as the predicted Mach 8 flight conditions. This was accomplished by undercooling the coolant flow routes. Hot wall temperature results presented later in this Section (Section 5.3.3.1.2) were evaluated from (1) a comparison of surface discolorations with Hastelloy X specimens that had been subjected to a known time-at-temperature history, and (2) data analysis based on measured flow route conditions. Hot wall-to-structure temperature differences were calculated by transient heat transfer analysis in the areas of surface discoloration. The discolorations indicate that temperatures as high as 1860°R occurred on the nozzle or about 1000°R higher locally than the Mach 8 prediction. This locally high temperature produced a hot wall-to-structure ΔT of 1000°R compared to a maximum predicted Mach 8 ΔT of 950°R on the leading edge. At the outerbody outlet manifold, ΔT's as high as 1400°R were measured at lower hot skin temperatures.

The density-adjusted pressure drop was calculated for most of the engine flow routes from measured hydrogen flow rates and inlet and outlet pressures

UNCLASSIFIED

and temperatures. Results to be presented in Section 5.3.3.2.2 are compared with the isothermal air results reported in Reference 5-6. The comparison of the hydrogen results with the air results is only fair because the measured pressure drops were of similar magnitude to the measurement uncertainty of the individual inlet and outlet pressure measurements. The coolant maldistribution, W_{MAX}/W_{MIN}, in the engine flow routes was estimated as high as 1.10 on the spike (Section 5.3.3.2.3). These estimates were based on coolant control-thermocouple measurements around the flow route circumference. The maximum coolant maldistribution based on inlet and outlet manifold pressure distributions during air tests was 1.033 on the leading edge route.

5.3.2 Test Data

The steady-state cooling performance evaluation was based on the measurements and test conditions of Test 41, Run 39 (3320 psia, 3400°R tunnel reservoir total conditions). This test run was at the maximum tunnel heating conditions for the test program and was one of the few test runs where thermal steady-state conditions were reached simultaneously on all flow routes. The hydrogen inlet temperature was approximately 160°R. The maximum hot wall temperatures and hot wall-to-structure temperature differences occurred during the thermal cycle test runs where the engine flow routes, particularly the aft routes, were undercooled. These runs (Test 42, Run 14 to Test 42, Run 38) were performed at 1380 psia, 2700°R nominal tunnel reservoir total conditions, and the engine was inserted and withdrawn from the tunnel test section up to three times per test run.

The data for the flow route pressure-drop results were obtained from test runs at several tunnel total pressures, hydrogen flows, and both cryogenic (160°R) and room temperature (520°R) inlet hydrogen. Flow distribution results were obtained from Test 41, Run 39 data. Data from Test 42, Run 45 (2250 psia, 3000°R tunnel reservoir total conditions) were also used because steady-state conditions were well established for this 115-sec run, and more structural and hydrogen temperature channels were recorded than during Test 41 runs. The 3-deg angle-of-attack tests (Test 41, Runs 51, 52, and 53 at 3350 psia, 2700°R tunnel reservoir total conditions) demonstrated the asymmetric heating effect as measured by the coolant control thermocouples.

5.3.3 Data Analysis and Discussion

5.3.3.1 Metal Temperatures and Temperature Differences

5.3.3.1.1 Thermal Performance Test Results

To evaluate the steady-state performance of the engine cooling design, a heat transfer analysis was performed on the hydrogen-cooled plate-fin panel surfaces. The inputs to the analysis corresponded to the surface heating distribution and coolant flow conditions for Test 41, Run 39 (3320 psia, 3400°R tunnel reservoir total conditions). The analytical hot and cold wall temperature distributions were compared with measured hot and cold wall temperature data for Test 41, Run 39. The general agreement of the analytical results with the measured data substantiates the overall cooling design concept and the

UNCLASSIFIED

cooling performance predictions for the Mach 8 flight condition.

The local surface heating distribution for the cooling-performance data analysis was obtained from the aerodynamic heating analysis described in Section 5.2.3.1 for Test 41, Run 39. As seen in Figure 5.2-6, differences of up to 43 percent occur between the test average heat fluxes and the data analysis average heat fluxes. The analytical average heat fluxes were obtained by integrating the analytical local heat flux curves over the segmented widths indicated in Figure 5.2-6. For purposes of the cooling-data analysis, the distributions of local heat transfer coefficient associated with the analytical heat flux in Figure 5.2-6 were multiplied by the ratio of average test-to-average data analysis heat flux. This simple procedure assured that the data analysis heat load and outlet coolant temperature on each flow route matched the measured test values and gave a realistic heat transfer coefficient distribution along the route. The data analysis was performed with a cooling-performance evaluation computer program that used a "marching-iteration" calculation technique. With heat transfer coefficient distribution and measured inlet hydrogen temperature and flow rate as input, the program proceeded from the flow route inlet to outlet in axial increments of 0.10 in.

The localized heating effects discussed in Section 5.2.3.2 are not included in the analytical heat flux results in Figure 5.2-6, and therefore are not included in the computer cooling-data analysis. As noted previously, the hot gas pressure distribution used in the aerodynamic-heating data analysis was based on surface-pressure measurements. The available pressure tap locations were unable to detect the large pressure gradients, particularly near the struts, that produce locally high heating. The aerodynamic heating data analysis calculates symmetrically average heat fluxes and for this additional reason cannot accommodate the unsymmetrical localized heating effects. The localized heating effects on surface temperature (in the vicinity of the struts) were added to the cooling data analysis by hand calculation. The local heat transfer coefficients were obtained from the estimated coefficient increases presented in Table 5.2-3.

The computer and hand-calculated results of the cooling data analysis are shown in Figure 5.3-1 for the spike, innerbody, and internal surfaces of the leading edge and trailing edge flow routes. Included are the hot and cold wall temperature data for Test 41, Run 39. The test hot wall temperatures indicated by the triangular points in Figure 5.3-1 are corrected hot-wall insert-thermocouple measurements. The correction procedure is described in Appendix A. To get better agreement with the data analysis, several of the hot and cold wall temperatures were further corrected for coolant flow maldistribution. Basically, the data analysis curves present average surface temperatures around the circumference at each location. Due to local variations in circumferential coolant flow, the locally measured temperatures will be higher or lower than the circumferential average, depending on whether the local flow is lower or higher, respectively, than the average coolant flow per unit width. The variation in circumferential coolant flow is determined from the distribution of coolant-control thermocouple data for each flow route and is discussed later, in Section 5.3.3.2.3.

AIRESEARCH MANUFACTURING COMPANY
Los Angeles, California
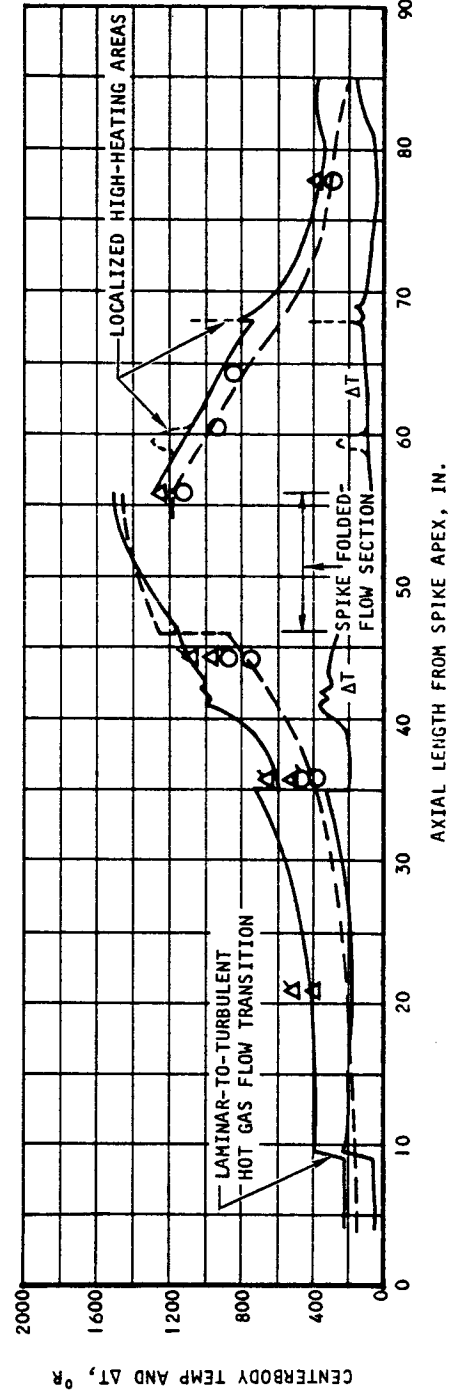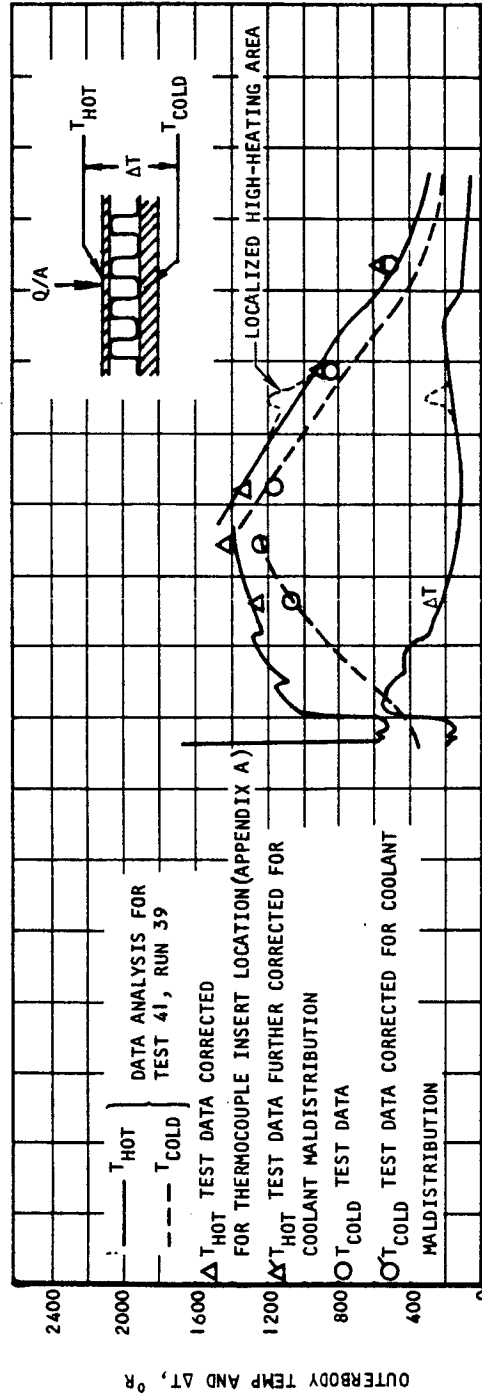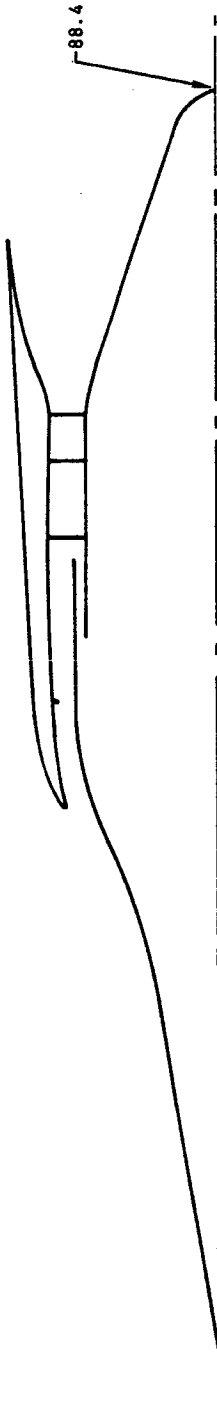
UNCLASSIFIED

71-7702
Page 5-66

Figure 5.3-1. SAM Test Thermal Performance – Test 41, Run 39 (U)

GARRETT
AIRESEARCH MANUFACTURING COMPANY
Los Angeles, California

S-67811

The correction for flow maldistribution brings the hot wall data into
very close agreement with the circumferential average data analysis (50°R or
less) except on the inner shell at axial Station 56. This location is in a
base-flow region just downstream of the spike rearward-facing step, so the
heat flux cannot be accurately predicted. The hot and cold wall data uncorrec-
ted for flow maldistribution deviates from the data analysis by up to 150°R
(axial Station 40.5 on the spike). In an operating engine, some amount of de-
viation from the average would be expected. Although coolant flow maldistri-
butions can be minimized by design iterations, unsymmetrical heating can occur
and produce temperature maldistributions.

For purposes of comparison with the Mach 8 surface temperature predictions,
the data analysis results are repeated in Figure 5.3-1. Data analysis surface
temperatures are generally lower than predicted Mach 8 temperatures except on
the spike. The maximum test temperatures are 1600°R at the end of the spike
(Station 55.76) and 1650°R on the outerbody, at the leading and trailing edges
route coolant outlet holes (Station 51.40). Corresponding predicted temperatures
at these locations for Mach 8 flight are 1850° and 2050°R, respectively.

The location of predicted maximum innerbody surface temperature for Mach
8 flight (2000°R at Station 57) appears to have shifted to Station 60 for
SAM testing. The Mach 8 predicted location was the effect of hot gas flow
reattachment caused by the rearward-facing step of the spike. Differences
in aerodynamic conditions in this region between Mach 8 flight and test, as
confirmed by metal surface discoloration, indicate that the reattachment point
has shifted downstream. The local peak in surface temperature of 900°R at
Station 66 on the nozzle is the result of shock impingement and occurs at six
localized areas around the circumference (approximately midway between the
struts). The average surface temperature at this location is 650°R. SAM test
temperatures are higher on the forward spike because the inlet coolant hydrogen
temperature (155°R) is slightly higher than for Mach 8 conditions (100°R), and
SAM test heat fluxes are higher than Mach 8 heat fluxes in this region.

SAM surface temperatures were predicted to be lower than Mach 8 flight
conditions because cooled-panel heat fluxes were predicted to be lower. How-
ever, test surface temperatures shown in Figure 5.3-2 for Test 41, Run 39 are
lower than temperatures predicted for this condition, particularly on the
innerbody, because hydrogen flow rates were in excess of the values required
to reach the 1600°R maximum design structural temperature. The excess of flow-
route coolant rates for Test 41, Run 39 is discussed later, in Section 5.3.3.2.1.

5.3.3.1.2 Thermal Cycle Test Results

Local maximum surface temperatures of higher level than for Test 41, Run
39 occurred during the thermal cycling runs (1380 psia, 2700°R tunnel reservoir
total conditions and ambient temperature inlet hydrogen). During these runs,
the coolant flow rates were reduced below the values required for adequate
cooling, for the purpose of increasing metal temperatures and metal temperature
differences (ΔT's) to values simulating the thermal loading during steady state
at Mach 8 flight conditions. Undercooling was used as a means of subjecting
the engine structure to the desired thermal environment because steady-state
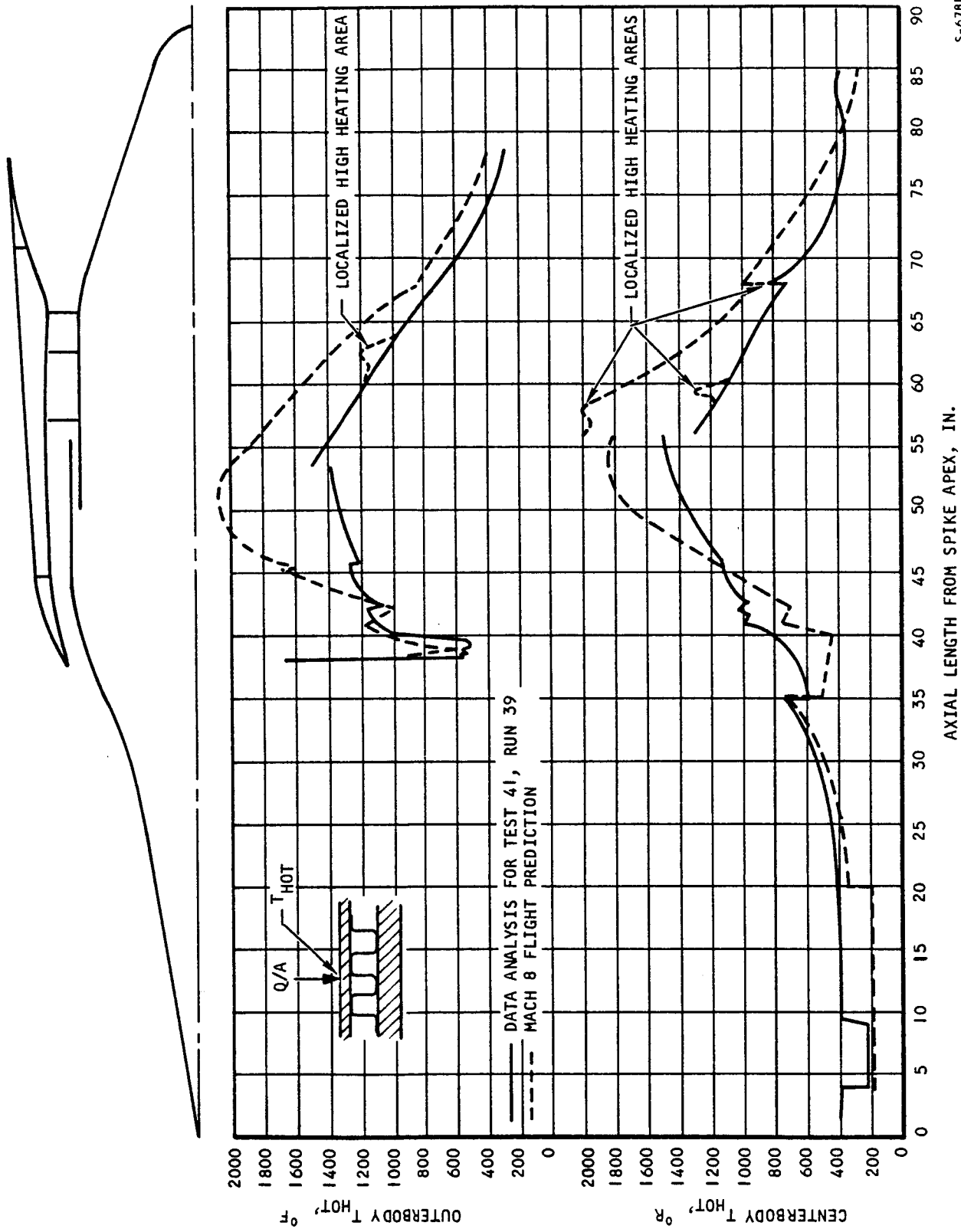
Figure 5.3-2. SAM Test and Mach 8 Flight Surface Temperatures (U)
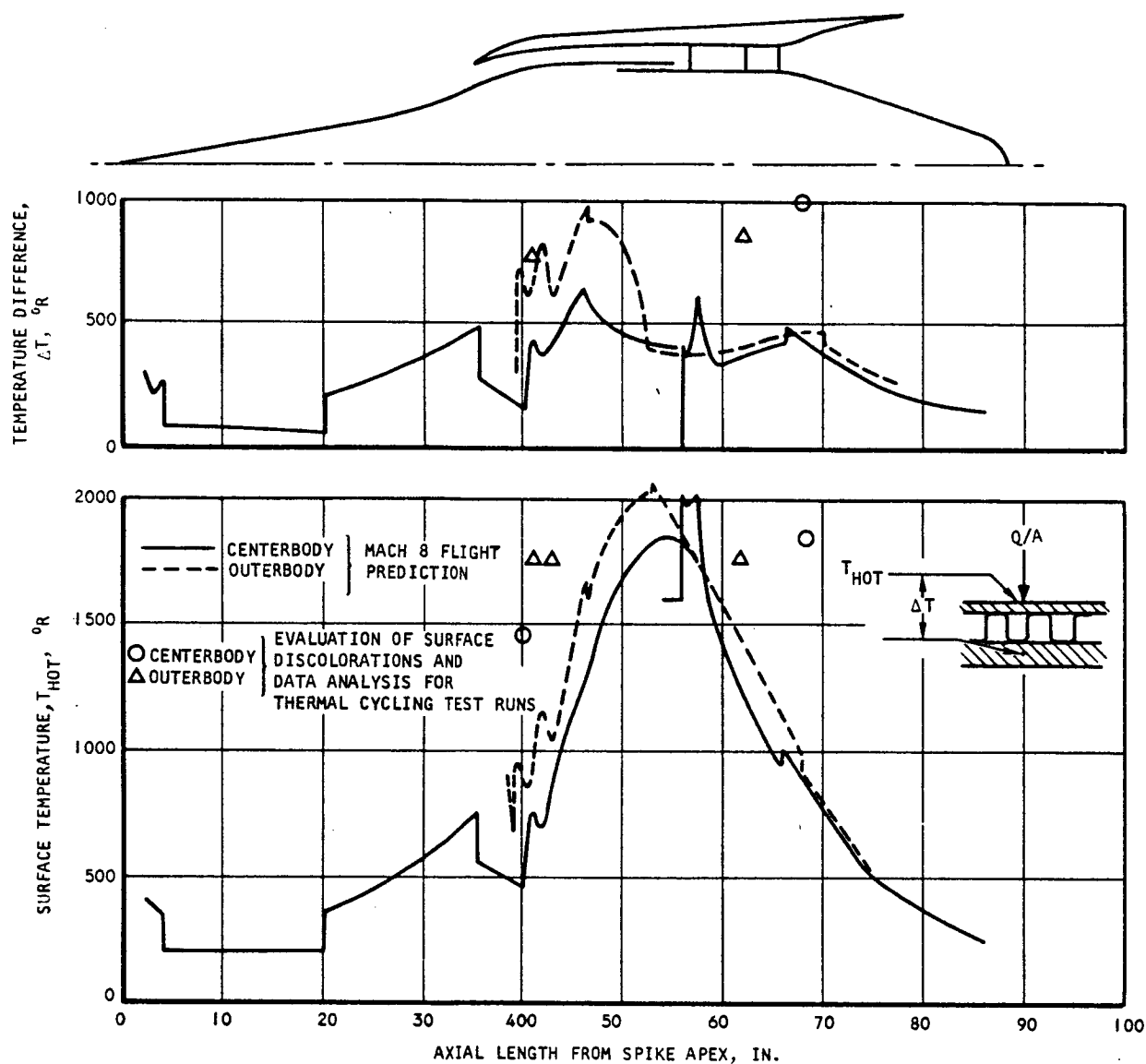
S-67810

temperatures and ΔT's in the cooled surfaces were predicted to be less than Mach 8 flight values for SAM testing.

Local metal temperature and metal ΔT results for these thermal cycling tests are presented in Figure 5.3-3 and are compared with the Mach 8 flight steady-state predictions. All of the test points in Figure 5.3-3 occurred in the locally highly heated zones that were produced by shock-boundary layer interactions as discussed in Section 5.2.3.2. The hot surface temperatures were evaluated by comparing hot surface discoloration patterns with discolored Hastelloy X specimens of known time-temperature exposure, as discussed in Section 5.1.2.1. These temperatures were further checked by transient heat transfer data analyses on the nozzle (1860°R) and aft outer shell (1760°R). The maximum panel ΔT's were produced because undercooling allowed surface temperatures to quickly increase above locally predicted steady-state values during transient test startup while structural temperatures were still below steady-state values. The maximum ΔT's are 750°R on the leading edge, 820°R on the outer shell, and 1000°R on the nozzle. The maximum temperatures and ΔT's on the spike and leading edge surfaces were uniformly distributed around the engine circumference, while the maximum values on the aft outer shell and nozzle were at localized regions around the circumference and between each of the six struts. At all locations the maximum test temperatures and ΔT's were locally larger than the predicted steady-state values at Mach 8 flight conditions. None of the maximum surface temperatures exceeded the maximum predicted Mach 8 temperature of 2060°R at axial Station 52 on the outerbody. The nozzle test ΔT of 1000°R exceeded the maximum predicted Mach 8 ΔT of 950°R (leading edge) while the aft outer shell test ΔT of 820°R was slightly less. In addition, the ΔT at the outerbody outlet manifold (hot skin to manifold) at Station 51.4 was near 1000°R for many of the thermal cycle tests and exceeded 1000°R for thermal performance runs using cryogenic hydrogen. This ΔT is not shown in the figure, since it is not directly comparable to the other ΔT's. Its evaluation is discussed in detail later, in Section 5.5.

5.3.3.1.3 Leading Edge Tip

The thermal performance of the Nickel 200 leading edge tip was evaluated primarily from metal discolorations during the test program. No distinct metal discolorations were observed directly at the leading edge stagnation point through Test 42, Run 38, although discolorations indicating temperatures up to 1200°F were observed as close away as 0.030 in. (Section 5.1.2.1). To this point in the test program, the spike bow-shock wave was outside the cowl lip (maximum spike retraction of 2.90 in. from the fully extended position) and the maximum tunnel (reservoir) total conditions were 2200 psia and 3000°R. Most of these test runs were at the thermal cycle conditions of 1380 psia, 2700°R and all runs used room temperature inlet hydrogen. Because of foreign object damage in the tip region early in the test program (beginning with Test 41, Run 13), the leading edge flow route was not excessively undercooled during these runs as were the other flow routes (W/W$_{IDEAL}$ = 0.82 minimum as defined in Section 5.3.3.2.1). For the maximum tunnel heating conditions of 2200 psia, 3000°R (Test 41, Runs 26 and 28) in this grouping to Test 41, Run 38, the predicted leading edge tip temperature (shock-outside-lip) was 1000°F. The lack of distinct tip discoloration is in agreement with this, indicating a tip temperature that was at or below 1000°F.

Figure 5.3-3. SAM Thermal Cycle Test and Mach 8 Flight Temperatures and Temperature Differences (U)

Test 42, Runs 41, 42, and 43 (1380 psia, 2800°R, and RT inlet hydrogen) were performed to determine the shock-on-lip spike retraction position. The tip discoloration (brass) after these runs still indicated a temperature of 1000°F or less. Due to oscillations in the hot gas flow, it is thought that the shock oscillated back and forth off the tip. The high pressure test runs to 3300 psia with shock-outside-lip and 160°R inlet hydrogen produced light straw yellow tip discoloration (below 1000°F). After Test 41, Run 39, a blue discoloration (1100°F) was observed over a 40-deg arc of the leading edge tip. During the 3-deg angle-of-attack runs (Test 41, Runs 51, 52, and 53), discolorations at two symmetrical locations on the tip circumference were expected due to the ovate intersection of the spike shock cone and the cowl lip. No such discolorations at the tip were observed. The shock impingement heating intensity of the intersection was probably damped out due to metal cross-conduction both in the axial and circumferential directions.

The maximum predicted tip temperature for the SAM tests was from 1020°F (turbulence factor, K, = 1.0) to 1470°F (K = 1.8). This temperature range corresponded to shock-on-lip operation at 3300 psia, 3600°R tunnel reservoir conditions, with 0.20 lb/sec hydrogen coolant flow at 320°R at the tip. A shock multiplier of 15.4 (times the shock-inside-lip stagnation heat transfer coefficient over a 0.040-in. band of the tip) was used in the prediction reported in Reference 5-6. Symmetrical shock-on-lip conditions were attempted but not obtained at 3300-psia conditions because of difficulty in interpretation of Schlieren results. However, the shock-outside-lip test conditions at 3300 psia were not expected to be significantly less than the shock-on-lip condition. To provide agreement between the test observations (a metal discoloration qualitatively indicating a tip temperature of 1000°F or less) and the prediction, the hot gas freestream turbulence factor (K) was probably closer to 1.0 (1020°F) than to 1.8 (1470°F).

The Nickel 200 discolorations at 0.030 to 0.050 in. in back of the tip were produced by the higher shock-outside-lip conditions (than the design case of shock-on-lip) and the duct flow-type internal cooling effect just aft of the tip. The tip is internally cooled by (higher-than-duct flow) jet impingement of the hydrogen flow.

5.3.3.2   Coolant System

5.3.3.2.1   Hydrogen Flow Rates

The range of hydrogen coolant rates to the engine flow routes, and the total during SAM testing are presented in Figure 5.3-4. These flow rates are presented relative to the ideal flow rate, W_{IDEAL}, required for steady-state operation at each tunnel condition and resulting in a maximum structural temperature of 1600°R. This ideal flow is the criteria used for design selection of hydrogen rates at flight conditions except where hot wall temperatures in excess of 2060°R are predicted. In terms of coolant outlet temperature, this reduces to the following:
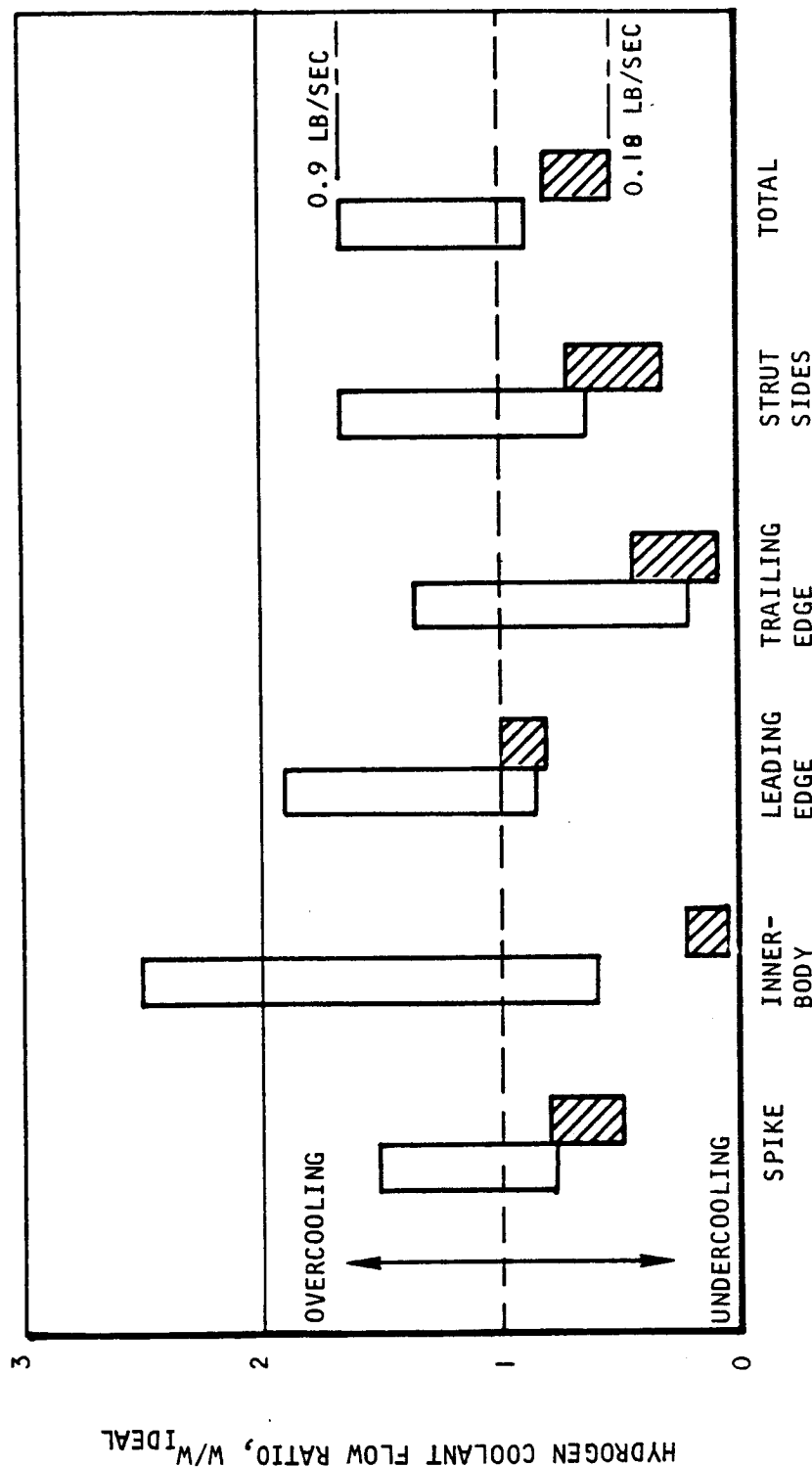
Figure 5.3-4. Flow Route Hydrogen Flow Rates (U)

S-67781

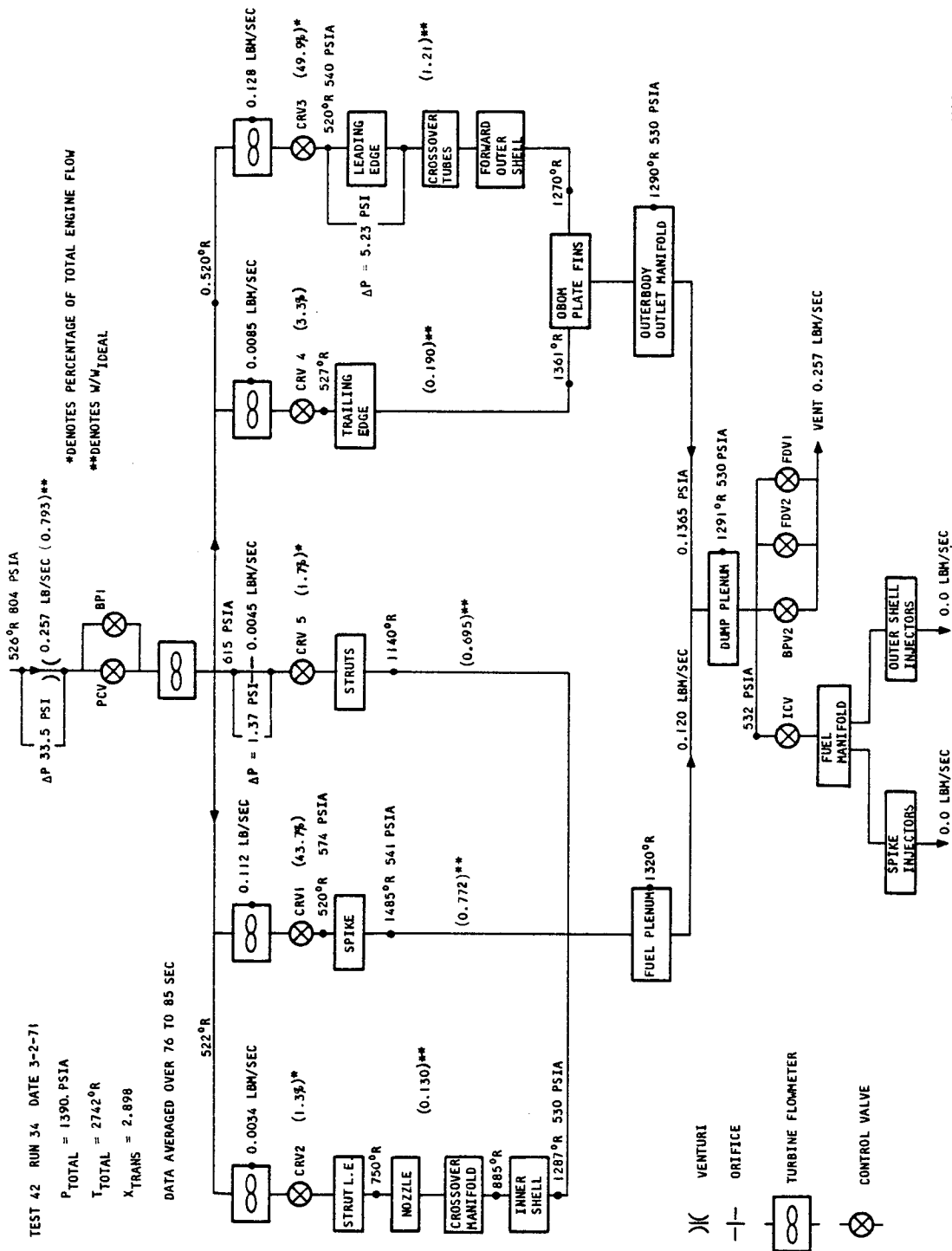| Flow Route	Hydrogen Outlet Temp, $^\circ R$
Spike	1350
Innerbody	1600
Leading edge	1600
Trailing edge	1600
Strut sides	1430
Total	1470

A value of W/W_{IDEAL} greater than 1.0 indicates overcooling relative to the design flow rate selection criteria; a value less than 1.0 indicates undercooling.

The flow rates presented are for two categories: (1) thermal performance runs at tunnel reservoir total conditions from 2200 psia, 3000°R, to 3320 psia, 3400°R, with 160°R hydrogen inlet temperature; and (2) thermal cycling runs at a nominal tunnel reservoir total condition of 1380 psia, 2700°R with room temperature inlet hydrogen. The object of the thermal performance runs was to achieve steady-state thermal conditions (as measured by route outlet hydrogen temperature) so that hydrogen heat loads could be correlated with aerodynamic heat loads calculated from hot gas surface pressure and tunnel measurements. As tunnel total pressure and temperature were increased from run to run during the test program, the first test run at a new tunnel condition was overcooled as indicated by maximum flow ratios of from 1.35 on the trailing edge route to 2.50 on the innerbody. For subsequent runs at a given tunnel condition, coolant flows were reduced to achieve W/W_{IDEAL} flow ratios close to 1.0.

Thermal cycle runs were performed for the purpose of accumulating low-cycle thermal fatigue performance data. Coolant rates, particularly in the aft routes, were reduced considerably below those required for adequate cooling at steady state. Flow ratios were reduced to as low as 0.06 for the innerbody, 0.08 for the trailing edge, and 0.32 for the strut sides. These reduced flow ratios increased hot wall temperatures and structural ΔT's to levels equal to and exceeding those predicted for Mach 8 flight operation. The leading edge route was undercooled only moderately (W/W_{IDEAL} = 0.82 minimum) so that the foreign object damage that occurred at the tip would not be aggravated. Flow ratios as low as 0.51 were tested on the spike.
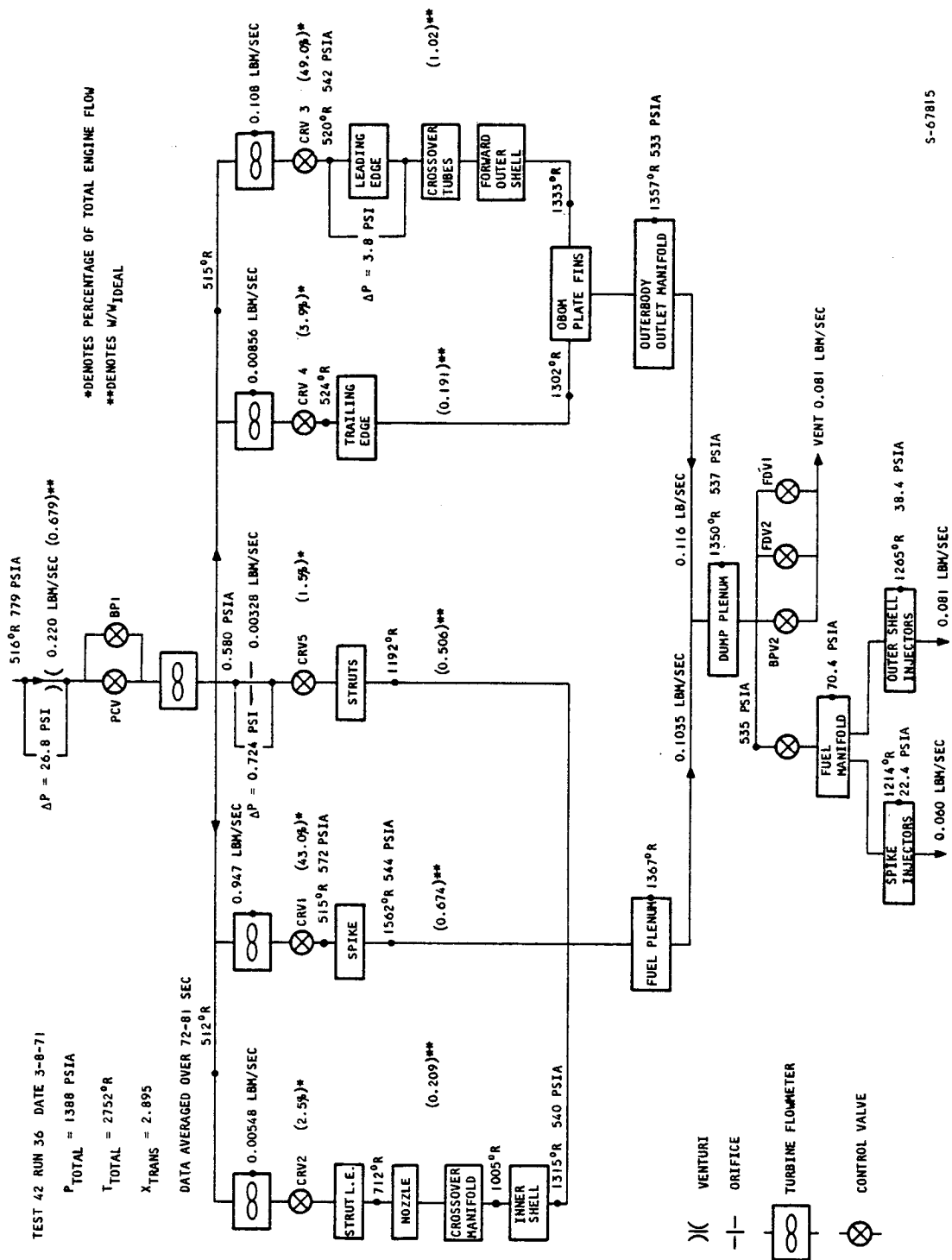
The range of hydrogen flow rates for the SAM test program was 0.18 to 0.90 lb/sec as indicated in Figure 5.3-4. Hydrogen rates in the individual flow routes are shown on the coolant schematics in Figure 5.3-5 to 5.3-8. These schematics present the overall hydrogen flow conditions (pressures, temperatures, flow rates) for two test runs each (one with hydrogen injection

Figure 5.3-5. Hydrogen Coolant Schematic - Thermal Cycle Test Condition, No Hydrogen Injection (U)

AIRESEARCH MANUFACTURING COMPANY
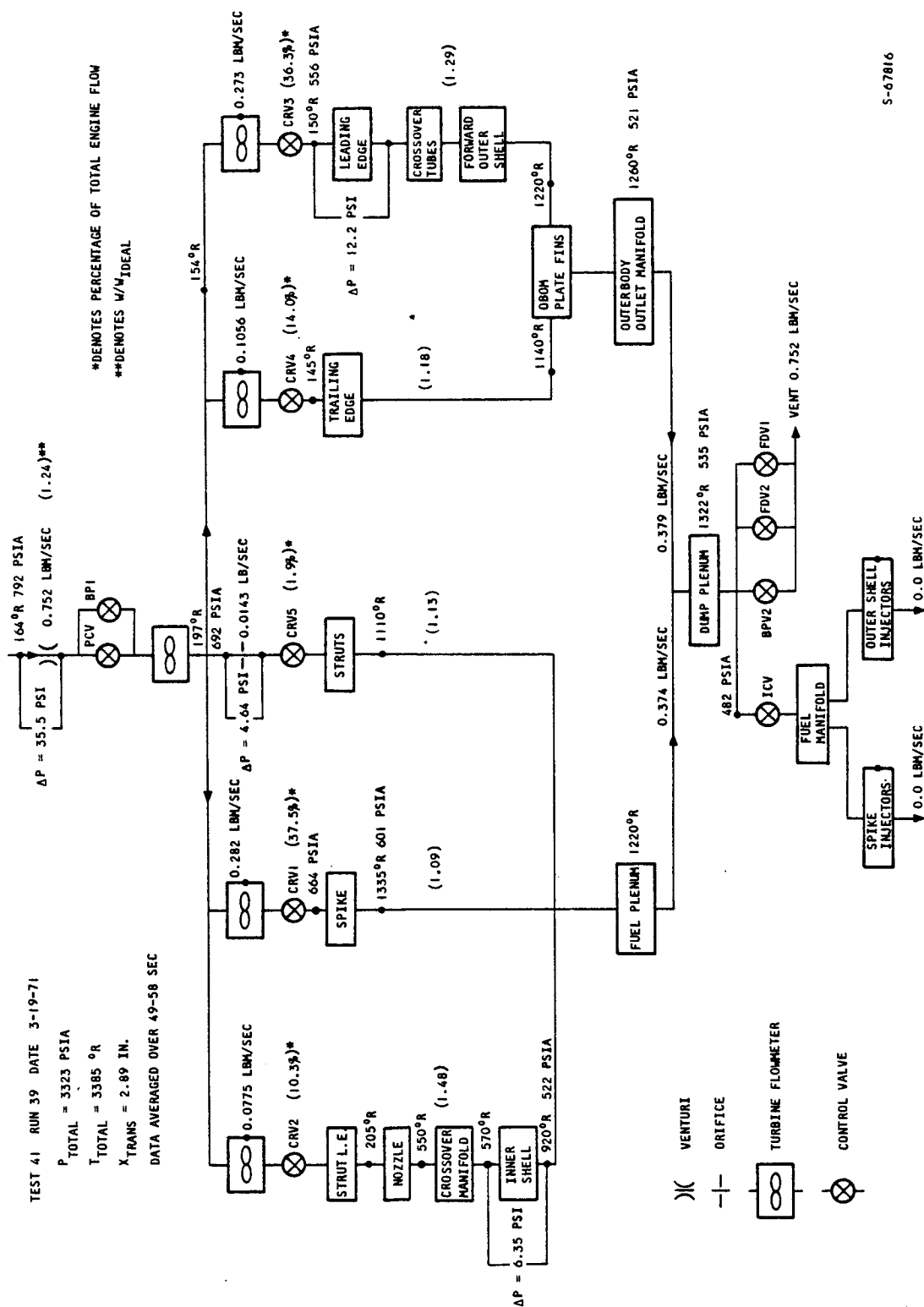Los Angeles, California

TEST 42 RUN 36 DATE 3-8-71

P_{TOTAL} = 1388 PSIA

T_{TOTAL} = 2752°R

X_{TRANS} = 2.895

DATA AVERAGED OVER 72-81 SEC

*DENOTES PERCENTAGE OF TOTAL ENGINE FLOW
**DENOTES W/W_{IDEAL}

516°R 779 PSIA

0.220 LBM/SEC (0.679)**

ΔP = 26.8 PSI

BP1

PCV

0.108 LBM/SEC

CRV 3 (49.0%)* 520°R 542 PSIA

LEADING EDGE

(1.02)**

CROSSOVER TUBES

FORWARD OUTER SHELL

ΔP = 3.8 PSI

515°R

0.00856 LBM/SEC

CRV 4 (3.9%)* 524°R

TRAILING EDGE

(0.191)**

1333°R

OBOM PLATE FINS

1302°R

1357°R 533 PSIA

OUTERBODY OUTLET MANIFOLD

0.580 PSIA

0.00328 LBM/SEC (1.5%)*

CRV5

STRUTS

1192°R

(0.506)**

ΔP = 0.724 PSI

512°R

0.947 LBM/SEC

CRV1 (43.0%)* 515°R 572 PSIA

SPIKE

1562°R 544 PSIA

(0.674)**

0.116 LB/SEC

DUMP PLENUM 1350°R 537 PSIA

FDV1

VENT 0.081 LBM/SEC

FDV2

BPV2

70.4 PSIA

1265°R 38.4 PSIA

OUTER SHELL INJECTORS

0.081 LBM/SEC

0.1035 LBM/SEC

535 PSIA

FUEL MANIFOLD

1214°R 22.4 PSIA

SPIKE INJECTORS

0.060 LBM/SEC

FUEL PLENUM 1367°R

0.00548 LBM/SEC (2.5%)*

CRV2

STRUT L.E. 712°R

NOZZLE

CROSSOVER MANIFOLD 1005°R

INNER SHELL 1315°R 540 PSIA

(0.209)**

VENTURI

ORIFICE

TURBINE FLOWMETER

CONTROL VALVE

S-67815

Figure 5.3-6. Hydrogen Coolant Schematic - Thermal Cycle
Test Condition, With Hydrogen Injection (U)

TEST 41   RUN 39   DATE 3-19-71

P_{TOTAL} = 3323 PSIA
T_{TOTAL} = 3385 °R
X_{TRANS} = 2.89 IN.
DATA AVERAGED OVER 49-58 SEC

*DENOTES PERCENTAGE OF TOTAL ENGINE FLOW
**DENOTES W/W_{IDEAL}

164°R 792 PSIA
0.752 LBM/SEC   (1.24)**
ΔP = 35.5 PSI
BPI
PCV
197°R
692 PSIA
ΔP = 4.64 PSI   -0.0143 LB/SEC

0.273 LBM/SEC
CRV3 (36.3%)*   150°R   556 PSIA
LEADING EDGE
CROSSOVER TUBES   (1.29)
FORWARD OUTER SHELL
1220°R
ΔP = 12.2 PSI

0.1056 LBM/SEC
CRV4 (14.0%)*   145°R
TRAILING EDGE
(1.18)
OBOH PLATE FINS   1140°R
OUTERBODY OUTLET MANIFOLD   1260°R   521 PSIA

154°R

CRV5 (1.9%)*
STRUTS   1110°R
(1.13)

0.282 LBM/SEC
CRV1 (37.5%)*   664 PSIA
SPIKE   1335°R 601 PSIA
(1.09)

0.0775 LBM/SEC
CRV2 (10.3%)*
STRUT L.E   205°R
NOZZLE   550°R
CROSSOVER MANIFOLD   (1.48)   570°R
INNER SHELL   920°R   522 PSIA
ΔP = 6.35 PSI

FUEL PLENUM   1220°R

0.379 LBM/SEC
DUMP PLENUM   1322°R   535 PSIA
FDVI
FDV2
BPV2
VENT 0.752 LBM/SEC
0.374 LBM/SEC
482 PSIA   ICV
FUEL MANIFOLD
OUTER SHELL INJECTORS   0.0 LBM/SEC
SPIKE INJECTORS   0.0 LBM/SEC

)(VENTURI
-|- ORIFICE
TURBINE FLOWMETER
⊗ CONTROL VALVE

S-67816

Figure 5.3-7. Hydrogen Coolant Schematic - High Pressure Test Condition, No Hydrogen Injection (U)

TEST 42 RUN 46 DATE 3-23-71

P_{TOTAL} = 3318 PSIA
T_{TOTAL} = 3245°R
X_{TRANS} = 2.90 IN.

DATA AVERAGED OVER 50 TO 59 SEC

*DENOTES PERCENTAGE OF TOTAL ENGINE FLOW
**DENOTES W/W_{IDEAL}

S-67817

159°R 797 PSIA
0.883 LBM/SEC (1.46)**
ΔP = 35.4 PSI

BPI
PCV

723 PSIA
ΔP = 3.62 PSI — -0.0144 LBM/SEC

194°R

0.300 LBM/SEC
CRV3 (34.0%)* 146°R 544 PSIA

LEADING EDGE
CROSSOVER TUBES
FORWARD OUTER SHELL
(1.42)**

ΔP = 14.1 PSI

1100°R

0.1086 LBM/SEC
CRV4 (12.3%)* 139°R

TRAILING EDGE
(1.21)**

1100°R

OBOM PLATE FINS

OUTERBODY OUTLET MANIFOLD 1048°R 509 PSIA

CRV5 (1.6%)*
STRUTS 1214°R
(1.13)**

0.334 LBM/SEC
CRV1 (37.8%)* 670 PSIA
SPIKE 1128°R 545 PSIA
(1.28)**

FUEL PLENUM 1087°R

0.4744 LBM/SEC

0.4086 LBM/SEC
DUMP PLENUM 1175°R 514 PSIA

FDVI
FDV2
VENT 0.535 LBM/SEC

507 PSIA
ICV
BPV2
FUEL MANIFOLD 166 PSIA

OUTER SHELL INJECTORS 1096°R 92 PSIA
0.200 LBM/SEC

SPIKE INJECTORS 1076°R 52 PSIA
0.148 LBM/SEC

0.126 LBM/SEC
CRV2 (14.3%)*
STRUT L.E. 186°R
NOZZLE
CROSSOVER MANIFOLD 460°R
(2.41)**
INNER SHELL 744°R 516 PSIA

)(VENTURI
—|— ORIFICE
TURBINE FLOWMETER
⊗ CONTROL VALVE

Figure 5.3-8. Hydrogen Coolant Schematic - High Pressure Test Condition, With Hydrogen Injection (U)

into the hot gas stream and one without) at the thermal cycle test condition (1380 psia, 2700°R tunnel reservoir total conditions), and the maximum tunnel test condition (3300 psia, 3400°R). Included are the percentage of the total hydrogen rate to each route and the W/W_{IDEAL} as defined above. The hydrogen rate percentages to the aft routes (innerbody and trailing edge) were 1.3 to 3.9 percent of total for the thermal cycling test condition and were increased to 10.3 to 14.3 percent for the maximum tunnel condition. As indicated by the W/W_{IDEAL} ratios in Figures 5.3-5 and 5.3-6, all flow routes except the leading edge were undercooled for the thermal cycling test condition. Though the aft routes were undercooled, their hydrogen outlet temperatures did not exceed 1600°R. The hot gas and tunnel conditions were such that the aft route hydrogen temperatures had not reached steady state after 67 sec (Test 42, Run 34) and 59 sec (Test 42, Run 36) in the tunnel. The innerbody, strut sides, and trailing edge hydrogen conditions in Figures 5.3-5 and 5.3-6 are averages of the transient data over the last 10 sec of in-tunnel test time. The spike and leading edge data in Figures 5.3-5 and 5.3-6 and all data in Figures 5.3-7 and 5.3-8 are essentially steady-state data. The transient responses of the flow routes are discussed in Section 5.4.

Outlet coolant hydrogen was injected into the hot gas stream through the first stage spike and outer shell injectors, as shown in Figures 5.3-6 and 5.3-8. The amount of hydrogen injection was controlled by the injection control valve (ICV). As the ICV was opened, the fuel dump valves (FDV's) automatically compensated to maintain an approximately constant coolant flow rate. A comparison of Figure 5.3-5 with Figure 5.3-6, or Figure 5.3-7 with Figure 5.3-8 indicates that the injection circuit operated successfully without affecting the flow conditions in the coolant flow routes. The injection rates shown in Figures 5.3-6 and 5.3-8 are 40 to 63 percent of the total coolant flow. For most of the other thermal cycle test runs, all of the coolant was injected in the hot gas stream with no adverse effects to the coolant system. As shown in Figures 5.3-6 and 5.3-8, 42.5 percent of the injected hydrogen flowed through the spike injectors while the remainder flowed through the outer shell injectors. The design objective was a 50-50 split. The injection flow distribution is presently controlled by flow-restricting orifices in the outer shell injection lines since the line pressure drop from the fuel distribution manifold to the spike injectors is greater than to the outer shell injectors. By resizing of these orifices, (reducing diameter), the design split could be readily obtained.

5.3.3.2.2 Flow Route Pressure Drop

The measurement of flow route hydrogen pressures, temperatures, and flow rates during SAM testing allowed an evaluation of hydrogen pressure drop with respect to the component pressure drop results obtained with isothermal air flow. The hydrogen data is presented as the product of component static pressure drop and average density, versus component flow rate. Results are compared with the isothermal air pressure drop results from Reference 5-6 for the spike, (Figure 5.3-9), inner shell (Figure 5.3-10), leading edge (Figure 5.3-11), forward outer shell (Figure 5.3-12) and aft outer shell (aft support to outerbody outlet manifold in Figure 5.3-13). In the case of the spike, subtraction of the inlet tube $\rho\Delta P$ from the air data makes the data equivalent.
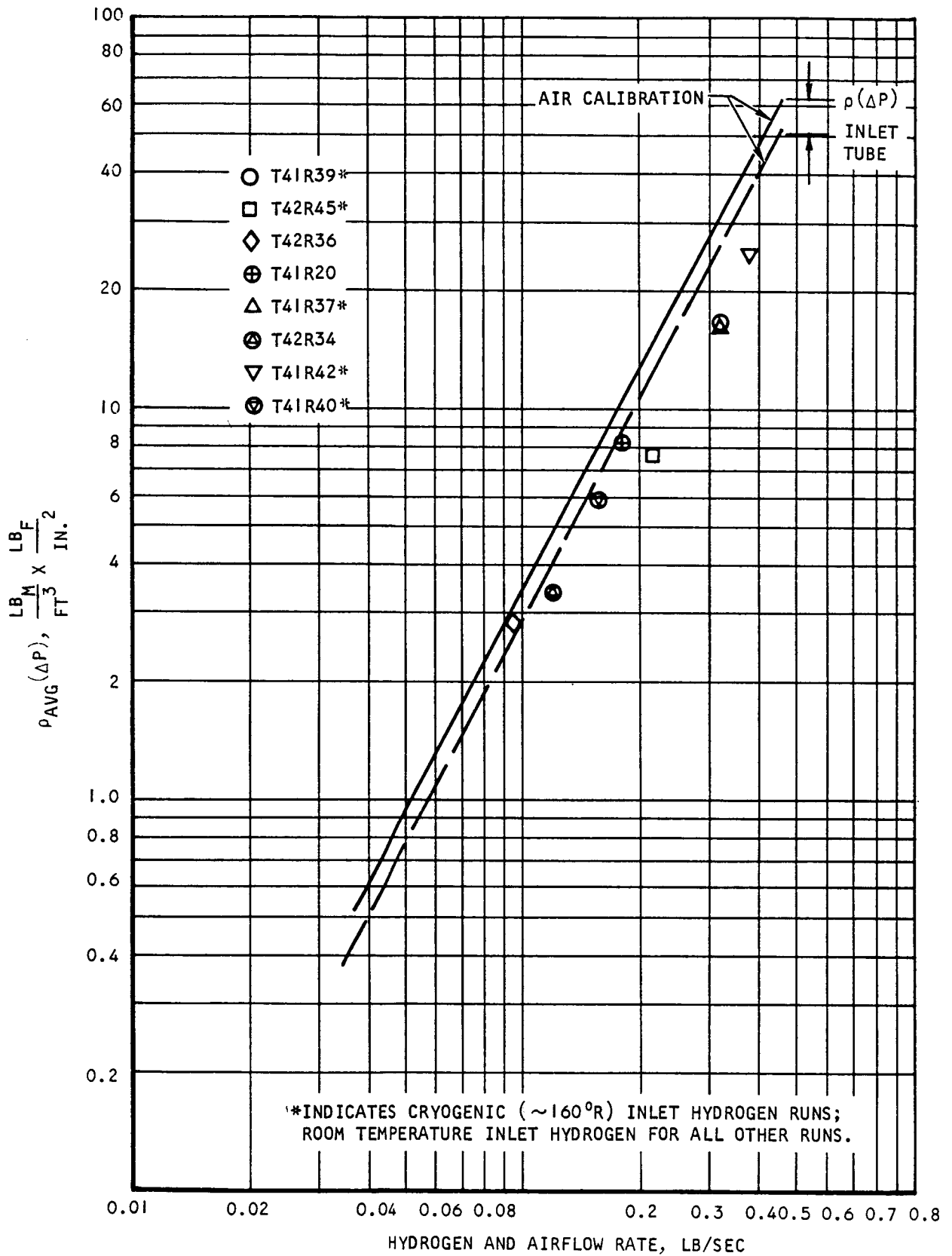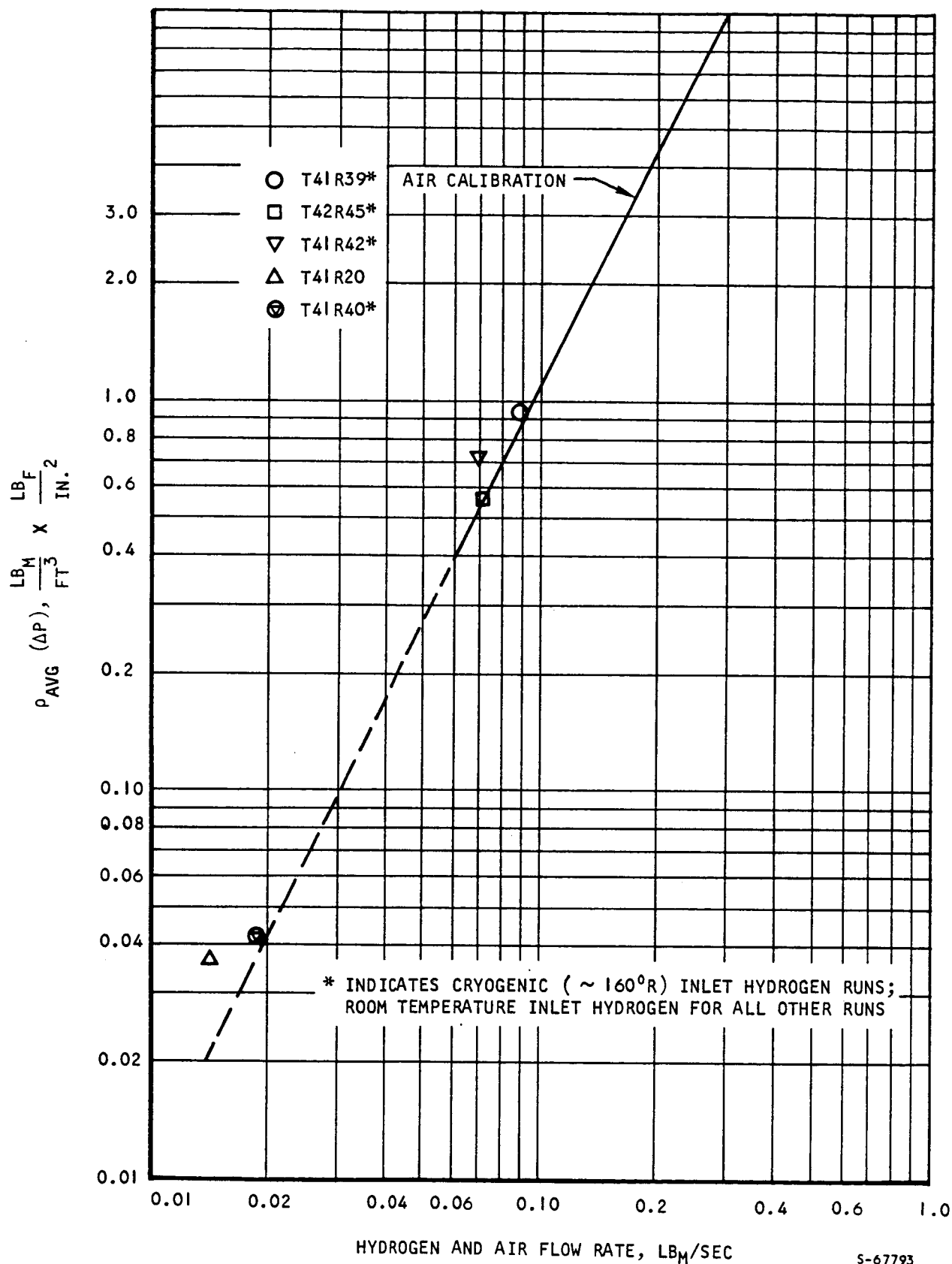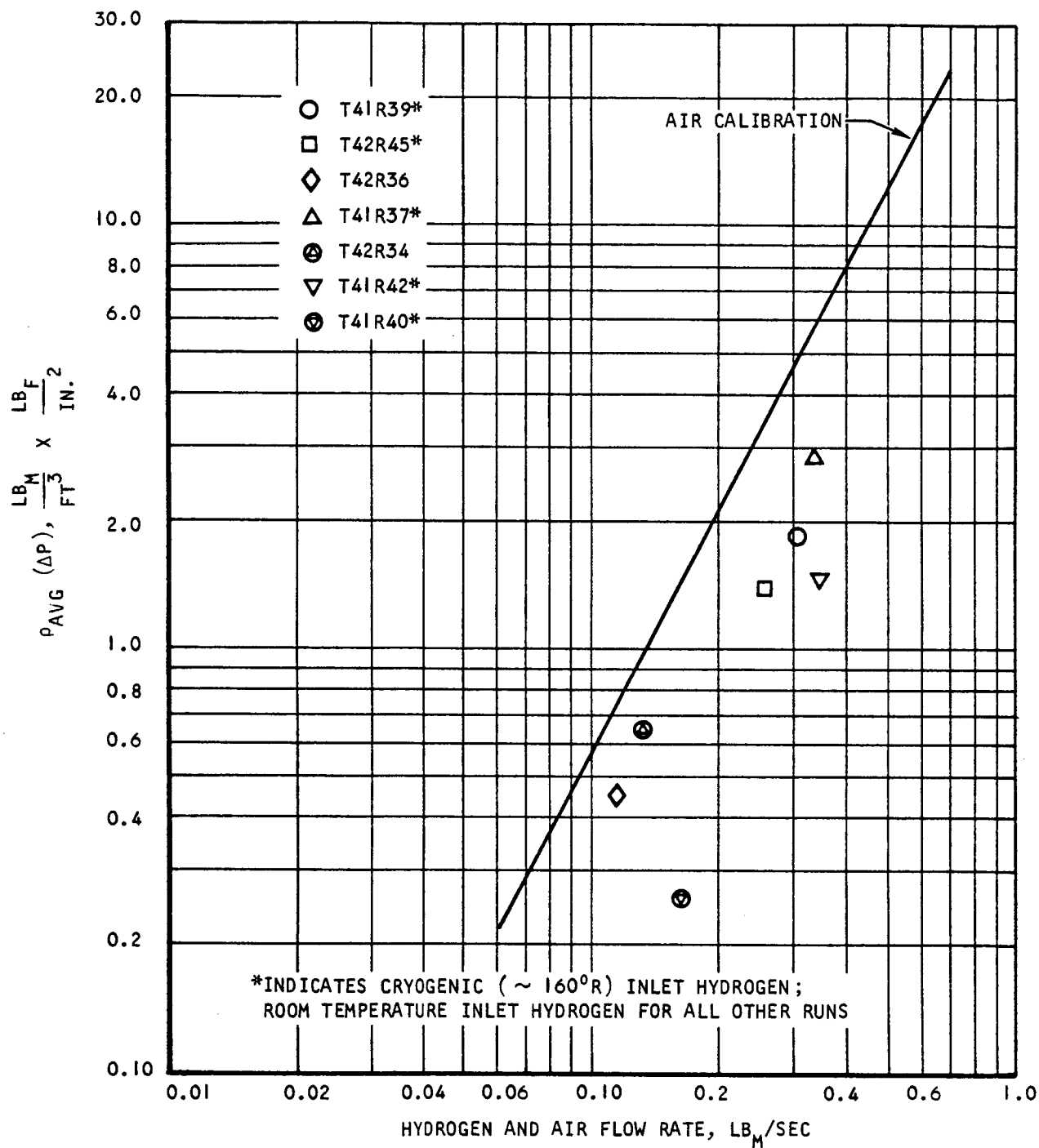
Figure 5.3-9. Spike Hydrogen Pressure-Drop Test Results (U)

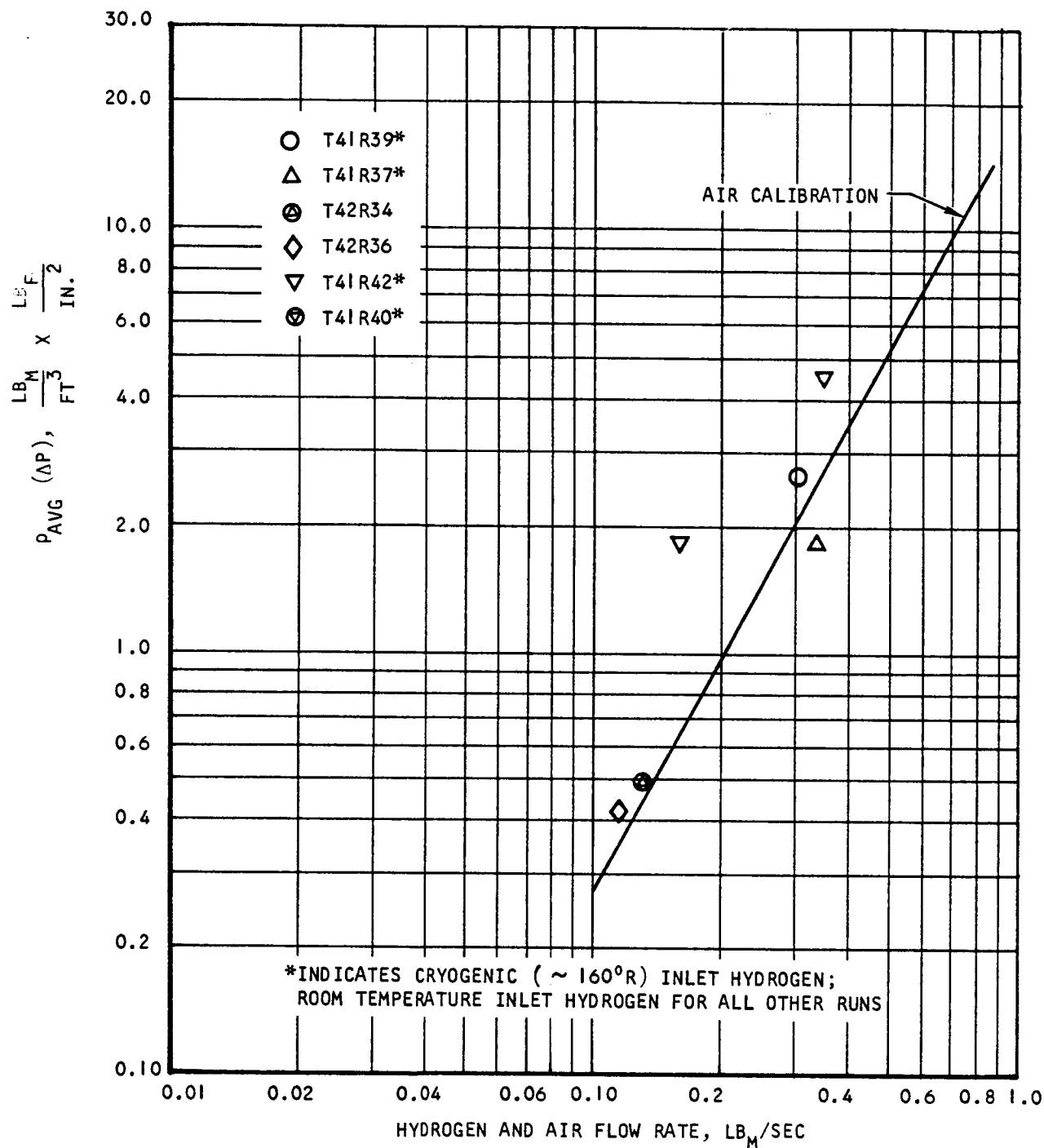Figure 5.3-10. Inner Shell Hydrogen Pressure-Drop Test Results (U)

AIRESEARCH MANUFACTURING COMPANY
Los Angeles, California

Figure 5.3-11. Leading Edge Hydrogen Pressure-Drop Test Results (U)

S-67790
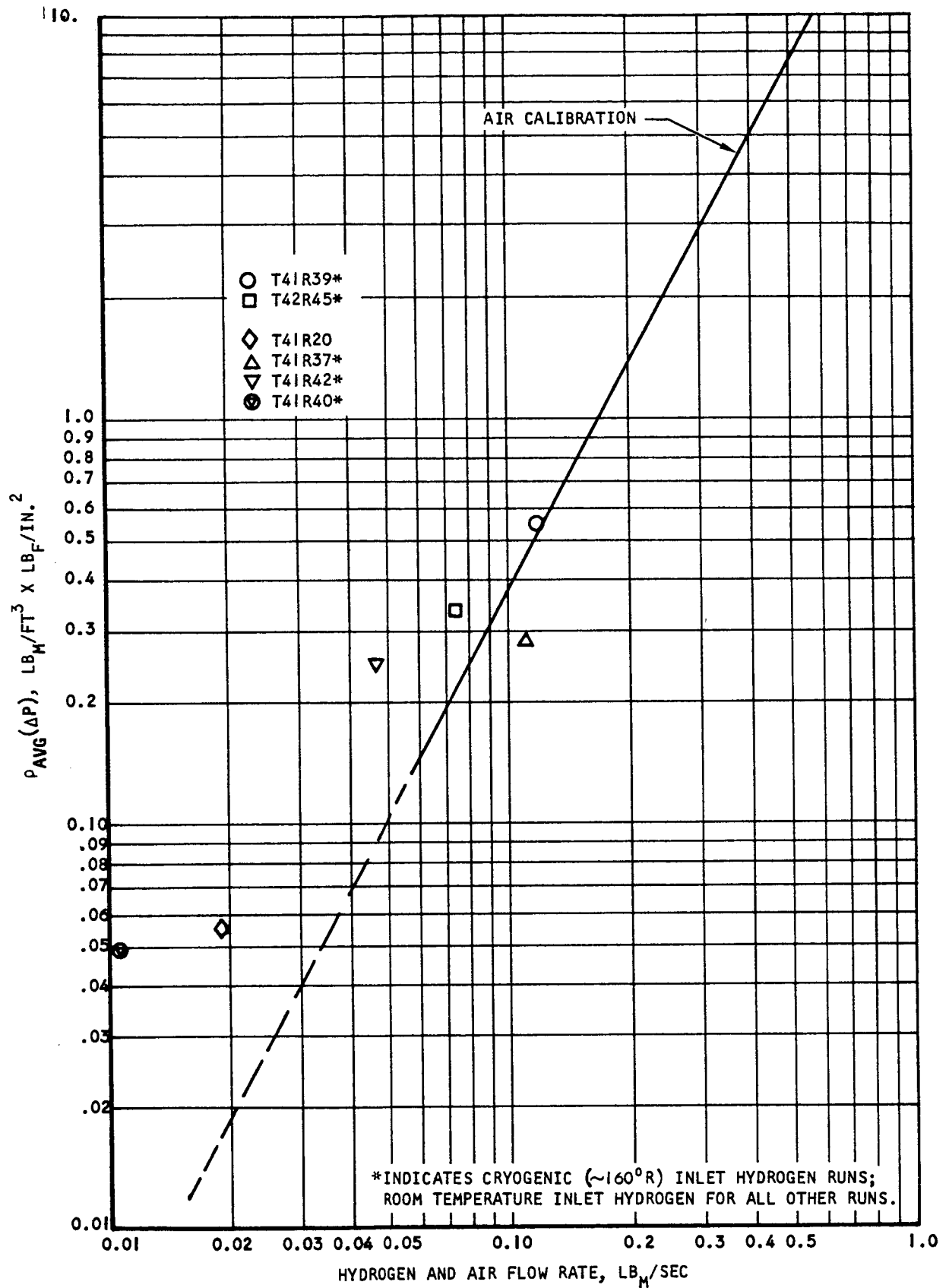
Figure 5.3-12. Forward Outer Shell Hydrogen Pressure-Drop Test Results(U)

S-67792

110.

AIR CALIBRATION

○ T41R39*
□ T42R45*

◇ T41R20
△ T41R37*
▽ T41R42*
◉ T41R40*

$\rho_{AVG}(\Delta P)$, $LB_M/FT^3 \times LB_F/IN.^2$

1.0
0.9
0.8
0.7
0.6
0.5
0.4
0.3
0.2

0.10
.09
.08
.07
.06
.05
.04
.03
.02
0.01

*INDICATES CRYOGENIC (~160°R) INLET HYDROGEN RUNS;
ROOM TEMPERATURE INLET HYDROGEN FOR ALL OTHER RUNS.

0.01   0.02   0.03 0.04 0.05   0.10   0.2   0.3 0.4 0.5   1.0

HYDROGEN AND AIR FLOW RATE, LB_M/SEC

S-67808

Figure 5.3-13.   Aft Outer Shell Hydrogen Pressure-Drop Test Results (U)

GARRETT AIRESEARCH MANUFACTURING COMPANY
Los Angeles, California

The nozzle pressure drop could not be evaluated because the measured inlet pressure, P96, was consistently reading lower than the outlet pressure, P89. Since the nozzle pressure drop was estimated at less than 2 psi for all SAM tests and the uncertainty of the individual pressure transducers is approximately ±5 psia (Reference 5-2), it was expected that the nozzle pressures would be unreliable for this purpose. The inner shell had an equally low pressure drop during SAM tests. Since the pressure drop here was considered more critical, it was more reliably measured with a pressure differential gage, ΔP4. The trailing edge pressure drop (inlet to aft support manifold) could not be evaluated because the hydrogen inlet pressure, P56, became inoperative early in the test program. There were no hydrogen pressure transducers at the inlet and outlet of the strut sides.

In general, the comparison of the hydrogen pressure drop results with the isothermal air results is only fair. The maximum hydrogen flow rates during SAM testing were, at most, only one-half of the design hydrogen flow rates at the Mach 8 flight condition. This produced flow route pressure drops that were equal to or less than one-fourth of the design pressure drops. The accuracy of these lower pressure drop results was affected by the measurement uncertainty of the inlet and outlet pressure transducers of approximately ±5 psi each, as mentioned above. During most test runs, the hydrogen flow rates and pressures fluctuated and the outlet hydrogen temperature did not reach steady state, so the results are further affected by these non-steady conditions. The test results in Figures 5.3-9 to 5.3-12 were based on time-averaged pressures, temperatures, and flow rates. In contrast, the isothermal air test data points were recorded after steady state had been reached for several minutes, and in most cases the data points were repeated. Thus, the hydrogen test results presented herein should not be considered as design performance data but as confirmation of the air test results which were performed under more exacting test conditions.

The difference in viscosity between hydrogen and air is a minor effect in the density-adjusted pressure drops for SAM test results and air calibration. The pressure drops in Figures 5.3-9 to 5.3-13 include inlet and outlet manifolding pressure drops of from zero percent (aft outer shell) to 32 percent (spike) which are independent of viscosity (or Reynolds number). The remaining frictional pressure drop in the fins is mildly viscosity-dependent. Specifically, the difference in friction factors resulting from the hydrogen and air viscosity difference at equal flow rates is less than 5 percent, with the hydrogen friction factor being lower. The resolution of the SAM test data is not fine enough to distinguish small percentage differences such as these.

5.3.3.2.3 Hydrogen Flow Distribution

The hydrogen distribution between the engine flow routes was discussed in Section 5.3.3.2.1. This section deals with the hydrogen flow distribution within each flow route. The flow distribution parameter W_{MAX}/W_{MIN} (maximum local flow rate at a circumferential location, divided by minimum local flow rate at another circumferential location) is a measure of the flow uniformity around the flow route circumference. It is generally desirable to have a uniform flow distribution ($W_{MAX}/W_{MIN} = 1.00$) so that one angular location of a

flow route is not coolant-starved while another location is overcooled. In flight application the coolant-starved location would dictate the coolant requirements for the flow route.

The flow route coolant distribution was estimated from the coolant control and coolant inlet thermocouple data during SAM testing. Data for up to six coolant control thermocouples per flow route were recorded for each test run. The flow distribution was estimated from the ratio at different angular locations of minimum (coolant control-to-inlet) ΔT_c and maximum ΔT_c:

$$\frac{W_{MAX}}{W_{MIN}} = \frac{\Delta T_c \text{ (Maximum recorded)}}{\Delta T_c \text{ (Minimum recorded)}}$$

Estimates obtained from this relation reflect the temperature distribution and, therefore, will also include the effects of differences in hot gas heating between the two strips of flow route where the two ΔT_c's are recorded. For example, circumferential variations in hot gas static pressure were observed on the spike and leading edge flow routes. On the spike, the maximum recorded circumferential pressure for most tests occurs in the same circumferential vicinity (180 deg clockwise looking aft (CWLA)) as one of the higher coolant control thermocouple readings (210 deg CWLA). This correspondence suggests a heating maldistribution more than a cooling maldistribution. Furthermore, the hot gas heating on the innerbody and trailing edge flow routes was circumferentially non-uniform due to the presence of the struts, as discussed in Section 5.2.3.2. The hot gas heating was definitely unsymmetrical during the 3-deg angle-of-attack test runs (Test 41, Runs 51, 52, and 53). Thus, correct interpretation of the flow distribution parameter W_{MAX}/W_{MIN}, as defined herein, must also consider the effects of hot gas heating maldistribution.

The circumferential temperature distribution of the six spike coolant control thermocouples (T28 to T33) is shown in Figure 5.3-14. The data is from the steady-state portion of Test 42, Run 45 (2250 psia, 3000°R tunnel reservoir total conditions). Included are the hydrogen inlet and outlet temperatures, T119 and T26, respectively. The coolant control thermocouples are located in the return half of the spike folded-flow section at axial Station 49.0 so the coolant control thermocouple readings were expected to be higher than the coolant outlet temperature at axial Station 46.0. The maximum recorded difference is 149°R and occurs between T29 (1343°R) at 90 deg CWLA and T33 (1234°R) at 330 deg. T28 at 30 deg is only slightly higher than T33 at 1236°R. Based on T29, T33, and the inlet temperature, T119, the W_{MAX}/W_{MIN} for the spike is 1.10. This pattern of coolant control temperature distribution was typical for several other test runs surveyed. Because of this temperature maldistribution, the cold wall temperatures, T17 and T23, were adjusted to indicate average circumferential values for heat load calculations. Temperatures T17 and T23 are at 355 and 5 deg respectively, as shown in Figure 5.3-14, and are angularly between coolant control thermocouples T28 (1236°R) and T33 (1234°F). These cold wall temperatures are adjusted upward by scaling them by the same temperature difference ratio as the (local coolant control-minus-inlet)-to-(average coolant control-minus-inlet) temperature-difference ratio. The arithmetic and the adjusted

$$\frac{W_{MAX}}{W_{MIN}} = \frac{T29 - T119}{T33 - T119} = \frac{1343 - 144}{1234 - 144} = 1.10$$

COLD WALL TEMPERATURES ADJUSTED FOR COOLANT MALDISTRIBUTION

$$T23' = T119 + \frac{T_{AVG} - T119}{T33 - T119} \cdot (T23 - T119) = 144 + \frac{1284 - 144}{1234 - 144}(746 - 144) = 773°R$$

$$T17' = T119 + \frac{T_{AVG} - T119}{T33 - T119} \cdot (T17 - T119) = 144 + \frac{1284 - 144}{1234 - 144}(339 - 148) = 348°R$$
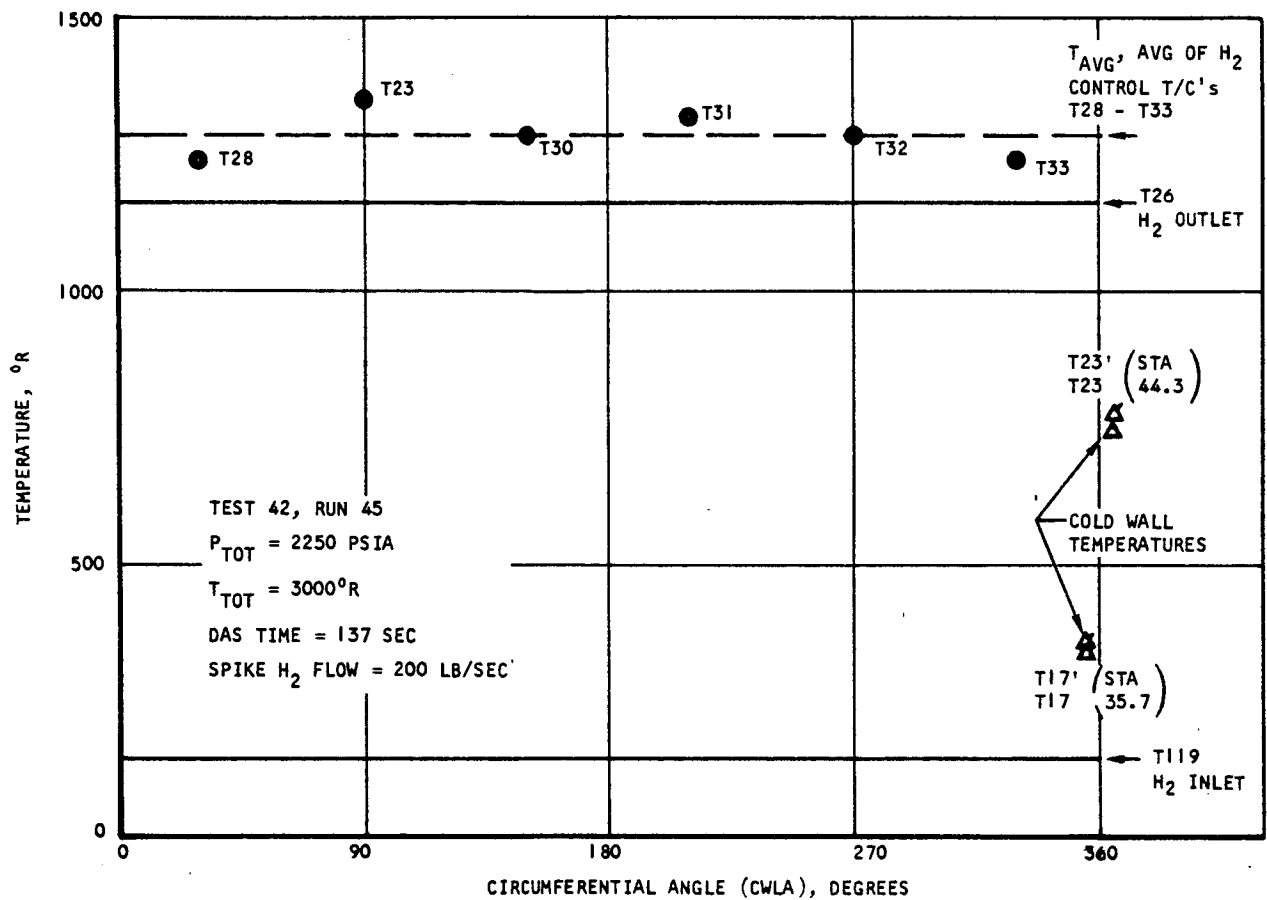

Figure 5.3-14. Spike Coolant Flow Distribution (U)

temperatures T17' and T23' are indicated in Figure 5.3-14. As discussed in Section 5.2.2.2, these (adjusted) cold wall thermocouple readings are nearly equal to the local coolant temperature in the plate-fin passages and were used to calculate intermediate heat loads on the spike.

The innerbody hydrogen temperatures are presented in Figure 5.3-15 as a function of circumferential angle for the steady-state portion of Test 41, Run 39 (3320 psia, 3400°R tunnel reservoir total conditions). The coolant control thermocouples (T36, T38, T40, and T41) are located downstream (in the hydrogen flow direction) of the struts at axial Station 52.0 (reference coordinates). Each is directly in line with a strut, circumferentially, and the hot skin above the control thermocouples is shaded from the hot gas by the overlapping portion of the spike. The control thermocouples were placed in line with the struts to monitor local coolant deficiencies due to possible flow blockage effects of the strut cutouts. The test results in Figure 5.3-15 indicate that the provisions made to compensate for this blockage provided at least adequate flow along the strut cutouts, since the average of the coolant control temperatures (915°R) is 245°R lower than the average outlet temperature (1160°R). Conversely, the local coolant outlet temperatures between the struts must have been higher than 1160°R. The outlet temperature distribution and the coolant flow distribution between the struts would be difficult to estimate because there are no local coolant thermocouples in this region and the hot gas heating is non-uniform between struts. An outlet temperature distribution was constructed for the trailing edge route from coolant and structural temperature measurements between the struts, as discussed below. Because the cooling design (plain flow channels between fins and header) and the hot gas heating patterns of the inner and outer shells are similar, the inner shell outlet temperature distribution is likely similar to that on the outer shell.

The hydrogen temperatures for the leading edge flow route are shown in Figure 5.3-16 for Test 41, Run 39 (3320 psia, 3400°R tunnel reservoir total conditions). Thermocouples T70, T72, and T75 are the available coolant control monitors at axial Station 50.4 (reference coordinates). The maximum difference in these thermocouples is 70°R and occurs between T72 (1245°R) at 150 deg (CWLA) and T75 (1170°R) at 330 deg. The W_{MAX}/W_{MIN} is 1.07 and is based on these available thermocouples and the inlet, T6, at 160°R. Also shown in Figure 5.3-16 are the hydrogen temperatures at the leading edge (T11) and forward outer shell side (T60) of the crossover manifold. These temperatures indicate that the flow distribution in the leading edge component alone is good since T11 (180 deg on the leading edge side) and T60 (354 deg on the outer shell side) are approximately equal. The possibility does exist for coolant maldistribution to occur in the leading edge route and be undetected by T70, T72, and T75 because there is an opportunity for unrestricted coolant crossflow in two halves of the crossover manifold. However, observed metal discoloration on the internal leading edge surface after the thermal cycling runs appeared circumferentially uniform, as discussed in Section 5.1.2, and indicate qualitatively that the leading edge coolant flow distribution was uniform.
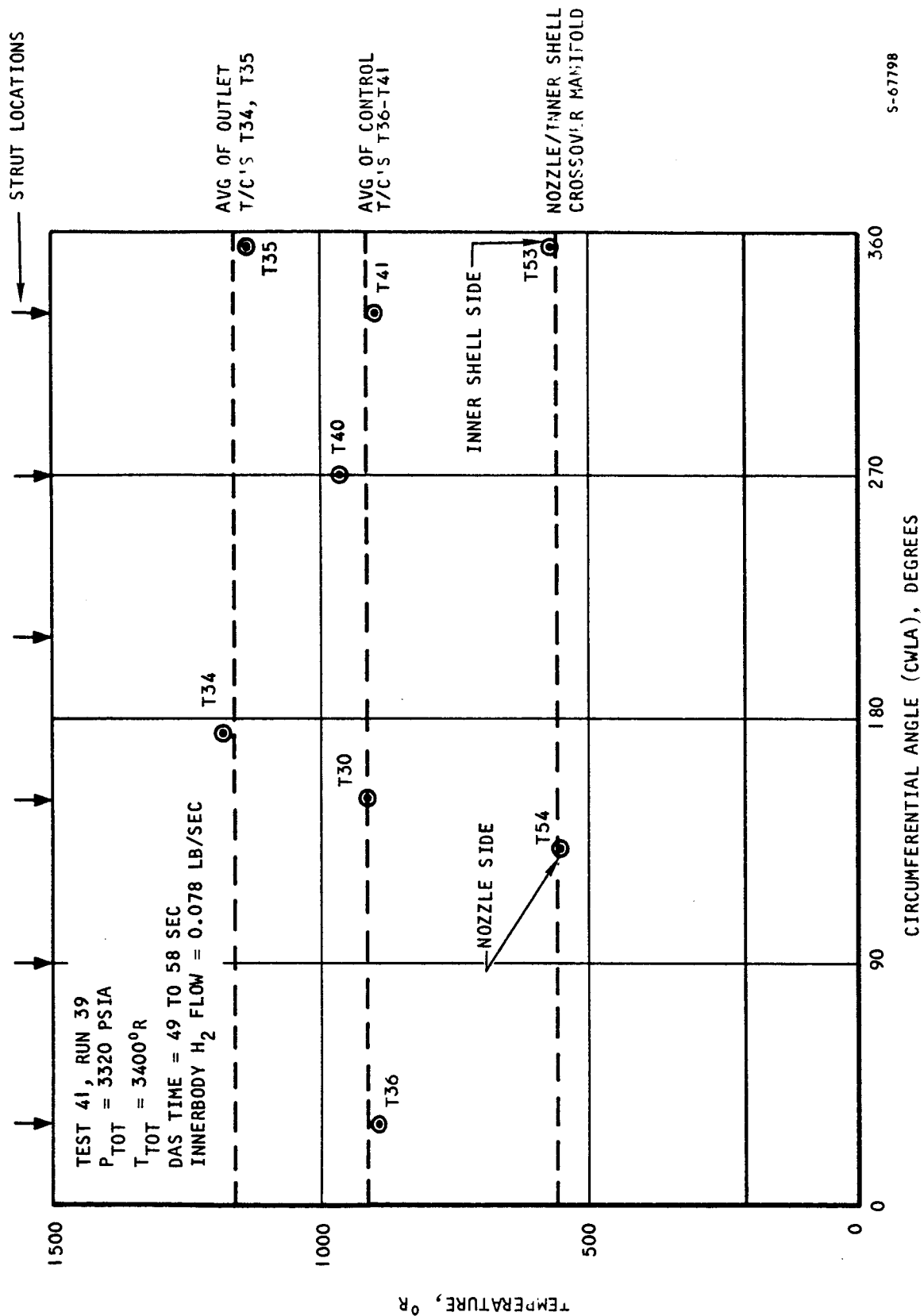
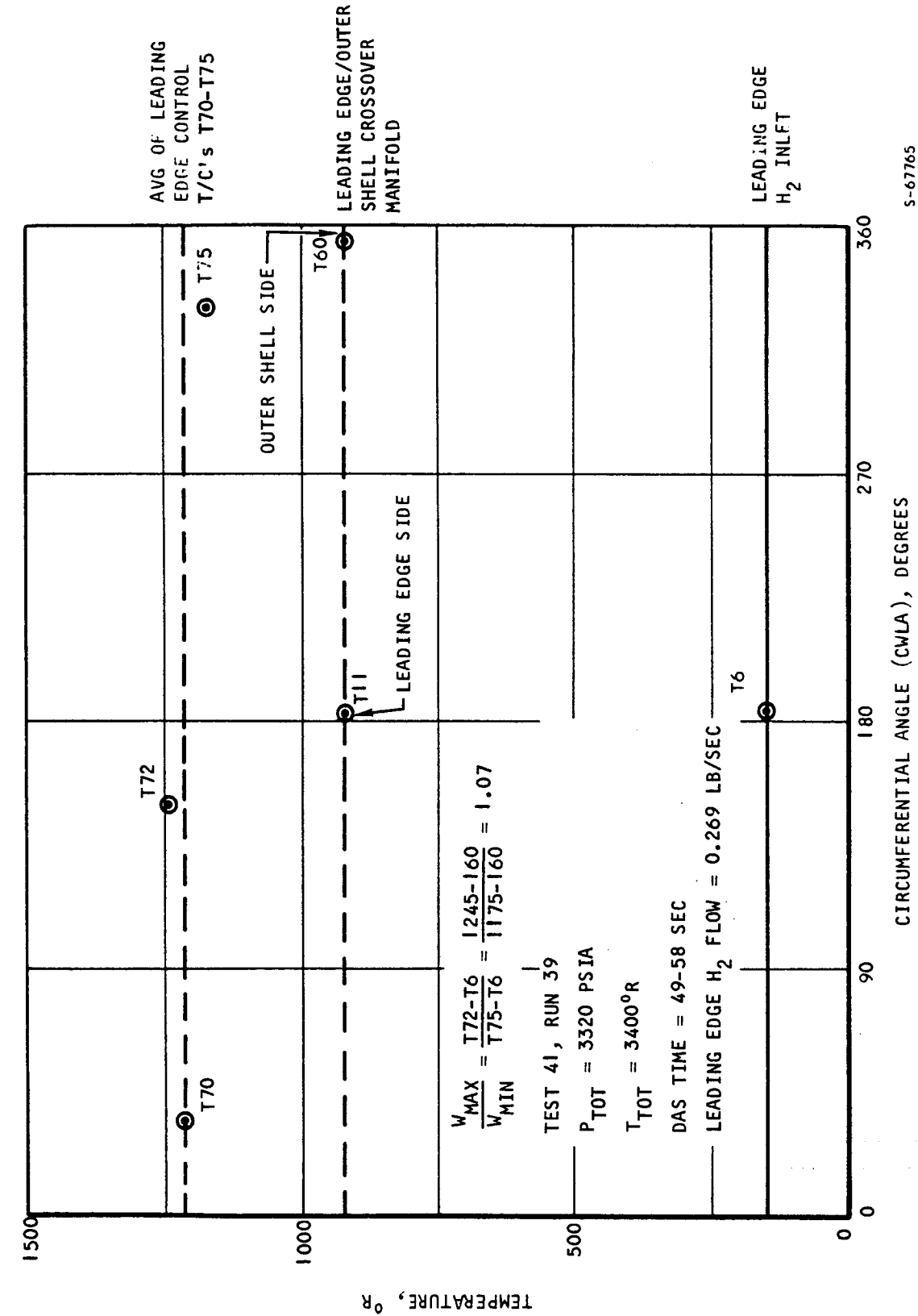Figure 5.3-15. Innerbody Coolant Temperature Distribution (U)

S-67798

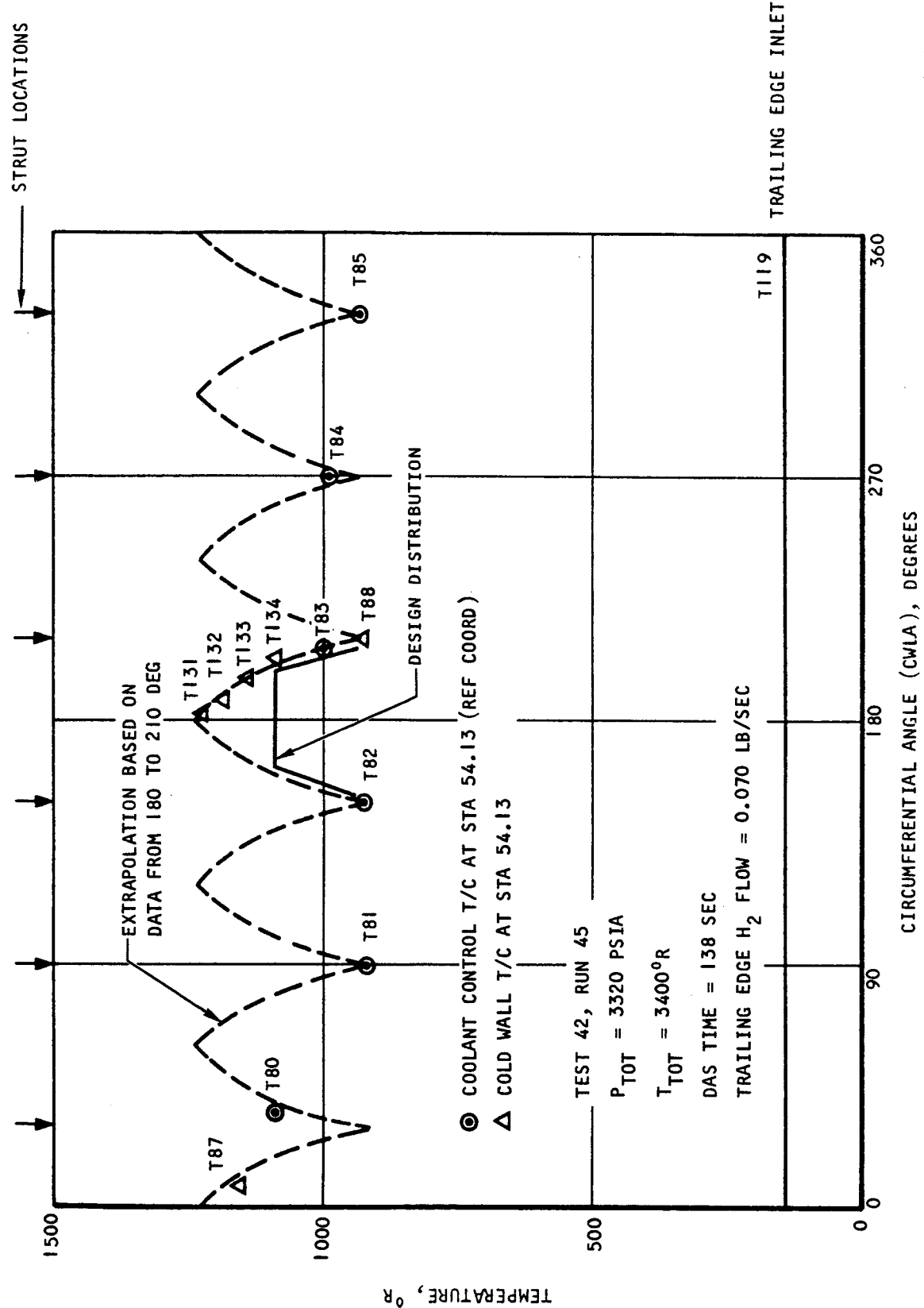Figure 5.3-16. Leading Edge Coolant Temperature Distribution (U)

AVG OF LEADING
EDGE CONTROL
T/C's T70-T75

LEADING EDGE/OUTER
SHELL CROSSOVER
MANIFOLD

LEADING EDGE
H₂ INLET

T75

OUTER SHELL SIDE

T60

T11

LEADING EDGE SIDE

T72

T70

T6

$$\frac{W_{MAX}}{W_{MIN}} = \frac{T72-T6}{T75-T6} = \frac{1245-160}{1175-160} = 1.07$$

TEST 41, RUN 39

$P_{TOT} = 3320$ PSIA

$T_{TOT} = 3400°R$

DAS TIME = 49-58 SEC

LEADING EDGE H₂ FLOW = 0.269 LB/SEC

CIRCUMFERENTIAL ANGLE (CWLA), DEGREES

TEMPERATURE, °R

0   90   180   270   360

0   500   1000   1500

S-67765

71-7702
Page 5-90

The structural cold wall and hydrogen coolant temperature profile at axial Station 54.13 (reference coordinates) on the trailing edge flow route is shown in Figure 5.3-17. The triangular points are measured steady-state structure temperatures and the circular points are measured coolant temperatures for Test 42, Run 45 (2250 psia, $3000^{\circ}R$ tunnel reservoir total conditions). At steady state, adjacent coolant and structure temperatures are within 5° to $10^{\circ}R$ of each other so the data points between 180 and 210 deg approximate the coolant temperature distribution near the trailing edge outlet. This distribution represents a stratification of $300^{\circ}R$ from midway between struts, at 180 deg, to strut centerline at 210 deg, and indicates coolant maldistribution. The curve drawn through the data points between 180 and 210 deg was repeated in a symmetrical pattern between the other struts as shown in Figure 5.3-17. With minor exception the other coolant and structural temperature data points (T80, T81, T82, T84, T85, and T87) agree favorably with the extrapolated curves indicating that the coolant distribution between other struts is similar to that between 180 and 210 deg. From an inspection of Figure 5.3-17, T80 is an approximate average of the detailed distribution between 180 and 210 deg. Because T131 through T134 were recorded for Test Group 42 runs only, T80 was used apriori as the average trailing edge outlet temperature for heat load calculations as discussed in Section 5.2.2.2. As seen, an arithmetic average of T80 through T85 would bias the average outlet temperature on the low side.

The stratification in coolant temperature between 302 deg ($1080^{\circ}R$) and 210 deg ($920^{\circ}R$) was expected, because provision was made in the outer shell (as well as the inner shell) design so that locally higher amounts of hydrogen could flow along the periphery of the strut cutouts. The coolant temperature profile from 180 deg ($1220^{\circ}R$) to 202 deg ($1080^{\circ}R$) was expected to be constant at the value of 202 deg. For circumferentially uniform heating conditions the coolant temperature stratification from 180 to 202 deg could be attributed to flow maldistribution alone. However, from posttest observations of outer shell metal discoloration (Figure 5.1-4, for example) and aerodynamic considerations (Section 5.2.3.2), it appears that the area between the struts was subjected to local high heating. In addition, the local high heating was non-uniform between the struts.

The coolant/heating maldistribution is also evident on the hot surface as observed from metal discoloration patterns near the coolant outlet holes. Subsequent to Test 41, Run 40 (2290 psia, $3000^{\circ}R$ tunnel reservoir total conditions), brown streaks in a blue field were observed near the outlet holes and circumferentially located midway between each of the six struts (shown in Figure 5.3-18). These streaks in the hot surface were produced from a locally higher coolant temperature at 180 deg rather than locally higher heating near the outlet holes because (1) the hot gas flow is symmetrical at this location (upstream of the struts in the hot gas stream), and (2) the hot surface on the leading edge side of the outlet holes was uniformly discolored brown.

The expected unsymmetrical heating of the engine flow routes was detected by the coolant control thermocouples during the 3-deg angle-of-attack runs, Test 41, Runs 51, 52, and 53. Physically, SAM centerline was pitched 3-deg downward with respect to the tunnel centerline, so that circumferentially, zero deg corresponded to the low-pressure side and 180 deg corresponded to the high-pressure side. The tunnel total pressure corresponded to the maximum heating
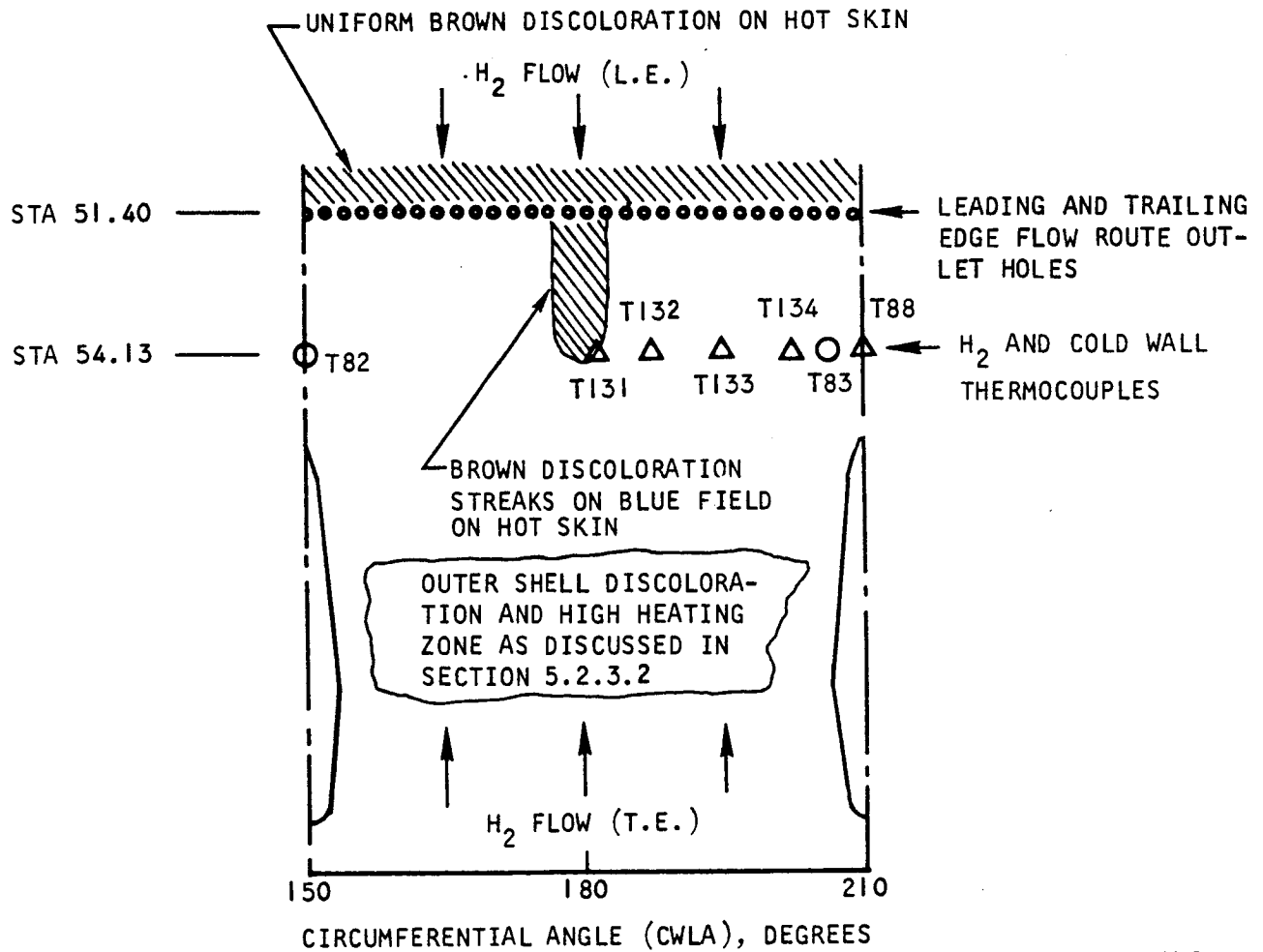
Figure 5.3-17. Trailing Edge Coolant Temperature Distribution (U)

S-67794

GARRETT AIRESEARCH MANUFACTURING COMPANY
Los Angeles, California

Figure 5.3-18. Trailing Edge Coolant
Flow Distribution

T = CONTROL THERMOCOUPLE TEMPERATURE

T_{IN} = INLET HYDROGEN TEMPERATURE

T_{AVG} = ARITHMETICAL AVERAGE OF RECORDED CONTROL THERMO-COUPLES

▽ T41R51
○ T41R52
□ T41R53
◆ T42R45
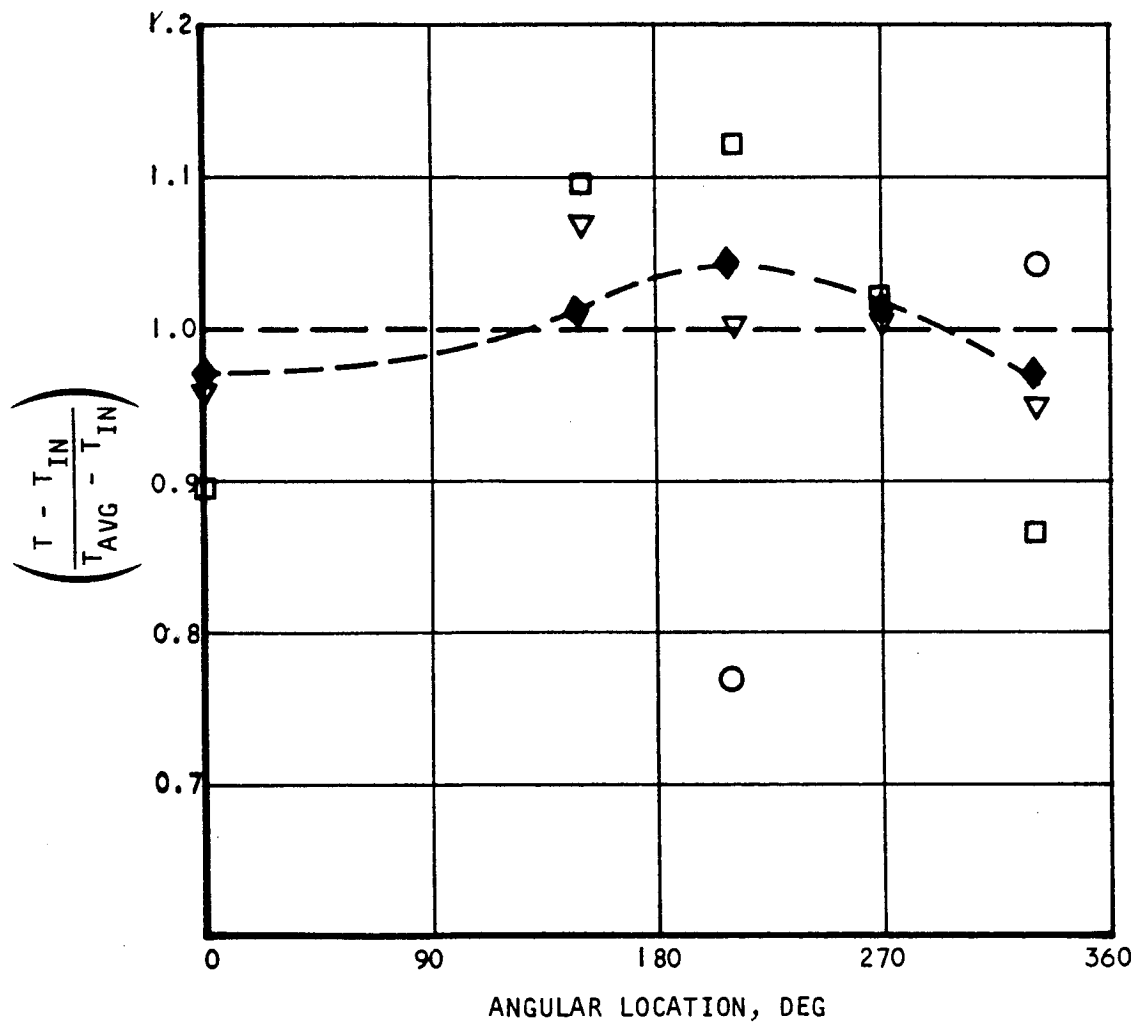
S-67779

Figure 5.3-19. Spike Control Thermocouples for 3-Degree Angle-of-Attack Tests (U)
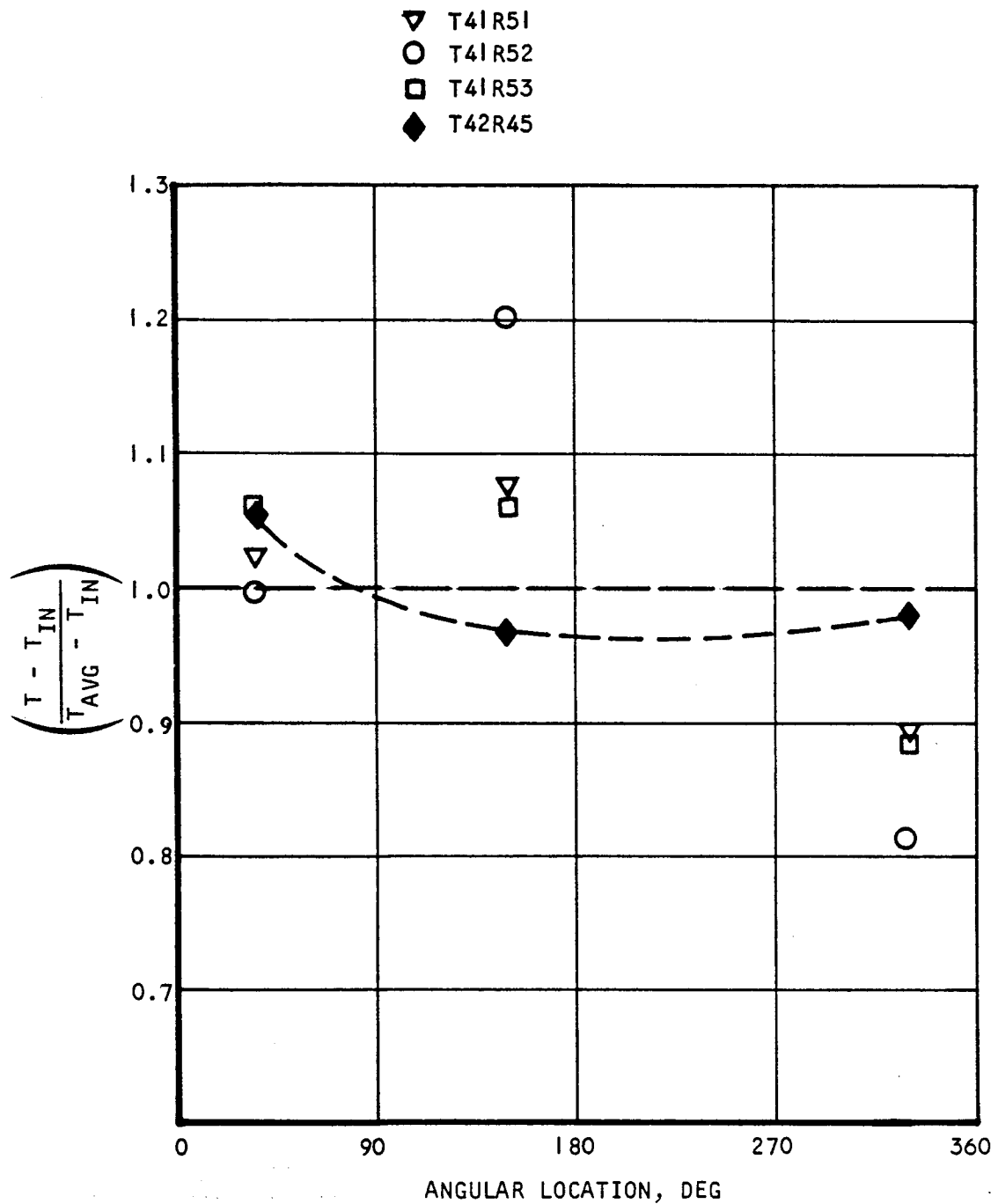
Figure 5.3-20. Leading Edge Control Thermocouples for 3-Degree Angle-of-Attack Tests (U)
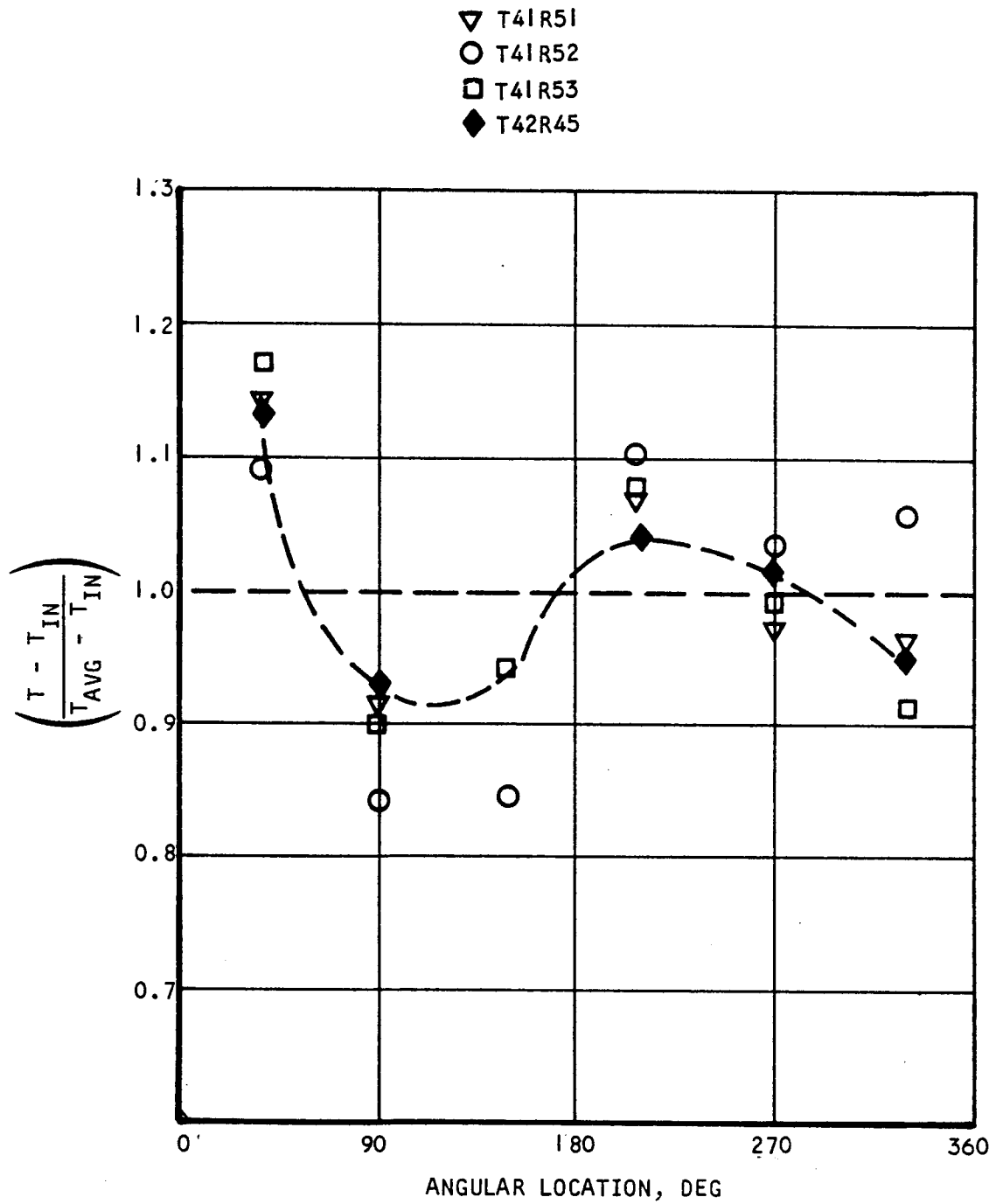
S-67778

Figure 5.3-21.   Trailing Edge Control Thermocouples for 3-Degree Angle-of-Attack Tests (U)

UNCLASSIFIED

3000°R tunnel reservoir total conditions with room temperature inlet hydrogen)
provided a basis for the data analysis for the transient behavior of hot wall
temperature and hot wall-to-structural temperature differences. Metal dis-
colorations on the nozzle and inner and outer shells were first observed dur-
ing these tests and were produced by the combined effect of locally high hot
gas heating and flow route undercooling.

5.4.3 Data Analysis and Discussion

5.4.3.1 Hydrogen Heat Loads

During the test runs, steady-state conditions (as determined by outlet
coolant temperature) were not reached simultaneously for all five flow routes.
At the low to moderate tunnel total pressures (900 to 2200 psia), for example,
the spike and leading edge flow routes reached steady state after about 20 sec
of hot gas exposure time. The innerbody, trailing edge, and strut sides did not
reach steady state after run times up to 68 sec. When hydrogen rates on the
aft routes were increased at fixed tunnel conditions, the coolant outlet tem-
peratures responded more quickly to the hot-gas heating. Correlation of the test
data and analyses has indicated two points: (1) the response time to steady
state for a flow route is independent of the heat load, and (2) the time to reach
steady state decreases with increasing coolant flow rate. These points are
illustrated below.

The transient heat load responses of the spike and innerbody flow routes
for 2200 psia, 3000°R tunnel reservoir total conditions and room temperature
inlet hydrogen coolant are shown in Figure 5.4-1. The solid lines are the
hydrogen heat loads in the routes as based on the product of flow rate and
enthalpy difference (outlet minus inlet), $(W\Delta H)_{H_2}$. These heat loads were calcu-
lated from analytical time response equations with input time constants reduced
from test data. This analytical procedure is discussed in the following section.
The dashed lines are the aerodynamic heat loads and were obtained from the hydro-
gen heat load at steady-state thermal conditions and multiplied by the hot gas
recovery-to-average wall-temperature-difference ratio, at times less than at
steady state. Hydrogen heat load responses are presented for a spike hydrogen
rate of 0.26 lb/sec and innerbody flow rates of 0.05 lb/sec and 0.01 lb/sec.
The spike flow rate of 0.26 lb/sec and innerbody flow rate of 0.05 lb/sec are the
flows required for adequate cooling at steady state; i.e., design point outlet
temperature of 1350°R in the spike and 1600°R in the innerbody. The innerbody
flow rate of 0.01 lb/sec represents a highly undercooled case of one-fifth the
required flow. During several thermal cycle runs the innerbody was undercooled
by this amount for the purpose of attaining hot wall-to-structure ΔT's as large
as those for Mach 8 flight. The responses are shown for 40-sec exposure time
in the hot gas stream which was typical for testing. The spike heat load reaches
steady state within 17 sec and the innerbody (0.05 lb/sec) reaches steady state
in 40 sec. The spike reaches steady state faster than the innerbody, not be-
cause the heat load level of the spike is higher, but because the flow rate is
higher, as indicated above. This is exemplified for the case of the undercooled
innerbody at 0.01 lb/sec. When the adequately cooled innerbody reaches steady
state at 40 sec (190 Btu/sec), the undercooled case has reached a level of

AIRESEARCH MANUFACTURING COMPANY
Los Angeles, California

UNCLASSIFIED
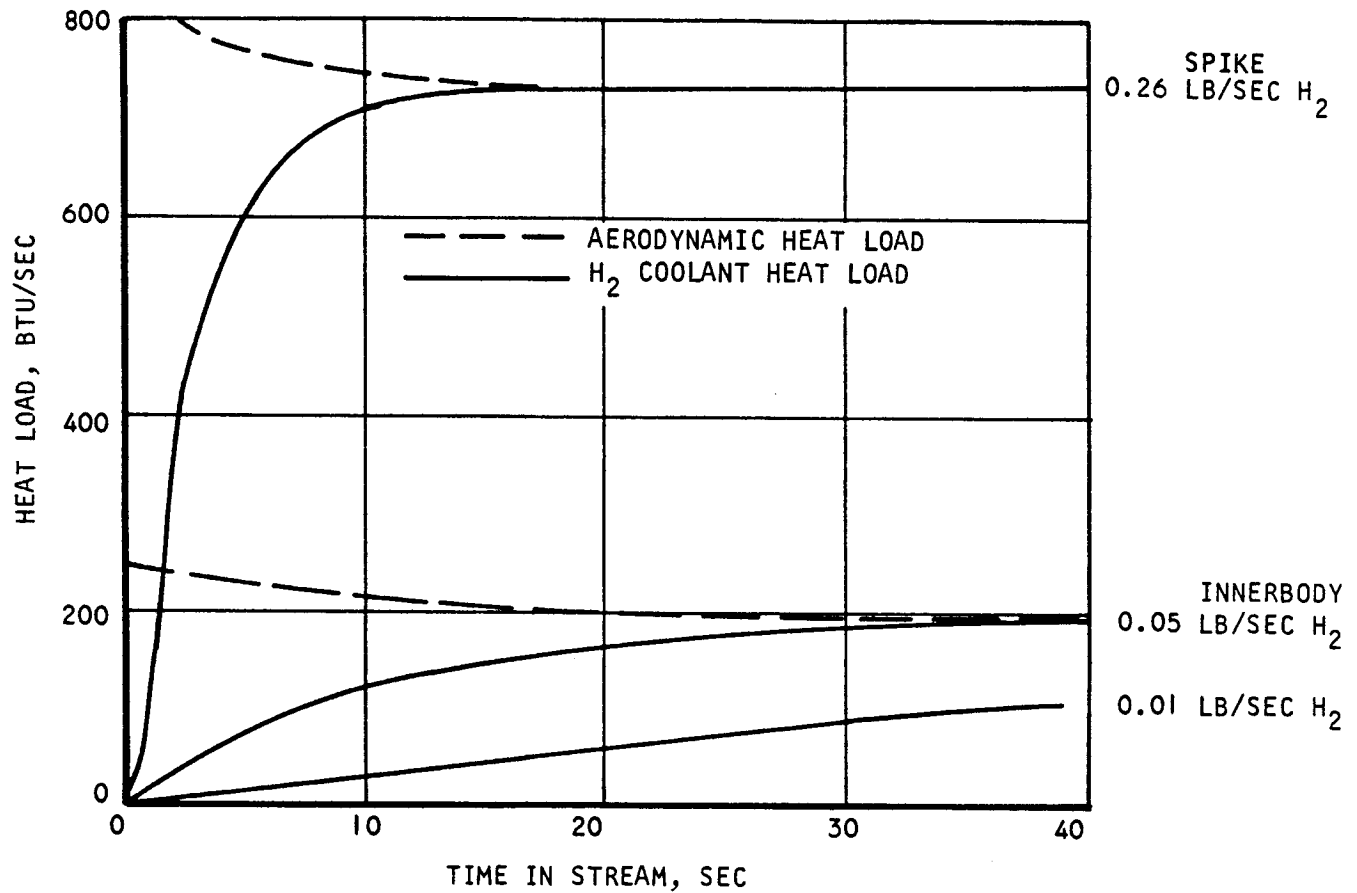
71-7702
Page 5-98

Figure 5.4-1.   Spike and Innerbody Transient Heat Loads
for 2200 psia, 3600°R Tunnel Reservoir
Total Conditions

hydrogen heat absorption of 100 Btu/sec. The time required to reach steady state for this undercooled case is estimated at 200 sec. Thus, undercooling increases the difference between the aerodynamic heat load and the hydrogen heat load and for longer periods of time during startup. This increased difference raises hot wall temperatures at a faster rate initially, and to higher steady-state temperatures after 200 sec.

5.4.3.2 Hydrogen Outlet Temperature Response

Test and analysis results indicate that the time required for the hydrogen outlet temperature to reach steady state is inversely proportional to the flow route hydrogen rate. The proportionality constant is a complicated function of the flow route coolant passage geometry and structural mass. However, a simple proportionality constant has been proposed that is dependent only on the specific heat of the hydrogen and the thermal capacitance of the flow route (structural mass times specific heat). The hydrogen outlet temperature was selected as an indicator of steady-state attainment because both test data and analysis indicate that all metal temperatures on a flow route have reached steady state before, or as the coolant outlet temperature reaches steady state.

The transient heat transfer analysis was performed on a plate-fin cooled panel structure similar in configuration to that on the SAM. The analysis was performed by thermally modeling the plates, fins, and structure of a flow route into a nodal network. Transient metal and hydrogen coolant temperature responses were calculated to steady-state conditions on a thermal analyzer computer program for several input values of hydrogen flow rate and step changes in hot gas heat load. The step change in heat load approximately simulates the engine insertion into the tunnel and spike retraction during SAM tests, and also simulates the spike retraction and onset of combustion during flight. For all the computer input cases the hydrogen outlet temperature could be described as a function of time (from the step change in hot-gas heating) by the single nodal response equation:

$$\frac{T(\theta) - T_f}{T_i - T_f} = \exp\ (-\theta/\tau)$$

where $T(\theta)$ = hydrogen outlet temperature at θ sec from the hot-gas step change

T_i = initial hydrogen outlet temperature

T_f = final hydrogen outlet temperature (at steady state)

τ = a time constant.

From an inspection of the input parameters and the geometry, the time constant

(τ) was found to be independent of the hot gas heat load and could be correlated by

$$\tau = 0.73 \frac{(MC)_{Structure}}{(\dot{W} C_p)_{H_2}}$$

where

$(MC)_{Structure}$ = thermal capacitance of flow route structure based on the total physical mass, Btu/$^{\circ}$R

$\dot{W}$ = hydrogen flow rate, lb/sec

C_p = hydrogen specific heat at constant pressure, Btu/lb$^{\circ}$R

The time constant (τ) was defined as the time required for the flow route hydrogen outlet temperature to reach 63.2 percent of the total transient change from initial (T_i) to final (T_f) values when subjected to a step change in hot gas heat load at time (θ) equal zero. The time to steady state is then approximately 4τ, or 98 percent of the total transient change.

In order to correlate the SAM test results with the above analysis, the outlet temperature data histories were reviewed and found to behave like the first order response equation, above. As an example, the spike and innerbody hydrogen outlet temperatures, T26 and T35 are shown in Figure 5.4-2 for Test 41, Run 39. For this run the engine is inserted into the tunnel and the spike retracted at 25 sec on the data acquisition time scale in Figure 5.4-2. The engine was withdrawn from the tunnel at 59 sec. The first order response of T26 (spike outlet temperature) can be seen from about 27 to 33 sec, while the first order response of T35 can be seen from about 30 to 50 sec. To calculate the time constant from these experimental temperature-time traces, the first-order response equation is differentiated with respect to time to get

$$\frac{dT}{d\theta} = \frac{T_f - T_i}{\tau} = \exp(-\theta/\tau)$$

This derivative is evaluated at any two time periods (where the first order response is valid). Dividing one derivative by the other gives

$$\frac{(dT/d\theta)_1}{(dT/d\theta)_2} = \frac{\exp(-\theta_1/\tau)}{\exp(-\theta_2/\tau)} = \exp\left(\frac{\theta_2 - \theta_1}{\tau}\right) = \exp\left(\frac{\Delta\theta}{\tau}\right)$$

Rearranging and approximating the derivatives by finite differences gives
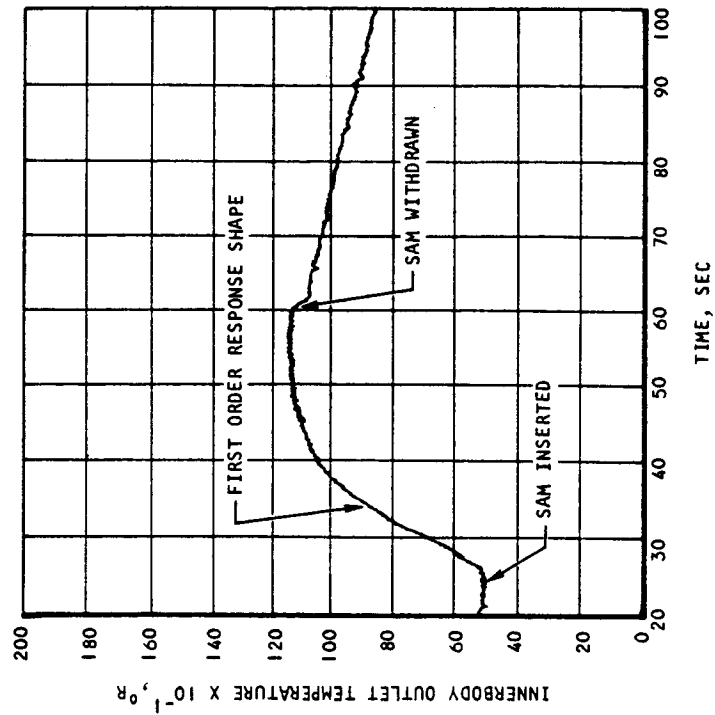
$$\tau \simeq \frac{\Delta\theta}{\ln\left\{\frac{(\Delta T/\Delta\theta)_1}{(\Delta T/\Delta\theta)_2}\right\}}$$
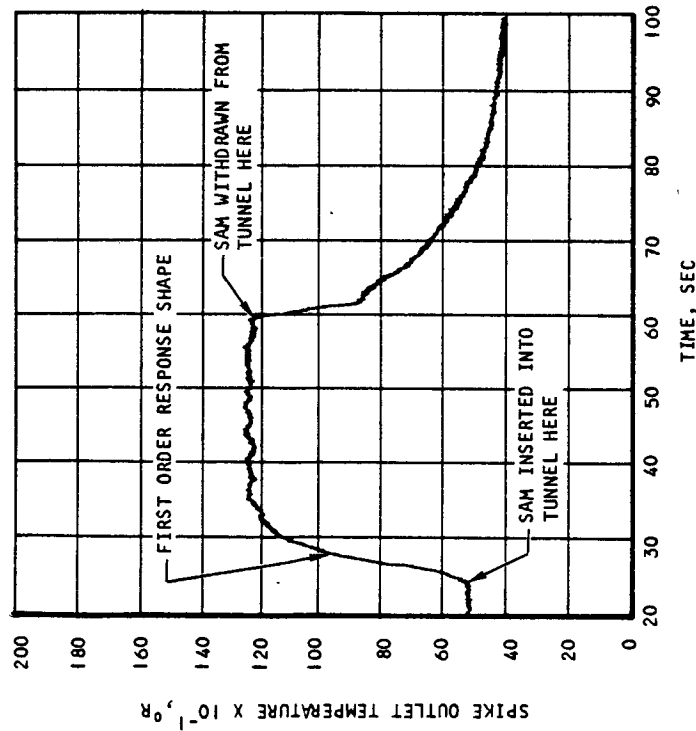
Figure 5.4-2. Spike and Innerbody Hydrogen Outer Temperature Histories for Test 41, Run 39 (U)

The time constant (τ) was calculated from the approximated time-derivatives at any two times and the difference in time between them ($\Delta\theta$). By dividing the derivatives of the first-order response equation rather than dividing the response equation by itself at two time locations, the final steady-state value (T_f) was eliminated from the calculation. This made the calculation

dependent on the shape of the temperature-time history curve only and not on the end points (T_f) and (T_i).

In the calculation procedure, the temperature data was time-smoothed to reduce the level of calculation errors. As an example, Figure 5.4-3 shows the PCM data history for the innerbody hydrogen control thermocouple, T40, for Test 41, Run 20. The recorded data appears to have a preferred random pattern. The curve through the data points shows the time-smoothed interpretation. The calculated time-derivatives are shown by the triangular data points and are based on the smoothed data curve. To further time-smooth the data, the line shown through triangular points was used to calculate time constants. Since the calculations are based on two time points per time-constant calculation, the time points were selected every two sec. Several other time-point pair calculations were performed and the resulting time constants were averaged.

The hydrogen outlet temperature time constants for each of the engine flow routes and the total engine, for Test 41, Run 39 (3320 psia, 3400°R tunnel reservoir total conditions) are shown in Figure 5.4-4. The computer analysis correlation is included for comparison. These experimental time constants were calculated from the experimental temperature-time histories (i.e.; Figure 5.4-2) and the calculation procedures outlined above. They are plotted against the normalized flow route hydrogen rates that were averaged over the same time periods as the time-constant calculation. The dashed line formed by the test data (except the innerbody) is about 25 percent lower than the computer analysis correlation. This apparent shift between test and analysis is probably due to experimental data uncertainties, oversimplification of the thermal capacitance normalized flow rate (the abscissa in Figure 5.4-4), and differences between the actual flow route geometries (compound-curved surfaces of cones and cylinders including cutouts for struts, fin height changes, and manifolding), and the computer analysis geometry (straight cylindrical surfaces, no cutouts, one fin height, and no manifolding). The time constant for the total engine was based on the mixed outlet temperatures of all routes, T101, and is less than the time constants for the aft routes (innerbody, trailing edge, and strut sides). This indicates dominance of the combined spike and leading edge flow rates (73 percent of total engine flow) on the mixed outlet temperature.

From the test results in Figure 5.4-4 and the discussion of data reduction methods above, the calculation of flow route time constant appears to be sensitive to many variables not included herein. Though the time constant, as defined herein, cannot be calculated precisely, the simple approach does provide a good indication of the transient operation at Mach 8 flight conditions. It has been established that the time constant is inversely proportional to flow rate and that the time to steady state (from the onset of spike retraction and lightoff at flight conditions) is approximately four time constants (4τ). The time to steady state at flight was estimated from the SAM test-time constants
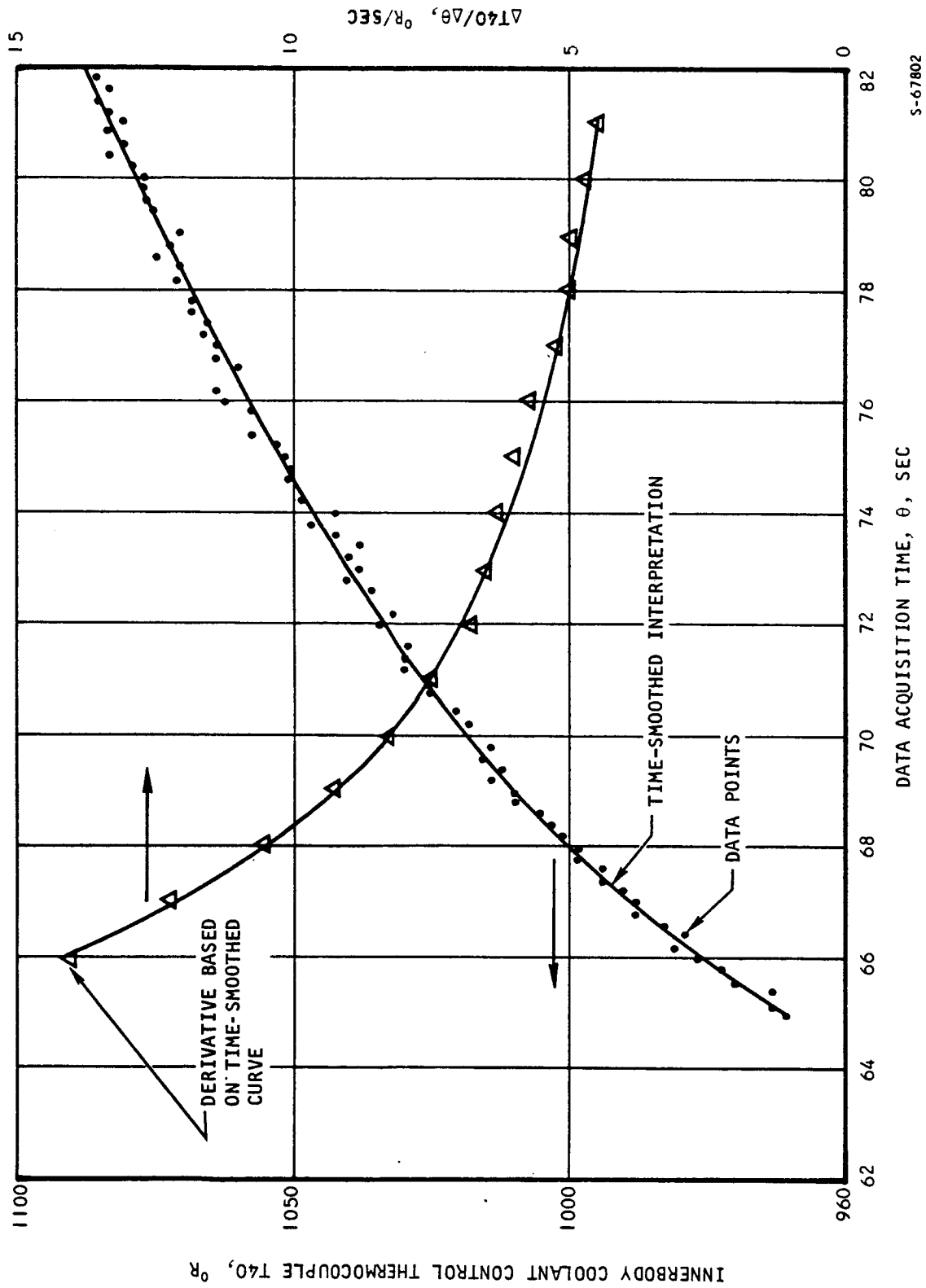
Figure 5.4-3. Temperature History of Innerbody Coolant Control Thermocouple for Test 41, Run 20 (U)

S-67802

HYDROGEN OUTLET TEMPERATURE TIME CONSTANT, τ, SEC

100

		H_2 RATE $\dot{W}$, LB/SEC	MASS $\dot{M}$, LB
$\triangle$	SPIKE	0.30	46.6
$\bigcirc$	INNERBODY	0.10	30.0
$\bullet$	LEADING EDGE	0.24	31.4
$\diamond$	TRAILING EDGE	0.10	41.5
$\square$	STRUT SIDES	0.015	10.0
$\triangledown$	TOTAL	0.70	159.5

$C = 0.105$ BTU/LB, $^{\circ}$R (HASTELLOY X)

$C_p = 3.5$ BTU/LB, $^{\circ}$R (NORMAL H_2)

10

COMPUTER ANALYSIS RESULTS

$$\tau = 0.73 / \left(\frac{W C_p}{MC} \right)$$

INTERPRETATION OF DATA
EXCLUDING INNERBODY

1

0.01   0.10   1.0

NORMALIZED FLOW ROUTE HYDROGEN RATE $- \dfrac{\dot{W}_{CP\ H2}}{(MC)_{STRUCTURE}}$, SEC^{-1}

S-67807
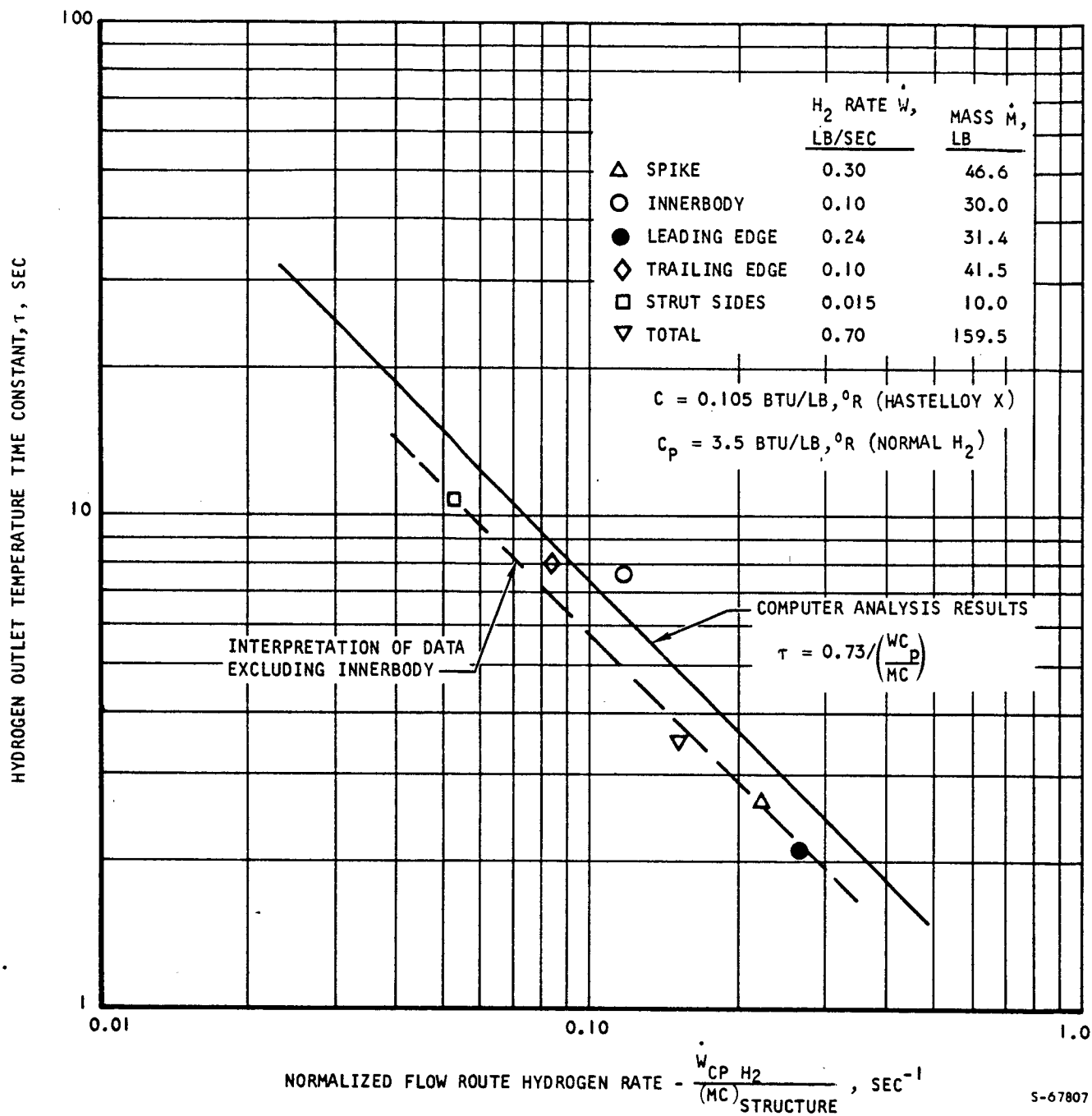
Figure 5.4-4.   Flow Route Time Constants for Test 41, Run 39 (U)

in Figure 5.4-4. For the total engine, this time is 4 sec (at a total hydrogen flow of 2.13 lb/sec at Mach 8, versus $4\tau = 14$ sec at 0.754 lb/sec for test). The time to flight-steady-state conditions on the strut sides will be the longest of all routes at about 8 sec (at a hydrogen flow of 0.092 lb/sec at Mach 8, versus $4\tau = 44$ sec at 0.0163 lb/sec for test).
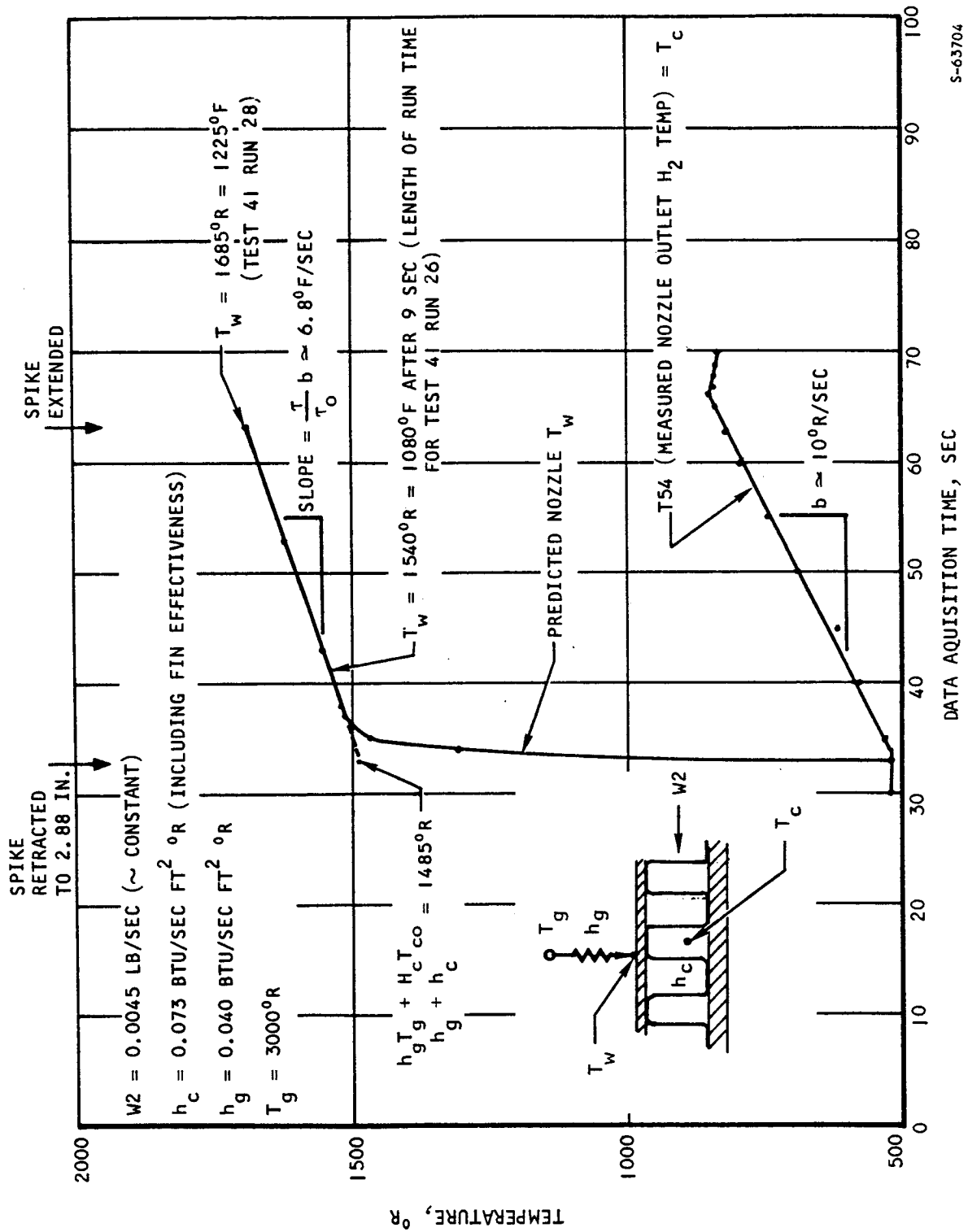
5.4.3.3 Metal Temperature Response

Starting with Test 41, Run 26 (2200 psia, 3100°R), metal discoloration caused by metal temperatures of 1000°F or higher was observed on the nozzle at the nozzle/inner shell surface, on the outer shell between the struts, and on the first wedge of the struts near the strut leading edge. A detailed description of these locations is given in Section 5.1.2.1. A discussion of the aerodynamic phenomena causing the local high heating is presented in Section 5.2.3.2. Transient heat transfer analyses were performed at these locations, and results are discussed below.

An analytical heat transfer model of a plate-and-fin structure and the derivation of the transient hot-wall response for a step change in hot gas heating and ramp change in hydrogen coolant temperature are presented in Appendix B. The predicted hot-wall temperature history for the nozzle discolored region (Test 41, Runs 26 and 28) is presented in Figure 5.4-5. Operating conditions for Runs 26 and 28 are similar, except the spike retraction time was 9 sec for Run 26, and 30 sec for Run 28. The hot gas heat transfer coefficient on the nozzle in the absence of local high heating was estimated at 0.013 Btu/sec ft^2-$^\circ$R. A factor of three was applied to this coefficient to account for the local heating (i.e., 0.040 Btu/sec^2-$^\circ$R). The hydrogen heat transfer coefficient, 0.078 Btu/sec ft^2-$^\circ$R, was based on a near-constant innerbody flow rate of 0.0045 lb/sec. The nozzle outlet hydrogen temperature, T54, was assumed to be equal to the local hydrogen temperature history at the discolored region and was approximated by a constant slope of 10°R/sec. The predicted nozzle hot wall temperature for Run 26 is 1540°R (1080°F) and 1685°R (1225°F) for Run 28. Both of these temperatures will produce metal discoloration as discussed in Section 5.1.2.1.

A similar calculation was performed on the outer shell discolored location between the struts. Results for Test 41, Run 26, are presented in Figure 5.4-6. The predicted wall temperature reached 1510°R (1050°F) after 9 sec. For Run 28, the predicted hot-wall temperature was estimated at 1800°R (1340°F). Included for comparison in Figure 5.4-6 is T92, the hot-wall insert temperature at approximately the same axial location (62.30 reference coordinates) on the outer shell as the predicted hot-wall temperature, but not in the local high-heating region.

The transient temperature results for the nozzle for Test 41, Runs 26 and 28 in Figure 5.4-5 represent a highly undercooled condition (innerbody hydrogen rate of 0.0045 lb/sec). In addition to producing high surface metal temperatures during transient operation, undercooling produced large hot surface-to-structure temperature differences. From aerodynamic heating considerations, the innerbody hydrogen rate required to produce a 1600°R outlet temperature
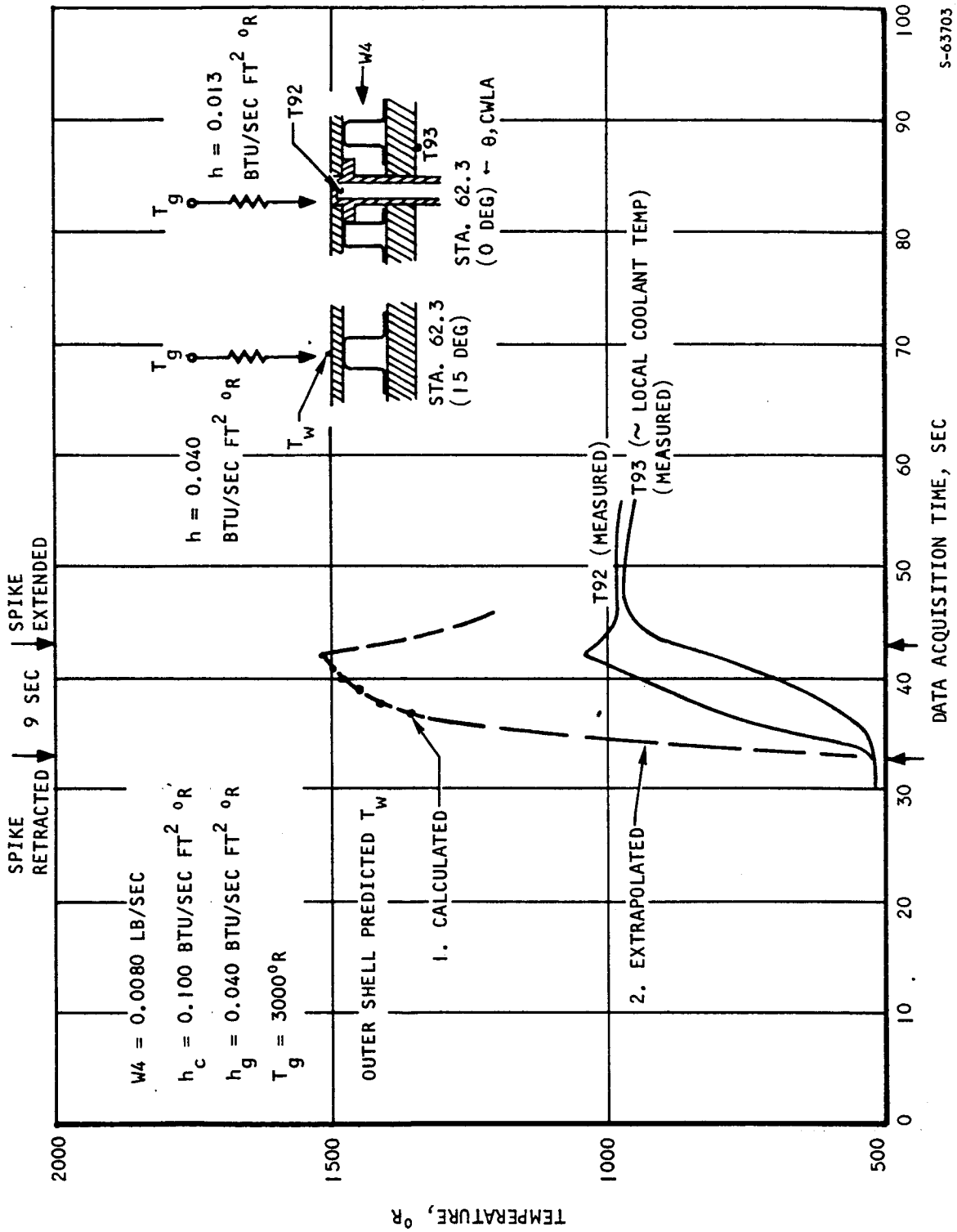
Figure 5.4-5. Nozzle Hot Wall Temperature Response, Test 41,
Runs 26 and 28 (2200 psia, 3000°R) (U)

S-63704

AIRESEARCH MANUFACTURING COMPANY
Los Angeles, California

Figure 5.4-6. Outer Shell Hot Wall Temperature Response, Test 41, Run 26 (2200 psia, 3000°R) (U)

S-63703

at steady state (i.e.; design flow rate selection criteria) is approximately 0.050 lb/sec, or more than 10-times the flow rate shown in Figure 5.4-5. An additional transient heat transfer analysis was performed on the same nozzle area as described above and in Figure 5.4-5 except the hydrogen flow was 0.050 lb/sec instead of 0.0045 lb/sec. Instead of a ramped hydrogen temperature rate of $10^{\circ}R$/sec, a coolant temperature history (approximately equal to structural wall history) was used that was based on the hydrogen temperature response rates described in Section 5.4.3.2. Results of the analysis are shown in Figure 5.4-7 and are compared with the results repeated from Figure 5.4-5. In addition to reaching a lower steady-state surface temperature of $1225^{\circ}R$ within 12 sec, the design case (0.050 lb/sec) produced a much lower hot surface-to-structure ΔT of $320^{\circ}R$. This lower ΔT resulted from a quicker-responding structure temperature and a lower steady-state hot surface temperature. More significantly, the maximum ΔT for the adequately cooled case occurred at steady state, while the maximum ΔT for the undercooled case ($970^{\circ}R$) occurred just after initial insertion into the stream. This undercooled behavior produced the transient maximum ΔT's discussed in Section 5.3.3.1.2. For flight application, therefore, the design flow rates are established in the flow routes at the onset of spike retraction and lightoff so that transient ΔT's larger than those predicted at steady state do not occur.

5.5 THERMAL FATIGUE

5.5.1 Summary of Results

5.5.1.1 Test Objectives

The primary test objective for thermal fatigue was to impose controlled thermal duty cycles that could be closely monitored during the test program. This allowed direct evaluation of the fatigue damage in each test cycle. It also provided data from the early runs to establish coolant flow rates, test cycle timing, and sequencing, to effect the desired cumulative fatigue loading during subsequent test runs. A specific test goal was to simulate the severity of the $Mach_{\infty} = 8$ design conditions in as many areas as possible.

Thermal transient analysis was carried out for the various critical areas in the engine. This analysis provided data for temperature-time histories in the struts, the outerbody outlet manifold, strut and cowl leading edges, and several other large manifolds. The maximum thermal fatigue damage for the intended test sequence was determined to be in the strut sides, with a calculated damage fraction of 0.428. The cumulative damage in the hot skin adjoining the outerbody outlet manifold (OBOM) was nearly the same. These were found to be the two most critical areas in the engine.

A number of thermocouples had been placed on the OBOM and on the hot skin at or near the OBOM. Although several thermocouples were installed within the strut bodies, the extremely low fins on the strut walls made it impractical to install thermocouples on the hot skins that would have provided reliable transient temperature data for the hot skins.

A further test objective was to discover problem areas not considered in

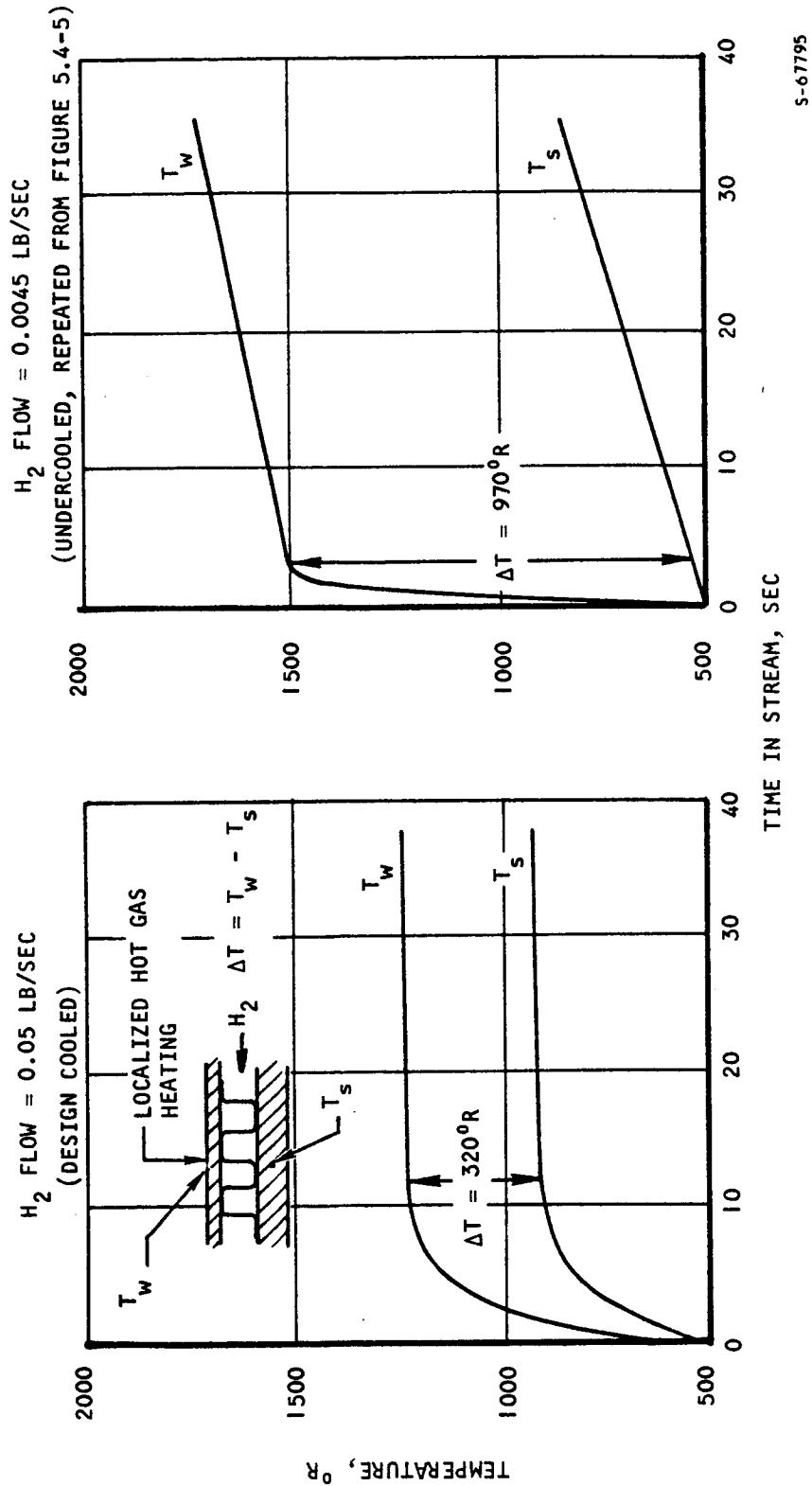Figure 5.4-7. Nozzle Temperature Difference Comparison for 2200 psia, 3000°R Tunnel Reservoir Total Conditions

the design phase. One such problem-area example would be regions of intensified heating due to shock interactions. Other possibilities would be inadequate cooling in local areas where there were interruptions in fin continuity.

An important objective of the SAM tests was the evaluation of design approaches used for the cooled structure. The construction and testing of a complete structural prototype permits the effect of the interactions between components under severe thermal loading to be evaluated in terms of structural capability and survival.

5.5.1.2 Engine Critical Areas

Several of the most critical thermal fatigue areas are shown in Figure 5.5-1. The first area depicted is the hot skin adjoining the outerbody outlet manifold (OBOM). The coolant is at its highest temperature, and this produces the hottest structural metal temperature in the outerbody. It is a region of high heat flux, and the hot skin temperature achieves its peak value at this location. Large temperature differences occur between the manifold and the hot skin as a result of startup and shutdown transients.

The strut sides, the strut sockets, and the strut leading edges are all critical areas. The design of the strut cooling passages on the strut sides involved the use of small (0.020-in. high) plain fins; the strut body is relatively massive to carry structural loads. Large thermal differentials occur here during the tunnel testing due to transients, and produce significant thermal fatigue damage. The strut leading edge is subjected to stagnation-line heating which leads to large ΔT from the strut body temperature. The strut sockets are mechanically heavily loaded and restrained between heavy stiffening rings. In turn, they constrain the inner and outer shells. Hot gas flow between the strut and the sockets results in high local temperatures that can cause significant thermal loading on the joints in these areas.

Shock interaction effects lead to local areas of high heat fluxes and occur in several places. One such area is the nozzle. This again creates zones of high skin temperature and high ΔT values, with resulting thermal fatigue damage.

The cowl leading edge is a region of high stagnation-line heating. The small leading edge radius of 0.030 in. results in a difficult cooling design problem. Large differential temperatures between the leading edge stagnation line and the cooler prime engine structure are produced at this location.

It was not possible to simulate or duplicate $M_\infty = 8$ differential temperatures in all of these areas during the wind tunnel tests. Because of the massiveness of the outerbody manifold, the hot-skin-to-cooled-structure ΔT could be produced most easily in this portion of the engine during the wind tunnel tests. Heat fluxes on the strut leading edge and cowl leading edge, and hence, thermal fatigue damage, were expected to be lower during the wind tunnel tests than at $M_\infty = 8$ operating conditions.

- SHOCK INTERACTION ZONES

HOT SKIN

COLD SHELL

ΔT

- COWL LEADING EDGE

0.030 RAD.
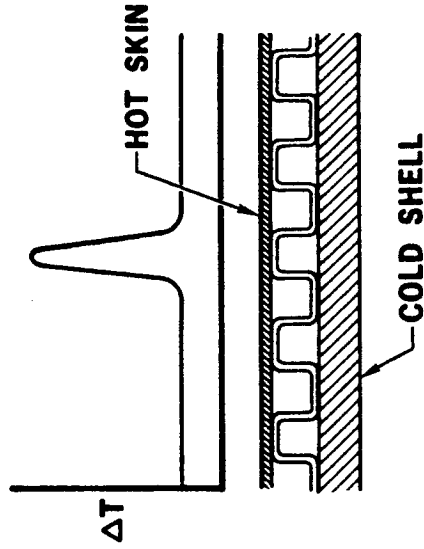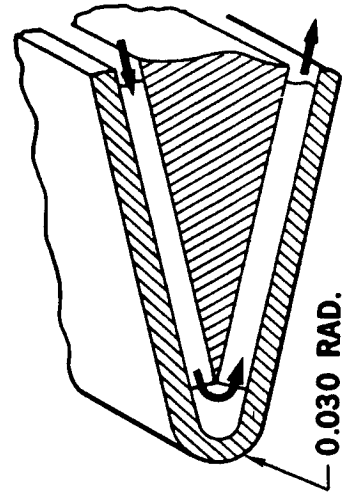
- HOT SKIN ADJOINING OUTERBODY OUTLET MANIFOLD

H₂

HOT SKIN

MANIFOLD

COLD SHELL

H₂
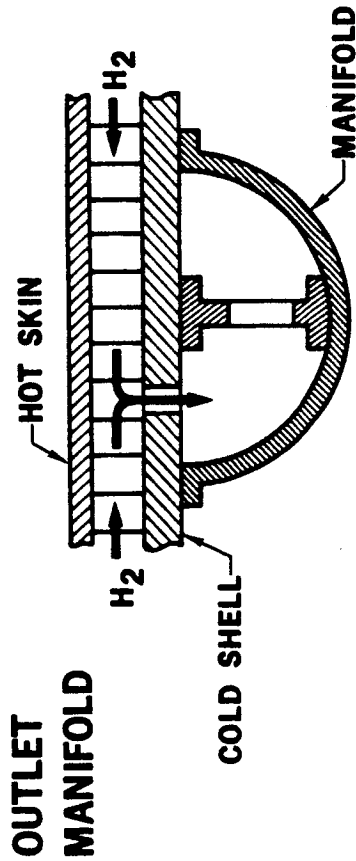
- STRUT: SIDE, LEADING EDGE, SOCKETS

HOT SKIN

COOLING PASSAGES

LEADING EDGE
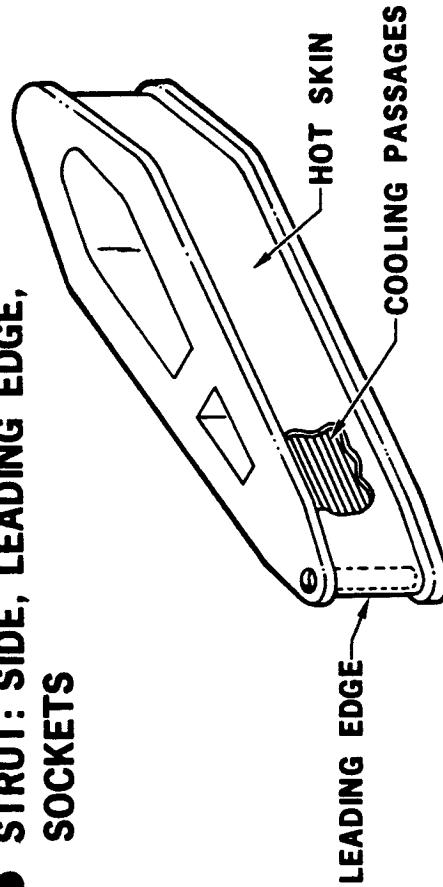
Figure 5.5-1. Thermal Fatigue Critical Areas

5.5.1.3 Outerbody Outlet Manifold Thermal Fatigue

The maximum shell ΔT at design conditions occurs at this location on the engine. As indicated above, thermal transient analysis showed that this would also be a critical area during the SAM wind tunnel tests. By adjustment in cycle timing, this was made the governing test region for thermal fatigue. It has also been noted that several thermocouples are installed on the OBOM and hot skin at or near the most critical area. The desired ΔT transients were obtained by timing of insertion and retraction sequences of the SAM engine during the test runs, and adjustment of coolant flow rates.

Figure 5.5-2 shows a cross-section of the OBOM and adjoining hot skin.
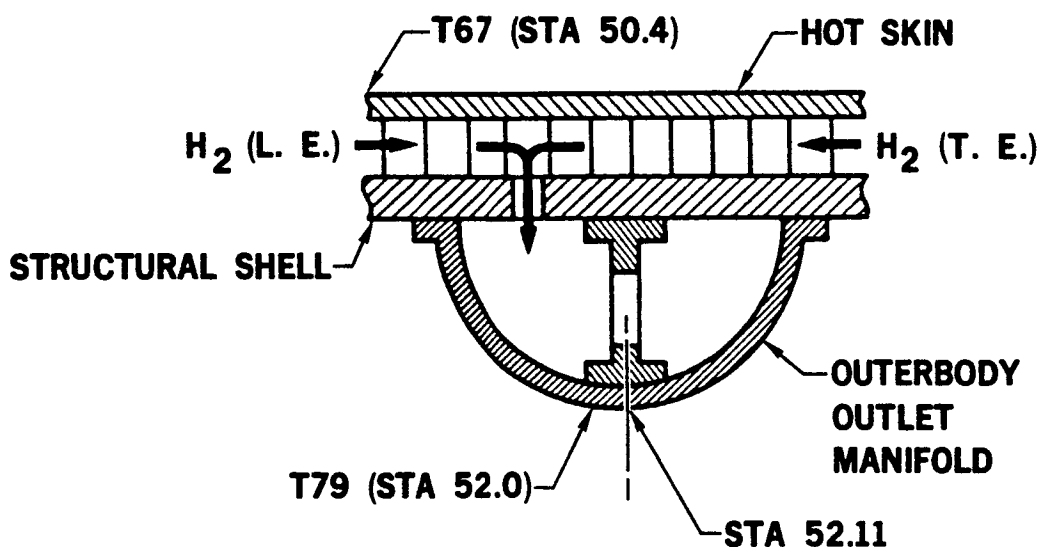
Figure 5.5-2. Outerbody Outlet Manifold Cross Section

Analysis of thermal data showed that thermocouple T67 (located at Station 50.4) readings provided a direct measure of the maximum hot skin temperature at the coolant outlet at Station 51.40. Similarly, T79, which was mounted at Station 52.00 on the OBOM, provided a direct reading equal to the effective average cold structural temperature at Station 52.11. Accordingly, the differential reading, T67-T79, provided a direct time history recording for the applicable ΔT. With these various data, it was a relatively straightforward procedure to compute maximum differential expansion, maximum hot skin temperature during each thermal fatigue cycle, and thermal fatigue damage fraction during each cycle.

5.5.1.4 Summary of Results

Table 5.5-1 presents a summary of the 58 thermal fatigue cycles applied to the engine at the OBOM. This table includes data from all of the applicable runs, in which the last three tests were carried out with the engine at an angle of attack of 3 deg to the tunnel centerline. Two cycles during

TABLE 5.5-1

THERMAL FATIGUE SUMMARY (OBOM) (U)

Tunnel Total Conditions		No. of Cycles	Time in Stream, sec	Avg. Cycle Temperatures		Damage Fraction, Percent
psia	°R			T_{max}, °R	ΔT, °R	
950	2600	5	172	1360	733	1.30
1300	2700	3	135	1445	950	2.12
1380	2700	33	829	1446	906	20.50
1500	2700	3	138	1571	1152	3.77
2200	3000	5	259	1591	1287	8.36
2800	3300	1	57	1435	1224	1.19
3300	3400	5	157	1522	1350	8.46
3350	2800	3*	37	1493	1150	2.30
TOTALS		58	1784 (28.7 min.)			49.0

*Model was at 3° angle of attack for these runs.

which the spike was not retracted (Test 41, Run 27 and Test 42, Run 16) are not counted.

The summary information is tabulated for the varying tunnel conditions employed during the test program. The chart shows that maximum temperature and ΔT generally increased as the tunnel conditions were intensified. The increased temperature conditions do not exactly increase in proportion to tunnel conditions, since coolant flow rates and time of the model in the tunnel stream also have an effect on the maximum metal temperatures and ΔT magnitudes.

The model accumulated a total of slightly under thirty minutes in the tunnel stream. The cumulative damage fraction was 49.0 percent, a slightly higher value than the projected damage fraction of 43.8 percent on the strut, from the analysis carried out prior to the wind tunnel tests. The damage fraction of 49.0 percent corresponds to 67 thermal duty cycles at $M_\infty = 8$ design conditions.

There was no visible evidence of thermal fatigue damage, i.e., cracking and leakage, anywhere on the engine surface at this time. In general, the tests have shown no basic weakness in the structural design concept for the HRE, from the standpoint of thermal fatigue.

5.5.2 Test Data

5.5.2.1 Thermocouple Data Interpretation

For purposes of data reduction, the metal thermocouples T67 and T79 were used to calculate the maximum hot wall temperature and maximum hot wall-to-structure difference at the outerbody outlet manifold. T67 is a hot wall insert thermocouple located at axial Station 50.4 (ref. coord.). This location is one inch upstream of the leading edge flow route outlet where the maximum hot wall temperature was expected to occur. To determine this maximum hot wall temperature, insert thermocouples T67 and T61 at axial Station 46.0 were corrected as per the procedure in Appendix A. The corrected temperatures were linearly extrapolated to the flow route outlet at axial Station 51.40. Though the trailing edge flow route also terminates at this location, the equivalent hot wall temperature extrapolation from trailing edge insert thermocouples was not included because these insert thermocouples showed temperatures which were much lower for almost all test runs. From an inspection of several leading edge insert thermocouple extrapolations, it was observed that the result was from 10^0 to $30^0 R$ lower than the uncorrected T67 thermocouple reading. For simplicity, then, the recorded value of T67 less $20^0 R$ was used as the hot wall temperature during the heatup portion of each test run. During the cooldown portion of the test cycle (intermediate or final withdrawal into the engine pod), the recorded value of T67 alone was used because, without hot gas heating, the insert and hot wall temperatures are almost equal to each other and axial temperature gradients are small.

Thermocouple T79 was used as the average structural temperature of the outerbody outlet manifold, and is located at the tip of the manifold (farthest away from the fins). Thermocouple T76 is also located on the manifold, but near the 0.060-in.-thick cold wall of the hydrogen fin passage. For most tests

T76 was no more than 50°R higher than T79 and was less than 30°R higher than T79 at the time of maximum temperature difference. At most, this would reduce the hot wall-to-structure temperature difference by 15°R if the average of T76 and T79 were used. It is noted that T76 and T79 are located at 45 deg (CWLA). This angular location was expected to have the fastest manifold temperature response since the highest manifold hydrogen flow rate occurs here near the tubes leading to the piggyback manifold. Because no other manifold temperatures were recorded, the interpretation of the average manifold temperature was biased toward the slower-responding and measured structural temperature near the out-let tubes, i.e., T79.

5.5.2.2 Metal Temperature-Time History

Figure 5.5-3 shows the metal temperature-time history for a typical test cycle for the outerbody outlet manifold. The data are for Test 42, Run 38, which involved two insertions and retractions of the model into and out of the wind tunnel stream.

Room temperature hydrogen was used in the test run. At the start of the test, the entire structure was approximately at RT. Immediately after insertion into the hot gas stream, the hot skin temperature increased rapidly; the cold structure responded quite slowly. The maximum ΔT of 944°F occurred just prior to model retraction, and the peak hot skin metal temperature of 1599°R occurred precisely at the time of retraction. After model retraction, the hot skin cooled down rapidly while the cold structure temperature continued to rise slowly. The hot skin passed below the cold structure temperature, resulting in a ΔT reversal.

Upon reinsertion of the model into the stream, the hot skin once again increased in temperature. The cold structure temperature at this time was substantially above room temperature. A relatively long time in the stream was employed for this cycle. The maximum positive ΔT of 529°F took place well before model retraction, and this positive ΔT was much lower than in the first cycle. At the time of the second retraction, the cold structure was hotter than at the first model retraction (approximately 1200°R vs 900°R). Upon re-traction from the tunnel, the hot skin rapidly cooled to RT, and the cold structure cooled more slowly. A ΔT reversal of 426°F was produced in the second thermal cycle. Total ΔT for the first cycle was 970°F; for the second cycle it was 975°F.

5.5.2.3 Temperature Data

The pertinent temperature data for all of the test runs has been provided in Table 5.1-1. This table provides the total ΔT, i.e., the sum of the posi-tive and negative ΔT's, the maximum metal temperature, the total differential expansion, and the fatigue damage for each full thermal fatigue cycle. The method of data analysis utilizing this information is treated in the following section.
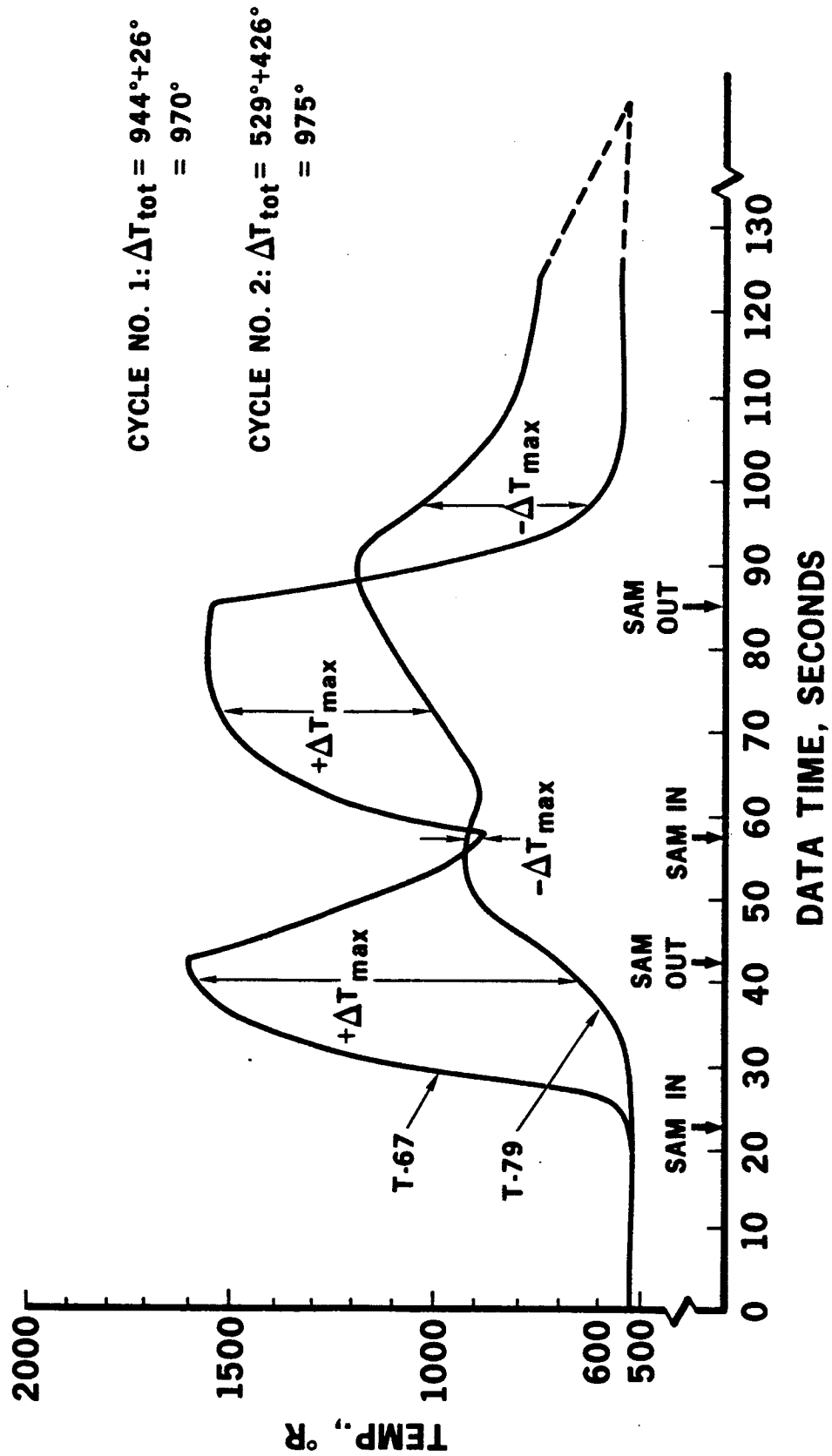
Figure 5.5-3. Typical Cycle Metal—Temperature History (U)

AIRESEARCH MANUFACTURING COMPANY
Los Angeles, California

UNCLASSIFIED

5.5.3 Methods of Data Analysis

5.5.3.1 Effect of Temperature-Time History on Hot Skin

Differential temperatures between the hot skin and the prime load-carrying structure of the engine lead to the generation of stresses in the hot skin well beyond the material yield strength. For Hastelloy X, repeated cycling with differential temperatures in excess of $400^\circ F$ will cause a plastic strain loop to occur during each cycle, and for the cyclic life to be finite. For the temperature-time history illustrated in Figure 5.5.3, the summation of the positive and negative ΔT's during each full cycle was above $900^\circ F$, and a substantial plastic strain loop occurred during each cycle.

Figure 5.5-4 shows the time-temperature history, the stress-time history, and the resulting plastic stress-strain loop in a typical test cycle. The hot skin starts each test cycle in a state of residual compressive stress from the previous test. The temperature-time history shown is with hydrogen inlet temperature at room temperature; i.e., no temperature drop below room temperature at startup or shutdown. At point (1) in all three figures, the engine is inserted into the tunnel stream. The maximum compressive stress and strain occur at point (2) in the cycle when the maximum positive ΔT is achieved. The increase in compressive stress from point (1) to point (2) is small because the hot skin is already past the knee of the compressive stress-strain curve at the start of the test cycle.

Immediately after the peak positive ΔT, hot skin compressive stress rapidly decreases, goes through zero, and achieves a peak tensile stress at point (3), the time at which the maximum ΔT reversal takes place. The subsequent cooldown of the engine at the completion of each cycle returns the entire engine to room temperature, eliminates the negative ΔT, and returns the hot skin to its initial state of compressive stress.

The quantity of interest is the plastic strain amplitude $\Delta\epsilon_\rho$. This is equal to the sum of the total strain ranges caused by the direct addition of the positive and negative ΔT values, minus the elastic strain range due to the change in stresses from points (2) to (3). The plastic strain amplitude is a direct measure of thermal fatigue damage in each usage cycle. The stresses and strains are, however, determined by the differential expansion history during each cycle. Since the expansion coefficient of Hastelloy X increases with increased temperature, ΔT differences produce much more differential growth at elevated temperatures, and hence, larger plastic strain-loops. For instance, the differential expansion from 70° to $870^\circ F$ causes a differential expansion of 0.0066 in./in., whereas from 800° to $1600^\circ F$ the differential expansion is 0.00785 in./in.

The test program has involved a series of separate runs with different thermal loads, times in the tunnel, and coolant flow rates. In particular, Test 42, Runs 19 through 42 have been designated as thermal cycling runs, and for the most part, the engine was inserted into the tunnel twice during each such run. The main purpose of these runs was to accumulate a large amount of fatigue damage, and this was accomplished. However, the engine experienced
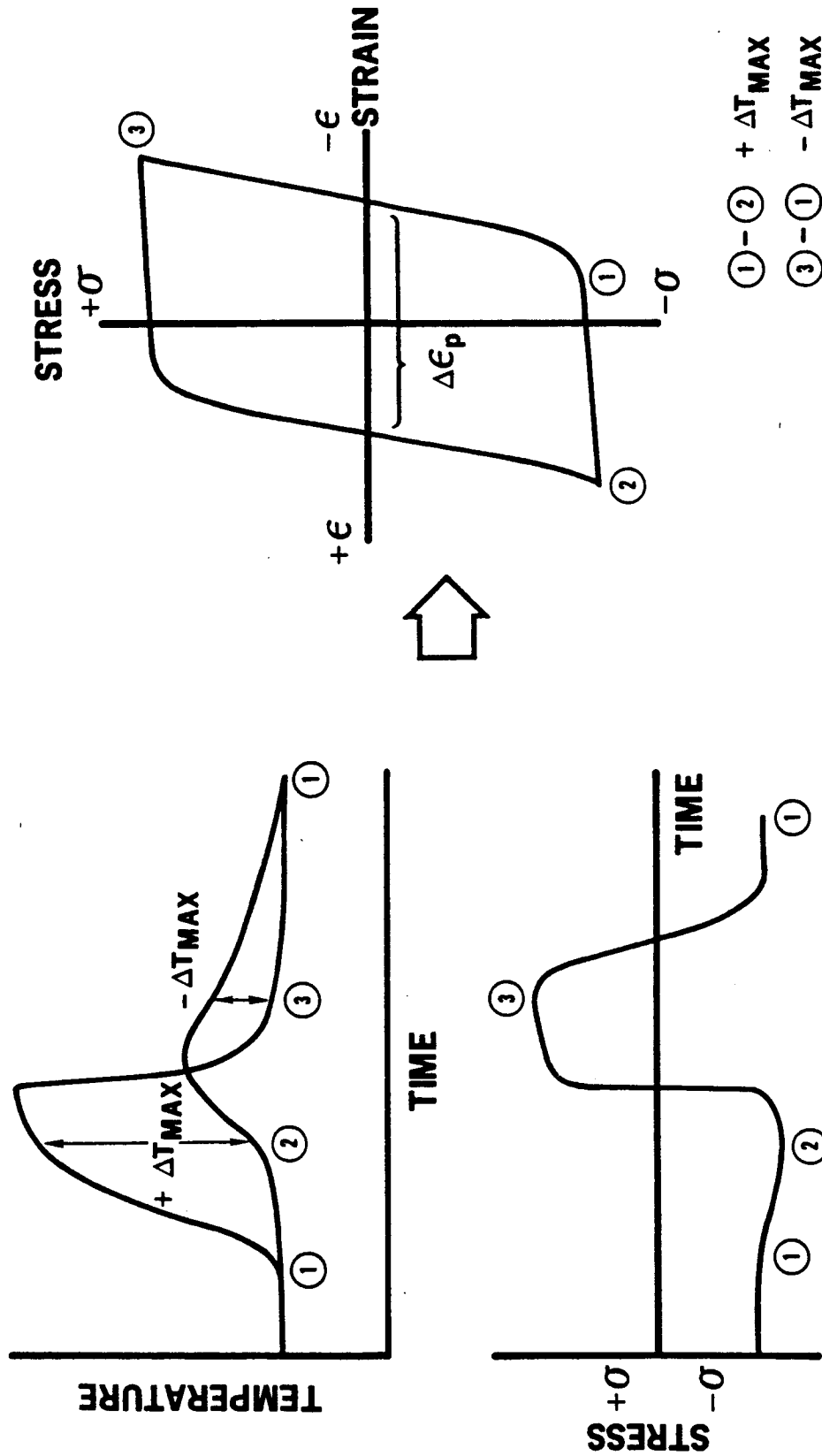
Figure 5.5-4. Typical Plastic Strain Loop

GARRETT AIRESEARCH MANUFACTURING COMPANY
Los Angeles, California

71-7702
Page 5-119

temperature and differential temperature cycles during every tunnel insertion and retraction of the model, and some fatigue damage took place in each cycle. The procedure used to calculate the fatigue damage during each cycle is discussed in the following paragraphs.

5.5.3.2 Data Reduction Basis

The basic low-cycle fatigue data was obtained from mechanical bending tests, Reference 5-7, and thermal fatigue tests conducted on small test panels during the HRE program, References 5-8 and 5-9. In these tests and in the engine, the hot skin was restricted from thermal growth by the prime load-carrying structures in such a way as to produce a condition of biaxial stress and strain in the hot skin. This biaxial condition had to be properly considered in both the original data reduction for the small test panels, and then in the application to the engine. The uniaxial cyclic stress-strain behavior of Hastelloy X was utilized to calculate the equal-biaxial stress-strain curves for Hastelloy X at various temperatures. These curves were then used to generate curves for equivalent plastic strain range versus applied total strain range at the various temperatures. It was found that the elastic modulus at elevated temperature diminished almost directly with the reduction in strength properties, such that the curves for plastic-strain amplitude versus applied strain range were virtually identical for temperatures from RT to 1600°F. This data was then used to develop a fatigue design curve for the engine. Figure 5.5-5 presents the curve developed from the mechanical bending tests and the thermal cycle tests. It shows cycles to failure versus engine ΔT. The panel fatigue tests were conducted over the range of ΔT from 650° to 950°F. The plotted curve is based upon a hot skin temperature of 1400°F, where the ΔT is the structural temperature subtracted from 1600°F.

5.5.3.3 Basic Low Cycle Fatigue Formulation

The basic formulation for low cycle fatigue analysis relates cycles-to-failure to material ductility and plastic strain range. The expression is

$$N = \left[C/\Delta\epsilon_\rho \right]^k$$

where

$\quad\quad\quad$ N $\quad$ = $\quad$ cycles to failure

$\quad\quad\quad$ $\Delta\epsilon_\rho$ $\quad$ = $\quad$ plastic strain range

$\quad\quad\quad$ C $\quad$ = $\quad$ ductility constant

$\quad\quad\quad$ k $\quad$ = $\quad$ exponent $\cong 2$

The ductility constant is related to material reduction of area (RA) in the fabricated form, which takes into account material thickness and manufacturing processes such as forming, brazing, welding, and annealing. The plastic strain range is determined from the total applied strain and accounts for multiaxial effects, elastic strain of the hot skin, elastic strain of the prime
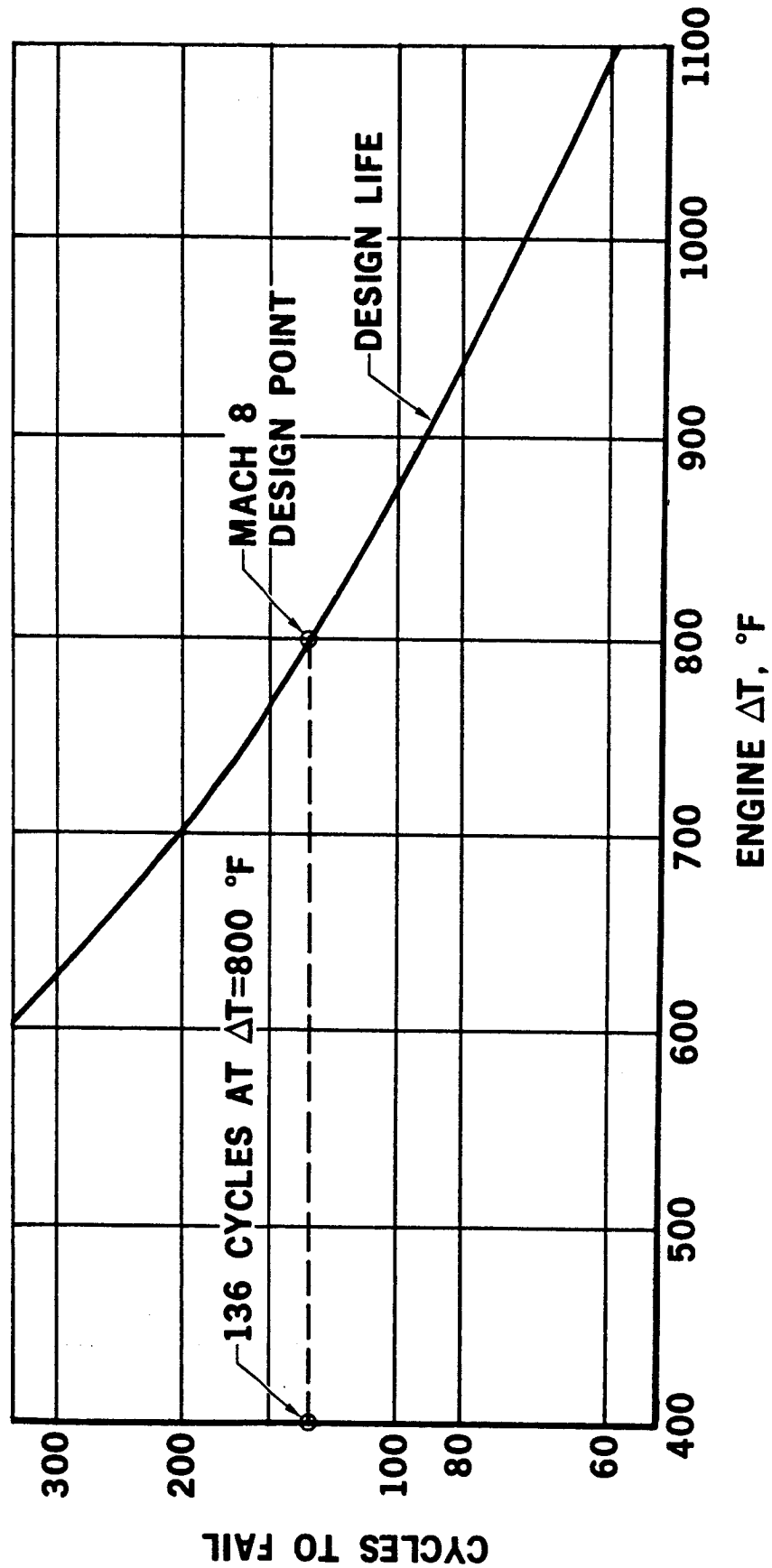
Figure 5.5-5. Basic Engine Thermal Fatigue Design Curve

GARRETT AIRESEARCH MANUFACTURING COMPANY
Los Angeles, California

structure and local strain concentration effects. A value of 2.0 for the exponent (k) was found to be valid over the strain ranges of interest for Hastelloy X.

The data from the mechanical bending tests on plate-fin specimens constructed with Palniro I braze alloy are illustrated in Figure 5.5-6. The tests were conducted at RT, 1340°F, and 1540°F. It can be seen that operation at elevated temperature leads to reduced life. This is due to reduced ductility, reduced strength, and material creep. Material creep at elevated temperature uses up a portion of the creep-rupture life. In addition, the plastic flow due to creep relaxation of thermal stresses leads to an increase in plastic strain range for the same magnitude of total applied strain range. It can be noted from Figure 5.5-6 that the measured cyclic life at 1540°F is not appreciably reduced from the 1340°F results. Although the creep effects are increased at the higher temperature, this has been substantially offset by the improved ductility for Palniro I-coated Hastelloy X at 1540°F (RA = 34 percent) as compared to 1340°F (RA = 29 percent).

In an operational thermal cycle, the compressive plastic strain essentially takes place at elevated temperature, while the tensile strain occurs during cooldown of the hot skin. An average line has been constructed in Figure 5.5-6 to be representative of the overall behavior during each thermal cycle. For purposes of data reduction, the effects of creep and ductility variations have been absorbed into the ductility constant (C). The effective ductility constant is 0.150 at RT, and for a thermal cycle with a maximum cycle temperature of 1340°F (1800°R) to 1540°F (2000°R), the effective ductility constant is 0.100. Over the temperature range from RT to 1340°F (1800°R), the ductility constant is taken to decrease as a straight-line function of temperature. A plot of (C) vs temperature, and the effect of temperature on cycles-to-failure is illustrated in Figure 5.5-7.

The introduction of elevated temperature effects into the basic low-cycle fatigue formula leads to the formulas for fatigue life given below.

$$N = \left[\frac{0.150 - 0.050\left(\dfrac{T_{max} - 530°R}{1270}\right)}{\Delta\epsilon_p}\right]^2 \qquad T_{max} \leq 1800°R$$

$$N = \left[\frac{0.100}{\Delta\epsilon_p}\right]^2 \qquad 1800°R \leq T_{max} \leq 2060°R$$

The first formula is valid over the temperature range from RT to 1340°F (1800°R), and it accounts for the linear reduction in ductility constant over this range. The second formula is valid over the temperature range from 1340°F (1800°R) to 1600°F (2060°R). The maximum metal temperature during the entire test cycle is denoted by T_{max}.
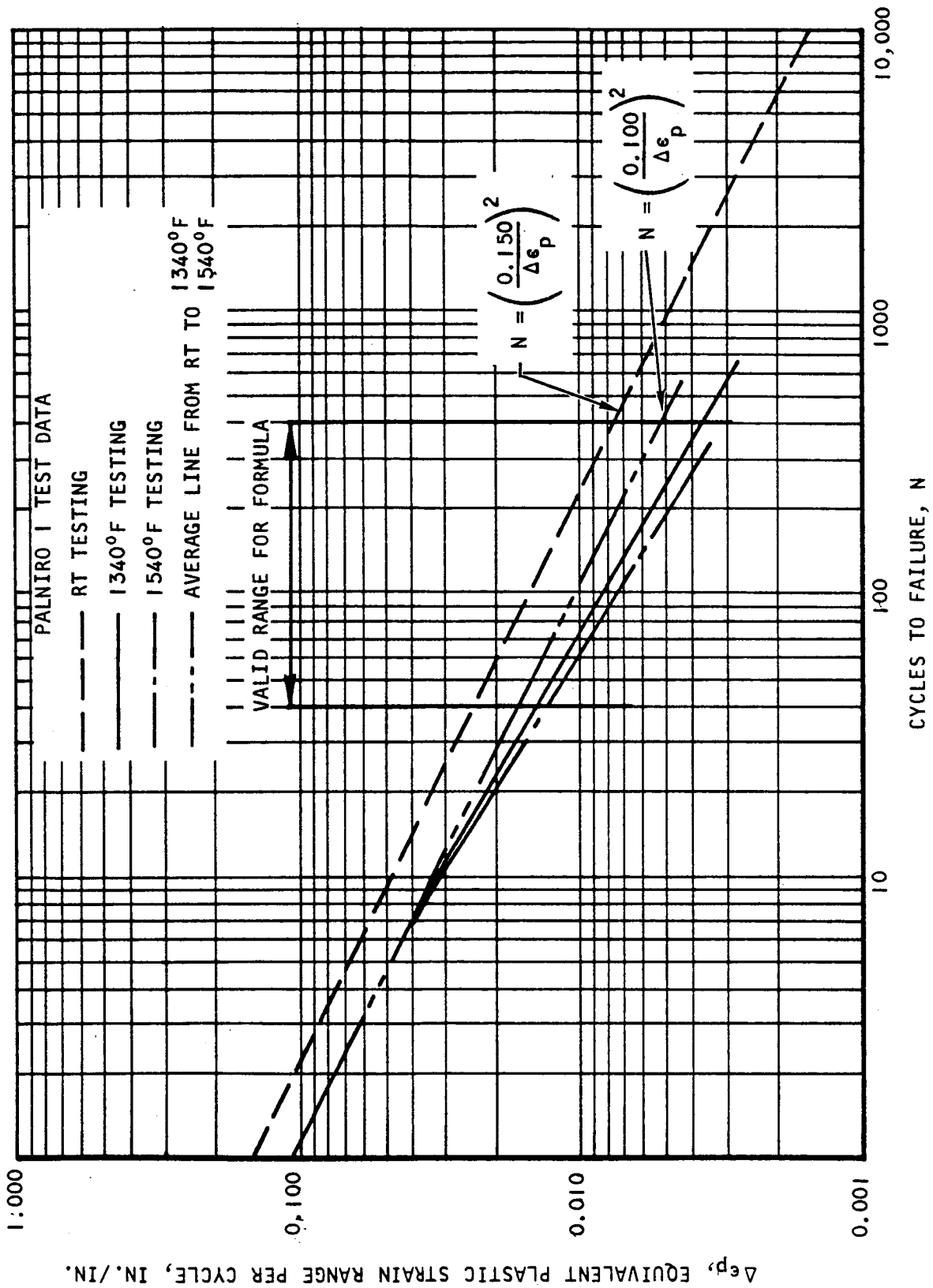
Figure 5.5-6. Hastelloy X Plate-Fin Low Cycle Fatigue Test Results

$$N = \left(\frac{0.150}{\Delta\epsilon_P}\right)^2$$

$$N = \left(\frac{0.100}{\Delta\epsilon_P}\right)^2$$

PALNIRO I TEST DATA
RT TESTING
1340°F TESTING
1540°F TESTING
AVERAGE LINE FROM RT TO 1340°F 1540°F

VALID RANGE FOR FORMULA

CYCLES TO FAILURE, N

$\Delta\epsilon_P$, EQUIVALENT PLASTIC STRAIN RANGE PER CYCLE, IN./IN.

Figure 5.5-7. Effects of Elevated Temperature on Fatigue Life

An expression was developed to convert the applied total differential expansion of the hot skin directly into plastic strain. The expression makes allowance for the biaxial effects, hot-skin elastic strains, and cold-skin elastic strains. This takes the form of a linear function as follows

$$\Delta \epsilon_p = -0.0050 + 1.75 \Sigma (\alpha \Delta T)$$

where the differential expansion is the summation of the positive and negative differential expansions between the hot skin and the prime structure. This linear formula is valid for total thermal expansions ranging from 0.005 in./in. to 0.020 in./in.

Figure 5.5-8 presents temperature data at the outerbody outlet manifold during Test 42, Run 38, test cycle 1. In this cycle, the maximum positive ΔT was $944^0 R$, and the maximum negative ΔT was $26^0 R$. The total differential expansion is shown in the figure. Maximum metal temperature was $1599^0 R$, and the related ductility constant was 0.1079. From the fatigue formula, the calculated life was determined to be 124 cycles. The engine would have survived this number of cycles at this particular condition. The inverse number, 0.0081, represents the fatigue damage fraction for this test cycle. A similar calculation was performed for each test cycle to determine cycle damage from each cycle, and the accumulated damage was the addition of the individual damage fractions. The results are tabulated in Table 5.1-1 for all of the test cycles.
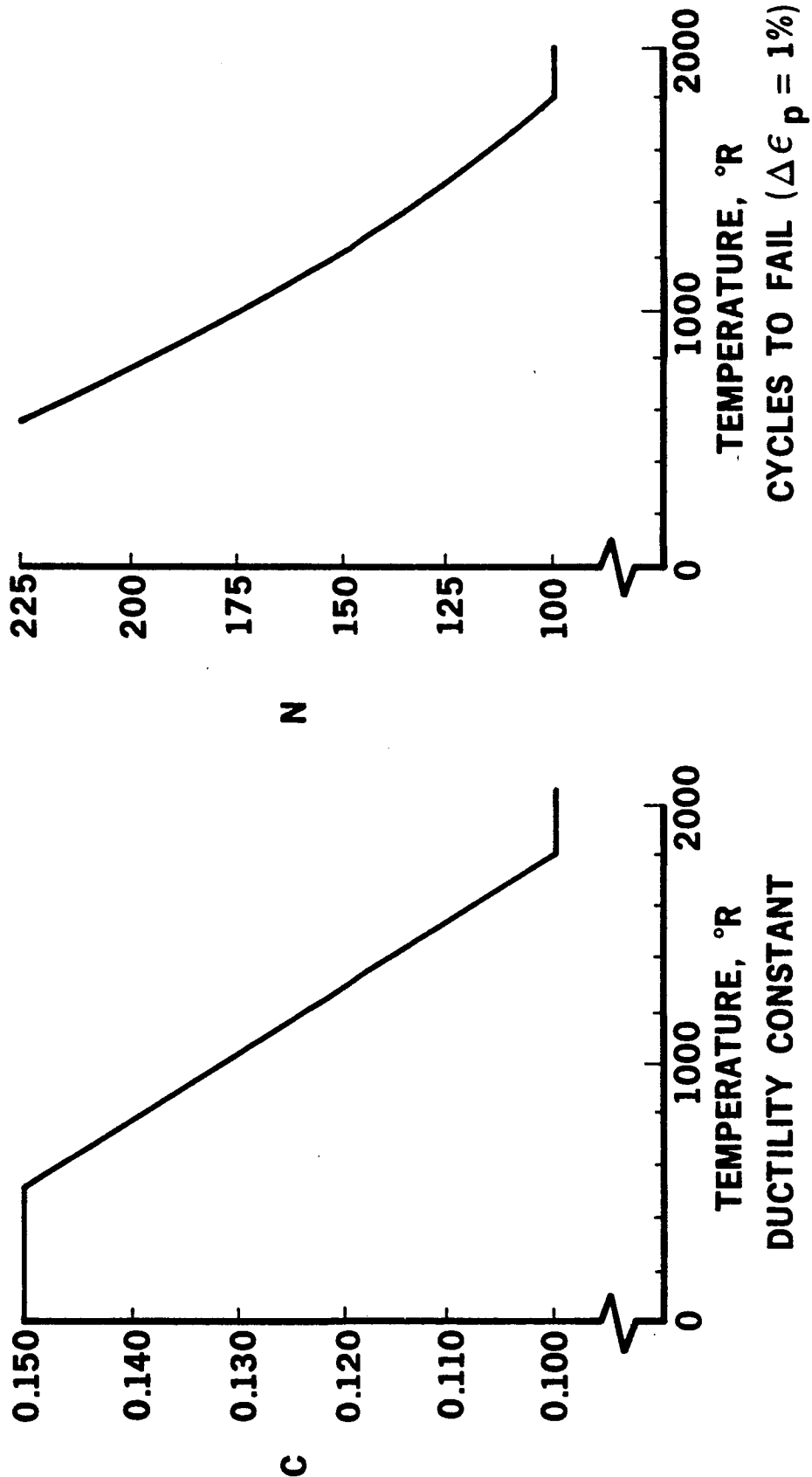
5.6 APPLIED STRUCTURAL LOADS

The principal objectives of the SAM test program as related to applied structural loads were to determine structural loading due to aerodynamic effects and to assess structural capability to withstand the applied loads. Internal pressure-containment capability was also verified with rated pressures at elevated temperatures, but not for the 10-hr design life of the engine.

The engine structure was designed to be compatible with all the loads occurring during the operation of the X-15A-2 aircraft. In addition to the gust and maneuver loads acting on the aircraft, it was designed to withstand the large internal loads due to inlet unstart. Symmetrical and asymmetrical inlet unstart loads and the vibration qualification loads governed the design of most parts of the engine. The design loads are tabulated in an abbreviated form in Table 5.6-1 for reference.

The peak tunnel operating condition during the SAM tests produced a dynamic pressure of 2010 psf (M = 7.06) during Test 41, Run 38. This exceeded the maximum dynamic pressure of 1770 psf that was originally planned for the testing, but was still well within the structural capability in terms of total applied design loads.

The structural load data was monitored and recorded utilizing the output from 12 strain gages and four uniaxial and three triaxial accelerometers. The strain gages were installed at locations (Figure 5.6-1) where the temperatures were sufficiently low to assure accurate functioning of these devices. Foil gages were used to form full-strain bridges to increase sensitivity and to

- **FROM T42 - R38, CYCLE 1**

$$+\Delta T = 944\ °R \qquad a\Delta T = 0.00808$$

$$-\Delta T = 26\ °R \qquad a\Delta T = 0.00022$$

$$\Sigma a\Delta T = 0.00830$$

$$T_{MAX} = 1599°R: \quad C = 0.1079$$

- **FROM FATIGUE FORMULA**

$$N = \left(\frac{0.1079}{-0.0050 + 1.75 \times 0.00830}\right)^2 = 124$$

$$1/N = \text{DAMAGE FRACTION} = 0.0081$$

Figure 5.5-8. Typical SAM Test Cycle Thermal Fatigue Calculation (U)

TABLE 5.6-1

HRE/SAM GOVERNING DESIGN LOADS

$F_{Iz} = 484$

$F_{vy} = 342$

$F_{Ax} = 303$

CG OF INNERBODY
AND NOZZLE

$F_{Ix} = 510$

$F_{Ix} = 1170$

$F_{Iy} = 259$

$F_{Iz} = 1100$

$F_{Iy} = 114$

-75

$F_{vy} = 778$

$F_{Iy} = 10800$

41.2

CG OF SPIKE
AND ACTUATOR

F_{Ax} 5650

F_v - VIBRATION LOAD
F_I^v - FRAME ACCELERATION LOAD
F_A^i - AERODYNAMIC PRESSURE LOAD

Outerbody-Innerbody Struts Critical Load Condition (Critical
Flight Condition: Transient, Unsymmetric Unstart)

NOTES: 1. ONLY LOADS ON SPIKE, ACTUATOR,
INNERBODY AND NOZZLE ARE SHOWN

a. CRITICAL FLIGHT CONDITION - TRANSIENT, SYMMETRICAL UNSTART

$\Sigma F_{A_X} = 5850$ (2)

805
195

F_v - VIBRATION LOAD
F_I - STATIC ACCELERATION
LOAD
F_A - AERODYNAMIC PRES-
SURE LOAD

$F_{Ix} = 1416$

$F_{Iz} = 2124$

3.19

$F_{vy} = 2124$

$F_{Iy} = 708$

1260

9600
200

15000

z
x
y

b. CRITICAL VIBRATION QUALIFICATION CONDITIONS
1. LONGITUDINAL INPUTS

2. LATERAL INPUT

$F_{vx} = 14100$

SPIKE
CG

SP

$F_{vy_{SP}} = 2100$

$F_{vy_R} = 4510$

CG OF ENGINE
LESS SPIKE

NOTES:
1. LOADS SHOWN AS "DOTTED ARROWS" ARE FOR COMPONENTS
2. TOTAL AXIAL ENGINE AERODYNAMIC PRESSURE LOAD

Engine Mount Critical Load Conditions

Vibration Qualification Loads

Description	Assumed Response
3.0-g longitudinal input	20-g longitudinal response for total engine
3.0-g lateral input	20-g lateral response for spike
	7.5-g lateral response for remainder of engine
3.0-g transverse input	20-g transverse response for spike
	7.5-g transverse response for remainder of engine

S-70128

Figure 5.6-1. Strain Gage Locations

UNCLASSIFIED

provide temperature compensation. S1 was located on the edge of a spike-cone reinforcing gusset located at 30 deg from the vertical engine axis, and it measured axial strain along this edge. S2, identical to S1, was located on a horizontal gusset of the spike cone. S3 measured stresses and loads due to vertical bending of the spike cone, and were located on the top and bottom vertical centerline of the cone. S5 measured bending of the actuator housing due to vertical bending moment, and the gages were located on top and bottom of the housing. S6 measured axial strain in the actuator support strut No. 1; S7 measured bending stresses in the actuator support strut No. 6; S12 measured vertical loads in the front support; S13 measured fore and aft loads at the front support; S16 and S17 measured vertical loads in the aft flexures; and S18 and S19 measured fore and aft loads at the end of the actuator.

Strain bridges S1 through S7 were tested and calibrated after installation inside the engine. The other gages were tested after installation on the particular part and prior to engine installation.

All test data were recorded on FM tape. The data were then digitized, then printed out as stress, strain, and force and/or moment versus time. Instantaneous values of the data were printed out at 0.05-sec intervals.

5.6.1 External Reactions

The SAM was supported in the wind tunnel with the support frame and the pylon facing down. Four strain gage bridges (S12, S13, S16, and S17) measured the external reaction components. The schematics of the support, the measured reaction components, and the resultant load are shown in Figure 5.6-2. It was assumed that the resultant of the external loads intersected the centerline of the engine. Then, the resultant vector of the external loads, $\bar{R}_E$, and its location, X_Y, was determined from the following basic static equations:

$$\bar{R}_E = \bar{R}_{EX} + \bar{R}_{EY} + \bar{R}_{EZ} \tag{5-1}$$

$$\Sigma P_X = 0; \quad \bar{R}_{EX} + \bar{R}_{XF} = 0$$

$$R_{XF} = -\bar{R}_{EX}$$

This value was measured by S13.

$$\Sigma \bar{P}_Z = 0; \quad \bar{R}_{ZF} + \bar{R}_{ZL} + \bar{R}_{ZR} - \bar{W}_E - \bar{R}_{EZ} = 0 \tag{5-2}$$

if

$$(\bar{R}_{ZL} + \bar{R}_{ZR}) = \bar{R}_{ZA}$$

then

$$\bar{R}_{ZF} = \bar{W}_E + \bar{R}_{EZ} - \bar{R}_{ZA}$$

and this was measured by S12.

Figure 5.6-2. SAM External Reactions
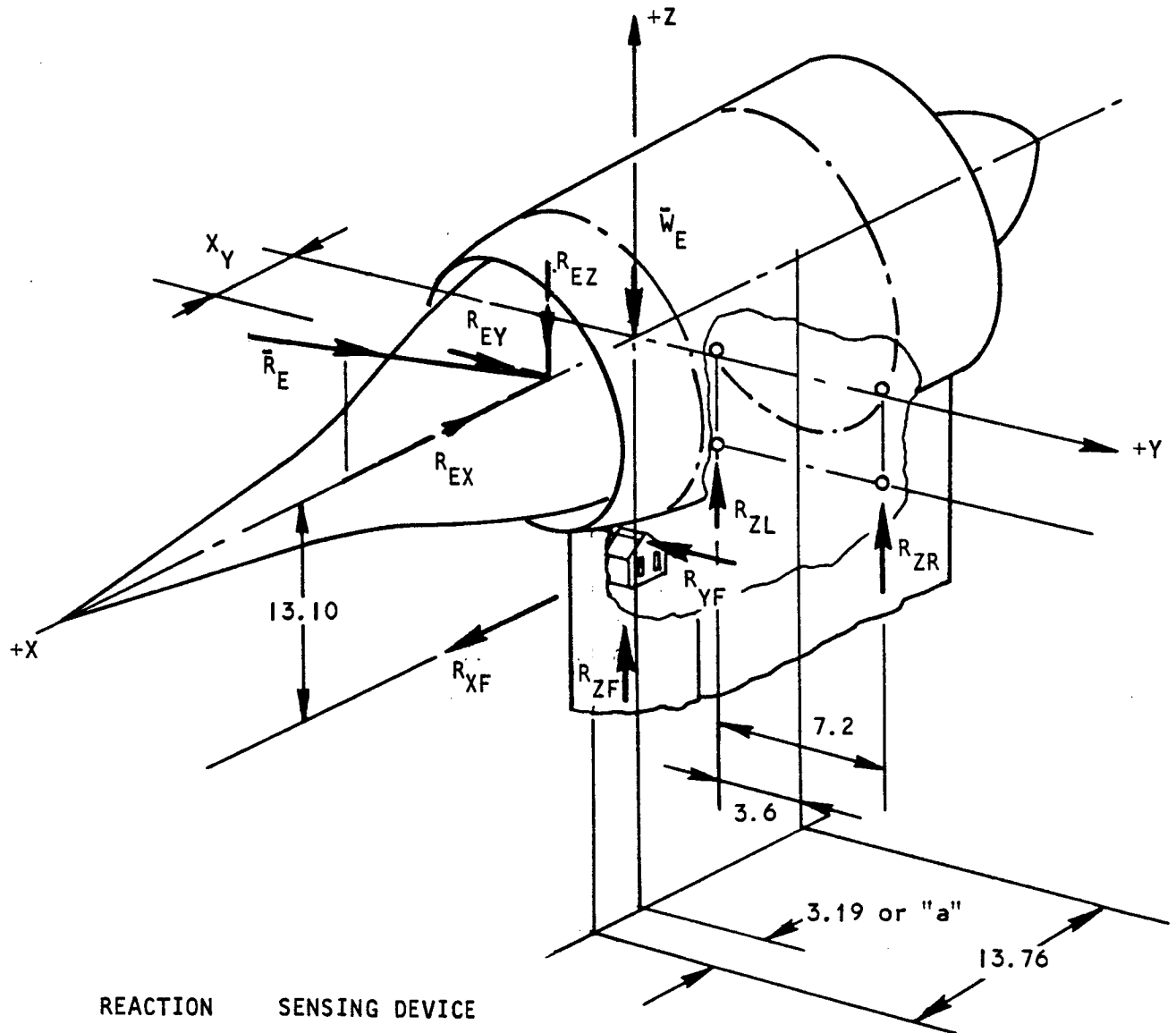
REACTION	SENSING DEVICE
$\bar{R}_{XF}$	S13
$\bar{R}_{ZF}$	S12
$\bar{R}_{ZL}$	S16
$\bar{R}_{ZR}$	S17

S-70132

$$\Sigma M_X = 0; \quad -13.1 \, \bar{R}_{YF} - 3.6 \, (\bar{R}_{ZR} + \bar{R}_{ZL}) = 0 \qquad (5-3)$$

$$\bar{R}_{YF} = \frac{3.6}{13.1} \, \bar{R}_{ZA} = 0.2748 \, \bar{R}_{ZA} = -\bar{R}_{EY}$$

$\bar{R}_{ZR}$ was recorded by S17

$$\Sigma M_Z = 0; \quad \bar{R}_{EY} X_Y - 3.19 \, \bar{R}_{YF} = 0 \qquad (5-4)$$

or

$$\bar{R}_{EY} X_Y - 2 \, \bar{R}_{YF} = 0$$

The 3.19-in. distance between the center of gravity of the engine and the thrust block was obtained from weight and c.g. calculations. Restraints imposed by the water-cooled cowl/pylon and the water and hydrogen plumbing resulted in an effective change in this distance, as calculated in the following. If it is assumed that no external force is acting on the engine,

$$\bar{R}_{EX} = \bar{R}_{EY} = \bar{R}_{EZ} = 0$$

and

$$\Sigma \bar{P}_Z = 0$$

then

$$\bar{R}_{ZF} + \bar{W}_E + (\bar{R}_{ZR} + \bar{R}_{ZL}) = 0$$

but

$$\bar{R}_{ZL} + \bar{R}_{ZR} = \bar{R}_{ZA} \text{ and } \bar{W}_E = -(\bar{R}_{ZF} + \bar{R}_{ZA})$$

Since

$$\Sigma M_y = 0$$

writing moments to the line of W_E equals

$$\bar{P}_{ZF} a - (\bar{P}_{ZL} + \bar{P}_{ZR}) \times (13.76 - a) = 0$$

where "a" is the distance between engine center of gravity and the thrust block. This can be expressed as

$$a = \frac{13.76 \, \bar{P}_{ZA}}{\bar{P}_{ZF} + \bar{P}_{ZA}} = \frac{13.76 \, (S16 + S17)}{S12 + S16 + S17}$$

This derivation is based on the assumption that readings on strain gages S16 and S17 are equal due to symmetry, and the axial load is zero. Such zero external-load condition existed during each run before the model was elevated into the tunnel. Readings on S16 were generally much lower than on S17 and approximately 500 lb was read on S13. The calculated "a" values are shown in

Table 5.6-2 and are indicative of structural restraints acting on the SAM as installed in the wind tunnel.

The mounting of the SAM is a modified version of the HRE mounting which was designed to attach the engine to the X-15A-2 aircraft. It consisted of a built-up welded rigid frame fabricated from Inconel-718 material. Loads applied to the mount pickup points are statically determinate. All fore and aft loads are reacted by the thrust block, located at Station 52.11, while the aft mounts located at Station 65.75 are made very flexible in this direction and react to vertical loads only. A simplified isometric drawing of the mounting frame, and tabulation of the maximum mounting loads is shown in Figure 5.6-3.

Data from the following runs was analyzed to determine applied structural loads, steady-state stresses, and dynamic loads.

Test 41 (No hydrogen injection)	Test 42 (Hydrogen injection)
Run 7	Run 3
13	14
20	16
26	17
28	19
37	45
40	46
42	47
53	

Maximum axial reactions (R_{XF}) and the simultaneously occurring vertical reaction components are shown in Table 5.6-3. The last column of the table shows the maximum change of R_{XF} during each run, which is calculated as the difference between the negative maximum and either the positive maximum or the negative minimum. Maximum vertical loads at the front supports are tabulated in Table 5.6-4. Maximum and minimum vertical reactions are shown for each investigated run in Tables 5.6-5 and 5.6-6. As shown by Figure 5.6-3, the measured loads are small, relating to the design loads, which was expected for these tests.

5.6.2 Spike-Actuator Loads

The inlet spike, a long (55.16 in.) and light shell structure, is attached to the forward flange of the actuator. The actuator provides the means of stroking the spike over a distance of 5 in. and also provides the structural support for the spike as shown in Figure 5.6-4. The front end of the actuator attaches to the sliding cylinder of the support structure by means of a pinned, self-aligning, spherical bearing. In turn, this bearing is attached to the actuator piston. At the aft end, the actuator cylinder is attached to the structural housing with a universal connection to eliminate side loads. The bearings between the inner and outer structural cylinders are made of bonded Fabroid (a woven fabric of fiberglass and Teflon). The deformations and dynamic behavior of this complex structure were important to the engine design. To
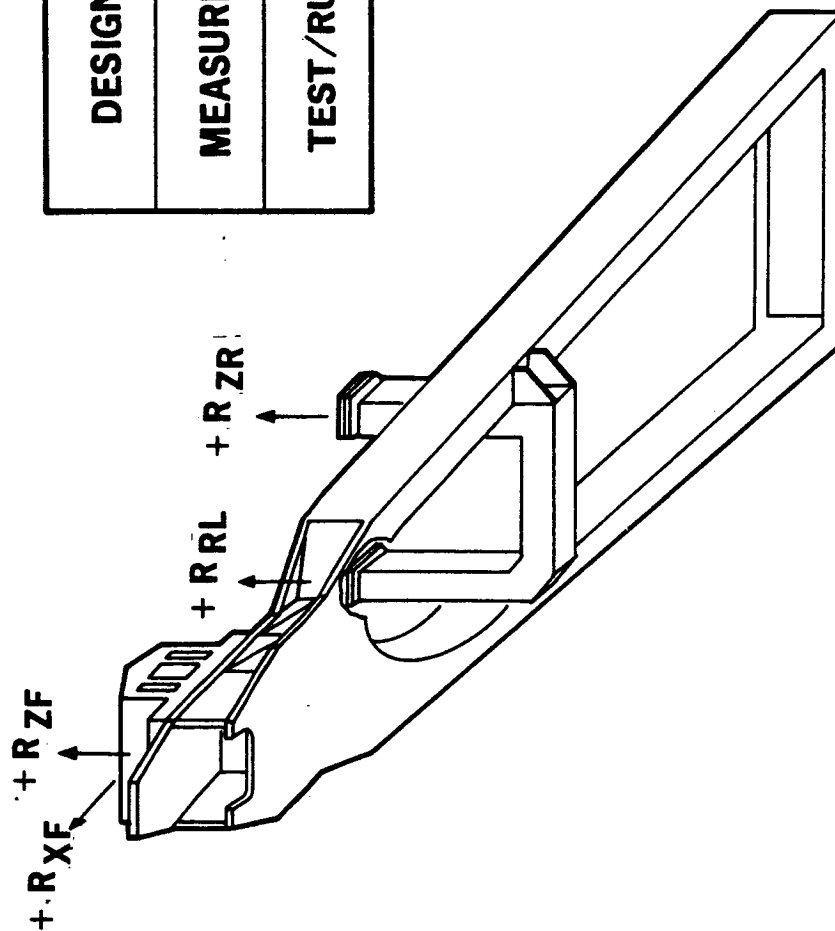
TABLE 5.6-2

THRUST BLOCK/ENGINE C.G. DISTANCE (U)

Test	Run	S17	R_{ZA} = 2×S17	S12	S13	13.1/13.76 (S13)	R_{ZF}	$R_{ZA}+R_{EF}$	a
41	7	521	1042	420	524	499	919	1961	7.311
	13	462	924	446	502	478	924	1848	6.88
	20	591	1182	206	-73	69.5	136.5	1318.5	12.33
	26	707	1414	346	253	241	587	2001	9.72
	28	749	1498	159	-130	124	35	1533	13.44
	37	1608	3216	831	715	681	1512	4728	9.36
	40	1655	3310	856	598	569	1425	4735	9.62
	42	1450	2900	687	891	848	1535	4435	8.99
	53	1286	2572	1216	387	368	1584	4156	8.51
42	3	543	1086	336	97	92	428	1514	9.87
	16	1076	2152	546	315	300	846	2998	9.87
	17	816	1632	347	547	521	868	2500	8.98
	19	614	1228	221	463	441	662	1890	8.94
	45	1568	3136	835	801	762.5	1598	4733.5	9.87
	46	1529	3058	765	573	546	1311	4369	9.63
	47	1421	2842	857	595	566	1423	4265	9.16

MAXIMUM LOADS, POUNDS

	R_{XF}	R_{ZF}	R_{RL}	R_{ZR}
DESIGN	-14100	-13100	-6065	-6065
MEASURED	-5611	-4906	-717	-2315
TEST/RUN	42 / 46	42 / 45	42 / 45	42 / 45

Figure 5.6-3. Mounting Frame and Measured Maximum Reactions (U)

S-70127

TABLE 5.6-3

FRONT SUPPORT - MAXIMUM AXIAL REACTIONS (U)

Test	Run	R_{XF} ←	R_{ZF} ↑	R_{ZR} ↑	R_A ↑	t, sec	$\lvert R_{XF} \rvert_{max}$
41	7	2055	876	738	1476	69.79	2123
	13	1298	401	435	870	48.24	1319
	20	1583	1101	819	1638	86.04	1680
	26	2980	860	804	1608	43.49	3129
	28	2355	218	602	1204	33.89	2744
	37	2726	1183	1321	2642	31.34	5072
	40	2213	1226	1532	3064	26.49	4716
	42	2583	1408	1241	2482	25.04	4432
	53	4493	3085	1176	2352	47.19	5251
42	3	1399	378	471	942	31.2	1434
	14	281	1393	1111	2222	81.08	1248
	16	1743	213	460	920	54.89	2673
	17	1930	538	730	1460	36.69	2023
	19	1990	607	770	1540	50.14	2001
	45	2052	1047	1332	2664	28.24	3951
	46	2984	1288	1209	2418	27.39	5611
	47	1788	1479	1598	3196	53.89	3763

TABLE 5.6-4

FRONT SUPPORT - MAXIMUM VERTICAL REACTIONS (U)

Test	Run	P, lb at	t, sec
41	7	1324	70.64
	13	567	39.89
	20	1463	86.29
	26	1316	49.19
	28	1174	66.74
	37	2405	86.70
	40	2847	86.04
	42	2848	63.49
	53	3480	47.89
42	3	1072	72.34
	14	1939	81.33
	16	1610	93.19
	17	1681	102.29
	19	1140	50.69
	45	4906	140.19
	46	2075	60.69
	47	2247	54.09

TABLE 5.6-5

SAM STRAIN GAGE RESULTS - MAXIMUM FLEXURE (AFT) REACTIONS (U)

Test	Run	Time, sec	P_{XF} (S13) ←	P_{ZF} (S12) ↑	$\frac{P_{ZR} ↑}{P_{ZL} ↑}$	$\frac{2P_{ZR}}{2P_{ZL}}$	Strain Gage No.
41	7	65.89	2448	959	542	1084	16
	7	69.84	2464	1042	757	1514	17
	13	38.99	481	478	267	534	16
	13	41.64	909	356	468	936	17
	20	86.39	844	1421	399	798	16
	20	86.44	650	1101	883	1766	17
	26	49.74	1635	1029	404	808	16
	26	49.49	1588	1206	958	1916	17
	28	63.49	1639	855	565	1130	16
	28	64.54	1298	1004	1139	2278	17
	37	86.79	375	2405	307	614	16
	37	88.99	1631	1794	1946	3880	17
	38	47.84	216	1386	308	616	16
	38	47.49	1388	975	1923	3846	17
	40	86.14	549	2847	494	988	16
	40	86.39	984	2616	2007	4014	17
	42	63.64	403	2525	240	480	16
	42	63.59	323	2591	1703	3406	17
42	3	69.14	1127	918	368	736	16
	3	71.14	1139	946	778	1556	17
	14	80.78	1651	1322	466	932	16
	14	79.68	1563	1789	1417	2834	17
	16	93.24	1666	1004	131	262	16
	16	93.34	615	957	1423	2846	17
	17	102.64	1138	1954	597	1194	16
	17	101.64	1483	1836	1294	2588	17
	19	49.79	2278	743	183	366	16
	19	50.94	1449	1081	838	1676	17
	45	140.19	610	4096	717	1434	16
	45	140.19	610	4096	2315	4630	17
	46	61.89	1577	1744	222	444	16
	46	60.69	170	2075	1747	3494	17
	47	24.69	2999	1254	-256	-512	16
	47	55.64	1067	1784	1712	3424	17

TABLE 5.6-6

SAM STRAIN GAGE RESULTS - MINIMUM FLEXURE (AFT) REACTIONS (U)

Test	Run	Time, sec	P_{XF} (S13)	P_{ZF} (S12)	$\frac{P_{ZR}}{P_{ZL}}$	$\frac{2P_{ZR}}{2P_{ZL}}$	Strain Gage No.
41	7	37.5	1005	569	195	390	16
	7	37.55	1005	401	420	840	17
	13	41.64	909	356	171	342	16
	13	41.69	930	337	367	734	17
	20	45.19	679	421	-84	-168	16
	20	45.14	519	163	455	910	17
	26	41.99	2786	750	233	466	16
	26	42.29	2798	860	765	1530	17
	28	29.89	1221	85	-73	-146	16
	28	29.54	1179	62	502	1004	17
	37	31.29	3379	1235	-77	-154	16
	37	29.94	2741	1118	1238	2476	17
	38	26.34	3164	1114	-8	-16	16
	38	27.44	4013	1268	1456	2912	17
	40	23.69	2004	922	3	6	16
	40	24.34	2301	1028	1469	2918	17
	42	23.59	2678	1064	-212	-424	16
	42	23.69	2742	1163	1070	2140	17
42	3	26.15	517	203	3	6	16
	3	25.85	454	215	461	922	17
	14	81.28	1469	1749	369	738	16
	14	83.48	631	1638	1026	2052	17
	16	93.39	461	420	-461	-922	16
	16	49.39	906	124	414	828	17
	17	31.94	1343	258	5	10	16
	17	31.49	1132	251	613	1226	17
	19	29.59	1117	279	-215	-430	16
	19	29.64	1140	265	405	810	17
	45	25.24	1914	875	-236	-472	16
	45	25.99	2243	1007	1307	2614	17
	46	27.24	3557	1268	-284	-568	16
	46	26.04	1149	3004	1117	2234	17
	47	25.49	1301	3541	-253	-506	16
	47	25.59	1354	3424	1104	2208	17
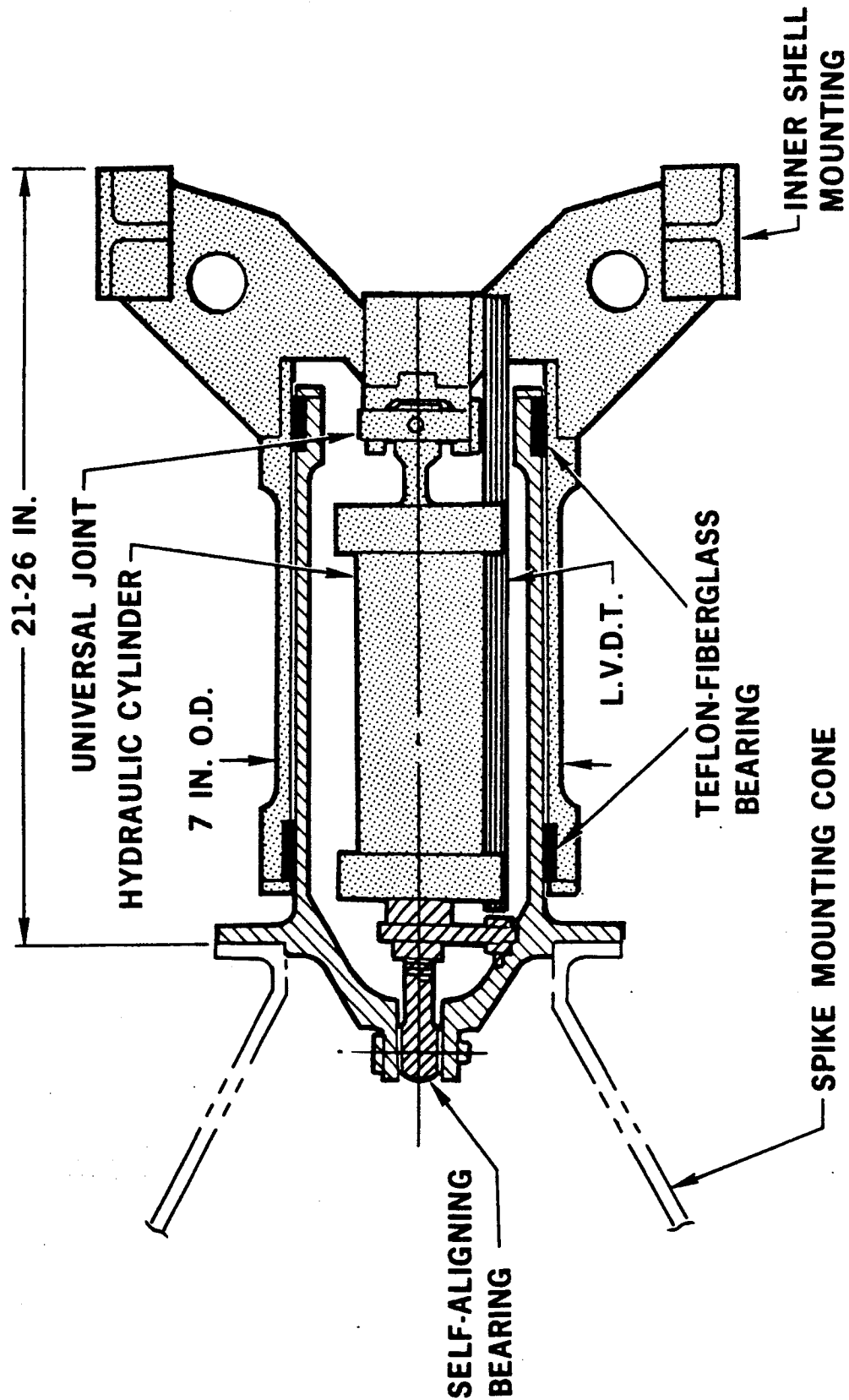
Figure 5.6-4. Inlet Spike Actuator

provide for verification of design and monitoring, a total of eight strain gage bridges were installed on the spike, the actuator housing, and on the actuator attachment.

The installation data of the strain gages is shown in Table 5.6-7. Two identical bridges, S18 and S19, were intended to measure the net load (P_{18}) at the aft end of the actuator. Only S18 data recordings were utilized because S19 became inoperative during the first runs. The following axial loads were acting on the spike-actuator assembly:

External aerodynamic force	P_A
Force due to N_2 purge pressure, (this load tends to close the spike)	P106
Force due to the change of the length of the bellows connecting the spike to the innerbody and connecting the coolant piping between the two, and the force due to pressure in the coolant bellows	P_B
Force due to friction between innerbody seal and spike	P_F
Force due to gas pressure acting on the bellows connecting innerbody and spike	P_P

A schematic representation of the spike and actuator assembly and the above-mentioned forces is shown in Figure 5.6-5. Forces other than axial are not shown, since the sensing device (S18) responded to axial loads only.

5.6.2.1 Actuator Load vs Time

The most significant loads were expected to occur during model insertion, spike retraction, and spike extension. A typical force-time history measured at the aft end of the actuator is shown in Figure 5.6-6. The steady-state condition between spike retraction and extension is not shown, as indicated by the discontinuity of the time scale on the diagram.

The following forces are marked in this figure and tabulated in Table 5.6-8.

Load before model inserted into tunnel	P_1
Load before spike is retracted	P_2
Load after spike is retracted 0.25 to 0.35 in	P_3
Maximum load during spike retraction	P_4
Average load between spike retraction and extension	P_5

TABLE 5.6-7

SAM STRAIN GAGE INSTALLATION DATA

No.	Strain Gage Properties			Gage Location			Gage Mounted On		Gage Description
	Type	Resistance, ohms	Factor	X, in.	Y, in.	Z, in.	Material	F_{TY}, psi	
1	SK-09-062TT-350	350 ±0.4 percent	1.985	44.50	2.20	3.81	Hastelloy X	45,000	Measures axial strain along spike cone reinforcing gusset (30 deg)
2	SK-09-062TT-350	350 ±0.4 percent	1.985	44.50	4.40	0	Hastelloy X	45,000	Same as 1, except on 90 deg reinforced gusset
3	SA-09-125AC-350	350 ±0.3 percent	2.085	44.50	0	3.55	Hastelloy X	45,000	Measures bending of the spike cone located on cone at 0 deg
5	SA-09-125AC-350	350 ±0.4 percent	1.985	55.50	0	3.4	4330	167,000	Measures bending of actuator housing. Located on the shell at 0 and 180 deg.
6	SA-09-062TT-350	350 ±0.4 percent	1.985	58.50	-2.7	4.7	4330	167,000	Measures axial strain in actuator support leg. Located on No. 6 strut leg.
7	SA-09-0125AC-350	350 ±0.4 percent	2.085	65.36	5.4	0	4330	167,000	Measures bending in actuator leg at strut No. 2
18	SK-09-062TT-350	350 ±0.4 percent	1.985	58.25	±1.0	0	4330	167,000	Measures axial load on spike at end of actuator. Two gages per leg.
19	SK-09-062TT-350	350 ±0.4 percent	1.985	58.75	±1.0	0	4330	167,000	Measures axial load on spike at end of actuator. Two gages per leg.

NOTES: 1. Gage factor tolerance is ±1.0 percent.
2. F_{TY} is 0.2 percent yield strength at 70°F.

S-70133

S_{18}

P_{18}

$\pm P_F$

P_P

P_B

P_{106}

P_A
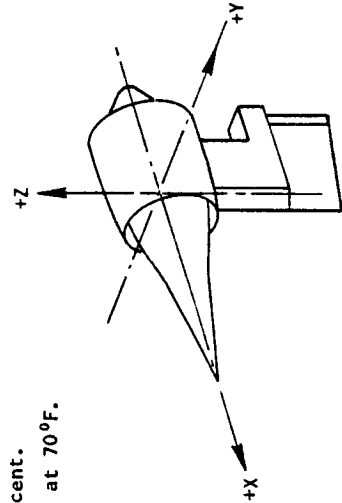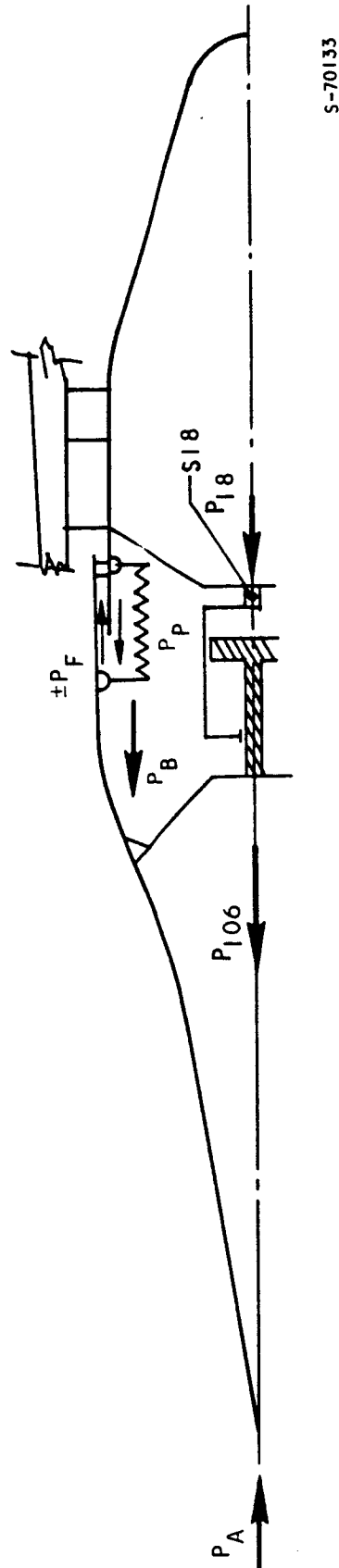
Figure 5.6-5. Spike and Actuator Load Schematics

Figure 5.6-6. Force at Aft End of Actuator (U)

TABLE 5.6-8

FORCE AT AFT END OF ACTUATOR (U)

Test	Run	P_1	P_2	P_3	P_4	P_5	P_6	P_7	P_8
41	7	1212	1233	1607	1855	1133	-165	1223	1122
	13	1102	1102	1837	2188	1532	106	1204	1147
	20	1795	1635	2186	2484	1738	372	1738	1876
	26	1965	1603	2231	2219	1235	-111	1314	1265
	28	1821	1507	2111	2353	1700	249	1337	1724
	37	1746	1380	1981	2194	1298	19	1107	1640
	38	1622	1173	1878	2049	1109	-162	970	1526
42	3	1321	1321	2223	2617	1691	257	1633	1205
	14	← Not Applicable →				1235	-250	1377	1389
	16	1488	1470	← No Spike Extension →					
	17	1504	1409	2074	2478	1765	268	1647	1837
	19	1692	1681	2286	2725	1835	399	1776	1989
	45	1663	1024	1620	1961	1524	556	1066	-

Minimum load during spike extension $\left(P_6\right)$

Load after spike is extended $\left(P_7\right)$

Load after model ejected from tunnel $\left(P_8\right)$

The pattern of the load variation was quite uniform throughout each test and similar to Figure 5.6-6.

5.6.2.2 Load Variations Due to Spike Position

The load measured at the aft end of the actuator as the spike was retracted or extended is tabulated in Table 5.6-9. Because the extension of the spike was much faster than the retraction, fewer data points were recorded during the 0.05-sec intervals used for data printout.

The governing load condition for the actuator design was the symmetrical inlet unstart case. This design condition and the corresponding load envelope measured during the test are shown in Figure 5.6-7. The loads recorded during the test are considerably less than the design loads, which were based upon a symmetrical unstart condition. No inlet unstart occurred for any of the tests.

5.6.2.3 Actuator Loads vs Total Tunnel Pressure

Two loads--the load before spike retraction (P_2) and the maximum load during spike retraction (P_4)--are plotted in Figures 5.6-8 and 5.6-9 as a function of reservoir total pressure. Load variation is a function of local rather than reservoir total pressure. Use of the latter was selected to permit direct tie-in with specific test runs, if desired. The measured load is shown to decrease as the tunnel pressure increases. This is due to the increased aerodynamic load acting on the spike, counteracting the load due to spike cavity pressurization.

5.6.3 Steady-State Stresses

The recorded strain gage signal was converted into digital form and the corresponding stress was calculated and printed out directly. Strain gage placement was limited by the accessibility of the structure and the operating temperature of the metal. It was known in advance that stresses during normal tunnel and SAM operation would be substantially lower than the design values for the flight environment. All gages selected were, nevertheless, based on the higher stresses and loads in order to insure adequate data under conditions of abnormal operation. Some strain gages were mounted on very stiff members (actuator legs) where deflection criteria limited the original design, and the design stresses were very low.

Maximum stresses were expected due to inlet unstart, which did not occur during the tests. A tunnel flow breakdown occurred as the SAM was being retracted during Test 42, Run 45, and resulted in higher than normal load for these conditions. Figure 5.6-3 also shows the effect of this flow breakdown. Maximum stress recorded on each strain gage, the test, and run when it occurred is shown in Table 5.6-10. The tensile yield strength of the materials at 600°F is shown for reference.

AIRESEARCH MANUFACTURING COMPANY
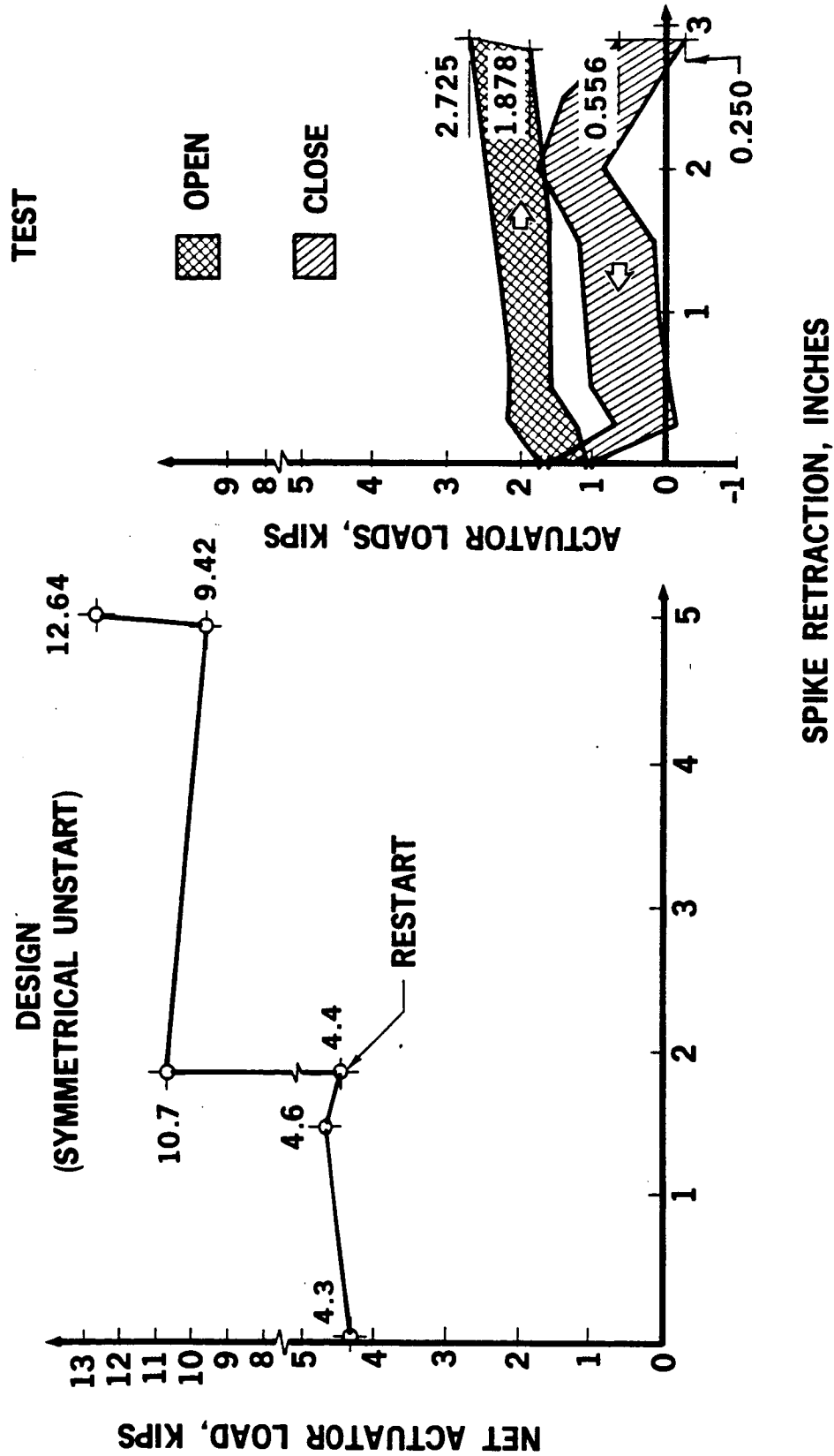Los Angeles, California

UNCLASSIFIED

TABLE 5.6-9

VARIATION OF ACTUATOR LOADS DURING SPIKE MOVEMENTS

Test	Run	Maximum Spike Retraction	Spike Movement, in.						
			0.0	0.25	0.5	0.75	1.0	1.5	2.0
41	7 →	2.80	1223	1225	1528	1528	1596	1697	1787
	← 7				1020		1178		
	13	2.89	1102	1837	1780	1780	1850	1916	2018
	13				140		350		1543
	20	2.86	1612	2186	2071	2071	2094	2197	2254
	20		1738		521		636	888	1749
	26	1.70	1615	1809	2074	2014	2074	2183	-
	26		1289	10	988		1181	1217	-
	28	2.87	1482	1773	1990	1978	2063	2075	2268
	28		1337	273			539	696	1750
	37	2.92	1330	1981	1831	1810	1799	1767	1874
	37			19	104		254	478	1320
	38	2.92	1194	1171	1686	1643	1643	1611	1686
	38		1034	19	141	77	30	1034	853
42	3	2.89	1344	2154	2108	2177	2258	2351	2374
	3		1633	257	317	384	477	604	1680
	14	2.89	Model was elevated into tunnel with spike retracted						
	14		1377	250			61	163	1447
	17	2.90	1409	2015	1967	2098	2146	2241	
	17		1670	292			684	1742	
	19	2.92	1692	2286	2238	2262	2369	2452	
	19		1692	482		636	767	1823	
	45	2.90	1024	1620	1535	1514	1492	1663	
	45			619		949	1471	1524	

NOTE: Numbers in upper row of each run represent loads during spike retraction. Numbers in the next lower row are loads during spike extension.

Figure 5.6-7. Actuator Loads vs Spike Movement (U)
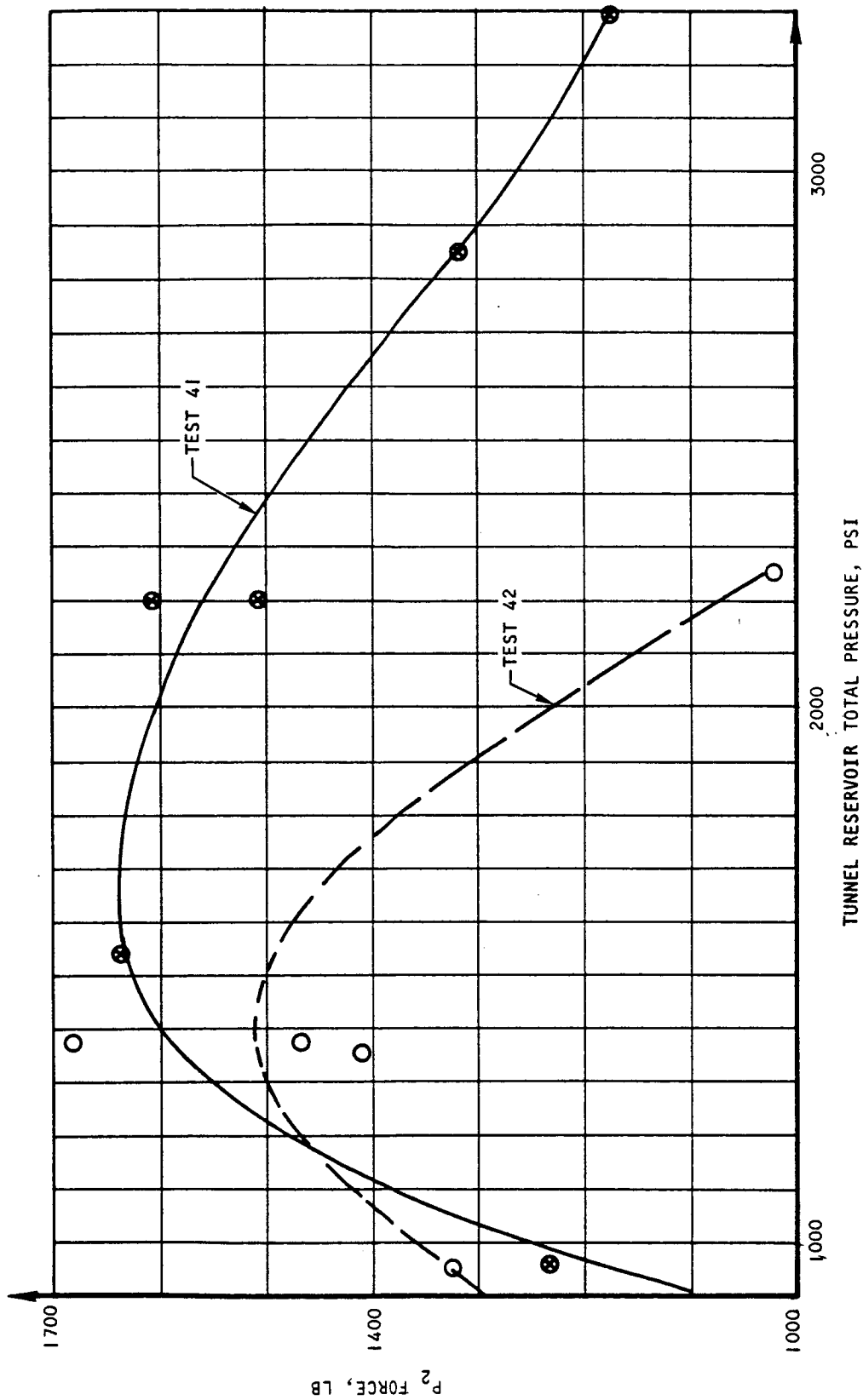
S-70126

Figure 5.6-8. P_2 vs Tunnel Total Pressure (U)

S-70136

AIRESEARCH MANUFACTURING COMPANY
Los Angeles, California

TUNNEL RESERVOIR TOTAL PRESSURE, PSI
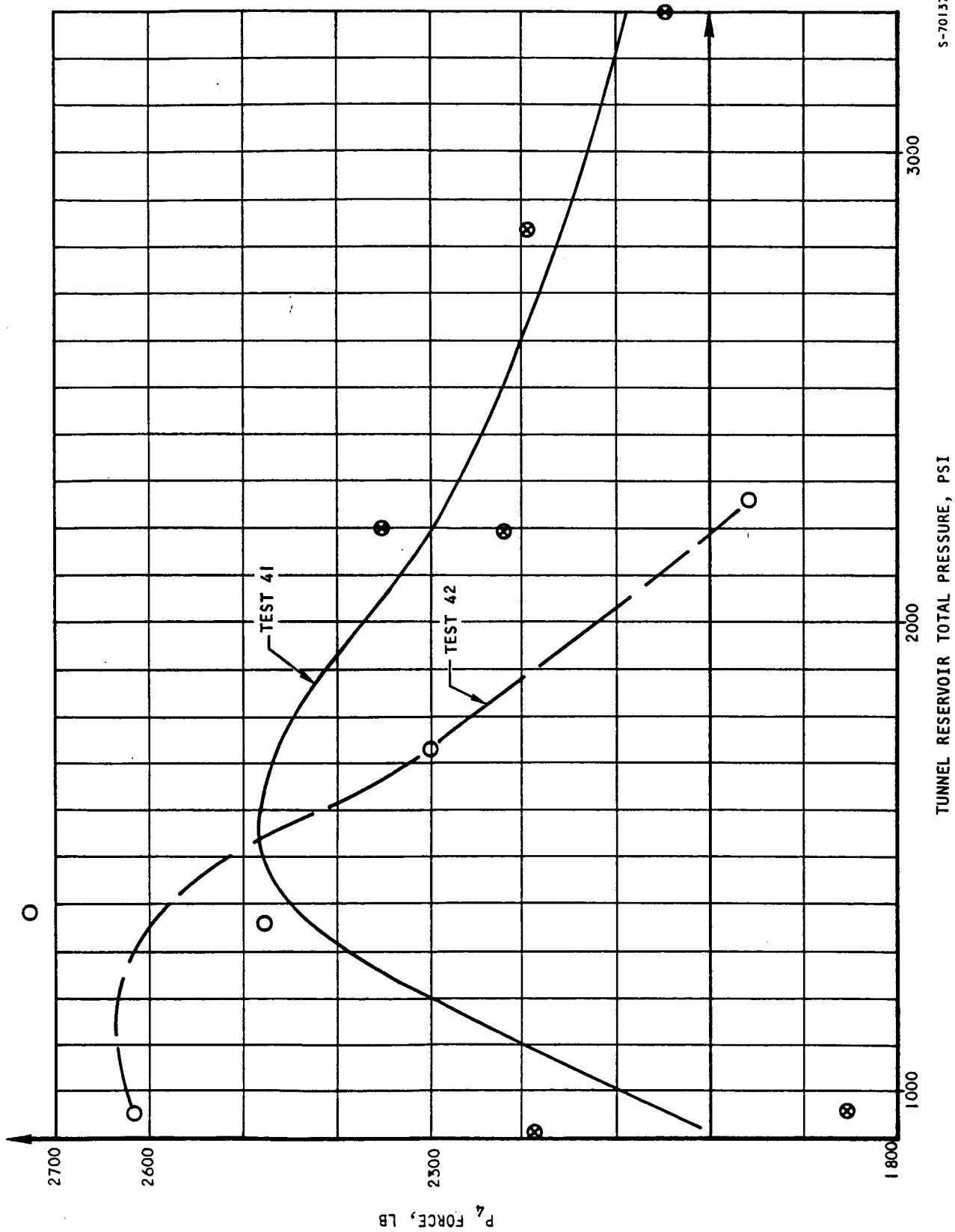
Figure 5.6-9. P_4 vs Tunnel Total Pressure (U)

S-70137

TABLE 5.6-10

MAXIMUM STRESSES (U)

Strain Gage No.	Maximum Stress, psi	When Occurred		Material	Tensile Yield Strength at 600°F, psi
		Test	Run		
1	8,698	41	53	Hastelloy X	36,000
2	11,466	41	53	Hastelloy X	36,000
3	1,168	41	5	Hastelloy X	36,000
5	2,235	42	45	4330 steel	147,000
6	2,528	41	53	4330 steel	147,000
7	1,086	42	45	4330 steel	147,000
12	3,534	42	45	17-4 PH	139,000
13	20,503	41	53	17-4 PH	139,000
16	6,892	41	53	Inconel 718	139,000
17	14,758	42	45	Inconel 718	139,000
18	7,524	42	19	4330 steel	147,000
19	16,112	41	5	4330 steel	147,000

The stress level at each observed point was quite low during the tests, as described in the previous paragraph, and well below the fatigue limit of the materials used in the SAM structures. Of the twelve gages recording loads, only S5 recorded any noticeable complete stress reversals, particularly during Test 41, Run 28, (shown in Figure 5.6-10) and Test 41, Run 7, although the stress levels were extremely low. Considering that some fluctuation of the stress level existed during all test runs, as in the typical example shown in Figure 5.6-10, it appears that the stress reversals indicated during Test 41, Run 28 were primarily due to a shifting of the mean stress above or below the zero-stress level with little or no vibratory stresses. Very low stress amplitudes (a few hundred psi) were superimposed on low mean-stress values, and all

this occurred between 8 to 30 Hz, resulting in less than 60×10^3 cycles during the whole test program.
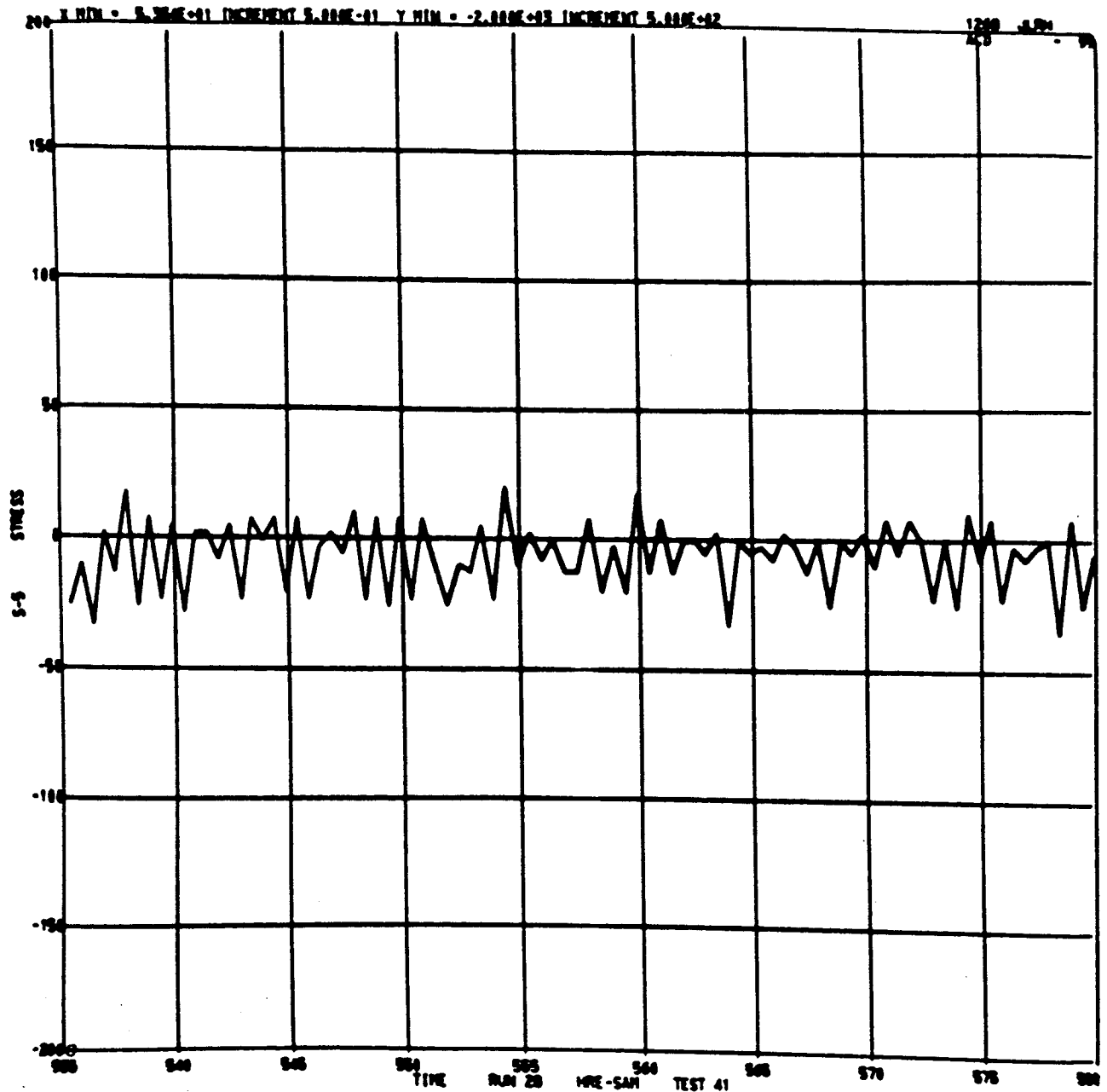
Figure 5.6-10. Test Showing Maximum Number of Stress Reversals

5.6.4 Dynamic Loads

The engine was designed to withstand dynamic loads due to inlet unstart combined with vibratory and inertia loads generated by the operation of the X-15A-2 aircraft.

In support of the design, dynamic analysis of the HRE was performed to develop a mathematical model that would enable evaluation of structural response for various types of loadings. The mathematical model was a simplified analog of the real structure, with sufficient similitude to provide accurate analysis results for the response of critical engine component parts. The main area of concern was the dynamic response to low frequency inputs to the HRE. Accurate description of total system mass, system mass distribution, and flexibility between the major mass elements was desirable in order to produce a sufficiently large matrix and obtain good accuracy for the lower frequencies. The principal difficulty in computing the amplitude of structural response to dynamic loading at system resonances was uncertainty in the estimation of structural damping.

The engine was represented for analysis as a system of elastically coupled rigid-mass elements shown in Figure 5.6-11, where each mass element had six degrees of freedom. The total number of degrees of freedom was six-times the number of mass elements representing the engine structure. The following 12 mass elements were selected, and a block diagram of the model, along with a sketch of the structure, is shown. The mount frame is denoted as mass Element 1, and it is shown with a flexible coupling to relative ground and Element 2. Element 2 is the key component in the entire model. It consists of the portion of the outer shell that runs from the front mounting ring to the aft mounting ring, and combines with the six struts and the portion of the inner shell from the manifold ring at the front end of the struts to the manifold ring located at the aft end of the struts. This multiple-ring construction is essentially rigidly connected radially by the six struts, and axially by the shear-stiffness of the shell sections between the rings. Element 3 is the trailing edge portion of the outer shell; Element 4 is the nozzle structure; Element 5 is the leading edge portion of the outer shell; and Element 6 is the fore-portion of the inner shell. The aft spike, spike mounting cone, and the fore spike are considered as separate elements, and they are denoted as Elements 7, 8, and 9, respectively. The inner actuator and outer actuator parts have been separated and denoted as Elements 10 and 11, respectively. Finally, Element 12 is the control computer, which was part of the flight design but not of the SAM. These twelve lumped masses lead to a 72-deg-of-freedom system. By virtue of its axisymmetric structure and mass distribution, the in-plane and out-of-plane responses are independent of each other; hence, the 72-deg-of-freedom problem was reduced to two 36-deg-of-freedom systems.

In order to be able to study the dynamic behavior of the engine structure, a total of seven accelerometers were installed on the structure, as shown in Figure 5.6-12. Of the seven, four were uniaxial and three were triaxial. The uniaxial accelerometers and their orientations are summarized as follows:

A1 Z-direction, and located on the No. 1 leg of the actuator

A2 X-direction, and located on the No. 4 leg of the actuator
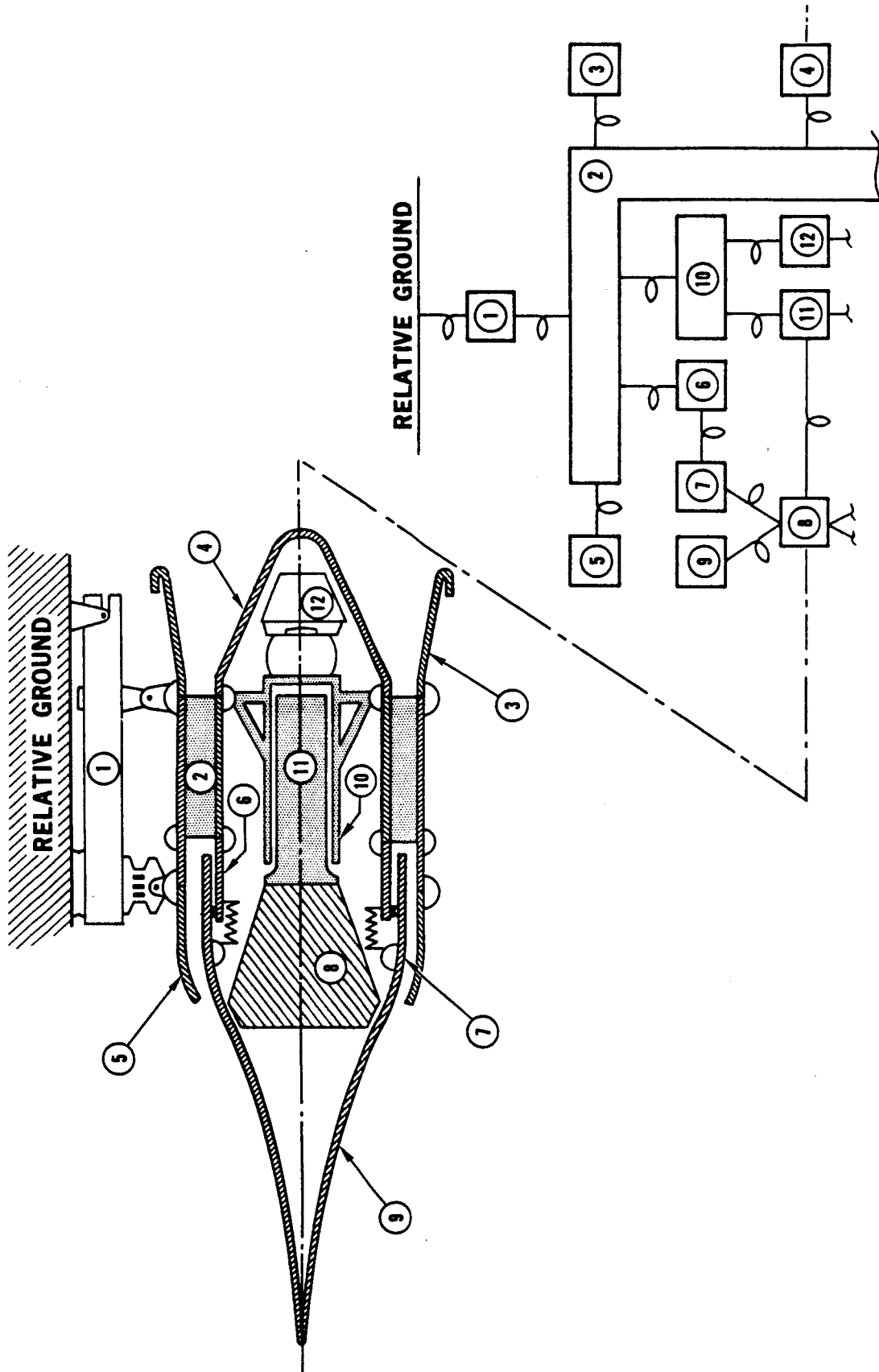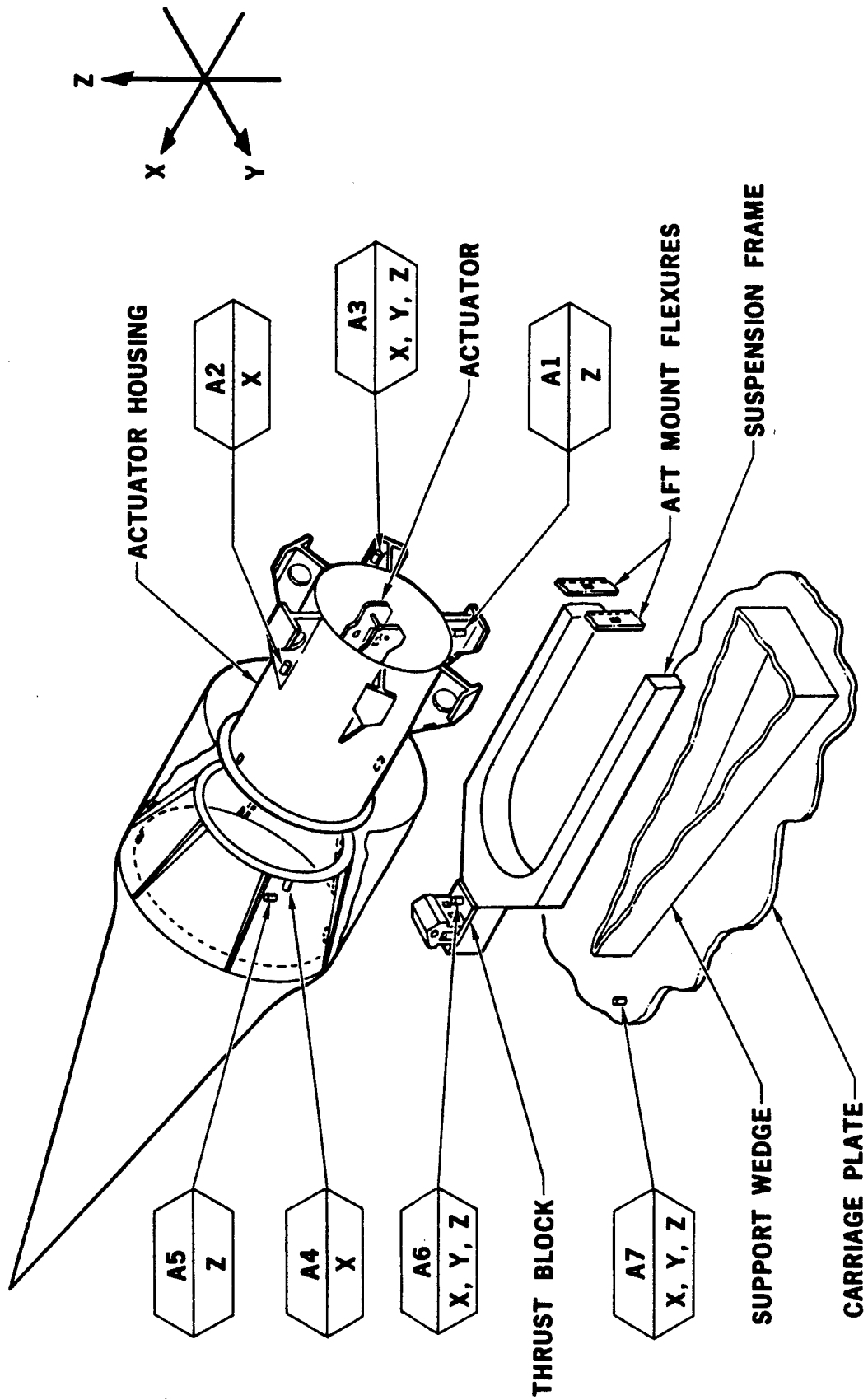
Figure 5.6-11. HRE Vibration Model

S-70123

Figure 5.6-12. Accelerometer Locations

GARRETT AIRESEARCH MANUFACTURING COMPANY
Los Angeles, California

UNCLASSIFIED

A4 X-direction, and located on the flange of the spike cone

A5 Z-direction, and located on the spike cone near A4

The triaxial accelerometers are:

A3 located on the No. 2 leg of the actuator

A6 located on the deflection (thrust) block

A7 located on the far side of the carriage plate in front of the support
     wedge

Each accelerometer was assembled to a Kistler impedance converter, and the combined units were calibrated prior to installation into the engine. Maximum peak output voltage from each accelerometer was predicated upon a maximum of 20-g peak acceleration at each accelerometer. The data from all 13 channels were recorded on one FM tape having a frequency response from 5 to 10,000 Hz at a tape speed of 30 ips. The test data were tabulated at every 0.01 sec in terms of instantaneous "g" units. Further processing of the test data produced acceleration plots; power spectra and histogram plots; and printout, computed maximum, minimum, and mean values of the accelerations utilizing the NASA-Langley Time Series Analysis Program. The data from the various channels were intended to provide information regarding resonant frequencies, mode shapes, and potential resonant amplifications.

The following nine runs were selected for the study of accelerometer data:

Test 41, Run 7   Test 42, Run 3
            13   14
            17   16
            26   17
            28

No useful data was obtained after Test 42, Run 43, apparently due to a coolant leak from the spike outlet bellows which rendered most accelerometers inoperative.

The maximum negative and positive instantaneous "g" levels of the runs studied are shown in Table 5.6-11. The selection of the runs was based on increasing total tunnel pressure level. The maximum "g" values shown in the table represent extremely short duration peaks in the data. With the exception of a single data point, these responses were all below the design response limit.

Acceleration-time plots of the above-mentioned runs were prepared for the periods of the tests when significant changes of model position or geometry were made. These plots represent wide-band random vibration. The most important parameters representing such vibration are the power density spectra and the magnitude-probability distribution. The power density spectra is a presentation of the dynamic excitation, indicating the distribution of vibration energy throughout the frequency range. For wide-band random vibration the vibration energy is distributed throughout the entire frequency range, and the

CONFIDENTIAL

TABLE 5.6-11

MAXIMUM INSTANTANEOUS ACCELERATIONS (U)

Axis	Gage	Maximum g		Design
Z	A7	19.04	-12.60	
	A6	4.00	- 3.75	
	A3	8.23	- 4.19	
	A1	4.46	- 4.01	
	A5	11.30	-26.50	
X	A7	14.61	-16.67	Input: 3.0 g
	A6	2.20	- 6.66	Response 20 g
	A2	13.7	- 3.02	
	A3	5.45	- 5.08	
	A4	7.67	- 3.33	
Y	A7	7.89	-9.69	
	A6	5.89	-5.29	
	A3	8.32	-3.45	

power density is a continuous spectrum of frequency. Sharp peaks at discrete frequencies indicate that the vibration is composed of discrete frequency vibrations superimposed upon random vibration. Such combined spectrum is representative of random environmental vibration excitation that includes the effects of structural resonances contributed by structural members in the load transmission path.

The NASA-Langley Time Series Analysis Program used the histogram technique for the estimation of probability densities. This technique divides both the magnitude scale and the time scale of the random vibration time history into a finite number of discrete increments. The number of occurrences (N_i) for which the instantaneous magnitude (F_i) has a value between the limits of (F) and $(F + \Delta F)$ is determined, (F) being the specific level of instantaneous magnitude and (ΔF) being the size of the discrete increments into which the magnitude scale of the random vibration has been divided. Plotting the ratio of

occurrences $N = \Sigma N_i$ as a function of the measured instantaneous magnitude $\left(F_i\right)$ provides a histogram (bar graph), such as that illustrated in Figure 5.6-13. The fraction of the total number of occurrences (N_i/N) for which the instantaneous magnitude $\left(F_i\right)$ will have a value between the limits of (F) and $(F + \Delta F)$, defines the relative frequency of occurrence. The probability of occurrence $P(F)$, of the instantaneous magnitude (F), is given by:

$$P(F) = \lim_{N \to \infty} (N_i/N)$$

The probability density $p(F)$, representing the probability per unit magnitude, is given by the ratio of the probability $P(F)$ to the magnitude interval ΔF over which the probability is defined; this may be expressed mathematically as follows:

$$p(F) = P(F)/\Delta F = \lim_{N \to \infty} (N_i/N)/\Delta F$$

The limitations of the histogram method are:

The division of the data into arbitrary increments (bins) may distort the distribution if there is curvature within an increment.

A large number of increments (degrees of freedom) is required to define the shape of a distribution, resulting in a very jagged histogram.

However, if the shape of the probability-density function of the data is not known, then the use of the histogram technique gives this shape, and from this a smooth probability distribution can be generated. Additional parameters for checking the form of the probability function and accuracy were calculated by the equations shown in Appendix C.

5.6.4.1 Forcing Functions

It was known well before the beginning of the tests that a 27- to 30-Hz vibration existed due to the tunnel combustor operation. Review of the data revealed no structural resonance either to this frequency or multiples of this frequency. No other sinusoidal forcing function was detected during testing.

5.6.4.2 Acceleration Levels

Acceleration-time history plots were the basic dynamic data recorded during testing and used as a basis for data reduction. Several typical samples are shown. Longitudinal (X-directional) acceleration-time history plots for two accelerometers are shown in Figures 5.6-14 and 5.6-15 for Test 41, Run 17. Accelerometer A7X is attached to the model support carriage and it showed higher instantaneous accelerations than A4X, which is attached to the spike cone. The instantaneous acceleration levels were quite low throughout the recorded tests. More meaningful information of the vibration level is shown on the power spectra and the magnitude-probability distribution, the histogram. Test 42, Run 19, accelerometer time history, power spectra, and histogram are shown in Figure 5.6-16 to show the relation between these functions. The
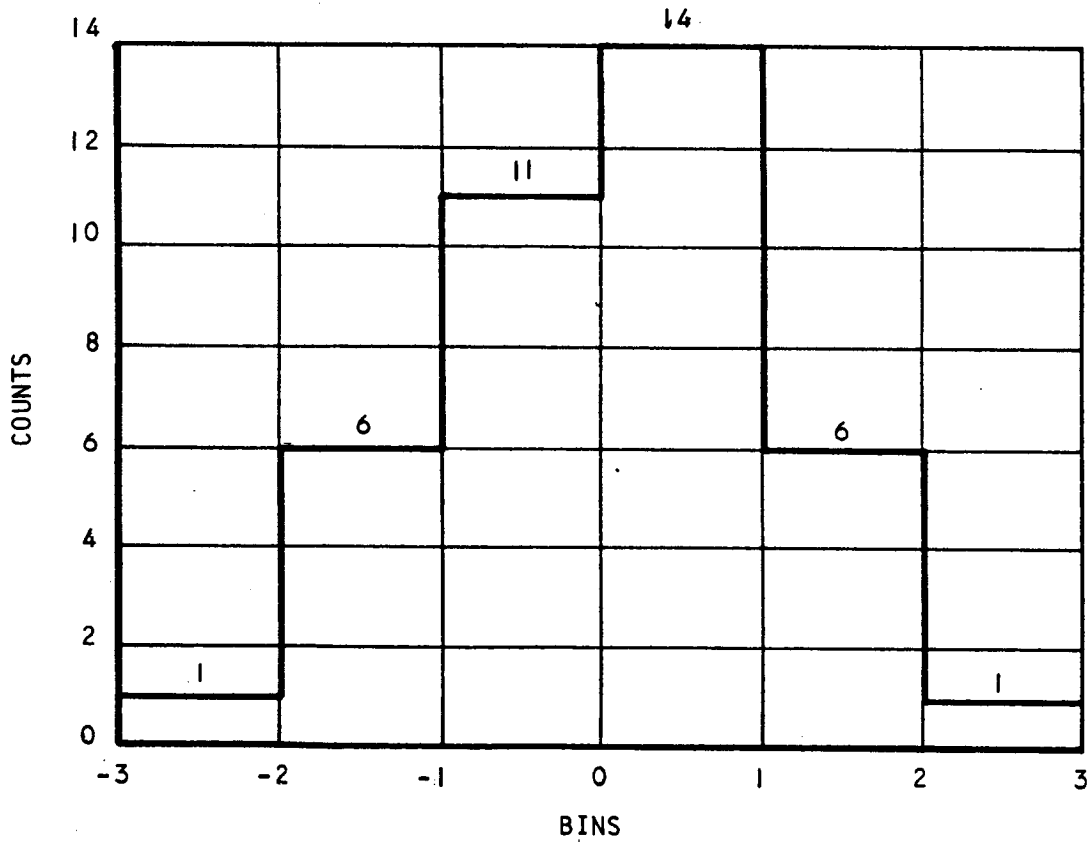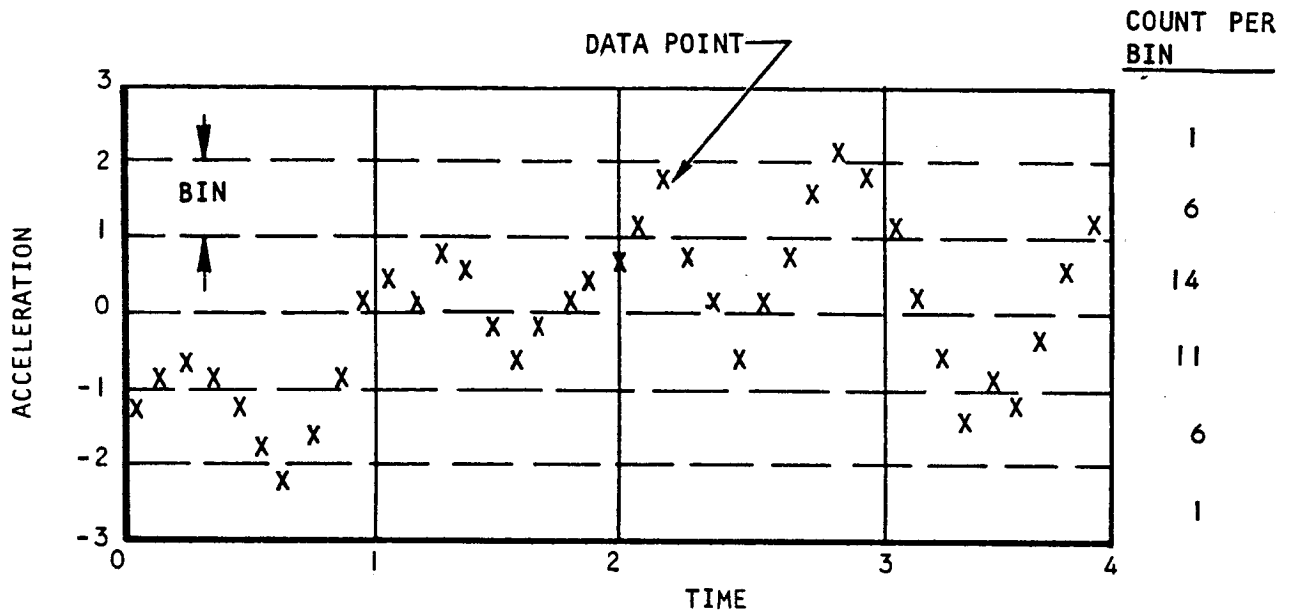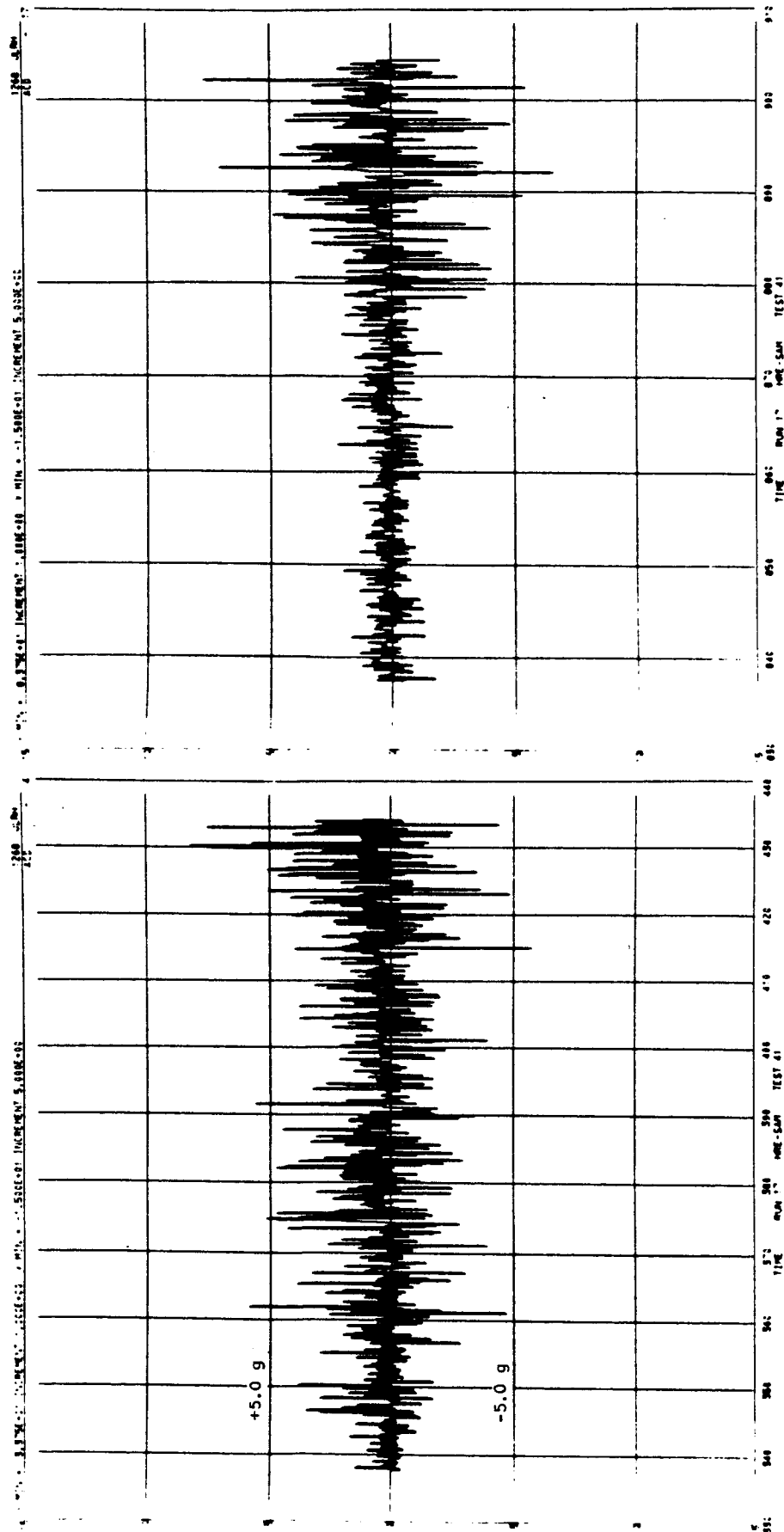
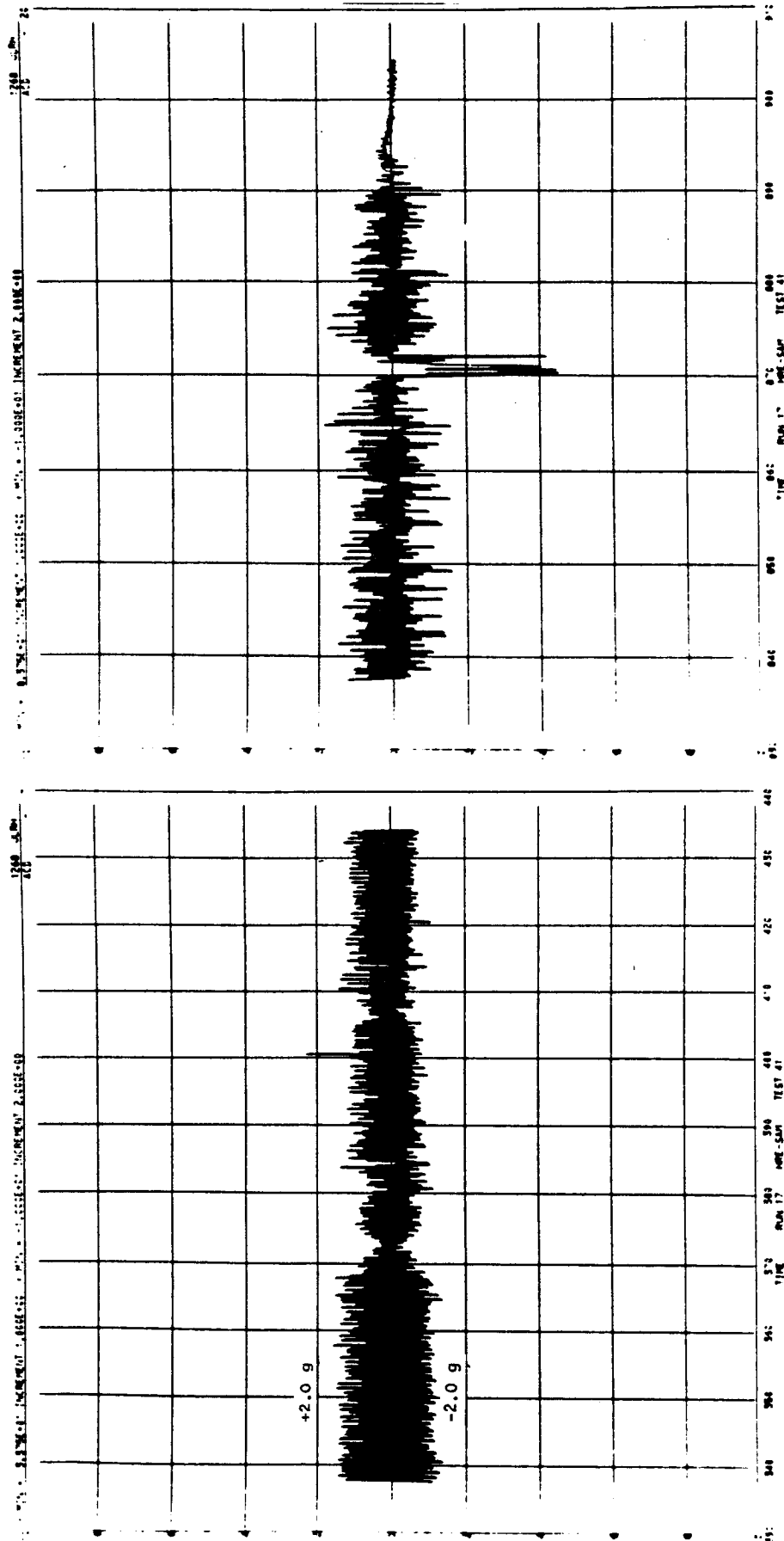Figure 5.6-13.   Example of Recorded Data and Histogram
Relation

Figure 5.6-14. SAM Test 41, Run 17 Acceleration-Time History, A7X Accelerometer (U)

S-70125

AIRESEARCH MANUFACTURING COMPANY
Los Angeles, California

Figure 5.6-15. SAM Test 41, Run 17 Acceleration-Time History, A4X Accelerometer (U)
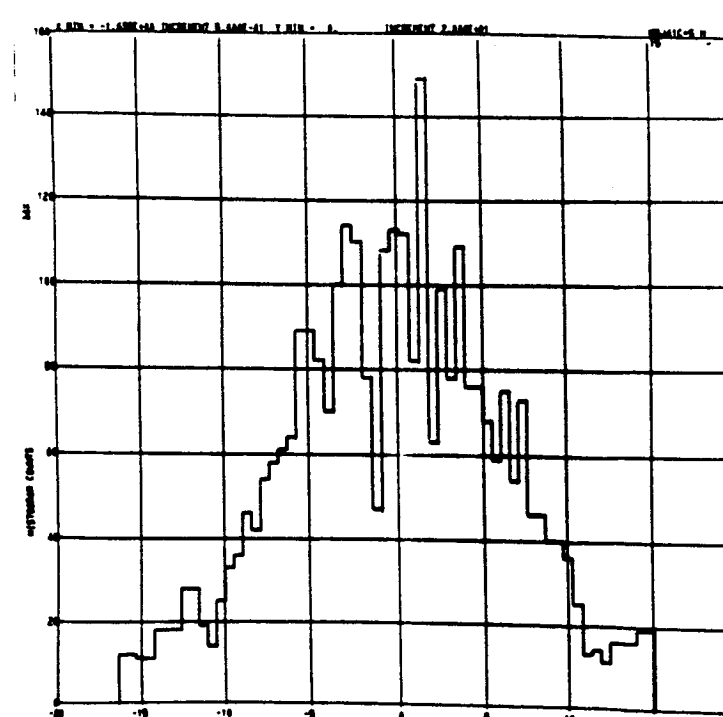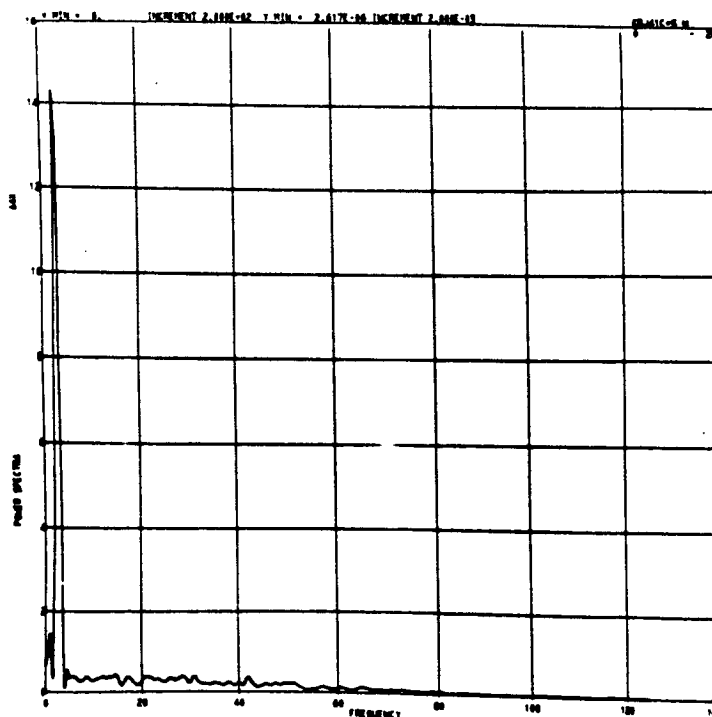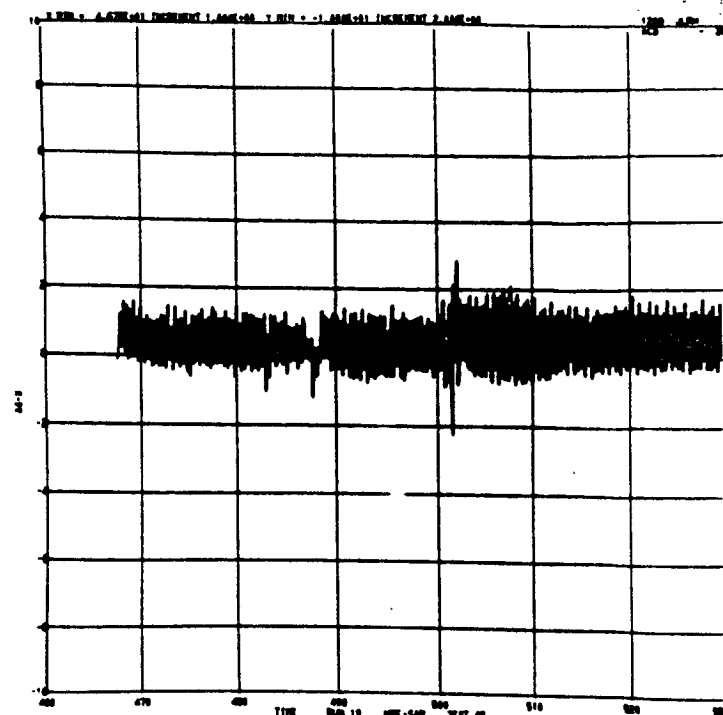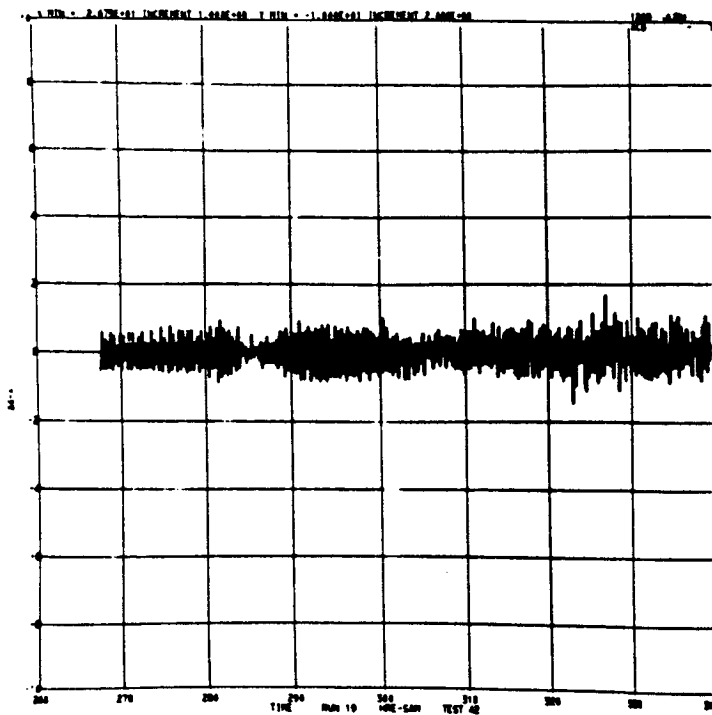
S-70124

+2.0 g

-2.0 g

Figure 5.6-16. SAM Test 42, Run 19 A4X Accelerometer Data (U)

acceleration-time history again indicates quite low instantaneous accelerations representing a wide-band random function. The power spectra shows a high peak at 3 cps for most tests, including this one. This peak is the result of a peculiarity in computing and has no significance. Data plots of the other runs also indicated low vibration levels; therefore, only the rms magnitudes, mean values, and features indicating the probability distribution in an abbreviated form were tabulated.

The total rms magnitude of a wide-band random vibration F(t) is given by:

$$F_{rms} = \sqrt{\frac{1}{T} \int_0^T \left[F(t)\right]^2 dt}$$

When dealing with the statistical properties of random vibration, the rms magnitude F_{rms} is called the standard deviation, where σ is defined in Appendix C of this report. A tabulation of the standard deviation for the nine runs studied is shown in Table 5.6-12. Of the 117 values shown in this table, only 29 are above 1.0 g; the maximum being 5.48 g. The number of readings exceeding g levels of 0.5, 1.0, 2.0, 3.0, and 5.0 are shown in Figure 5.6-17.

Mean acceleration values are shown in Table 5.6-13. Numerous values substantially exceed zero, indicating that a random phenomena was recorded.

The magnitude-probability distribution is given on the histogram plots, and an example of these was shown in Figure 5.6-15 earlier. All of the histogram plots show a large number of bins (degrees of freedom) and, as a consequence, very jagged histograms were plotted. In order to provide an easy review of the test data analyzed, third central moments (skewness, β) and fourth central moments (kurtosis, K) values were tabulated in Table 5.6-14. Only 13 runs indicate a resemblance to Gaussian distribution, having a skewness value of near 0 and a kurtosis value of about 3. The chi-square value, Y, the degrees of freedom (number of bins), K, and $\chi^2_{K;\alpha}$ (chi-square value for (K) degrees of freedom and α Type I error) are tabulated in Table 5.6-15. The tabulation indicates that distribution of the data cannot be accepted as normal because in all cases $Y >> \chi^2_{K;\alpha}$.

5.6.4.3 Responses

Several components of the engine are quite rigid elements. The vibration analysis indicated that the lowest natural frequency of the most flexible assembly--the spike-actuator-strut unit--is about 140 Hz, a fairly high frequency. It was felt that this assembly would be the only component that would be excited at its own natural frequency. The dynamic response of the engine as a unit would essentially be that of a rigid body.

To verify the behavior of the structure and correlate the acceleration level between various parts, instantaneous acceleration readings in the X, Y,

TABLE 5.6-12

SAM TEST STANDARD DEVIATIONS OF NINE RUNS (U)

Test	Run	A6X	A6Y	A6Z	A7X	A7Y	A7Z	A4X	A5Z	A1Z	A2X	A3X	A3Y	A3Z
44	7	1.5356	1.0326	0.8430	1.5618	0.7437	2.0671	2.8289	5.4800	1.0315	3.3853	1.1423	33.0192	2.3574
	13	1.0631	0.9895	0.7450	0.5083	0.3579	0.7394	1.7781	2.9068	0.6896	2.2354	0.7706	0.0121	1.4545
	17	0.2798	0.1860	0.1831	2.6848	2.7319	5.2222	0.5136	1.4997	0.2009	0.6085	0.2402	0.0156	0.5304
	26	0.6167	0.3857	0.3298	0.6901	0.1929	0.5997	0.7712	2.3645	0.4366	0.8168	0.4612	0.0097	0.6168
	28	0.5806	0.2872	0.3334	0.5207	0.1844	0.6638	0.9007	0.4953	0.4055	1.0725	0.4144	0.0229	0.9443
42	3	0.2247	0.1579	0.1300	1.6089	0.5180	1.1636	0.4411	0.5307	0.1677	0.5261	0.1814	0.0061	0.4446
	14	0.5873	0.3483	0.4528	1.3446	0.2418	0.6467	0.8065	1.1597	0.4867	0.9511	0.4941	0.0121	0.8102
	16	0.5837	0.7170	0.7385	3.8275	0.4172	0.5527	0.3571	0.3654	0.4080	0.3827	0.5585	2.0325	0.4733
	17	0.4523	0.3426	0.3647	0.3778	0.1178	0.4661	0.7064	3.0885	0.3245	0.7895	0.3723	0.0162	0.6680

Invalid Data—Defective Accelerometer

$$\sigma = \sqrt{\frac{1}{N-1} \sum_{i=1}^{N} \left(x_i - \bar{x} \right)^2}$$
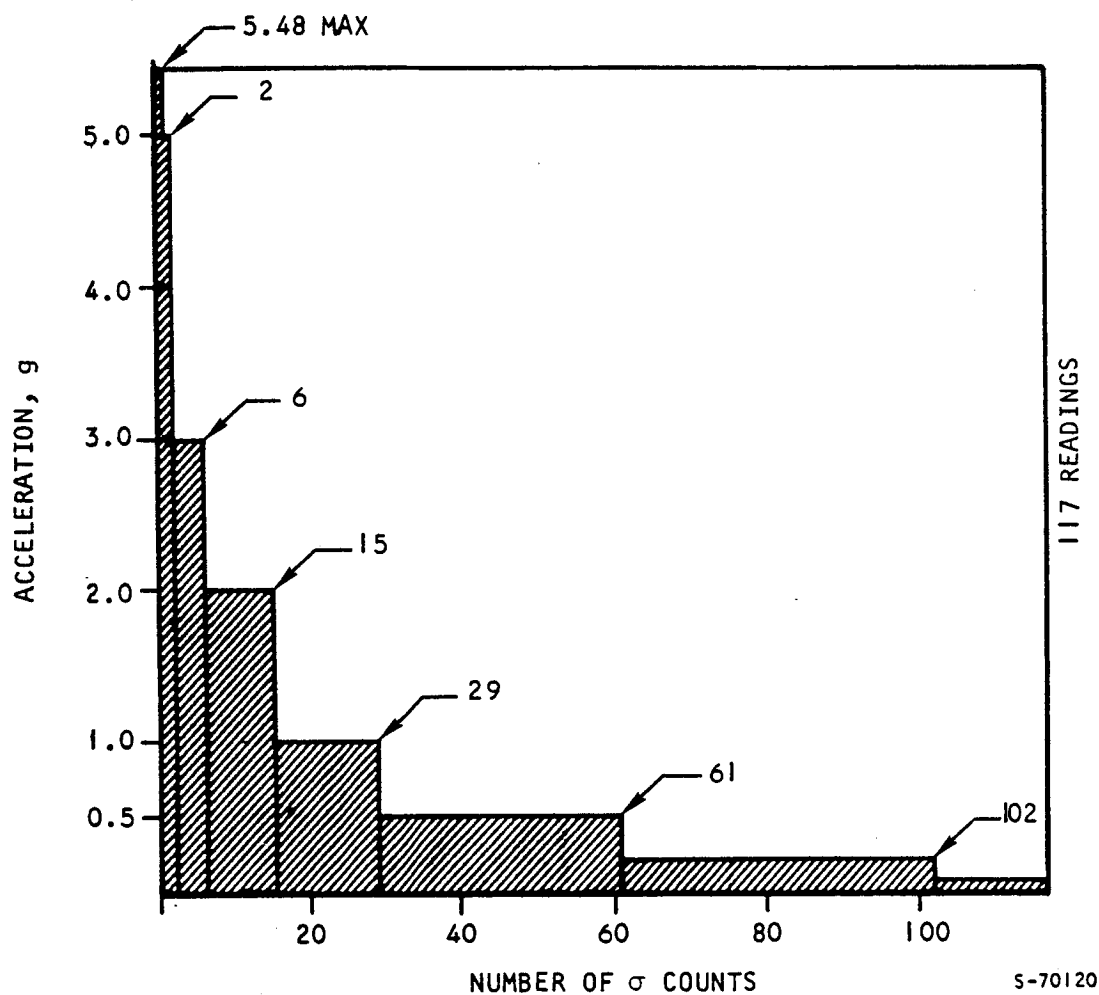
Figure 5.6-17.   SAM Test Vibration Magnitude Evaluation (U)

SAM TEST MEAN ACCELERATION VALUES OF NINE RUNS (U)

Test	Run	A6X	A6Y	A6Z	A7X	A7Y	A7Z	A4X	A5Z	A1Z	A2X	A3X	A3Y	A3Z
41	7	-2.1575	1.7133	0.79622	4.1283	2.5085	-0.3907	1.8978	1.6729	1.2917	7.1021	2.1323	0.1482	3.076
	13	-1.8000	2.0379	0.6980	4.1515	2.1127	-0.0778	1.4119	1.4076	-0.5596	6.2578	2.0887	2.6595	3.026
	17	0.1026	0.0987	0.0508	-2.9543	-2.1417	3.7883	0.1176	1.5860	0.21513	0.1328	0.0790	0.1180	0.2276
	26	0.0578	0.0428	-0.0491	0.0178	-0.2299	-0.0638	0.3808	1.6391	1.1042	0.3642	0.0168	-0.1198	-0.158
	28	0.0846	0.0321	0.0254	-0.0231	-0.3242	-0.0420	0.0431	0.0575	0.0690	0.0532	0.0167	0.0371	-0.2074
42	3	0.0865	0.0577	0.1007	-0.1897	0.1231	-0.5779	0.1400	0.2229	0.2361	0.21917	-0.0874	0.0662	0.0250
	14	0.10825	0.0554	-0.0428	-0.5172	-0.3345	0.0534	0.3003	0.3310	0.9464	0.4131	0.0401	0.0784	0.0707
	16	0.0311	-0.0737	-0.1115	-1.2453	-0.7709	-0.0632	-0.2868	0.0960	0.5010	0.1986	-0.0891	1.3582	-0.0038
	17	0.0705	0.0251	-0.0376	-0.0322	0.0195	0.0378	0.2035	0.7366	0.7694	0.3352	0.0206	0.0485	-0.2363

$$\bar{X} = \frac{1}{N} \sum_{i=1}^{N} x_i$$

TABLE 5.6-14

SAM TEST - RANDOM VIBRATION MAGNITUDE
PROBABILITY DISTRIBUTION FEATURES (U)

Third Central Moment (Skewness)

$$\beta = \frac{\frac{1}{N-1}\sum_{i=1}^{N}(x_i - \bar{x})^3}{\sigma^3}$$

Fourth Central Moment (Kurtosis)

$$K = \frac{\frac{1}{N-1}\sum_{i=1}^{N}(x_i - \bar{x})^4}{\sigma^4}$$

TEST	RUN	β/K	A6X	A6Y	A6Z	A7X	A7Y	A7Z	A4X	A5Z	A1Z	A2X	A3X	A3Y	A3Z
41	7	β	-0.350	0.107	0.030	-2.705	-6.639	0.910	0.180	-0.971	0.289	0.134	0.068	0.326	0.171
		K	2.146	3.149	2.977	28.666	279.200	18.878	1.676	4.400	2.735	1.568	2.583	3.995	1.721
	13	β	-0.297	-0.001	0.318	0.240	-0.071	0.071	0.147	-1.388	-0.357	0.169	0.046	0.189	0.012
		K	2.425	3.056	3.492	2.205	2.581	2.427	1.727	5.726	3.415	1.703	2.876	2.728	1.803
	17	β	-0.553	-0.047	-0.384	-0.362	-1.026	-0.133	0.190	-0.471	0.423	0.241	-0.434	-0.375	0.201
		K	2.684	3.325	3.398	2.305	3.025	2.841	1.698	3.491	2.446	1.612	2.399	2.060	1.607
	26	β	-0.335	-0.190	-0.300	0.164	0.177	-0.135	0.154	-0.351	0.429	0.289	-0.372	-1.680	0.450
		K	2.208	3.360	3.066	1.908	4.266	1.895	3.136	3.037	2.475	1.613	2.617	7.609	1.893
	28	β	-0.474	-0.125	-0.427	-0.208	-1.182	0.046	0.309	-0.817	0.535	0.264	-0.579	0.701	0.344
		K	2.127	3.008	3.465	2.502	9.324	4.013	1.589	4.301	2.927	1.454	2.723	3.445	1.713
42	3	β	-0.431	0.009	0.238	-1.642	1.993	-2.564	0.248	-0.049	0.081	0.366	-0.324	-1.481	0.154
		K	2.685	3.648	3.490	11.977	24.902	11.586	1.756	5.299	2.406	1.759	2.727	3.402	1.698
	14	β	0.001	0.036	-0.414	-1.921	-4.347	-0.068	-0.457	-0.648	-0.002	0.480	0.033	-1.547	0.383
		K	2.84	2.705	6.214	7.989	35.037	5.121	1.784	3.499	1.895	1.806	2.171	5.201	1.701
	16	β	-1.144	-1.132	-0.427	0.905	-2.985	-1.106	-1.708	-3.481	-0.731	-2.511	-1.359	1.658	-2.83
		K	7.804	6.887	3.389	11.056	18.135	6.950	10.723	22.180	5.397	15.399	8.935	5.088	16.332
	17	β	0.023	0.071	-0.434	-0.128	-4.086	-0.171	0.251	0.128	0.032	0.33	0.076	-0.973	0.389
		K	3.1036	2.716	9.607	2.976	45.021	2.835	2.437	2.574	2.284	1.620	2.808	3.282	1.718
															VOID

Legend

Gaussian Distribution β | 0.00 |
                        K | 3.00 |

Mesokurtic   K = 3 | |

Platykurtic   K<3 | X.XX |

Leptokurtic   K>3 | Y.YY |

Negative Skewness = Elongated Left Tail

Positive Skewness = Elongated Right Tail

S-70122

TABLE 5.6-15

SAM TEST DATA NORMALITY TEST (U)

Test	Run	Funct.	A6X	A6Y	A6Z	A7X	A7Y	A7Z	A4X	A5Z	A1Z	A2X	A3X	A3Y	A3Z
41	7	γ	787	623	851	6.4×10^6	3.36×10^{14}	1130	1964	1083	936	2445	702	960	2245
		K	55	37	37	14	11	19	59	45	42	60	44	55	60
		$\chi^2_{K;\alpha}$	73.3	52.2	52.2	23.7	19.7	30.1	78.0	61.7	58.1	80.2	60.5	73.3	80.2
	13	γ	964	411	716	439	447	1223	2016	6570	1400	1913	884	571	1575
		K	41	43	34	19	15	30	55	41	29	59	34	3	48
		$\chi^2_{K;\alpha}$	56.9	59.3	48.6	30.1	25.0	43.8	73.3	56.9	42.6	78.0	48.6	7.82	65.2
	17	γ	1100	1012	755	893	7776	87.5	1437	222	1312	2159	1145	1619	2497
		K	50	37	53	43	51	53	50	44	50	64	48	4	57
		$\chi^2_{K;\alpha}$	67.5	52.2	71.0	59.3	68.7	71.0	67.5	60.5	67.5	83.7	65.2	9.49	75.6
	26	γ	657	281	496	1308	1200	772	449	156	663	1933	696	48740	1542
		K	56	40	52	43	37	57	46	51	57	62	56	3	59
		$\chi^2_{K;\alpha}$	74.5	55.8	69.8	59.3	52.2	75.6	62.8	68.7	75.6	81.4	74.5	7.82	78.0
	28	γ	1171	438	533	797	398400	177	2425	686	759	3595	832	483	1852
		K	60	50	40	38	31	36	62	42	52	64	58	6	66
		$\chi^2_{K;\alpha}$	80.2	67.5	55.8	53.4	45.0	51.0	81.4	58.1	69.8	83.7	76.8	12.6	86.0
42	3	γ	919	1450	930	371400	125300	980200	1370	942	771	1721	872	3450	1920
		K	52	38	39	35	25	34	60	42	49	65	49	0	60
		$\chi^2_{K;\alpha}$	69.8	53.4	54.6	49.8	37.6	48.6	80.2	58.1	66.3	84.8	66.3	0	80.2
	14	γ	551	416	63260	1151	6.1×10^8	425	537	107	415	2894	566	1646	2663
		K	51	48	35	37	18	43	42	54	49	66	47	3	61
		$\chi^2_{K;\alpha}$	68.7	65.2	49.8	52.2	28.9	59.3	58.1	72.2	66.3	86.0	64.0	7.82	80.2
	16	γ	6272	37590	312	39650	3.26×10^7	6817	442200	1.78×10^8	1330	2.2×10^8	7202	8282	3.5×10^6
		K	33	36	42	22	33	37	31	29	38	31	30	54	33
		$\chi^2_{K;\alpha}$	47.4	51.0	58.1	33.9	47.4	52.2	45.0	42.6	53.4	45.0	43.8	72.2	47.4
	17	γ	861	406	6511	12960	6.41×10^{11}	188	2915	345	950	2733	488	6347	2831
		K	59	45	41	35	22	28	48	49	54	65	54	2	63
		$\chi^2_{K;\alpha}$	78.0	61.7	56.9	49.8	33.9	41.3	65.2	66.3	72.2	84.8	72.2	5.99	82.5

$$\gamma = \sum_{i=1}^{(K+2)} \frac{(N_i - NP_i)^2}{NP_i} \leq \chi_{K;\alpha}$$

and Z directions were plotted, and the X-directional acceleration-time history
is shown in Figure 5.6-18. The time interval selected was with the model in
the tunnel, but the spike not yet retracted. In the X- (fore- and aft-) direc-
tion, the three accelerometers which are attached to the actuator and the spike
(A2X, A3X, A4X) show the highest acceleration level. Substantially lower in-
stantaneous acceleration levels were recorded on the thrust block (A6X) and the
carriage plate (A7X). In the Y-direction, very low acceleration was measured
inside the engine (A3Y). This was somewhat amplified at the thrust block level
(A6Y) and a considerably lower acceleration level was recorded at the carriage
plate. Z-directional (vertical) acceleration displays similar behavior to that
in the X-direction.

Studies of other time periods--elevation of model into the tunnel, spike
retraction and extension, and lowering of the model--revealed similar patterns,
indicating that substantial structural damping exists. This conclusion is fur-
ther supported by the instantaneous maximum and rms accelerations tabulated
elsewhere.

5.7 VISUAL OBSERVATION OF STRUCTURE

As a result of the tests, a number of conditions which are pertinent to
the design were visually observed in the structure. The operation of the SAM
was not apparently impaired by any of the observed conditions. Each of these
conditions is discussed in the following sections.

The general performance of the cooled structure was satisfactory. Speci-
fically, no fatigue cracks, as evidenced by leakage, could be observed in the
hot skins of the shells. The inserts--that is, the fuel injectors and instru-
mentation inserts--showed no signs of overheating. There was also no leakage
at the inserts so far as these areas were inspectable. This indicates that
no basic design or manufacturing problems exist with the basic structure.

5.7.1 Foreign Object Damage

Figure 5.7-1 shows selected areas on the tip section of the cowl leading
edge with the different types of foreign object damage sustained by the leading
edge. The photo on the left shows a complete perforation of the nickel skin of
the leading edge tip. The hole is about 1/16 in. diameter. The dent shown in
the center photo is about 1/16 in. deep and has a small leak. This dent is
deep enough to completely block off the coolant passage behind the stagnation
line. The figure on the far right shows a dent on the external surface of the
leading edge tip section remote from the stagnation line. The deformation
here is sufficiently deep to have closed some of the 0.020-in.-high fin passages.

All of the damage shown here occurred fairly early in the test program.
The dent in the right photo occurred during the sixth test run (Test 41, Run
17); the dent in the center photo during the seventh test run (Test 41, Run 20);
and the hole in the left photo during the ninth test run (Test 42, Run 11).
Numerous other damage areas exist on the leading edge, several as severe as
those shown. None of these areas shows signs of distress or overheating as a
result of subsequent testing, much of which was at heating conditions which were
far more severe than in these early runs. In particular, the leading edge was
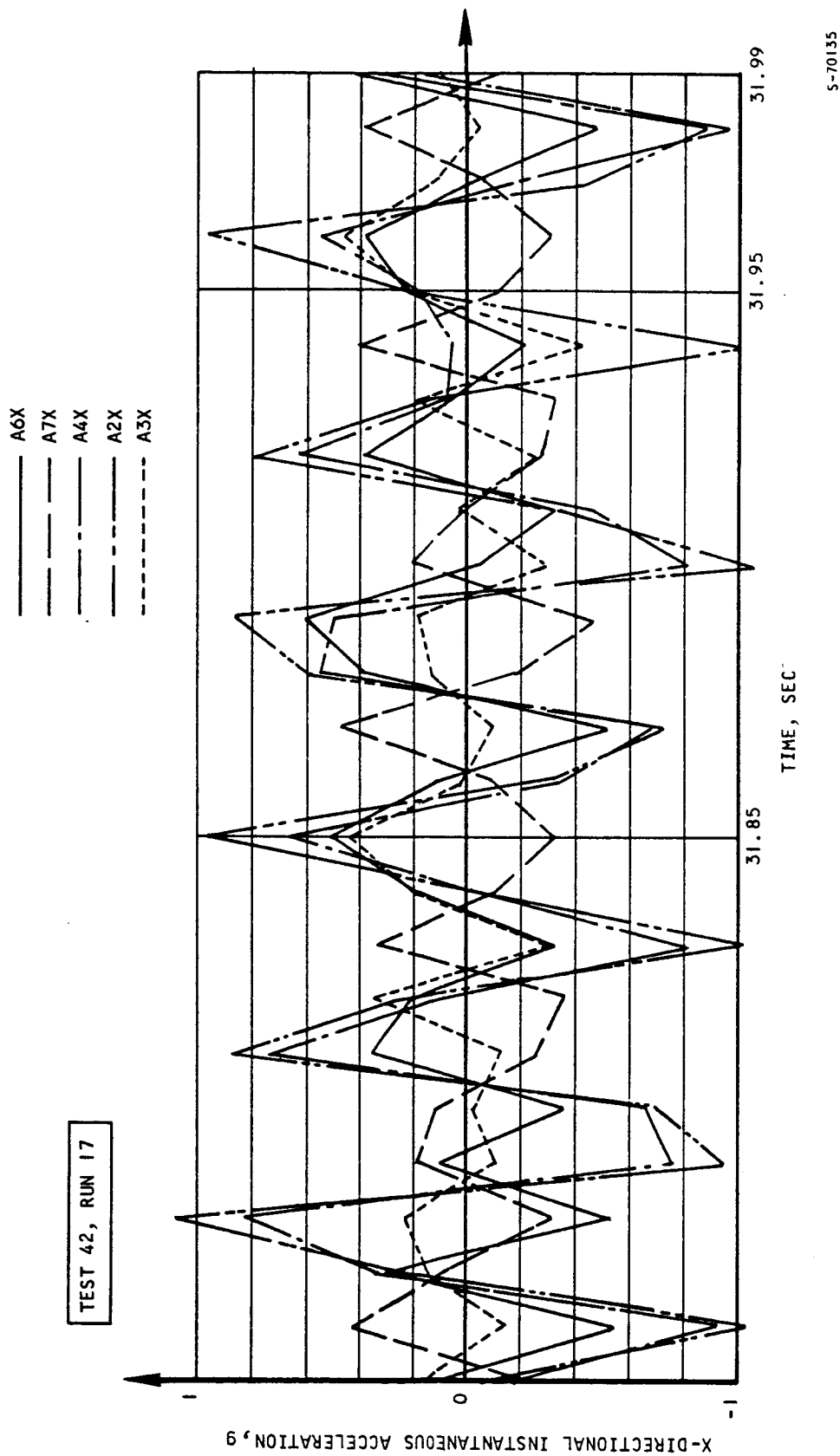
Figure 5.6-18. Instantaneous Acceleration, X Direction (U)

S-70135

GARRETT AIRESEARCH MANUFACTURING COMPANY
Los Angeles, California

F-13831

Figure 5.7-1. Leading Edge Foreign Object Damage

run with shock-on-lip and at angle of attack at the 3300 psia, 3400°R tunnel total conditions (Test 41, Run 53). The conclusion from this is that the leading edge, as designed, has considerable tolerance toward foreign object damage. A basic requirement for this type of tolerance, however, is the internal coolant flow routing, which is perpendicular to the leading edge stagnation line. Cooling can also be provided by flow parallel to the stagnation line, a configuration that was investigated during the program. For the latter, there will be a complete loss of cooling for the type of damage shown in the center photo and a partial loss of cooling as a result of a leak like that in the left-hand photo.

5.7.2 Leakage

As discussed above, there was leakage from the leading edge tip area as a result of foreign object damage. In addition, leakage was observed in the spike coolant outlet bellows and around the strut cutouts in the inner and outer shells.

5.7.2.1 Bellows

Figure 5.7-2 is a schematic of the coolant bellows configuration. The design requires a 5-in. stroke within an extended length of only 11.5 in. The bellows assembly outside diameter is 2 in. and the tube diameter is 1.25 in. Retraction of the spike causes extension of the bellows from the fully compressed condition. The bellows material is Inconel 718.

The failure in the bellows was evident as a large leak, with gas blowing through the gap between the coolant outlet tube and the bellows assembly shell. Inspection of the bellows is not possible with the SAM assembled. The probable point of failure is in the weld joints of the convolutions, which are highly stressed. Table 5.7-1 shows results of tests of the bellows. A single bellows was bench-tested at the conditions shown, with nitrogen as the pressurizing gas. The cycles imposed on the bellows during the SAM test are listed in chronological sequence of application. By comparison with the bench tests, failure was premature. Without inspection of the failure, the reason for this cannot be determined.

TABLE 5.7-1

SPIKE COOLANT OUTLET BELLOWS TEST RESULTS

	Temp, °F	Stroke, in.	Cycles
Bench Test	1000	3.5	503
	1000	4.5	10
SAM Test	900	2.9	39
	60	2.3-4.5	50
	900	3.9	1

UNCLASSIFIED
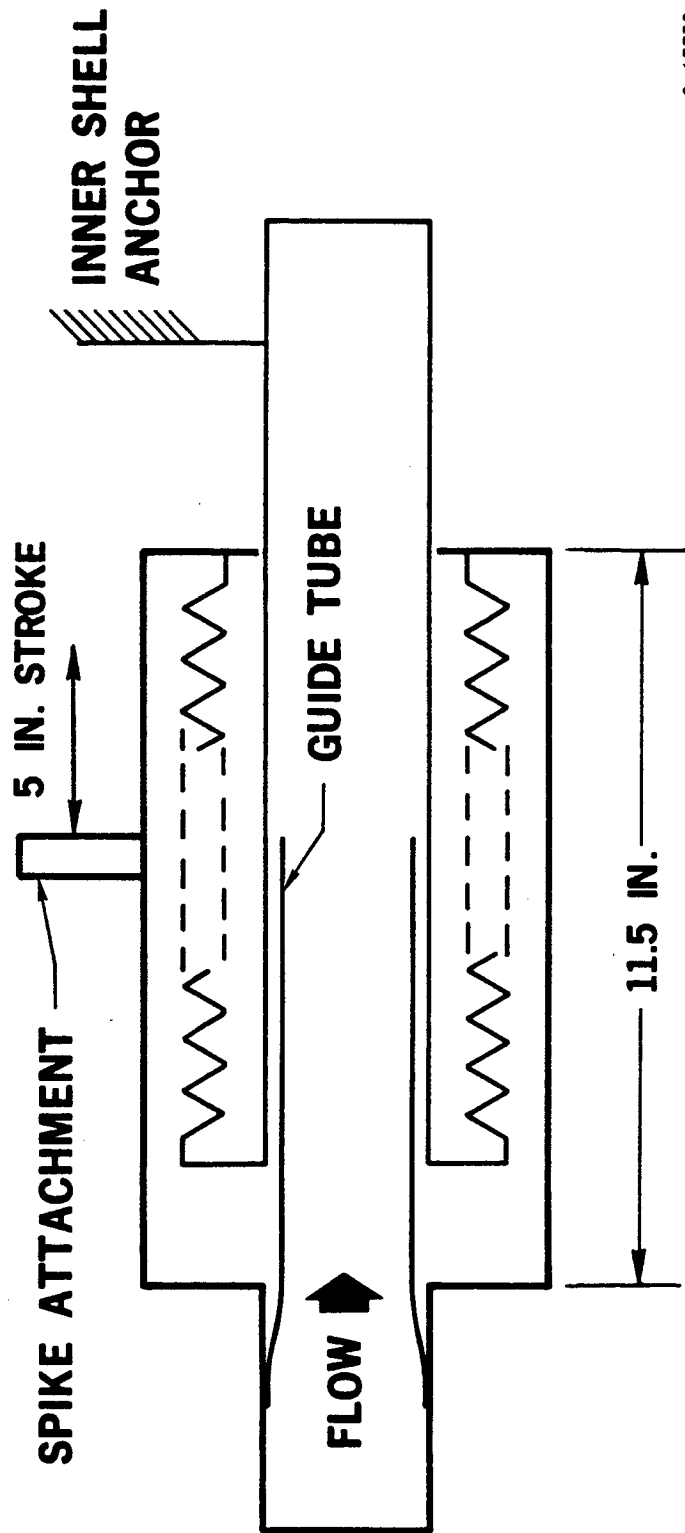
Figure 5.7-2. Configuration of Spike Coolant Outlet Bellows

UNCLASSIFIED

From the design point of view, modification of the available bellows envelope in the HRE would appear desirable and would be recommended in place of the present envelope. The high stroke-to-length ratio results in high stresses and allows little margin for manufacturing variances.

5.7.2.2 Shell Strut Cutouts

Leakage of hydrogen occurred at the forward end of several of the strut cutouts. It is most likely that the leakage was from either the hot skin-to-header joint or the strut socket-to-shell joint as shown in the enlarged view of Figure 5.7-3. Leakage from the strut side is not considered likely, and actual determination of the leakage area would require disassembly of the SAM. The reasons for suspecting the indicated areas as the cause of the leakage are as follows:

(a) A tooling-positioning problem resulted in undercutting of the headers at the forward end of some of the cutouts. Although repaired, the integrity of the joint may not have been fully restored.

(b) The braze joint between the strut socket and the inner shell required repair at a number of areas as a result of a braze-filler alloy application problem. Loss of seal in one or more of these repair areas is possible.

Both of the above conditions reflect specific problems which are associated with manufacturing of first-run parts and do not appear to be inherent in the design. Thus, during the component wind tunnel tests of the struts, gas heating conditions were more severe than in the SAM wind tunnel tests. The results of the component tests showed that the strut cutout region was structurally satisfactory for a greater number of cycles than imposed during SAM tests. Differences in constraint between the component test assembly and the SAM can influence the results but are not believed to have been important.

5.7.3 Outerbody Flange Bolt Damage

After Test 41, Run 53 it was observed that the cowl leading edge was displaced forward and slightly tilted with respect to its normal, installed position. Closer inspection, obtained by removing the water-cooled forward cowl panels, showed that the leading edge and outer shell flanges were completely separated. The leading edge was being held in place by the coolant crossover tubes connecting the leading edge and the outer shell. Pressurization of the engine cavity by the hot ram air was observed in the data and by inspection of the cavity. There was, however, no secondary damage to the structure as a result of the flange separation. Specifically, no hydrogen leakage occurred. There was also no visible evidence of overheating of the cold structure. Some of the silicone rubber that coated the fiberglass insulation used in various areas of the outerbody cavity vaporized and coated parts of the engine cavity. Figure 5.7-4 is a general view of the flange area following the final test.

The bolts and nuts were collected and have been photographed, Figure 5.7-5.

FIN STRIPS

0.050 JOINT

0.060 GAP

A

A

COLD SHELL

STRUT SOCKET

SECTION A-A

0.050

0.11

0.060

BRAZE
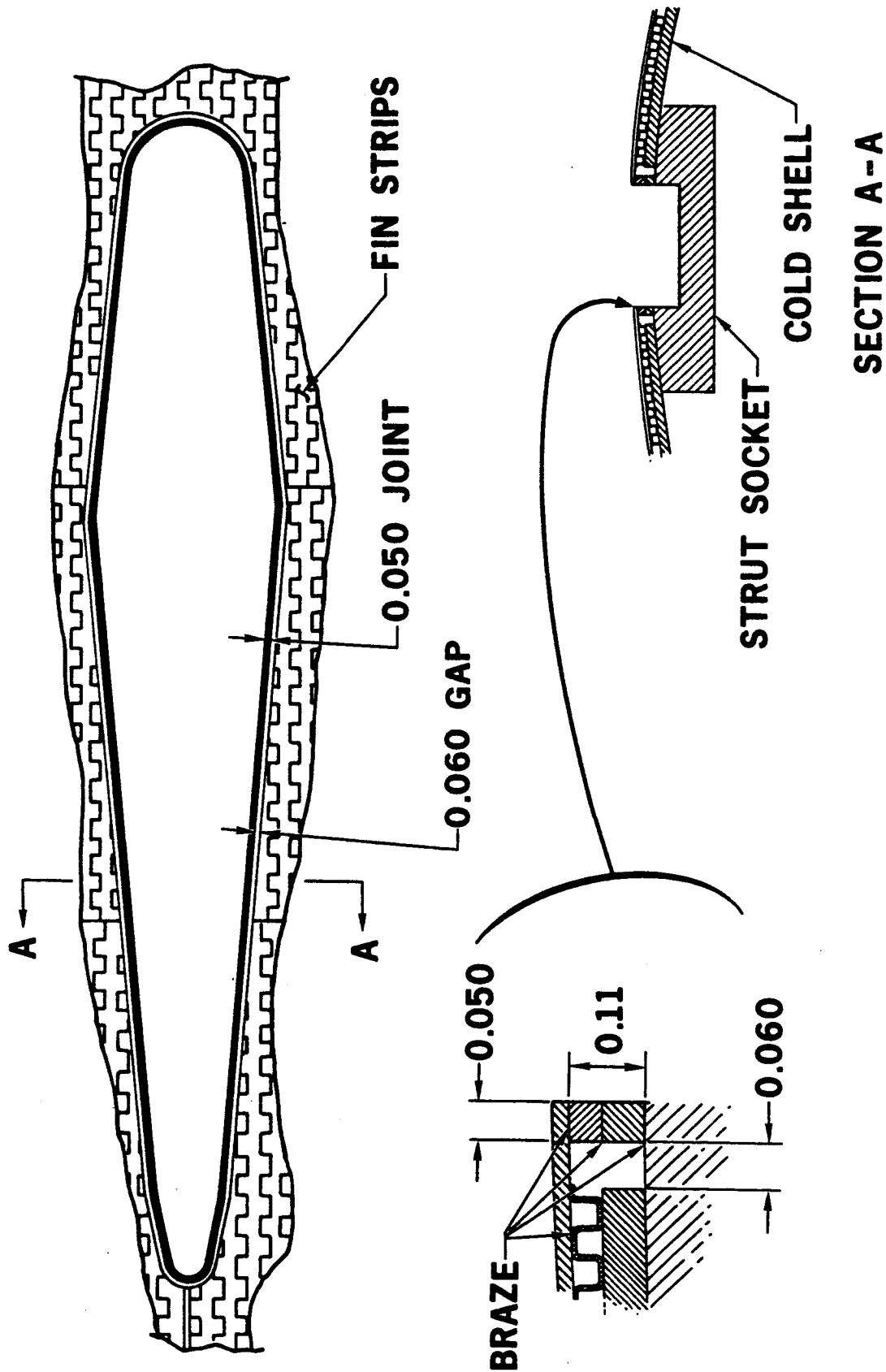
Figure 5.7-3. Joint Configuration of Shell Strut Cutout

AIRESEARCH MANUFACTURING COMPANY
Los Angeles, California

71-7702
Page 5-174
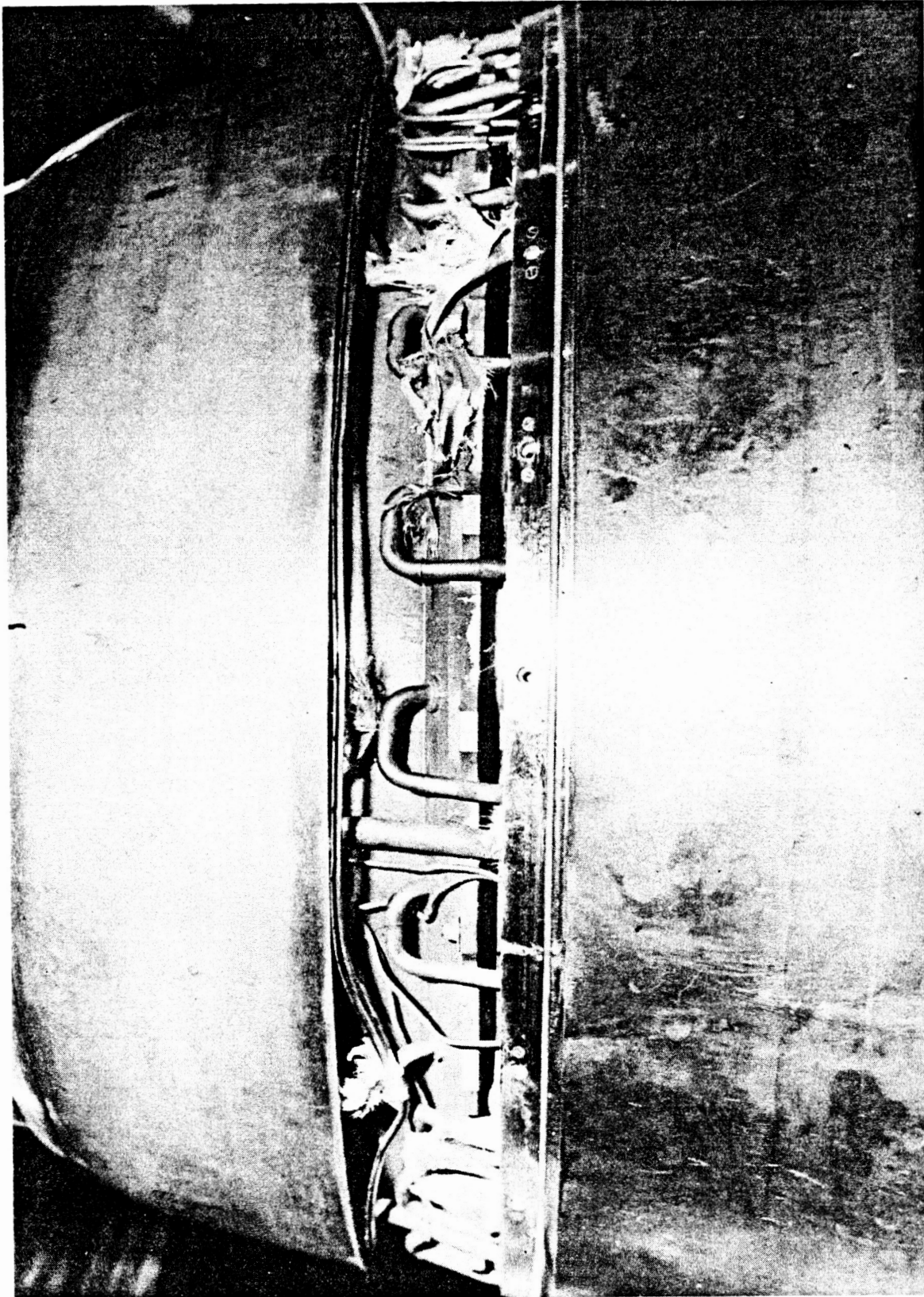
UNCLASSIFIED

F-13827

Figure 5.7-4. Leading Edge/Outer Shell Flange Area
After Final Test

UNCLASSIFIED
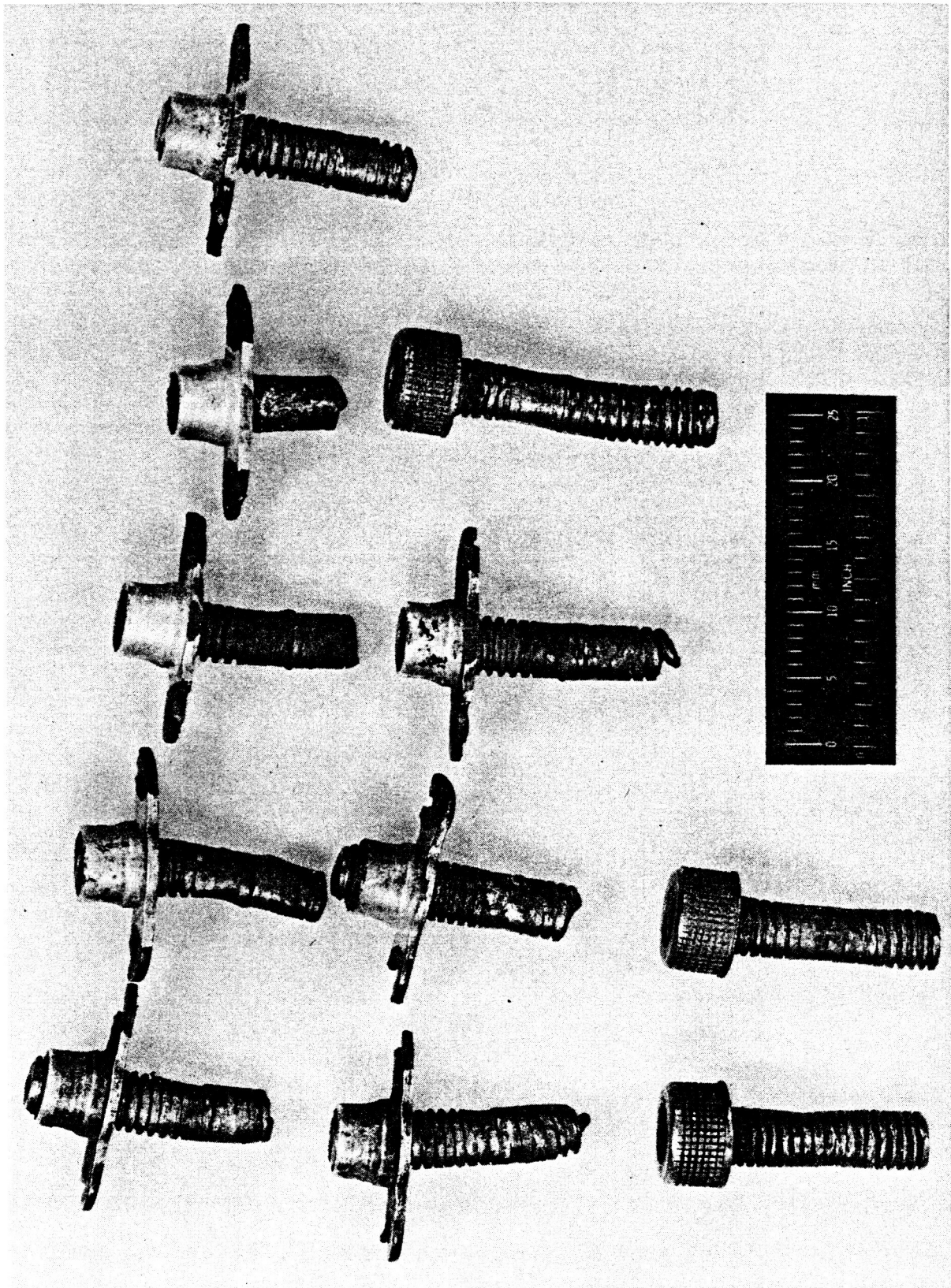
71-7702
Page 5-175

F-13829

Figure 5.7-5. Outerbody Flange Bolts After Final Test

Inspection showed that

    (a) All of the 24 bolts had failed.

    (b) Twenty-one of the 24 bolts had ruptured. One bolt came out entire.

    (c) Thirteen nut plates remained in place on the leading edge flange.

    (d) Eight nut plates broke off the flange.

    (e) Three nut plates are missing.

    (f) Two bolts are missing.

Reasoning from the similarity of test conditions and the appearance of the hardware, it is probable that progressive degradation was involved in producing the bolt damage. In addition, the undercooling during Test 41, Run 52, probably resulted in a relatively large amount of damage.

A condition possibly related to the bolt damage in the flange involves the clearances between the leading edge tip and the spike, as shown in Figure 5.7-6. The as-installed gap between the leading edge and the spike was measured prior to start of the tests and is indicated. After Test 42, Run 25, the gap had increased non-symmetrically. Another measurement after Test 41, Run 42, indicated essentially the same gap as measured after Test 42, Run 25. The pressure loads during the test were lower than would be required to distort the leading edge. Since the leading edge was installed to the outer shell by use of a rounding-up clamp, some residual out-of-roundness would be retained in the tip area, as observed. It is considered likely that following some thermal cycling, the tightening torque on the bolts was lost, resulting in relaxation of the flange to its original out-of-round condition. This does not account for the increase in average gap but merely offers an explanation of the shape of the gap. After the final test, the flange diameters on the leading edge were measured. These are plotted with respect to the minimum flange diameter. The out-of-round condition of the flange is again observed and is in the direction indicated by the leading edge tip measurements. The following sections contain an analysis of possible causes of the damage to the leading edge/outer shell flange area.

5.7.3.1 Thermal Analysis

As a result of the flange and bolt damage, transient heat transfer analyses were performed to determine whether structural temperature differences could have contributed to the observed condition. Two types of temperature differences were investigated. The first was the structural temperature difference between the two halves of the coolant crossover manifold. The effects that create this structural temperature difference are (1) unsymmetrical coolant heating due to different hydrogen heat transfer coefficients on each half of manifold during transient test startup, and (2) the additional heating of the forward outer shell half of the manifold only, due to hot hydrogen flow through the outer shell injector tubes. Each of these effects was considered separately.
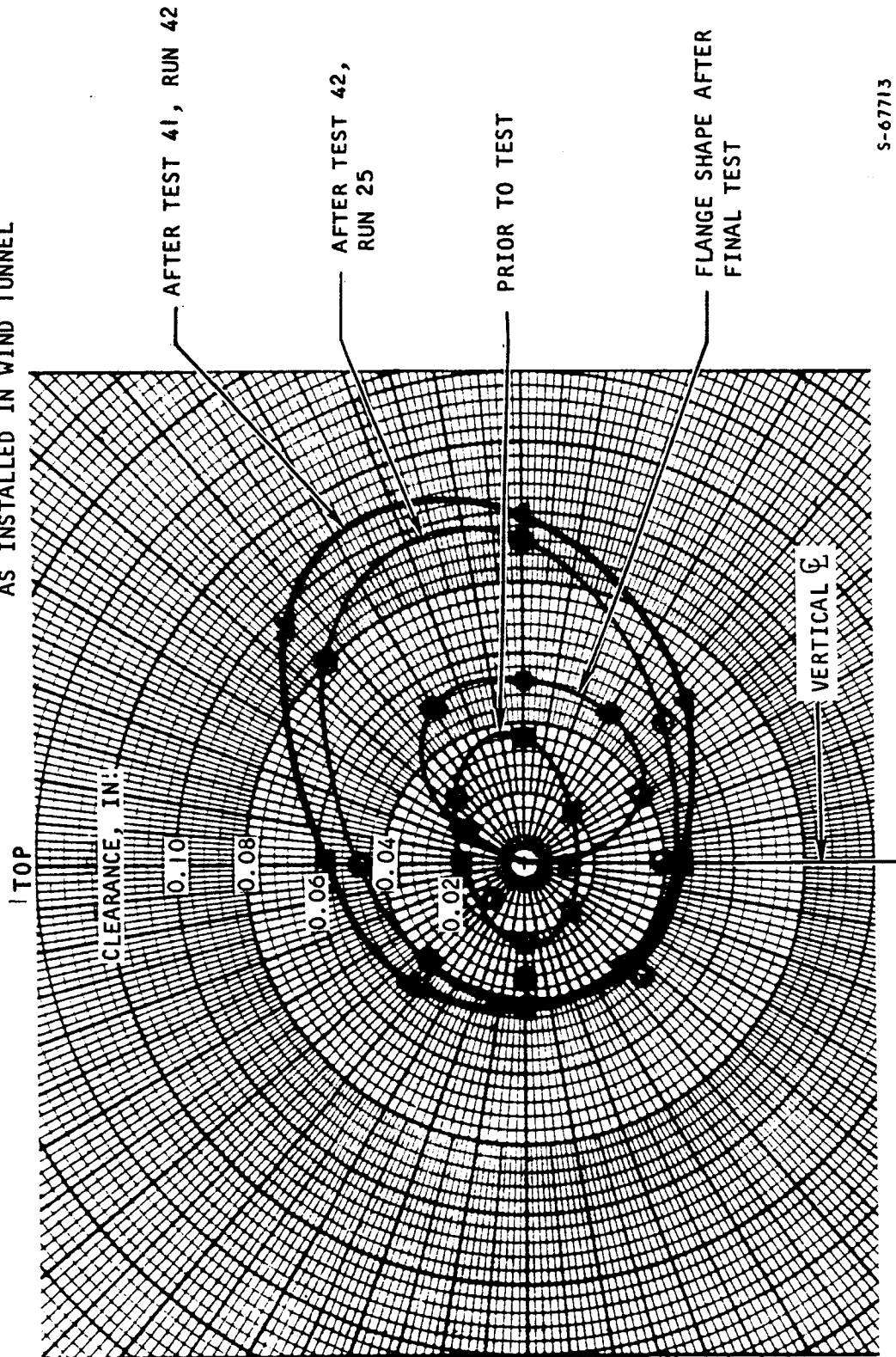
UNCLASSIFIED

Figure 5.7-6. Leading Edge/Spike Gap Clearances

The hot gas heating was approximately equal on both sides of the manifold so this was not expected to produce structural temperature differences. The second type of temperature difference investigated was that between the hot wall and structure within each half of the manifold. This temperature difference was created by a fast response of the hot wall during transient startup and shutdown and a slow response of the structure. Results of the analyses indicate a 167°R structural temperature difference between manifold halves created by unsymmetrical hydrogen heating (Test 41, Run 39). The added effect of hydrogen flow through the injector tubes decreased this temperature difference for runs with injection. The maximum hot wall-to-structure temperature difference within each manifold half was 940°R (Test 42, Run 28). Associated with this maximum positive temperature difference was a negative reversal difference of -245°R, or a total two-way difference of 1185°R. The maximum two-way temperature difference was 1290°R (Test 42, Run 34).

The structural temperature differences between manifold halves was investigated by thermally modeling the structure into a nodal network as shown in Figure 5.7-7. Only the center-post section of the manifold was modeled, since the remainder of the structure is similarly heated by the hydrogen on both sides (without hydrogen injection). In addition to the uniform hot gas heating, the leading edge side (near the hot skin) receives jet-impingement heating from the hydrogen leaving the leading edge fins. The remainder of the hydrogen heating on this side is from low-velocity convection. On the outer shell side, the hydrogen leaving the crossover tubes creates jet-impingement heating on the center of the modeled structure. For calculation purposes, the impingement effect was averaged between the 24 crossover tubes around the circumference. The remainder of the hydrogen heating on the outer-shell side is from low-velocity convection. Using the measured hydrogen temperature history, T10 (leading edge side), the leading edge hydrogen flow rate, and the hot gas heating for Test 41, Run 39, the structural temperatures were calculated (on a digital computer) for the transient startup portion of the test (no hydrogen injection). Test 41, Run 39 was selected because it was at the tunnel maximum heating condition (3320 psia, 3400°R tunnel reservoir total conditions), similar to the tunnel conditions (except zero angle of attack) for the run (Test 41, Run 53) during which the bolts failed. The hot gas heating has been defined in Section 5.2.3.1. Two cases were run; (1) perfect thermal contact between manifold halves, and (2) no thermal contact. During one of the post-run inspections, portions of the O-ring installed between manifold halves was observed in the hot-gas annular passage indicating poor thermal contact. Results for the two cases are presented in Figure 5.7-8. These temperatures are area-weighted average structure temperatures for the nodal network in Figure 5.7-7. The maximum temperature differential is 167°R (no thermal contact). The individual temperatures producing this average difference are shown in Figure 5.7-9. Though the average difference is 167°R, there is a 665°R difference (1220°R vs 1885°R) between local adjacent positions of the manifold near the hot skin. This larger difference is created by the jet-impingement-hydrogen convection of the leading edge side and low-velocity-hydrogen convection on the outer shell side.

The added heating effect of hydrogen flow through the injector tubes (shown in Figure 5.7-7) is demonstrated by the histories of hydrogen manifold
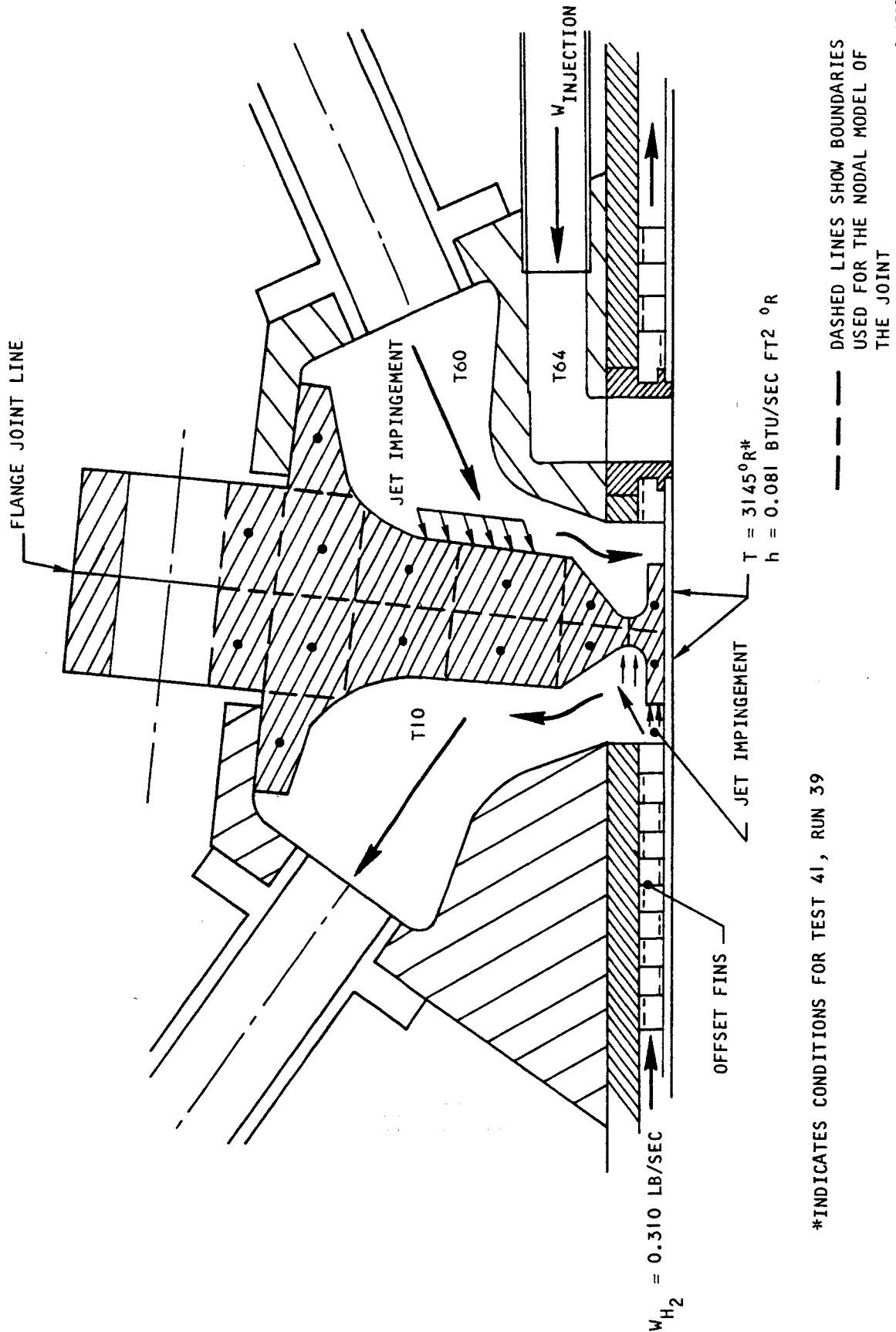
UNCLASSIFIED

Figure 5.7-7. Leading Edge/Forward Outer Shell Crossover Manifold

*INDICATES CONDITIONS FOR TEST 41, RUN 39

— DASHED LINES SHOW BOUNDARIES USED FOR THE NODAL MODEL OF THE JOINT

S-67800

UNCLASSIFIED

GARRETT AIRESEARCH MANUFACTURING COMPANY
Los Angeles, California

71-7702
Page 5-180

JOINT LINE OF CONTACT

FORWARD OUTER SHELL (F.O.S.) SIDE

L. E. SIDE

ZERO THERMAL CONTACT

F.O.S. AVG

L.E. AVG

167°R MAXIMUM ΔT

TEMPERATURE, °R

TIME, SEC

S-67767

PERFECT THERMAL CONTACT AT JOINT

F.O.S. AVG

L. E. AVG

57°R MAXIMUM, ΔT

TEMPERATURE, °R

TIME, SEC
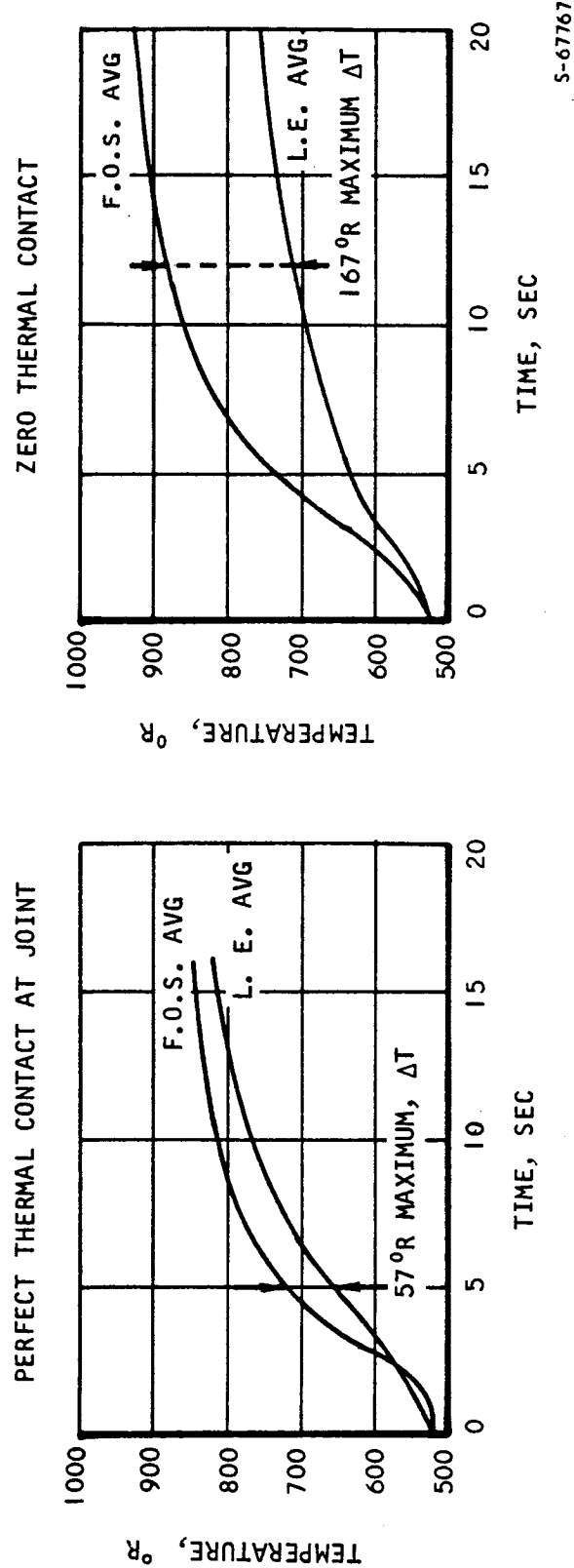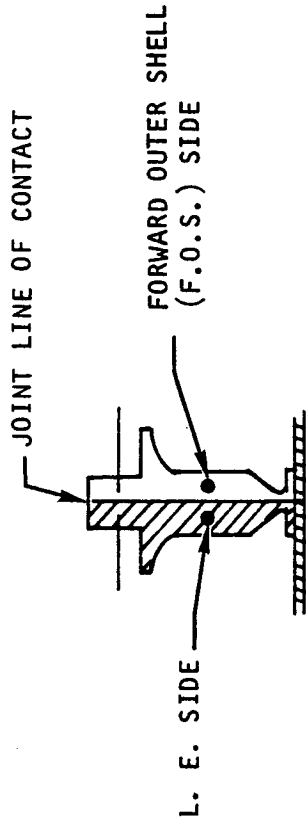
Figure 5.7-8. Leading Edge/Forward Outer Shell Joint Transient Thermal Response

AIRESEARCH MANUFACTURING COMPANY
Los Angeles, California

BOLT CENTER-LINE

536°R	554°R
600	584	712	650
663	966

LEADING EDGE SIDE   FORWARD OUTER SHELL SIDE

856	1062
1036	1226
1220	1885
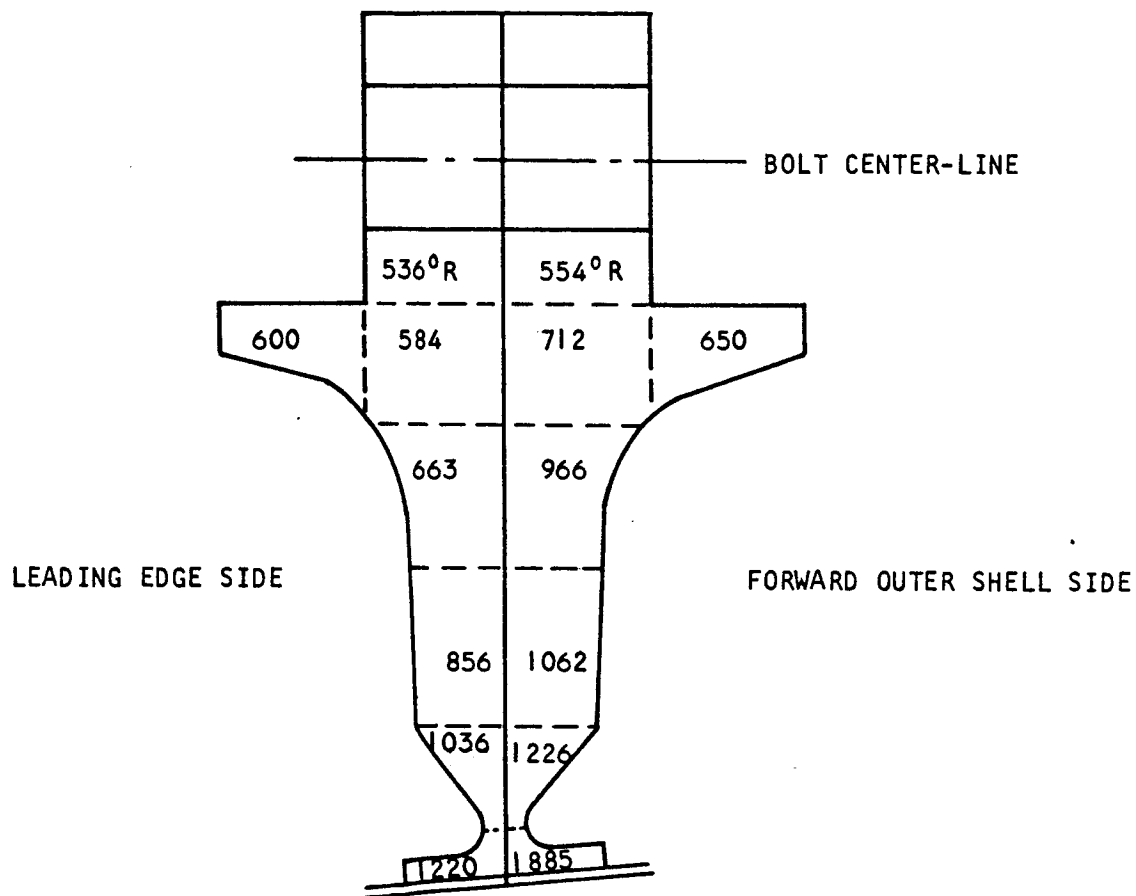
NOTE: TEMPERATURES CORRESPOND TO 12 SEC (ZERO THERMAL-CONTACT
        CASE) IN FIGURE 5.7-8

S-67776

Figure 5.7-9.   Temperature Distribution at Time of Maximum
                Temperature Difference

temperature T60 and hydrogen injection temperature T64 for Test 42, Run 36 (1380 psia, 2200°R tunnel condition) in Figure 5.7-10. Though the injection hydrogen at T64 is from the flow route outlets, it is lower than the forward outer shell hydrogen temperature, T60, for most portions of the test. It is seen in Figure 5.7-8 that the average structural temperature of the forward outer-shell-manifold side is higher than the leading edge side. The injection hydrogen at T64 will tend to retard the rate of temperature increase on the forward outer shell side and produce a lower structural temperature difference.

Hot wall-to-structure temperature differences on the leading edge manifold side were calculated from measured temperature histories of the structure T12 and the manifold hydrogen, T10, and an estimate of the hydrogen-to-hot-wall ΔT. Results for Test 42, Run 36 (1380 psia, 2700°R) are shown in Figure 5.7-11. The maximum positive ΔT is 750°R during transient heatup. When the negative reversal ΔT is added, the total two-way ΔT is 1210°R. This total ΔT is useful for low-cycle thermal fatigue calculation. The hydrogen temperature T10 is used as the hot wall temperature for the reversal ΔT, since the two temperatures are nearly equal during the shutdown portion of the test run (after 83 sec in Figure 5.7-11). A summary of the ΔT's for several other test runs are shown in Table 5.7-2. Only test group 42 runs are shown, since T12 was recorded for this test group only. The runs shown are representative of the range of tunnel conditions, from the thermal cycle runs to the high-heating runs.

TABLE 5.7-2

LEADING EDGE/FORWARD OUTER SHELL MANIFOLD TRANSIENT SUMMARY (U)

Test	Run	* $\left(T_{WALL}\right)_{max.}$, °R	** $(\Delta T)_{max.}$	$(\Delta T)_{min.}$	ΔT_{Total}
42	36	1475	750	-460	1210
42	45	1410	850	-230	1080
42	46	1330	790	-340	1130
42	34	1450	890	-400	1290
42	28	1530	940	-245	1185
41	52	1420	870	Not Estimated	Not Estim.

* $\left(T_{WALL}\right)_{max.}$ is based on $(T10)_{max.}$ plus the estimated ΔT across the hot wall.

** (ΔT) is the temperature difference between the hot skin and the joint structure near the bolt circle (T12).
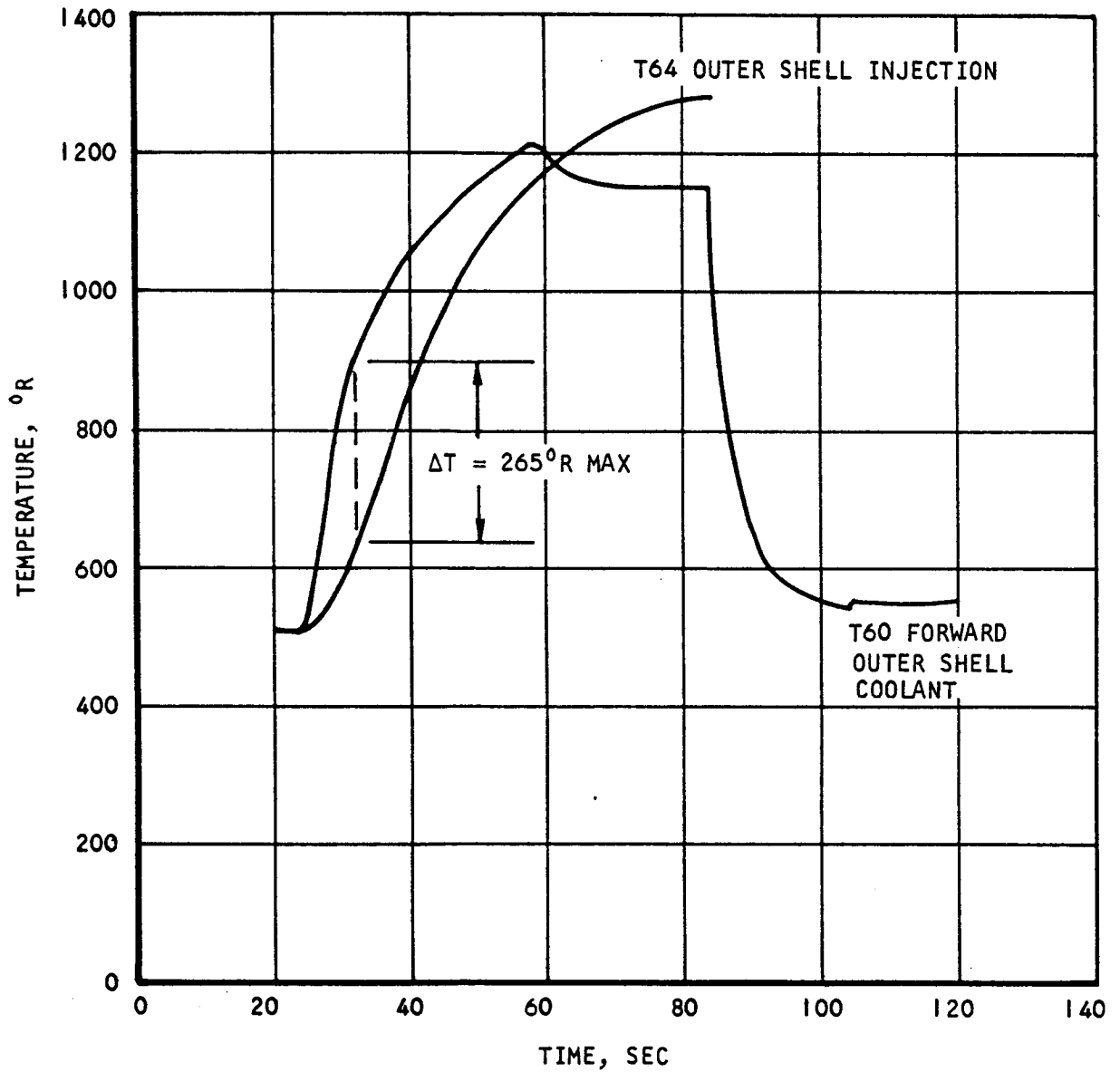
TEST 42 RUN 36

Figure 5.7-10. Leading Edge/Outer Shell Coolant and Injection
Temperatures.(U)

S-67766
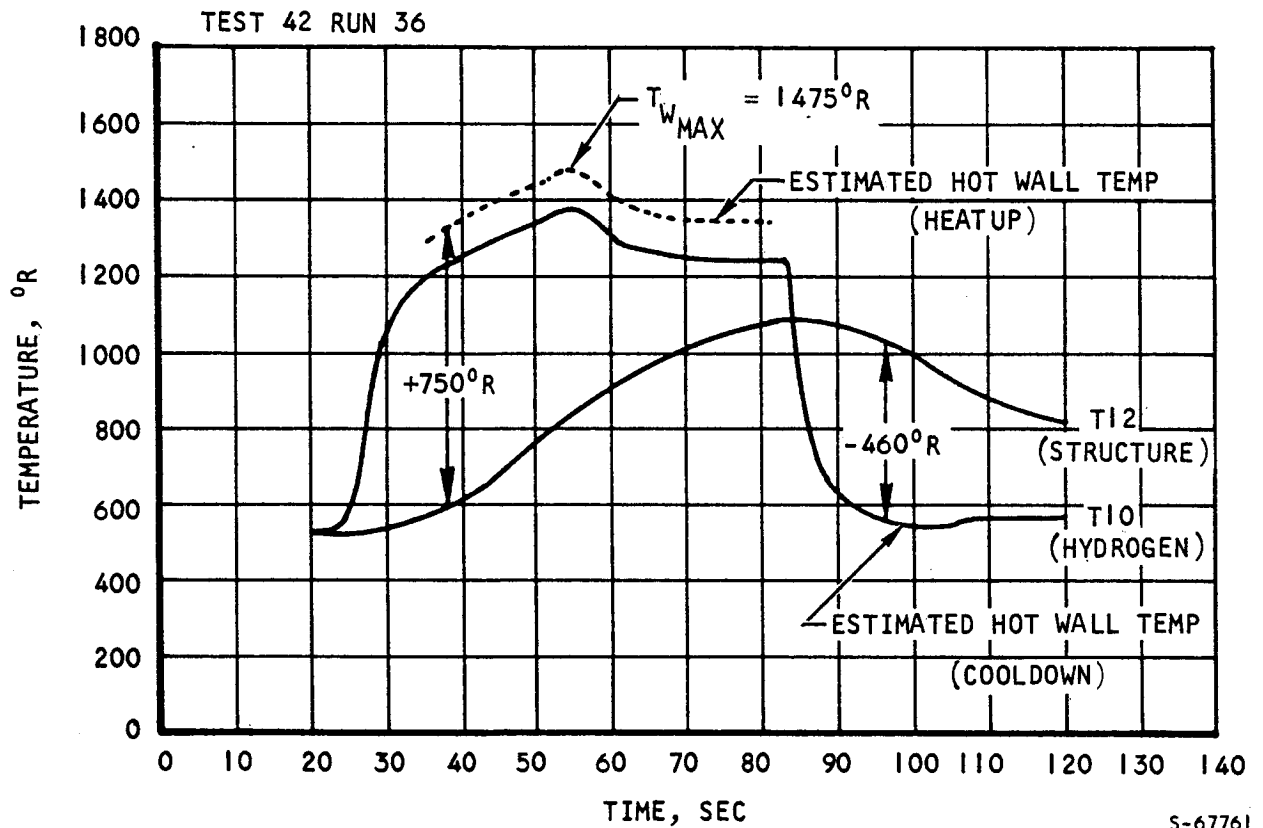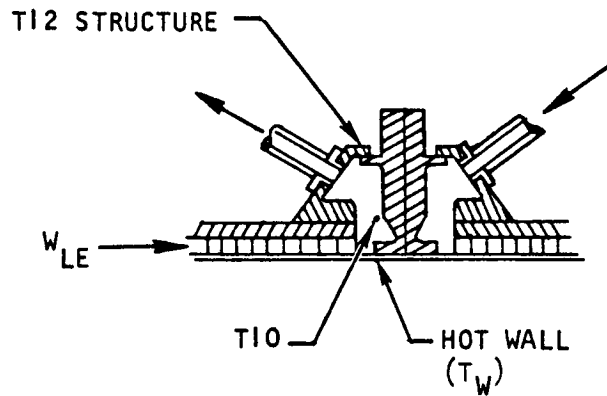
Figure 5.7-11. Leading Edge/Forward Outer Shell Manifold
Thermal Response (U).

5.7.3.2 Structural Analysis

The leading edge outlet manifold and the outer shell inlet manifold are fastened together with 24 stainless steel No. 10-32 screws. Section proper- ties of these two manifolds are as follows:

Manifold	Cross Sectional Area, in.^{2}	Moment of Inertia, in.^{4}	
		I_x	I_y
Leading edge outlet	0.4002	0.0421	0.0193
Outer shell inlet	0.4303	0.0363	0.0243

The geometry of the two manifolds is shown in Figure 5.7-12. Both mani- folds are brazed assemblies of Hastelloy X material. Mating flanges were scalloped in order to facilitate the assembly.

The No. 10-32 screws were fabricated from 300-series corrosion resistant steel. Mechanical properties of this screw as listed in Federal Specification FF-S-86C are:

Mean stress area of thread, in.^{2}	0.02
Ultimate load capacity, lb	1600
Tensile yield strength, lb	600

The full length of the screw was threaded. The moment of inertia (I) of the screw, based on the mean stress area, is 0.00003183 in.^{4}, and the section modulus, S = 0.0003989 in.^{3}.

Assuming a tensile yield strength of 30,000 psi, the bending moment on the screw causing yield of the outer fibers, without taking into consideration the effect of stress concentration due to the threads, is M_{po} = 11.967 in.-lb.

The screws were torqued during installation using T_M = 25-30 in.-lb torque without lubrication. The axial load, Q, and the tensile stresses, σ, due to T_M, using different friction coefficients, are as follows:

T_M, in.-lb		Friction coefficient, μ		
		0.2	0.15	0.10
25	Q	1,710	1,280	1,023
	σ	85,500	64,000	51,300
30	Q	2,050	1,535	1,230
	σ	102,500	76,800	61,500

0.060

0.50
0.20

A-A

S-70118

R = 10.844
R = 11.0

0   0.2   0.4   0.6   0.8   1.0

ALL DIMENSIONS IN INCHES

A

A

21.688 DIA
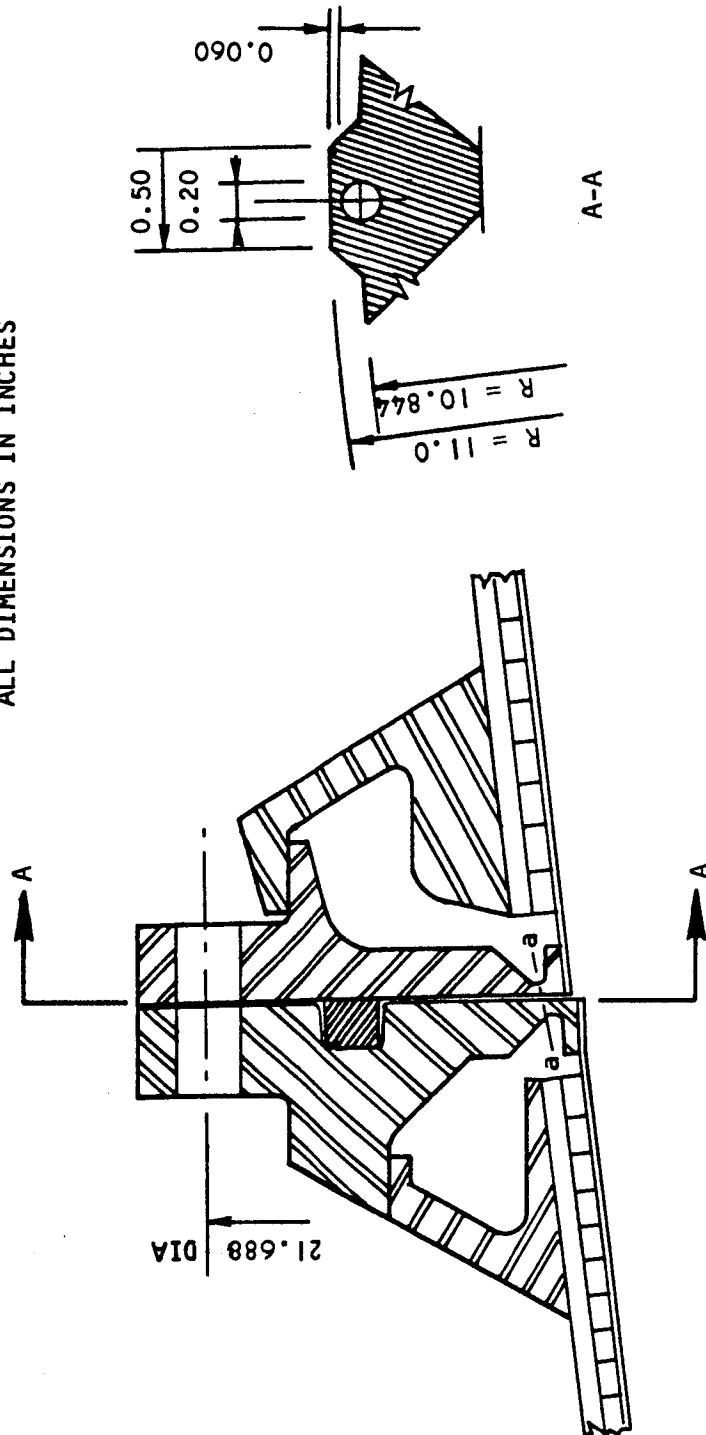
Figure 5.7-12.   Manifold Geometry

In order to verify the uncertainties associated with the installation, three identical screws were torque-tested using 30 in.-lb initial torque and increasing it by 10 in.-lb increments until the strain exceeded 0.2 percent. The 30 in.-lb installation torque included 5 in.-lb running torque.

Screw No.	Initial Length, Lo, in.	Length at 30 in.-lb torque, L30, in.	ΔL, in.	Stress at 30 in.-lb torque, $\sigma = \frac{\Delta L}{L} E$, psi
1	0.94095	0.94170	0.00075	23,115
2	0.9401	0.9413	0.0012	37,017
3	0.94097	0.94195	0.00098	30,171

As the above listed results indicate, substantial difference in preload existed between screws, but there was no yielding for any of the three screws. Yielding (0.2 percent offset) occurred at approximately 43,000 psi stress. The A-286 steel projection-welded nuts were elliptically offset to produce a locking torque on the screws. It was found during testing that this locking torque diminished when the screw was used more than twice.

Referring again to Figure 5.7-5, the following features are evident

(a) The threads are deformed as though they were hammered around the perimeter. This is most severe at an area corresponding to the position of the flange faces.

(b) A total of 14 screws failed due to tension.

(c) A total of 14 screws are substantially bent. The resistance-welded nuts were broken off the outerbody flange and severely bent.

(d) A substantial variation of thread engagement in the nuts is noticeable. This indicates loosening of the screws due either to multiple installations into the nut plates or severe load cycling.

The shape of the flanges (outside diameter) was measured after the bolt failure, both on the leading edge and in the outer shell. The diameters are plotted in Figure 5.7-13 as the function of θ, the angle around the perimeter (see also Figure 5.7-14). Mean values of the diameters were calculated and deviations from these mean values are plotted in Figure 5.7-14. Bolt holes on the leading edge flange were elongated as shown on Figure 5.7-15 and show a "peened" appearance, but the bolt holes on the outerbody flange were not noticeably deformed. Thus, the evidence points to some fairly severe form of loading.
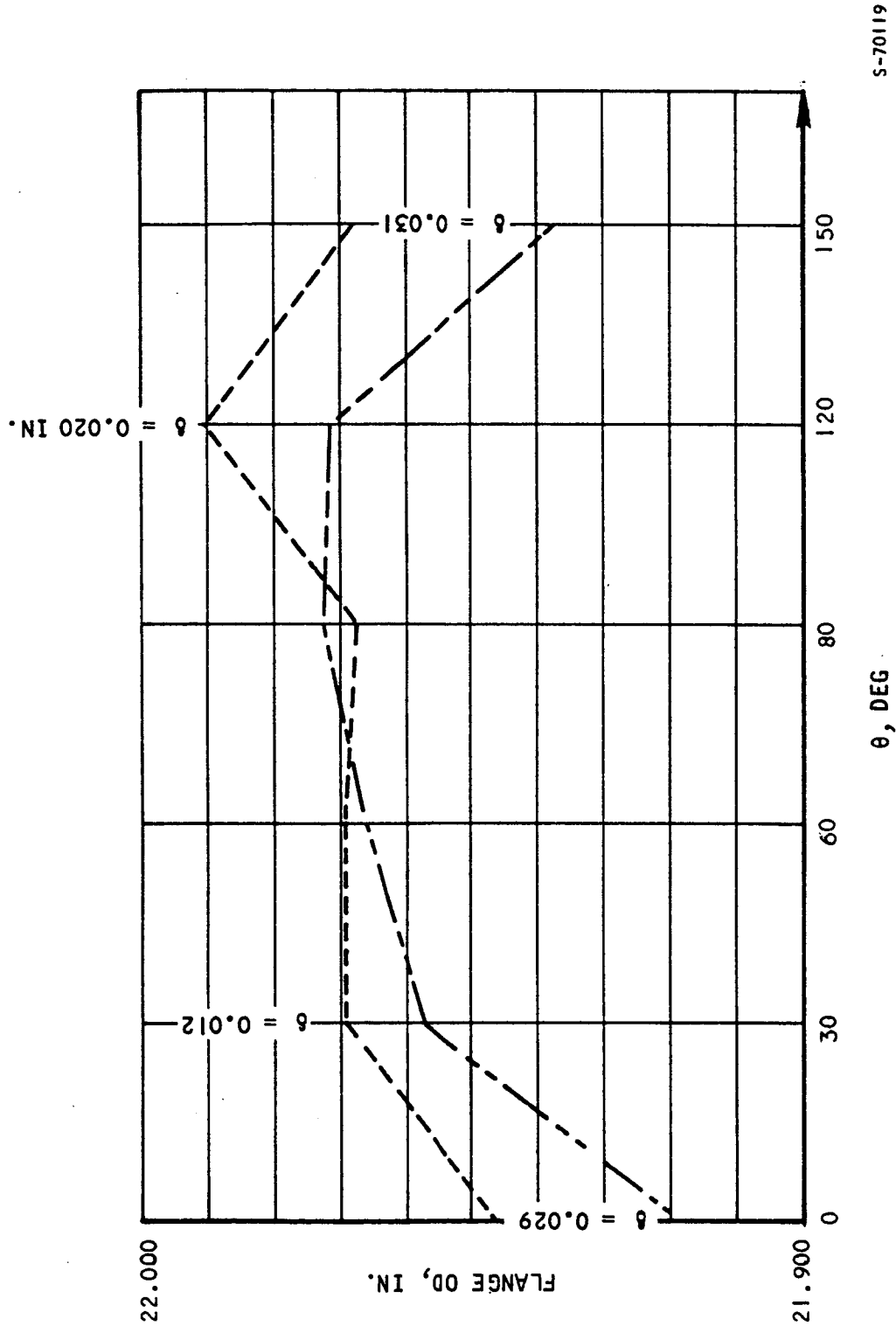
Figure 5.7-13. SAM Manifolds at Station 43.445 – Diametrical Differences

S-70119

AIRESEARCH MANUFACTURING COMPANY
Los Angeles, California

71-7702
Page 5-189

LEADING EDGE

MEAN DIA: 21.953 L.E.
21.9683 O.S.

0.0006
0.00366
0.0006
0.01266
-0.028
-0.036

-0.00133
0.0186
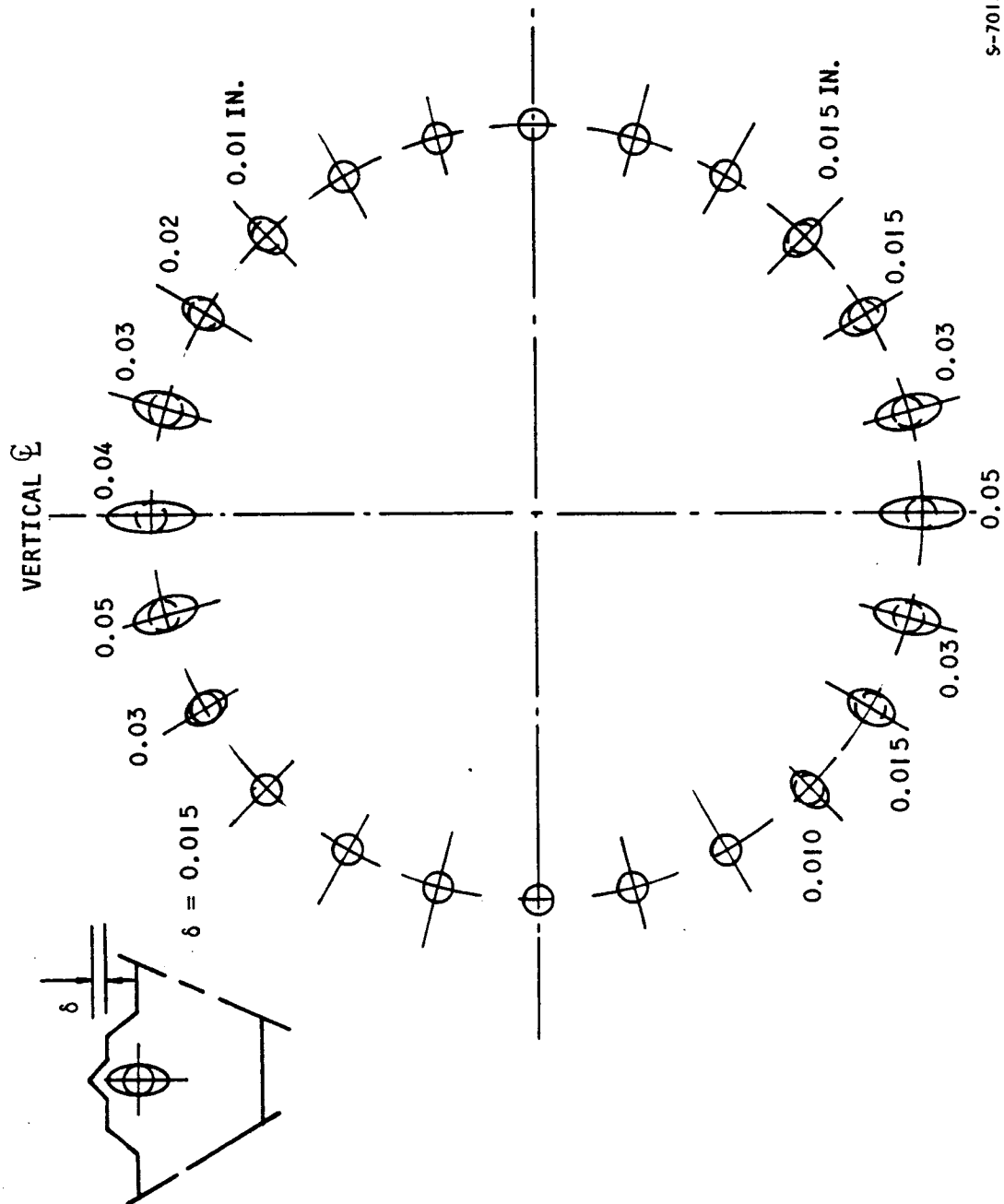
0.02166
0.0176
0.0006
-0.0163

OUTER SHELL

S-70121

ALL DIMENSIONS IN INCHES
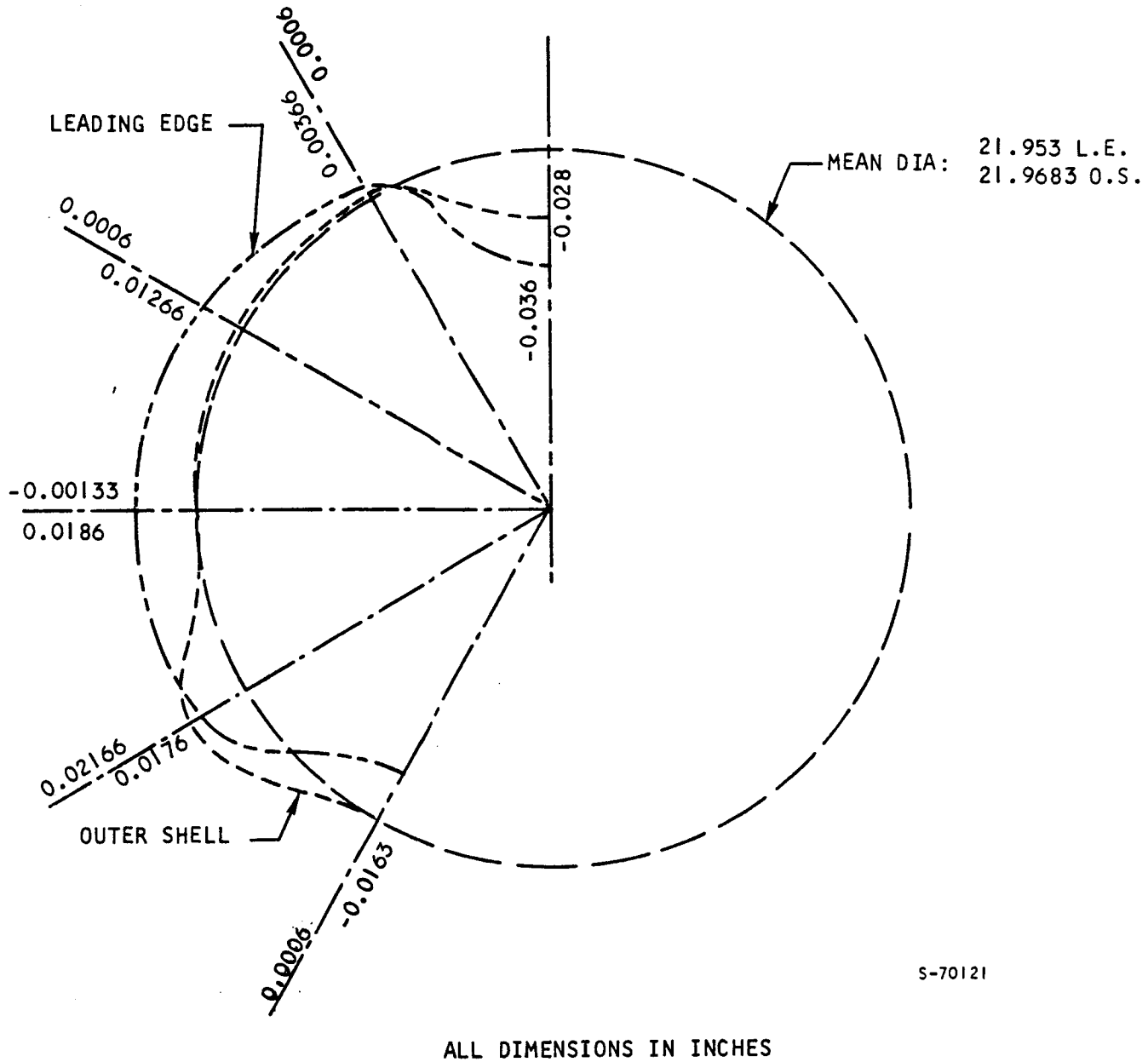
Figure 5.7-14. SAM Leading Edge and Outer Shell Deviation
From Mean Diameter

AIRESEARCH MANUFACTURING COMPANY
Los Angeles, California

Figure 5.7-15. Leading Edge Flange – Bolt Hole Deformation

S-70138

The influence of the hot skin thermal expansion and the shear flow due to temperature differences between manifolds was studied to explain the failure of the screws and the observed condition of the flanges.

Temperature of the hot wall was estimated at $1475^\circ R$ and the maximum positive ΔT between the structure and the hot wall is $750^\circ R$. The cross section of each manifold is basically a rigid frame. One peculiar feature of these cross sections is the 0.075-in. long, 0.015-in. thick hot wall which ties the "legs" of the rigid frame. This hot wall is attached to a weakened area ("a-a" in Figure 5.7-12) of the flange face. Formation of a plastic hinge at "a-a" would require a moment

$$M_p = P_p \frac{t}{2} = \frac{\sigma_y t^2}{4}$$

Using σ_y = 45,000 psi at room temperature, and 32,400 psi at $1000^\circ F$, the value of this plastic moment,

$$M_p = 13.78 \text{ in.-lb at R.T.}$$

$$= 9.222 \text{ in.-lb at } 1000^\circ F$$

A force P_w acting at the hot wall to create such a moment would have the magnitude of

$$P_w = \frac{1}{0.08 \text{ in.}} \times 13.78 = 1720 \text{ lb at R.T.}$$

$$\times 99.22 = 1240 \text{ lb at } 1000^\circ F$$

The hot skin temperature is considerably higher than that of the bulk of the structure. Assuming uniform temperature across the 0.015-in. hot skin, the ΔT required between the hot skin and the structure to produce the force calculated above:

$$P = AE \alpha \Delta T = 0.015 \times 24 \times 10^6 \times 8.4 \times 10^{-6} \Delta T = \begin{cases} 1720 \\ 1240 \end{cases}$$

and from this:

$$\Delta T = 569^\circ F \text{ at R.T.}$$

$$= 440^\circ F \text{ at } 1000^\circ F$$

A review of the thermal response of the two manifolds shown in Figure 5.7-11 indicates that higher temperature differences than this existed during testing. The elastic restraint of the remainder of the section is not sufficient to prevent the two hot walls exerting an axial load on their abutting ends. This force has to reach a value of $\frac{1600 \text{ lb}}{2.84 \text{ in.}} = 564 \text{ lb-in.}$ only to exceed the tensile strength of one connecting bolt.

The effect of the shear flow created by temperature differences can be expressed as follows: Assuming that two manifolds with cross-sectional areas of A_1 and A_2, having a common radius R, are exposed to temperature differences, then the hoop directional growth of each manifold:

$$\delta_1 = R\epsilon = \frac{VR^2}{EA_1} \qquad \delta_2 = R\alpha\Delta T - \frac{VR^2}{EA_2}$$

Where (E) is the modulus of elasticity, (V) is the shear load between manifolds, and (ϵ) is the radial strain.

Since the manifolds are bolted together, the radial growth

$$\delta_1 = \delta_2 \text{ and}$$

$$\frac{VR^2}{EA_1} = R\alpha\Delta T - \frac{VR^2}{EA_2}$$

$$V = \frac{E\alpha\Delta TA_1}{R}\left(\frac{1}{1 + A_1/A_2}\right)$$

The shear load per bolt,

$$V_b = \frac{2\pi rV}{N}.$$

Using the section properties listed earlier, an average metal temperature of $600°F$, and maximum temperature difference of $\Delta T = 167°F$, the shear load per bolt is

$$V_b = \frac{2\pi EA_1\alpha\Delta T}{N(1 + A_1/A_2)} = \frac{2\pi(27 \times 10^6)\,0.4002\,(7.0 \times 10^{-6})\,167}{24\,(1 + 0.4002/0.4303)} = 1933.6 \text{ lb}$$

The shear stress $\tau = \frac{1933.6}{0.0175} = 110,491$ psi; an extremely high value.

It is very likely that the bolt failure and the peening of the bolt holes was due to the combined effect of both features in a gradual process. The non-uniformly preloaded bolts were exposed to increasing axial and shear loads as the temperature increased during each run. Unequal load conditions around the perimeter resulted in the failure of a few bolts at first, possibly followed by an accelerated failure during the runs at angle of attack. These produced unsymmetrical thermal loads which were aggravated in Test 41, Run 52, by under-cooling of the leading edge flow route.

The substitution of high-strength bolts for the 300-series corrosion re-sistant bolts will eliminate the problem encountered in the SAM tests for the design life of the engine. This is particularly so since the differential

postulated in calculating the shear flow represents an extreme. The actual differential, and hence, bolt loading, is expected to have been less (see also Figure 5.7-8). The effect of the restraint of the high-strength bolts on thermal fatigue will not be significant. This aspect of the tests is further discussed below.

5.7.3.3 Hot Skin Thermal Fatigue

The data reduction results from the test runs indicated in Table 5.7-2 were utilized to obtain an estimate of comparative thermal fatigue at this flange location, compared to that applied at the outerbody manifold (OBOM). The data analysis procedures presented in Section 5.5 were employed. The five selected runs were among the most severe thermal fatigue cycles at the OBOM, and they should also provide a good measure of thermal fatigue on the hot skin at the leading edge-to-outerbody-flange connection. The results at the flange and at the OBOM are summarized in Table 5.7-3.

TABLE 5.7-3

THERMAL FATIGUE COMPARISON AT FLANGE AND OBOM (U)

Test No.	Run No.	Flange				OBOM			
		T_{MAX}	ΔT_{TOT}	N	1/N	T_{MAX}	ΔT_{TOT}	N	1/N
42	28-1	1530	1185	83.8	0.0121	1576	1139	83.5	0.0120
42	34	1450	1290	72.4	0.0138	1575	1388	51.0	0.0198
42	36	1475	1210	83.9	0.0119	1570	1183	80.8	0.0124
42	44	1410	1080	115.1	0.0087	1511	1128	41.7	0.0240
42	45	1330	1130	108.6	0.0092	1458	1326	91.8	0.0109
				$\Sigma 1/N = 0.0557$				$\Sigma 1/N = 0.0791$	

The results for thermal fatigue damage are approximately 30 percent lower at the flange than at the OBOM for the five cycles. It can be reasonably concluded that the total fatigue damage for the entire test program was less at the flange than at the OBOM.

5.7.4 Nozzle/Inner Shell Joint

The cross section through the joint is shown in Figure 5.7-16 and is taken at one of the ten crossover ports through which coolant flows from the nozzle to the inner shell. The nozzle is located on the inner shell by means of a pilot, and bolted to it with a pair of bolts for each port. Shock impingement in this joint area, combined with some intentional undercooling, caused local deformation of the nozzle shell, as shown in the figure, and some distortion of the nozzle manifold. The deformed shell areas extended over a circumferential
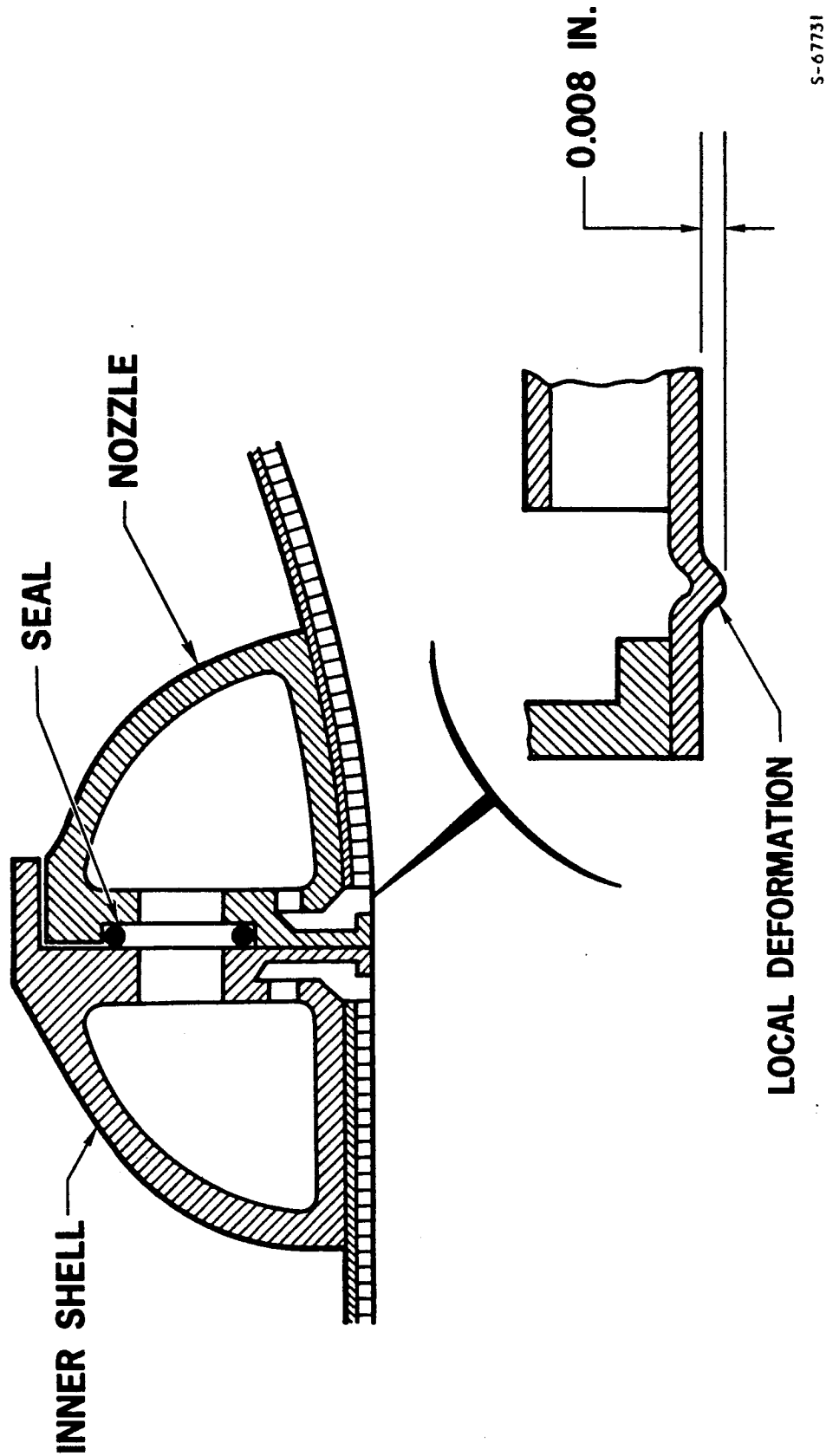
0.008 IN.

S-67731

SEAL

NOZZLE

INNER SHELL

LOCAL DEFORMATION

Figure 5.7-16. Nozzle/Inner Shell Joint Configuration

AIRESEARCH MANUFACTURING COMPANY
Los Angeles, California

UNCLASSIFIED

length of approximately 4 in. and were centered between the struts in the area of shock coalescence described elsewhere. The distortion of the nozzle manifold resulted in leakage of hydrogen past the port seals. In addition, a single leak developed in one of the affected areas on the inner shell.

Once the coolant flow rates were increased to design levels, there was no further indication of high temperatures in the area shown in the figure. Following the thermal cycle runs, also, the nozzle manifold was locally relieved to fit the mating surface on the inner shell pilot. The resulting fit was adequate to restore sealing at the ports. On the other hand, no attempt was made to repair the leak at the joint of the inner shell hot skin and the inner shell manifold. This leak was minor and caused no difficulties. In the course of the tests, it showed no tendency to propagate.

The condition observed on the nozzle and the inner shell reflects an unrealistic thermal loading. When flow rates are increased to the design levels at each of the conditions, the resulting temperature increase due to shock coalescence in this area is well within the capability of the structure. In fact, the conditions used during thermal cycling, even though much more severe than the design condition, did not result in impairment of operation of the SAM. Consequently, no redesign of this joint or change in axial location of the joint is indicated. Indeed, the joint area has shown a very satisfactory performance under high-heating conditions and with as little as 10 percent of the design coolant flow.

UNCLASSIFIED

6. CONCLUSIONS

The primary objective of the SAM wind tunnel tests was to evaluate the flight-designed, regeneratively-cooled structure of the HRE in a realistic environment. This has been accomplished. It was possible, in particular, to subject the structure to severe thermal loading. The cooled structure performed well, both in terms of its design requirements and in terms of its ability to survive under the imposed loads. Test results presented in this report show performance that is generally in good agreement with design predictions. From the structures point of view, the results indicate that the basic design concepts and approaches used in the HRE are valid. The cooled structure proved to be rugged and capable of sustaining considerable abuse without degradation of performance. Some specific results are summarized below.

6.1 THERMAL PERFORMANCE

Heat transfer data reduction and analyses were directed toward (1) correlation of test hydrogen heat loads with heat loads and fluxes calculated from the measured aerodynamic test conditions and the flight design analytical methods; (2) evaluation of the steady-state cooling performance in terms of metal temperatures, temperature differences, and hydrogen coolant usage, pressure drop, and flow distribution; and (3) evaluation of the transient response of the engine in terms of hydrogen coolant, metal temperatures, and metal temperature differences.

6.1.1 Aerodynamic Heating

The flight design heat transfer calculation method (flat-plate method with Eckert's reference enthalpy technique for hot gas property evaluation), when used in conjunction with the test pressure distribution and the one-dimensional flow solution, predicted heat fluxes to within ±20 percent over most surfaces of the engine. Based on this good agreement, the heat load level of 10,800 Btu/sec and hydrogen coolant requirement of 2.19 lb/sec (at $100^\circ R$ inlet) predicted for Mach 8 flight conditions is realistic.

The correlation of heat loads did not include the effect of combustion. Although outlet hydrogen coolant was injected into the captured hot gas stream, no hydrogen combustion was expected in the methane-air combustion products and none was detected in test heat loads.

Localized heating occurred in the engine combustor and nozzle sections during testing. When interpreted in terms of local aerodynamic conditions, the relative intensity of the local heating during flight will be less than encountered during testing. Hydrogen coolant increases are not expected to be

AIRESEARCH MANUFACTURING COMPANY
Los Angeles, California

UNCLASSIFIED

71-7702
Page 6-1

required for cooling of these areas of localized heating.

6.1.2 Cooling Performance

Steady-state hot wall temperatures were maintained at or below acceptable design limits at the most severe tunnel heating conditions. Though test heat flux levels were lower than defined for Mach 8 design flight conditions, good agreement ($\pm 50^\circ$R) was achieved between test hot wall temperatures and temperatures predicted for the hot wall at these lower heat flux levels. During the thermal cycle tests, the engine structure was subjected to a thermal environment (hot wall temperatures and hot wall-to-structure temperature differences) as severe as the predicted Mach 8 flight conditions. This was accomplished by undercooling the hydrogen flow routes. Undercooling produced a nozzle temperature that was about 1000°R locally higher than the Mach 8 prediction and a hot wall-to-structure ΔT of 1000°R. The maximum plate-fin panel ΔT at Mach 8 flight conditions is 950°R on the leading edge. In the area of the outer-body outlet manifold, ΔT's ranged to 1400°R. The SAM satisfactorily survived these conditions. Cooling performance of the leading edge during the test program was also satisfactory. There was no evidence of overheating even though foreign object damage created dents and hydrogen leakage holes in the hot surface.

Test results of flow route density-adjusted-pressure drop were in fair agreement with isothermal air calibration test results. Scatter is ascribed to test measurement uncertainties rather than to differences in hydrogen and air test conditions. The coolant maldistribution, W_{MAX}/W_{MIN}, in the engine flow routes was estimated as high as 1.10 on the spike, as measured by temperature distributions obtained from coolant control thermocouples. This caused no apparent problems in the tests. The maximum coolant maldistributions based on inlet and outlet manifold pressure distributions during isothermal air calibration tests was 1.033 on the leading edge route.

6.1.3 Transient Operation

The transient behavior of the engine flow routes was investigated by analytical methods and the results were correlated with experimental data. Basically, the time required for the hydrogen outlet temperature to reach steady state (when subjected to a step change in hot gas heating) is inversely proportional to the hydrogen flow rate. The estimated time for all engine flow routes to reach steady state at the Mach 8 flight conditions is 8 sec if the design flow rates are established at startup (onset of spike retraction and light off).

In addition to producing higher-than-design hot wall temperatures, undercooling the flow routes (hydrogen flows less than operational requirements) will produce higher hot wall-to-structure ΔT's during transient heating than at steady state. To avoid larger-than-steady-state ΔT's at the Mach 8 flight conditions, the design hydrogen flow rates must again be established at the onset of spike retraction and light off.

6.2 THERMAL FATIGUE

At the Mach 8 design point, the design life of the engine was computed to be 136 cycles. The engine design objective was to produce a design life of 100 operating cycles at these conditions, which was based upon a maximum hot skin metal temperature of $1600^{0}F$ and a ΔT of $800^{0}F$ between the hot skin and the prime structure. The SAM test program exposed the engine to 58 thermal cycles of varying temperature differentials and maximum hot skin metal temperatures, resulting in a computed fatigue damage fraction of 49.0 percent in the area of the outerbody outlet manifold. This damage fraction corresponds to 0.49 x 136 = 67 engine operating cycles at the Mach 8 design point.

Upon completion of the test program, the engine showed no visible evidence of thermal fatigue damage, i.e., cracking or leakage anywhere on the hot skin. Local distortion occurred on the nozzle due to local shock interaction effects and undercooling but this did not lead to failure in the hot skin. Calculations for thermal fatigue damage were also carried out for the hot skin at the flange joint connecting the leading edge to the outerbody. The accumulated damage for the five runs used in the analysis was some 30 percent lower than at the OBOM station for the same runs and is, generally, expected to have been less than at the OBOM.

The earlier work on mechanical bend tests and thermal cycle tests clearly demonstrated that thermal fatigue was a major problem area in the design of the HRE. The SAM test program demonstrated that the selection of Hastelloy X and the Palniro braze alloys was a sound one for the design.

6.3 APPLIED LOADS

The test results indicate that the static and dynamic loads were below the design level. This resulted from much lower inertia load and vibration levels during tunnel testing. In addition, no inlet unstarts, which form a significant part of the internal design loads, were encountered in the tests. The structure was able to satisfactorily carry all of the applied test loads.

The only forcing function known in advance--a 27- to 30-Hz vibration due to tunnel combustor operation--created no resonance in the structure. Instead of amplification, substantial structural damping was experienced during the SAM tests. Vibration data reduction results show that the calculated natural frequencies were not excited, presumably due to lack of forcing function in that frequency. The low level wide-band random vibration recorded during the test had no resemblance to a Gaussian distribution.

6.4 STRUCTURAL PERFORMANCE

Damage sustained in various areas of the cooled structure indicates no problems so far as the basic design is concerned. The leak in the spike coolant outlet bellows and the bolt damage at the outerbody flange, however, require review of the design in these areas. Solution of the spike-bellows problem is possible in a direct way by reducing bellows stroke/length. The outerbody flange damage appears to have had several causes. The design can be

upgraded with the addition of high-strength bolting. This will insure that the performance of this area is compatible with that of the rest of the structure. When the tests were terminated due to the damage at the outerbody flange area, the cooled structure was still capable of performing at its design conditions.

REFERENCES

5-1. Engineering Staff, Hypersonic Research Engine Project- Phase II, Structures Assembly Model Test Plan, AiResearch Report No. AP-70-6120, Data Item No. 64.01, 11 March 1970.

5-2. Engineering Staff, Hypersonic Research Engine Project - Phase II, Structures and Cooling Development, Fourteenth Interim Technical Data Report, AiResearch Report No. AP-70-6640, Data Item No. 55-7.14, 1 September, 1970.

5-3. Engineering Staff, Hypersonic Research Engine Project - Phase IIA, Structures and Cooling Development, Ninth Interim Technical Data Report, AiResearch Report No. AP-69-5075, Data Item No. 55-7.09, 3 June 1969.

5-4. Engineering Staff, Hypersonic Research Engine Project - Phase IIA, Structures and Cooling Development, Eighth Interim Technical Data Report, AiResearch Report No. AP-69-4759, Data Item No. 55-7.08, 27 February 1969.

5-5. Engineering Staff, Hypersonic Research Engine Project - Phase IIA, Category I Test Report on Fin Heat Transfer and Pressure Drop Testing, AiResearch Report No. AP-69-5348, Data Item No. 63.02, 7 August 1969.

5-6. Engineering Staff, Hypersonic Research Engine Project - Phase IIA, Structures and Cooling Development, Tenth Interim Technical Data Report, AiResearch Report No. AP-69-5390 Data Item No. 55-7.10, 26 August 1969.

5-7. Richard, C. E., et al, Low Cycle Fatigue Evaluation for Regeneratively Cooled Panels, NASA Contractor Report NASA CR-1652.

5-8. Engineering Staff, Hypersonic Engine Project - Phase IIA, Structures and Cooling Development Fourth Interim Technical Data Report, AiResearch Report No. AP-68-3250, Data Item No. 55-7.04, 1 March 1968.

5-9 Engineering Staff, Hypersonic Research Engine Project - Phase IIA, Category I Test Report on Braze Alloy Investigation and Flat Panel Testing, AiResearch Report No. AP-68-3813, 27 May 1968.

This material contains information affecting
the national defense of the United States within
the meaning of the espionage laws, Title 18,
U.S.C., Sections 793 and 794, the transmis-
sion or revelation of which in any manner to
an unauthorized person is prohibited by law.

APPENDIX A

HOT WALL THERMOCOUPLE CORRECTION PROCEDURE

APPENDIX A

HOT WALL THERMOCOUPLE CORRECTION PROCEDURE

Hot wall thermocouple inserts are located at 13 locations on the SAM. These inserts extend through the plate-fin hydrogen passages as shown in Figure A-1. They do not record true hot-wall temperature adjacent to the hot gas, since the thermocouple junction is still 0.015 to 0.020 in. beneath the surface. Adjacent to each insert are thermocouples attached to the 0.060-in.-thick or 0.015-in.-thick (nozzle and leading edge outer surface) cold structural wall. The locations of these thermocouple pairs on the SAM are presented in Table A-1.

The 13 thermocouple inserts were calibrated analytically so that the wall-surface temperature adjacent to the hot gas, and in the vicinity of the insert, could be calculated for the SAM test program data reduction. The calibration, which is applicable for steady-state thermal conditions only, was obtained by thermally modeling the insert and plate-fin passage into a nodal network as shown on the left-hand side of Figure A-1. Insert junction-to-hydrogen coolant-temperature difference was determined from a thermal analyzer computer program for several input hot-gas heat fluxes, coolant passage flow rates, and coolant temperatures. Results of the parametric study were correlated and stored in tabular form in the computer program used to reduce the test data.

The development of the insert thermocouple calibration and the calculation procedure in the data reduction computer program are discussed below. A by-product of the hot-wall calibration procedure was the local hot-gas heat flux. This heat flux was very useful in correlating heat fluxes obtained from the aerodynamic-heating data analysis. As indicated, the insert-thermocouple calibration procedure is applicable for steady-state operation only. An analysis was performed to provide an indication of the thermal transient behavior of the insert-thermocouple temperature in relation to the adjacent unmeasured hot-wall temperature during transient startup of SAM tests. Results of this analysis are also presented below.

Insert-Thermocouple Calibration

The thermocouple insert and adjacent plate-fin passage was thermally modeled into a nodal network diagram as shown in Figure A-1. The symmetry of the cross section allowed the problem to be reduced to two dimensions. A fine grid mesh was used near the insert-thermocouple junction to detect the larger thermal gradients in this region, both radially (from the axis of symmetry) and vertically (from the hot surface downward). A coarser grid was used in the plate-fin passage section where thermal gradients are smaller. Conduction down the thermocouple lead wire and through the MgO insert packing material was also included in the thermal model.

Two cross-section geometries were considered in the calibration procedure: (1) a 0.060-in. cold structural wall thickness with 28R - 0.050 - 0.100(0) - 0.006 offset fins in the coolant passage, and (2) a 0.015-in. cold structural
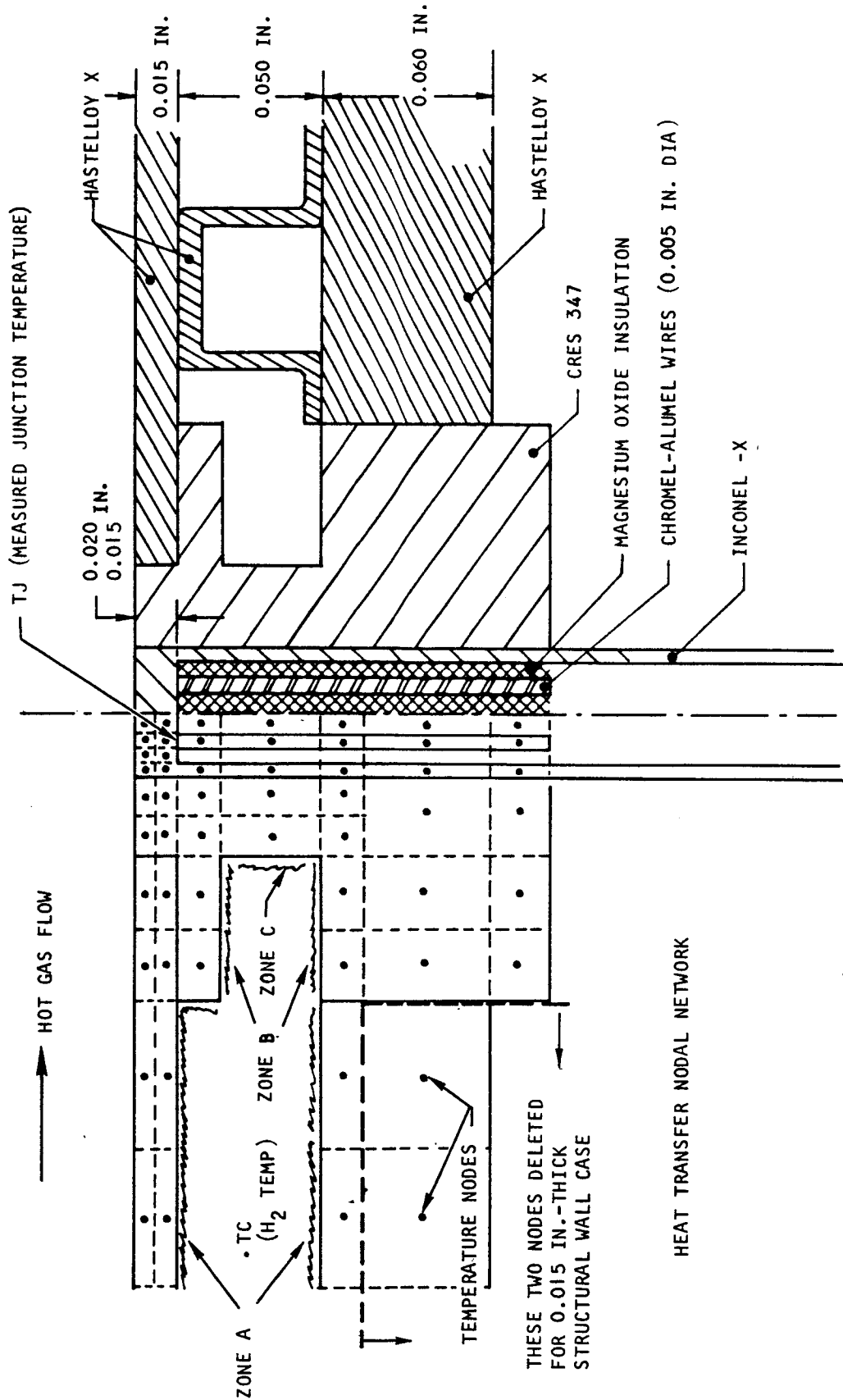
Figure A-I. Hot Wall Insert Thermocouple Installation

S-67804

HASTELLOY X

0.015 IN.

0.050 IN.

0.060 IN.

HASTELLOY X

TJ (MEASURED JUNCTION TEMPERATURE)

0.020 IN.
0.015

CRES 347

MAGNESIUM OXIDE INSULATION

CHROMEL-ALUMEL WIRES (0.005 IN. DIA)

INCONEL -X

HEAT TRANSFER NODAL NETWORK

HOT GAS FLOW

ZONE C

ZONE B

ZONE A

TC
(H₂ TEMP)

TEMPERATURE NODES

THESE TWO NODES DELETED
FOR 0.015 IN.-THICK
STRUCTURAL WALL CASE

GARRETT AIRESEARCH MANUFACTURING COMPANY
Los Angeles, California

TABLE A-I

HOT WALL INSERT AND STRUCTURAL WALL THERMOCOUPLE DESCRIPTIONS

Integer, I	Ref. Axial Location, in.	Insert T/C Designation, TJ(I)	Angular Location of TJ(I), degrees CWLA	Structural Wall T/C Design, TS(I)	Angular Loc. of TS(I), CWLA, degrees	H_2 Flow Rate Designation, W(I)	Flow Route Radius, in. RAD(I)	Component	Fin Spacing/Struct. Wall thickness Fins per inch/in.
1	35.70	T16	5	T17	355	W1	7.00	Spike	28/0.060
2	40.50	T18	5	T19	355	→	8.75	→	→
3	44.30	T24	355	T23	5		9.35		
4	54.00	T42	0	T43	5	W2	9.55	Inner shell	
5	62.30	T50	5	T51	0	→	9.54	→	
6	75.60	T57	345	T58	350	W3	5.92	Nozzle	20/0.015
7	38.20	T1	5	T3	0	→	10.17	Leading edge (outer surface)	→
8	40.25	T2	0	T4	5		10.64	→	
9	46.00	T61	358	T62	354		10.12		
10	50.40	T67	5	T68	10	W4	10.45	Outer shell	28/0.060
11	54.13	T86	180	T88	210		10.72		
12	62.30	T92	0	T93	5	→	10.90	→	→
13	70.10	T99	5	T100	185		11.75		

wall thickness with 20R - 0.050 - 0.100(0) - 0.006 offset fins. The latter cross-section geometry was located on the nozzle and leading edge outer surfaces of the SAM. The geometry in Figure A-1 shows the 0.060-in.-thick structural wall. The nodal network for the 0.015-in.-thick structural wall is identical to that in Figure A-1 except the structural wall nodes further than 0.015 in. away from the coolant were deleted.

The coolant convective heat transfer to and from the solid surfaces was divided into three zones, A, B, and C, indicated in Figure A-1. Convective heat transfer coefficients in Zone A were based on the Colburn factor (j), obtained from experimental data for each of the two types of offset fin passages (i.e., 20 and 28 fins/in.). Coefficients in Zone B were calculated from a standard duct heat transfer equation. Zone C was treated as a cylinder in crossflow, with the coefficient evaluated as an average around the circumference. All coefficients were evaluated from the transport properties of normal hydrogen at the bulk hydrogen temperature. Metal thermal conductivities were evaluated at the respective metal temperatures.

The steady-state temperatures of the nodal network were calculated on a thermal analyzer computer program for several input combinations of hot gas heat flux (a constant value on all hot surface nodes per computer run), coolant-passage Reynolds number based on the fin geometry, and hydrogen coolant temperature in the vicinity of the insert. Heat fluxes were varied from 50 to 220 Btu/sec-ft^2. Three Reynolds numbers of 1000, 5000, and 10,000, and three hydrogen temperatures of 200°, 600°, and 1000°R were used and are typical of conditions expected for SAM testing.

Calculated temperature results were reduced to the form of an overall conductance, U, across the insert and fin passage and defined as

$$U = \frac{q_{HG}}{T_J - T_c}, \text{ Btu/sec-ft}^2\text{-}°R$$

where

$\quad q_{HG}$ = hot gas heat flux, Btu/sec-ft^2

$\quad T_J$ = measured insert thermocouple temperature during test, °R

$\quad T_c$ = hydrogen coolant passage temperature adjacent to the insert, °R

It was hypothesized that the conductance across the insert and hydrogen passage geometry was a function of the coolant flow rate (Reynolds number) and the temperature-dependent hydrogen transport properties and metal thermal conductivity. This is not an unreasonable hypothesis, since the thermal conductance across a plate-fin passage (hot surface-to-coolant) in the absence of a thermocouple insert can be modeled in this manner. After attempting several correlations, the best fit of data could be described by

$$U = f\left(Re, \bar{T}\right)$$

where

$$\bar{T} = 0.2\,T_c + 0.8\,T_J$$

Results of this correlation are presented in Figure A-2 for the 20 fin/in., 0.015-in.-thick structural wall geometry and for the 28 fin/in., 0.060-in.-thick structural wall geometry. In general, all data points (one data point per computer run) fall within ±1 percent of curves drawn through the points except for the 20-fin/in. case where differences of 2 and 3 percent are seen (Re = 5000, $\overline{T}$ = 400° and 570°R). These curves were cross-plotted on log-log coordinates with Reynolds number as the main independent variable and are shown in Figure A-3. In these cross-plots the correlated data was extrapolated out to a Reynolds number of 30,000 to eliminate linear computer extrapolation beyond a Reynold number of 10,000. Most of the plate-fin passage Reynolds numbers during SAM testing were expected to be between 1000 and 10,000. However, during the test runs with cryogenic inlet hydrogen and large hydrogen flow requirements, Reynolds numbers of up to 20,000 were expected in the spike flow route. The curves in Figure A-3 were stored in tabular form in the SAM data reduction computer program and used to calculate hot surface temperatures adjacent to the thermocouple inserts.

Hot-Surface Temperature Calculation

The hot surface temperatures adjacent to the 13 thermocouple inserts were calculated in the data reduction program at selected time increments (usually every 1 sec of test run time) and when the thermal steady-state criteria at each thermocouple location was satisfied. The physical model used in the calculation is shown in Figure A-4. This model shows the plate-fin panel cross section with the thermocouple insert, and an adjacent panel section with the structural wall thermocouple. The insert and structural wall thermocouples are generally separated by 5 or 10 deg circumferentially. On a 15- to 20-in. flow route diameter, this angular separation is equivalent to 1 or 2 in. Since the plate-fin section thickness is 0.125 in., (with 0.060-in.-thick structure) an angular separation of 1 in. is larger, relative to panel thickness. For this reason, the plate-fin section with the structural wall thermocouple is essentially thermally isolated from the panel section with the insert thermocouple.

The analysis makes two assumptions: (1) the hot gas heat fluxes are equal at both circumferential sections, and (2) the hydrogen coolant temperatures at both sections are equal. The mathematical heat transfer model and formulation for the panel section at the structural thermocouple location is shown in Figure A-4. The mathematical formulation and the additional relation from the insert thermocouple calibration gives four equations and four unknowns: hot surface temperature (TWO), inner surface temperature (TWI), hydrogen coolant temperature (TC), and hot gas heat flux (FLUX). These four equations are solved iteratively so that the hydrogen transport properties are evaluated at the bulk hydrogen temperature (TC), and the metal thermal conductivities are evaluated at their respective average temperatures.

The FORTRAN IV listing of the hot surface calculation procedure in the SAM data reduction computer program is shown in Table A-2. The correspondence of nomenclature between Figure A-4 and Table A-2 is fairly apparent. Additional notes are included in Table A-2 to indicate some of the tacit features of the calculation procedure. For purposes of calculation, the temperatures TJ and TS were considered at steady state if their time rate of change was equal or
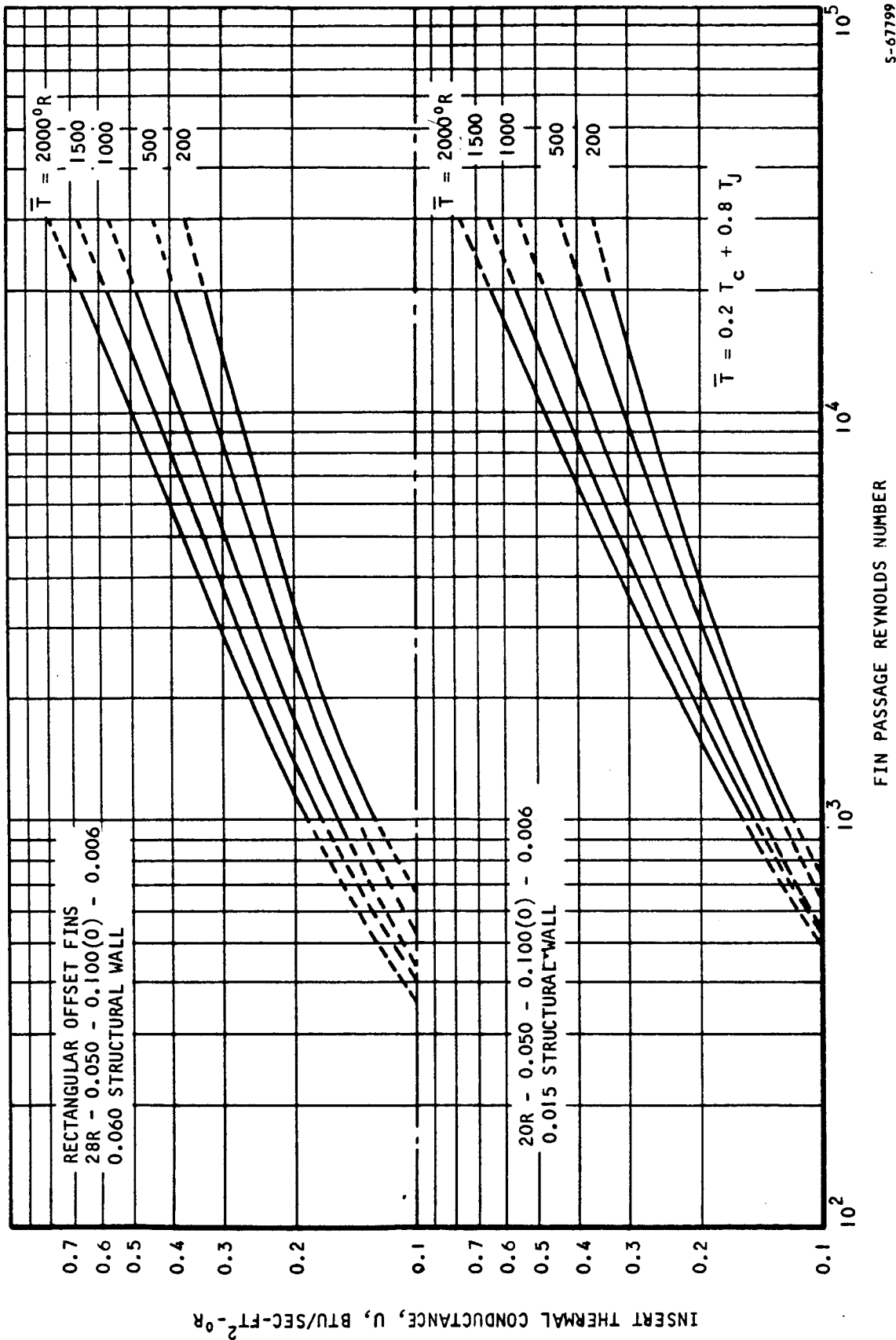
RECTANGULAR OFFSET FINS

28 R - 0.050 - 0.100 (O) - 0.006
0.060 STRUCTURAL WALL

Re = 10^4

Re = 5 x 10^3

Re = 10^3

20 R - 0.050 - 0.100 (O) - 0.006
0.015 STRUCTURAL WALL

Re = 10^4

Re = 5 x 10^3

Re = 10^3

INSERT THERMAL CONDUCTANCE, U, BTU/SEC-FT^2-°R

$\bar{T} = 0.2\ T_c + 0.8\ T_J$, °R
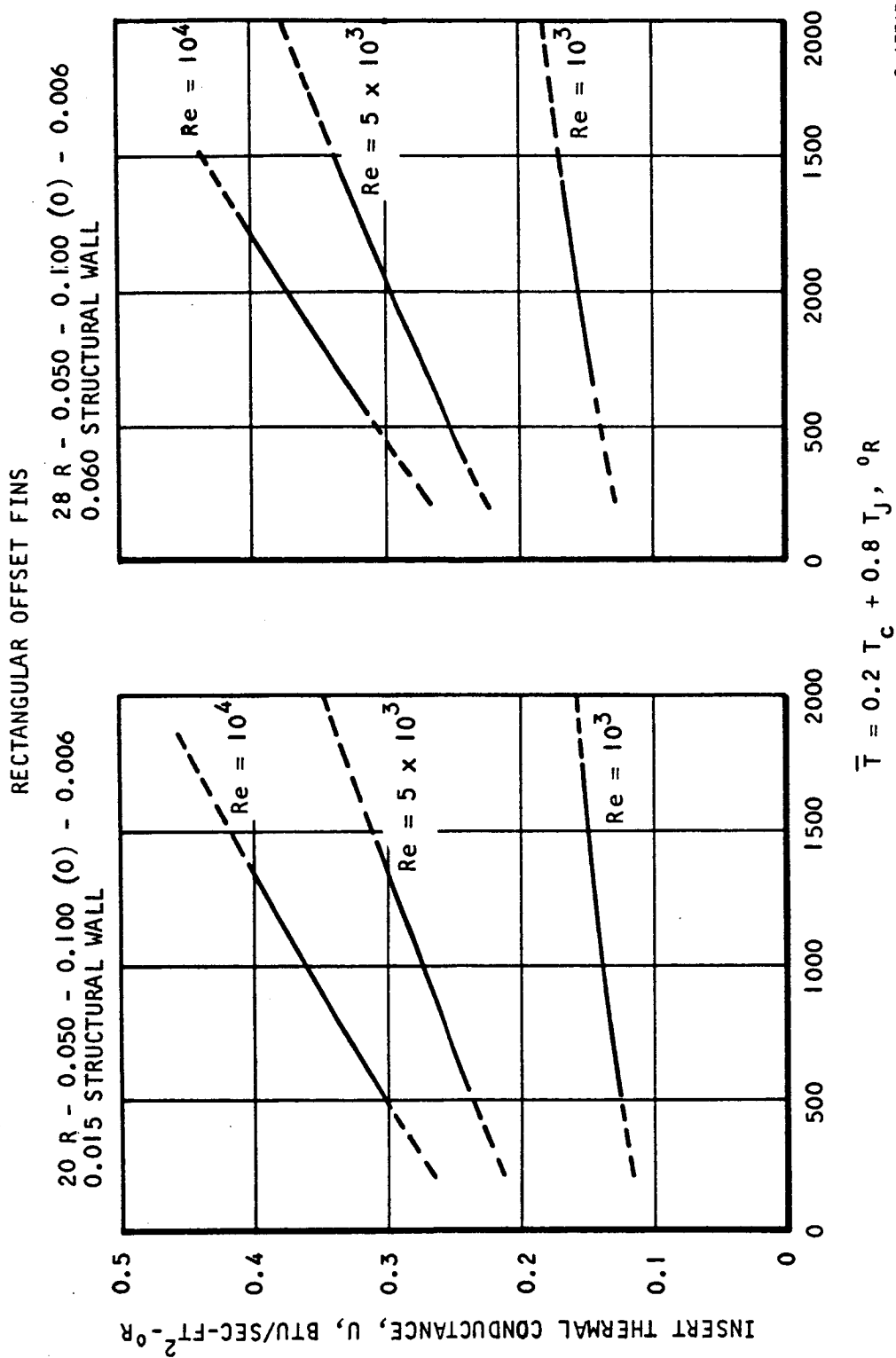
S-67763

Figure A-2. Hot Wall Insert Thermocouple Calibrations

Figure A-3. Hot Wall Insert Thermocouple Calibrations

GARRETT AIRESEARCH MANUFACTURING COMPANY
Los Angeles, California
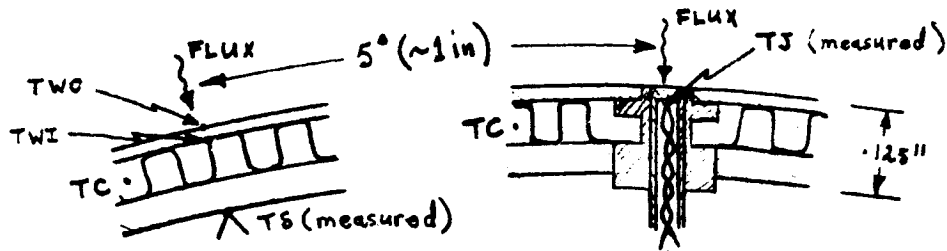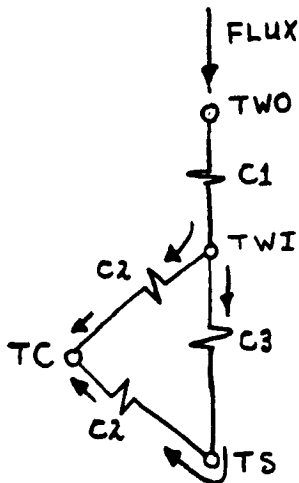
PHYSICAL MODEL

MATHEMATICAL
MODEL

TJ = measured insert temperature

TS = measured structural temperature

TWO = hot surface temperature

TWI = inner surface temperature

TC = hydrogen coolant temperature (assumed
equal at both sections)

FLUX = hot gas heat flux (assumed equal at
both sections)

$C1 = k_w/x$, (conductance across hot wall, $x = .015$ in)

$C2 = k_H m \left(\dfrac{A_f}{w x}\right) \left\{\dfrac{\cosh(m\ell) - 1}{\sinh(m\ell)}\right\} + h\left(\dfrac{A_p}{w x}\right)$, (convection conductance from hot and cold wall to H₂)

$C3 = k_H m \left(\dfrac{A_f}{w x}\right) \dfrac{1}{\sinh(m\ell)}$, (conductance between hot and cold wall via the fins)

$TWI = TS + FLUX/(C2 + 2C3)$

$TWO = TWI + FLUX/C1$

$TC = TWI - (1 + C3/C2)(TWI - TS)$

$FLUX = U(TJ - TC)$

Four equations and four unknowns, TWO, TWI, TC and FLUX.

└─ from insert calibration table lookup
at Re and $\bar{T} = 0.2\, TC + 0.8\, TJ$

Figure A-4. Physical and Mathematical Models

NOMENCLATURE

k_W = hot wall thermal conductivity evaluated at $(TWO + TWI)/2$

X = hot wall thickness, .015-in.

k_f = fin thermal conductivity evaluated at TVF

m = $\sqrt{2h/k_f\delta}$

h = $j\,G\,C_p\,/\,Pr^{2/3}$, H_2 coolant heat transfer coefficient in fins

δ = fin thickness, .006-in.

j = Colburn factor for fins (a function of fin passage RE)

G = H_2 coolant mass flux in fins, WC/A_c

C_p = H_2 coolant specific heat evaluated at TC

Pr = H_2 coolant Prandtl no. evaluated at TC

l = fin height, .050-in.

RE = fin passage Reynolds no., $\dfrac{W}{A_c} \cdot \dfrac{Dn}{\mu}$

WC = H_2 coolant flow rate (calculated from flow meter data)

A_c = H_2 coolant flow area at T/C insert location, $2\pi \cdot RAD \cdot l \cdot \dfrac{A_c}{WX}$

RAD = Radius of flow route at T/C insert location.

μ = H_2 coolant dynamic viscosity evaluated at TC

TVF = $TC + \dfrac{\cosh(ml)-1}{(ml)\sinh(ml)}\left\{ (TWI - TC) + (TS - TC) \right\}$, average fin temp.

Dn = fin passage hydraulic diameter $\begin{cases} .0440\text{-in. for } 20R \text{ fin} \\ .0365\text{-in. for } 28R \text{ fin} \end{cases}$

$\dfrac{A_c}{bW}$ = fin passage-free flow-to-frontal area ratio. $\begin{cases} .744 \text{ for } 20R \text{ fin} \\ .732 \text{ for } 28R \text{ fin} \end{cases}$

$\dfrac{A_f}{WX}$ = fin passage fin-to-outer plate area ratio $\begin{cases} .120 \text{ for } 20R \text{ fin} \\ .168 \text{ for } 28R \text{ fin} \end{cases}$

$\dfrac{A_f}{WX}$ = fin passage inner-to-outer plate area ratio $\begin{cases} .880 \text{ for } 20R \text{ fin} \\ .832 \text{ for } 28R \text{ fin} \end{cases}$

Figure A-4. (Continued)

S-67788

TABLE A-2

FORTRAN IV LISTING

```
      C   CORRECTION CALCULATION PROCEDURE FOR SAM HOT WALL THERMOCOUPLES
      C
      C   DEFINE INPUT PARAMETERS
      C
          DO 401 I=1,3
      401 WC(I)=W1
          DO 402 I=4,6
      402 WC(I)=W2
          DO 403 I=7,10
      403 WC(I)=W3
          DO 404 I=11,13
      404 WC(I)=W4
      C
          TJ(1)=T16
          TJ(2)=T18
          TJ(3)=T24
          TJ(4)=T42
          TJ(5)=T50
          TJ(6)=T57
          TJ(7)=T1
          TJ(8)=T2
          TJ(9)=T61
          TJ(10)=T67
          TJ(11)=T66
          TJ(12)=T92
          TJ(13)=T99
          TS(1)=T17
          TS(2)=T19
          TS(3)=T23
          TS(4)=T43
          TS(5)=T51
          TS(6)=T58
          TS(7)=T3
          TS(8)=T4
          TS(9)=T62
          TS(10)=T68
          TS(11)=T88
          TS(12)=T93
          TS(13)=T100
      C
          DO 439 I=1,13
          TJLTS(I)=TJ(I)-TS(I)
          IF(ITEMP.EQ.0)GO TO 420
          IF(TIME-TSTAR)410,410,411
      410 TJL(I)=TJ(I)
          TSL(I)=TS(I)
      411 IF(TJ(I).LT.150..OR.TJ(I).GT.3000.)GO TO 420
          IF(TS(I).LT.150..OR.TS(I).GT.3000.)GO TO 420
          IF(TJLTS(I).LT.0..OR.TJLTS(I).GT.1500.)GO TO 420
          DELTJ=ABS((TJ(I)-TJL(I))/TSTEP)
          DELTS=ABS((TS(I)-TSL(I))/TSTEP)
          IF(DELTJ.GT.20.)GO TO 420
          IF(DELTS.GT.20.)GO TO 420
          IF(WC(I).LT..001.OR.WC(I).GT.1.00)GO TO 420
          IF(I.GT.5.AND.I.LT.9)GO TO 412
      C   28R FINS,.060 INCH COLD WALL
          AFWX=0.168
          APWX=0.832
          ACBW=0.732
          DH=0.0355
          GO TO 413
      C   20R FINS,.015 INCH COLD WALL
```

Assignment of instrumentation data to array storage locations WC, TJ, and TS at time = TIME (sec)

$W1$ = spike H_2 flow rate

$W2$ = innerbody H_2 flow rate

$W3$ = leading edge H_2 flow rate

$W4$ = trailing edge H_2 flow rate

Checking procedure to determine whether calculations can be realistically performed (includes steady-state criteria)

For $I = 1$ to 5 and 9 to 13, use 28 fin/inch data

For $I = 6$ to 8 use 20 fin/inch data

TABLE A-2 (Continued)

Iteration Loop

Initial assumptions for fluid and metal property evaluation

FLAGIN and XYZMAP are function subprograms for table lookups and interpolation

Maximum No. of iterations = 20. Only 4 or 5 are usually required.

Convergence criteria of 1°R on TWO, TWI and TC

```
Seq.
No.

412    AFWX=0.120
       APWX=0.880
       ACBW=0.774
       DH=0.044
C  CALCULATIONS START HERE
413    TOUT=TJ(I)
       TIN=TJ(I)
       TH2=TS(I)
       TVF=TS(I)
       ITER=1
       AC=6.2832*RAD(I)*FL*ACBW/144.
       G=WC(I)/AC
414    UM=FLAGIN(0,TI,UMI,NTI,TH2,YANS,JTI,KTREXP,1)
       RE=G*DH/(UM*12.0)
       TV=0.20*TH2+0.80*TJ(I)
       IF(1.GT.5.AND.I.LT.9)GO TO 415
C  2BR FIN TABLE LOOKUPS
       U=XYZMAP(1,RE2B,U2B,NU2P,TU2B,NTU2B,JU2B,RE,TV,ANS,KTX,KTY,1)
       AJ=FLAGIN(-1,RE2B,AJ2B,YANS,JJ2B,KTREXP,2)
       GO TO 416
C  20R FIN TABLE LOOKUPS
415    U=XYZMAP(1,RE20,U20,NU20,TU20,NTU20,JU20,RE,TV,ANS,KTX,KTY,2)
       AJ=FLAGIN(-1,RE20,AJ20,NJ20,RE,YANS,JJ20,KTREXP,3)
416    CP=FLAGIN(0,TII,CPII,NTII,TH2,YANS,JTII,KTREXP,4)
       PR=FLAGIN(0,TIII,PRIII,NTIII,TH2,YANS,JTIII,KTREXP,5)
       AKF=FLAGIN(0,TIV,AKIV,NTIV,TVF,YANS,JTIV,KTREXP,6)
       TVW=(1OUT+TIN)/2.0
       AKW=FLAGIN(0,TIV,AKIV,NTIV,TVW,YANS,JTIV,KTREXP,7)
       HTC=AJ*G*CP/PR**0.6666
       AM=SQRT(24.0*HTC/(AKF*FT))
       AML=AM*FL/12.0
       C1=AK*12.0/0.015
       C2=AKF*AFWX*AM*(COSH(AML)-1.0)/SINH(AML)*HTC*APWX
       C3=AKF*AFWX*AM/SINH(AML)
       FLUX(I)=U*(TJ(I)-TH2)
       TWI(I)=TS(I)+FLUX(I)/(C2*2.0*C3)
       TWO(I)=TWI(I)+FLUX(I)/C1
       TC(I)=TWI(I)-(1.0-C3/C2)*(TWI(I)-TS(I))
       IF(ITER.GT.20)GO TO 430
C  TEST FOR CONVERGENCE
       IF(ABS(TWO(I)-TOUT)-1.0)417,417,419
417    IF(ABS(TWI(I)-TIN )-1.0)418,418,419
418    IF(ABS( TC(I)-TH2 )-1.0)430,430,419
C  CONVERGENCE TEST WAS FAILED
419    TOUT=TWO(I)
       TIN=TWI(I)
       TH2=TC(I)
       TVF=(COSH(AML)-1.0)/(AML*SINH(AML))*((TIN-TH2)*(TS(I)-TH2))*TH2
       ITER=ITER+1.0
       GO TO 414
C  CONDITIONS FOR CALCULATION TO BE PERFORMED HERE NOT FULFILLED
420    TWO(I)=TJ(I)
       TWI(I)=TJ(I)
       TC(I)=TS(I)
       FLUX(I)=0.0
430    TWOLTS(I)=TWO(I)*TS(I)
       TJL(I)=TJ(I)
439    TSL(I)=TS(I)
```

AIRESEARCH MANUFACTURING COMPANY
Los Angeles, California

S-67787

less than 20°R/sec (card sequence Nos. 418 to 421). In the absolute sense, a
time rate of change of 20°R/sec is far from steady state. However, because
the temperature data, particularly on the PCM data acquisition system, was
erratic within a band of up to ±20°R, even at steady state, it was felt that
a steady-state filter of less than 20°R/sec would virtually eliminate all data
from qualifying for calculation. Consequently, all hot-wall temperature cal-
culations were subject to a review of the input TJ and TS time-temperature
histories.

The output of the hot-wall calculation procedure is illustrated in
Figure A-5 for the thermocouple insert located at Station 50.40 on the outer
shell (Test 41, Run 17, with 1290 psia, 2700°R tunnel reservoir total conditions).
Included are the measured insert (TJ) and structural wall (TS) temperatures
(T67 and T68) on which the calculation was based. It is noted that the calcu-
lated hot-wall temperature, TWO, adjacent to the hot gas is lower than the
insert temperature, T67, even though the insert junction is 0.015- to 0.020-in.
beneath the hot surface. This was produced by a larger hot surface-to-structure
thermal conductance through the fins than through the insert. The calculated
hot-surface temperature is 1370°R vs 1430°R for the insert thermocouple reading.

Included in Figure A-5 is the calculated local hot gas heat flux, FLUX.
The average value of FLUX between 54 and 80 sec is 27 Btu/sec-ft^2. A calcula-
tion of the aerodynamic heat flux at this outer shell location was made using
measured tunnel conditions and wall static pressures. Using fully turbulent
duct-flow relations and the adiabatic wall reference-temperature method, the
resulting heat flux is 28 Btu/sec-ft^2.

Estimates of the errors incurred in the insert thermocouple calibration
and hot-wall temperature calculation procedure are presented in Table A-3. The
total error from these sources is ±13 percent.

Certain of the thermocouple pairs could not be used for wall-temperature
and heat flux estimates because of systematic characteristics that were un-
acceptable. For example, two structural wall thermocouples (T19 and T51 in
Table A-1) were consistently reading higher temperatures than their respective
insert thermocouples (T18 and T50). They were eliminated from use since the
calibration is based on a higher insert thermocouple reading. Two thermocouple
pairs on the outerbody (T86, T88 and T99, T100 in Table A-1) were considered
unreliable for hot-wall temperature calibration; the relative angular locations
between the insert and structural thermocouples were 30 and 180 deg, respectively.
With angular separations such as these, the validity of the assumptions made in
Figure A-4 (heat flux and coolant temperature are equal at both the insert and
structure thermocouple locations) is questionable. The heat flux and coolant
temperature were expected to be angularly unsymmetric in this region due to
shock wave/boundary-layer interactions and non-uniform coolant flow distribu-
tion near the outerbody panel strut cutouts. Finally, the remaining thermo-
couple pairs on the innerbody and aft outer shell were subject to critical re-
view since the heat flux and hot-wall temperature calculations are local angular
values. They cannot be compared directly with aerodynamic heating and cooling
performance data analysis which are based on average angular conditions.
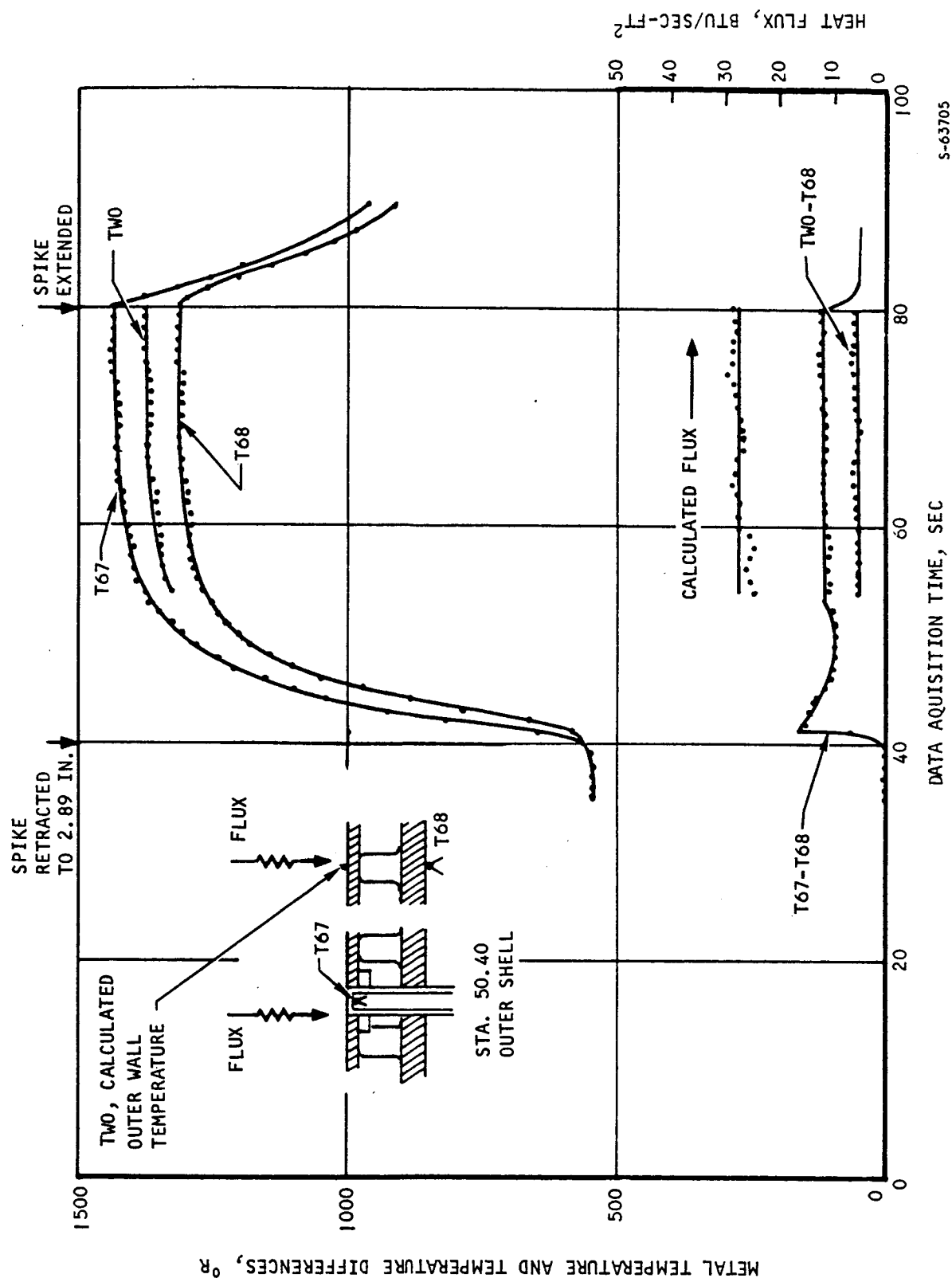
Figure A-5. Corrected Hot Wall Temperate Calculation, Outer Shell, Test 41, Run 17 (1290 psia, 2700°R) (U)

AIRESEARCH MANUFACTURING COMPANY
Los Angeles, California

TABLE A-3

ESTIMATED ERRORS FOR INSERT THERMOCOUPLE CALIBRATION

	Effect on Flux and TWO-TS, %
PRIMARY	
Variation in thickness of the end plate, ±0.0025 in.	±7
Variation in radial location of TC wires	±4
Variation in cooling coefficient	±2.7
Subtotal	±13.7
rss Subtotal	± 8.50
SECONDARY	
Flush location of thermocouple face	±1.0
Variation in thickness of skin	±2.0
Filleting at braze corners	±0.5
Incomplete braze	±1.0
Conduction along thermocouple wire	±0.5
Filleting in thermocouple tube to cap	±2.0
Deviation of calibration data from correlation curves in Figures A-2 and A-3	±3.0
Variation in radiation from thermocouple due to increased temperature	±0.1
Normal thermocouple and readout errors and miscellaneous	±1.0
Subtotal	±11.1
rss Subtotal	± 4.53
Simple Arithmetic Total	±24.8
Root Sum Squares Total	±13.03

Transient Operation

The insert-thermocouple calibration and hot-wall temperature calculation procedures described above are applicable for steady-state thermal conditions only. During transient operation (SAM insertion into or withdrawal from the tunnel) there are insufficient data to determine the heat flux which is needed to relate insert thermocouple readings to the hot-wall temperature. In order to estimate hot-wall temperature for transient operation, the hot-gas heat transfer coefficient is assumed to be the same as at steady state. This assumption is reasonable since the tunnel conditions are unchanged during the run. Several tunnel conditions and coolant temperature histories are then used in a thermal analyzer program to develop a correction factor for the hot-wall thermocouples. To avoid the need of using the computer to conduct a parametric study on the several variables, the effects of the important variables are delineated using a simplified conduction model. While the closed-form solution of the simplified model provides the general expression for the correction factor, the computer outputs were used to evaluate all the coefficients. The result is expressed as follows:

$$C = 0.046(2500 - T_g) + 1150 (0.08 - h_g) - 0.32(286 - \frac{dT_c}{d\theta}) \qquad \text{(A-1)}$$

where (C) is the correction factor which, when added to the thermocouple readings, yields the wall temperature.

$$TWO = TJ + C$$

The rate of coolant temperature change can be estimated by noting the thermocouple location relative to the coolant inlet and outlet stations. The coolant temperature history at the inlet and outlet stations is known from the thermocouples at these stations.

The correction factors vs time for the five computer cases are shown in Figure A-6. The values (C) after the system becomes stable are shown in the following table:
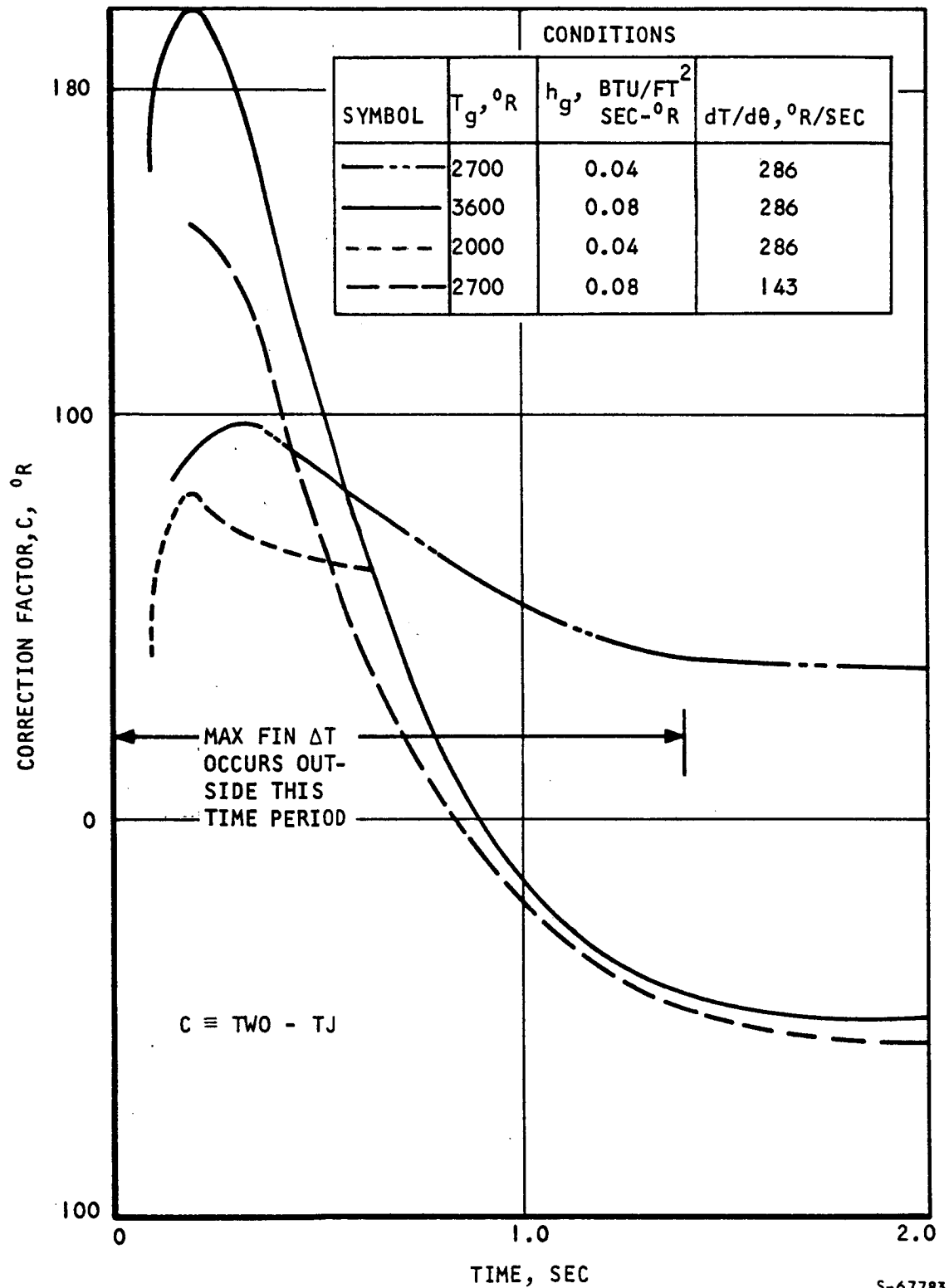
m, $^\circ R/sec$	286			143
T_g, $^\circ R$	3600	2700	2000	2700
h_g	Correction Factor "C"			
0.04	(-4)	+38*	+62 (+69)	(-9)
0.06	(-27)	(+14)	(+46)	(-32)
0.08	-50*	-8*	(+23)	-46*

*These data were used to develop Equation (A-1)

Data shown inside a bracket were computed with Equation (A-1)

Figure A-6. Correction Factors vs Time

The conduction nodal network for this analysis is shown in Figure A-7. Because the stability of the solution requires that the maximum time between calculations be limited by the size of the heat sink, the heat capacities are arbitrarily regrouped to shorten the computation time. For this analysis, the heat capacities within each zone, indicated by the heavy lines, are transferred to a single node which is designated by shading.

The terminologies for the one-dimension model are shown in Figure A-8.

$$T_g = CONSTANT, \quad h_g = CONSTANT$$

$$\frac{1}{U_g} = \frac{1}{h_g} + \frac{\Delta X_1}{k}$$

HOT GAS SIDE

ΔX_1

δVC

ΔX_2

COOLANT
SIDE

S-67759

$$\frac{1}{U_c} = \frac{1}{h_c} + \frac{\Delta X_2}{k}$$

$$TC = 540 + m\theta; \quad h_c = CONSTANT$$
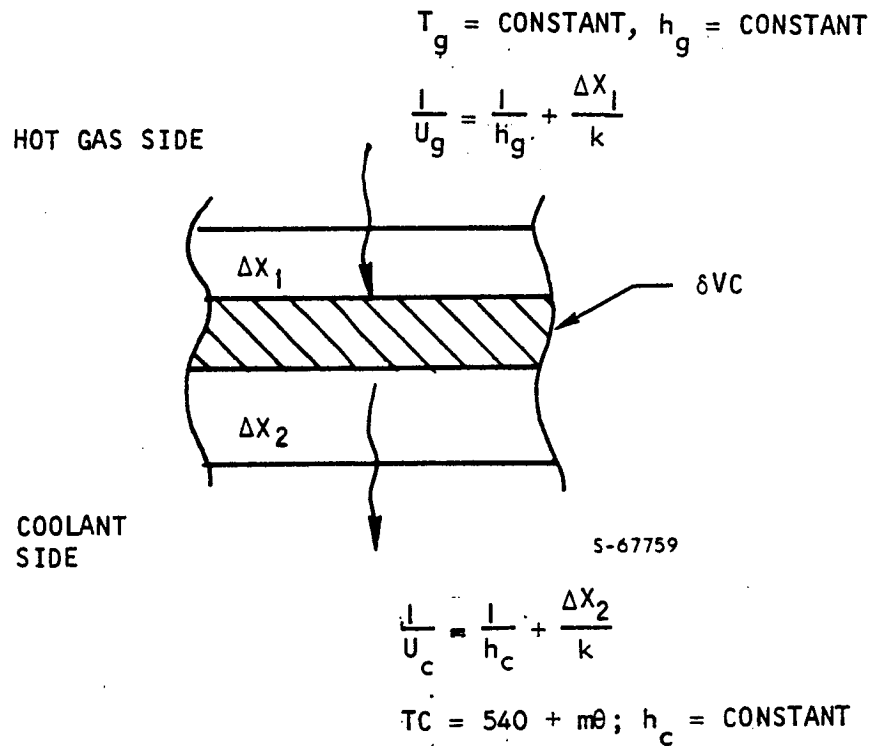
Figure A-8. Simplified Thermal Model

The differential equation is:

$$\rho VC \frac{dt}{d\theta} = U_g (T_g - T) - U_c (T - TC) \tag{A-2}$$

where the coolant temperature TC varies with time during the starting period; TC = 540 + mθ. The other terms are:
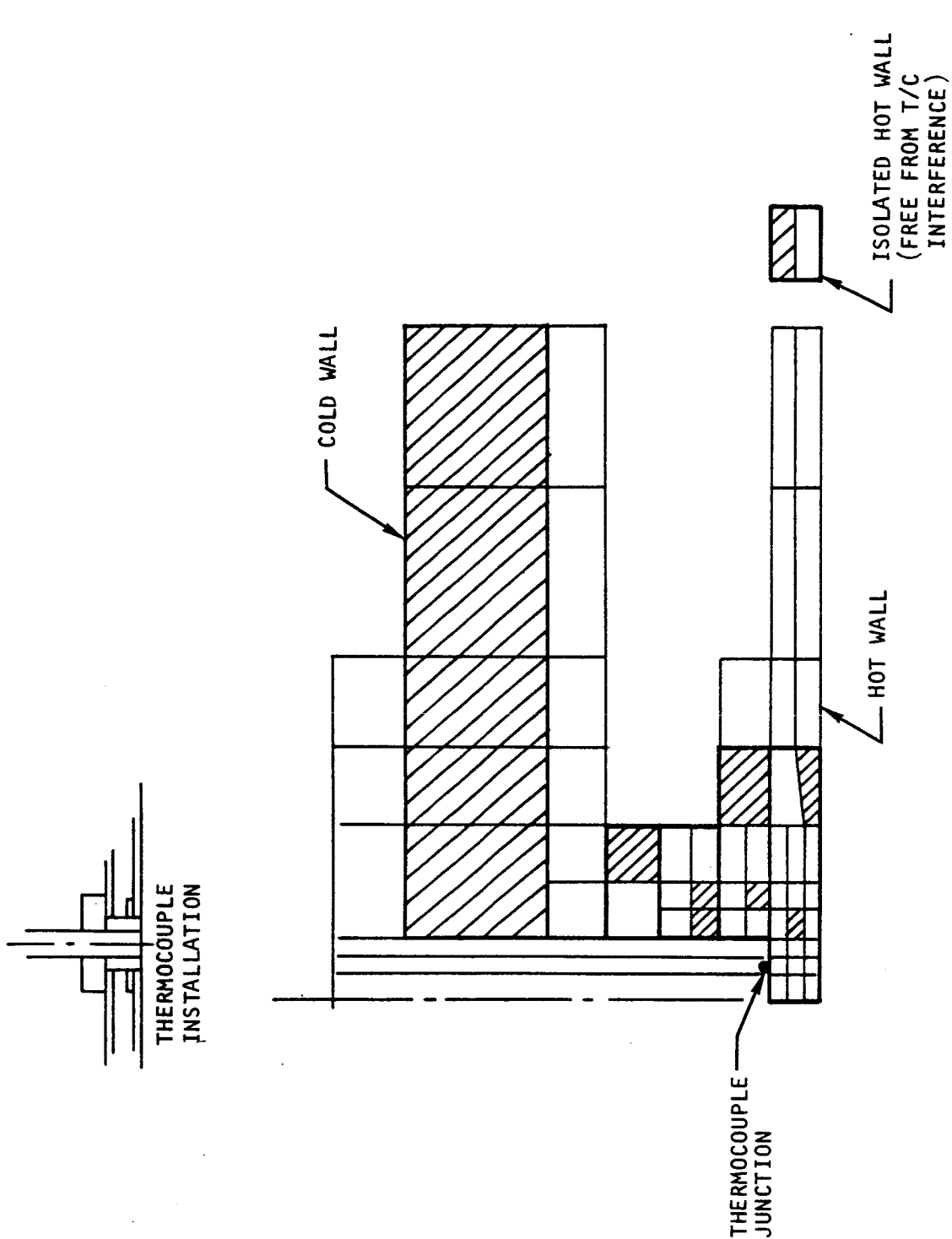
$\quad T_g$ = hot gas total temperature, $^\circ$R

$\quad \theta$ = time, sec

$\quad m$ = rate of coolant temperature change, $^\circ$R/sec

ISOLATED HOT WALL
(FREE FROM T/C
INTERFERENCE)

S-67775

COLD WALL

HOT WALL

THERMOCOUPLE
INSTALLATION

THERMOCOUPLE
JUNCTION

HEAT CAPACITIES WITHIN THE HEAVY BOUNDARY ARE
LUMPED INTO THE SHADED NODES TO REDUCE THE
COMPUTATION TIME

Figure A-7. Thermal Nodal Network

U_g, U_c = the overall heat transfer coefficient for the hot-gas side and the coolant side, respectively, $Btu/ft^2\text{-}{}^{\circ}R\text{-}sec$

ρVC is the heat sink, $Btu/{}^{\circ}R\text{-}ft^2$

The initial conditions for all nodes is a constant temperature of $540^{\circ}R$.

The solution of Equation (A-2) is

$$T - T_o = \left(\frac{RT_g + T_o}{1 + R} - \frac{M}{\beta (1 + R)^2} - T_o\right)\left(1 - e^{-d\theta}\right) + \frac{m\theta}{1 + R} \qquad (A\text{-}3)$$

where

$$R \equiv \frac{U_g}{U_c}$$

$$\beta \equiv \frac{U_c}{\rho VC}$$

$$\alpha \equiv (1 + R)\beta$$

The value α for the present analysis varies from 2 to 6. For time greater than 1.5 sec, the exponential term drops out, and Equation (A-3) may be rewritten as:

$$T - T_o = \frac{RT_g + T_o}{1 + R} - \frac{m}{\beta (1 + R)^2} - T_o + \frac{m\theta}{1 + R} \qquad (A\text{-}4)$$

The metal temperatures for the wall and for the thermocouple junction are:

$$TWO - T_o = \frac{R_w T_g + T_o}{1 + R_w} - \frac{m}{\beta_w (1 + R_w)^2} - T_o + \frac{m\theta}{1 + R_w} \qquad (A\text{-}5)$$

$$T_J - T_o = \frac{R_J T_g + T_o}{1 + R_J} - \frac{m}{\beta_J (1 + R_J)^2} - T_o + \frac{m\theta}{1 + R_J} \qquad (A\text{-}6)$$

The orders of magnitude of terms are as follows:

$$R_W = \left(\frac{U_g}{U_c}\right)_W \simeq 0.1 \text{ to } 0.2; \qquad 1 + R_W \simeq 1.15$$

$$R_J = \left(\frac{U_g}{U_c}\right)_T \simeq 0.2 \text{ to } 0.45; \qquad 1 + R_J \simeq 1.3$$

$$\beta_W = \left(\frac{U_c}{\rho VC}\right)_W \simeq 5.3$$

$$\beta_J = \left(\frac{U_c}{\rho VC}\right)_J \simeq 1.2$$

$$m \approx \frac{dT}{d\theta} = 150^\circ \text{ to } 300^\circ R/sec$$

The correction factor, which is the difference between the wall temperature and the thermocouple readings, can be written approximately as:

$$C = T_W - T_J = \frac{(R_W - R_J)T_g}{1 + \overline{R}} + \frac{m}{\beta_J}(1 - 2R_J) + m\theta(R_J - R_W) \qquad (A-7)$$

where $\overline{R} \equiv \frac{1}{2}(R_W + R_J)$

The variation of the correction (C) with the gas total temperature, coolant temperature change rate, and the hot gas heat transfer coefficient can be estimated as follows:

$$\frac{dC}{dT_g} \approx \frac{R_W - R_J}{1 + \overline{R}} \equiv A_1$$

$$\frac{dC}{dm} = \frac{1 - 2R_J}{\beta_J} + \theta(R_J - R_W) \equiv A_2$$

$$\frac{dC}{dh_g} \approx \left(\frac{T_g}{1 + \overline{R}} - m\theta\right)\left(\frac{dR_W}{dh_g} - \frac{dR_J}{dh_g}\right) - \frac{2m}{\beta_J} \cdot \frac{dR_J}{dh_g} \equiv A_3$$

The coefficients A_1, A_2, and A_3 were evaluated using the computer outputs and Equation (A-1) was obtained.

APPENDIX B

PLATE-FIN HOT WALL TEMPERATURE RESPONSE

APPENDIX B

PLATE-FIN HOT WALL TEMPERATURE RESPONSE

Conditions:

1. Step change in hot gas heating at $\Theta = 0$

2. Constant coolant flow rate

3. Ramp change in coolant temp.

Θ = time, sec

ρ = 0.30 lbs/in³

C_p = 0.10 Btu/lbm·R

h_G = hot gas heat transfer coefficient

h_c = coolant heat transfer coefficient (includes fin effectiveness)

T_G, T_w, T_c = hot gas, hot wall, and coolant temp.

A heat balance on a unit area of surface is

$$h_G (T_G - T_w) - h_c (T_w - T_c) = \rho C_p t \frac{d T_w}{d\Theta} \qquad (1)$$

Introducing $T_c = T_{co} + b\Theta$ (b = constant coolant temp slope and rearranging gives,

DATE_____
PREPARED BY_____
CHECKED BY_____

CALC. NO_____
MODEL _____
PART NO_____

$$\frac{dT_w}{d\theta} + \left(\frac{h_G + h_C}{\rho c_p t}\right)\left[T_w - \frac{h_G T_G + h_C T_{co}}{h_G + h_C}\right] = \frac{h_G b}{\rho c_p t}\theta \qquad (2)$$

Let $\quad T_w^* = T_w - \dfrac{h_G T_G + h_C T_{co}}{h_G + h_C}$

$$\tau_C = \frac{\rho c_p t}{h_C} \quad , \quad \tau_G = \frac{\rho c_p t}{h_G}$$

and $\quad \dfrac{1}{\tau} = \dfrac{1}{\tau_C} + \dfrac{1}{\tau_G}$

Then Equation (2) becomes

$$\frac{dT_w^*}{d\theta} + \frac{T_w^*}{\tau} = \frac{b}{\tau_C}\theta \qquad (3)$$

Two items are noticed at this point:

1. The quantity $(h_G T_G + h_C T_{co})/(h_G + h_C)$ is the steady state wall temperature ^is the coolant temperature was maintained constant at T_{co}.

2. τ_C and τ_G can be considered as the wall time constants when the wall is exposed to the coolant and hot gas, separately. When exposed to both heating and cooling, the reciprocal of the time constants are additive, so: $\dfrac{1}{\tau_C} + \dfrac{1}{\tau_G} = \dfrac{1}{\tau}$. The net result is a time constant less than the individual time constants.

The solution of Eq. (3) is

$$T_w^* = e^{-\theta/\gamma} \left\{ \frac{b}{\gamma_c} \int \theta e^{\theta/\gamma} d\theta + C \right\}$$

or

$$T_w^* = e^{-\theta/\gamma} \left\{ \frac{b}{\gamma} e^{\theta/\gamma} \left[\gamma\theta - \gamma^2 \right] + C \right\} \qquad (4)$$

where C is an integration constant. With boundary conditions that

$$\text{at } \theta = 0, \quad T_w = T_{wo}$$

$$\text{or } T_{wo}^* = T_{wo} - \frac{h_G T_G + h_c T_{co}}{h_G + h_c}$$

then

$$T_w^* = b\left(\frac{\gamma}{\gamma_c}\right)(\theta - \gamma) + \left[T_{wo} + b\left(\frac{\gamma}{\gamma_c}\right)\gamma \right] e^{-\theta/\gamma} \qquad (5)$$

For $\theta \gg \gamma$ (usually $\theta/\gamma > 4$) the exponential term approaches zero so that

$$T_w^* = T_w - \frac{h_G T_G + h_c T_c}{h_G + h_c} \simeq b\left(\frac{\gamma}{\gamma_c}\right)(\theta - \gamma)$$

For the nozzle conditions for Test 41, Run 26 (See Figure 5.4-5)

$h_G = 0.040$ Btu/sec.ft^2°R

$h_c = 0.073$ Btu/sec.ft^2°R   (WIB = .0045 lbs/sec)

$\rho C_p t = 0.0648$ Btu/ft^2.°R   (t = .015 in)

$b = 10$ °R/sec   UNCLASSIFIED

$T_{co} = 500$°R , $T_G = 3000$°R

Then

$$\tau_c = 0.886 \text{ sec}$$

$$\tau_G = 1.62 \text{ sec}$$

$$\tau = 0.60 \text{ sec}$$

$$\frac{h_G T_G + h_c T_{co}}{h_G + h_c} = 1485°R \ (1025°F)$$

For $\theta > 4\tau = 4 \times 0.60 \simeq 2\frac{1}{2} \text{ sec}$

$$T_w = 1485 + 10 \left(\frac{0.60}{0.866}\right)(\theta - .60)$$

$$= 1485 + 6.8 (\theta - 0.60)$$

$$\simeq 1485 + 6.8 \, \theta \quad , \quad \theta \gg \tau = 0.60 \text{ sec}$$

This prediction for the locally high heated outer wall of the nozzle is plotted in Figure 8.2. It is noted that after $2\frac{1}{2}$ sec (4τ) the wall temperature is essentially tracking the coolant temperature. The slope of T_w is not equal to the slope of T_c since the heat flux is decreasing with increasing T_w. It can be shown that the T_w and T_c slopes would be equal if the heat flux were constant *instead of* h_G *as used herein*

APPENDIX C

ACCELERATION ANALYSIS
PROBABILITY FUNCTIONS

APPENDIX C

ACCELERATION ANALYSIS
PROBABILITY FUNCTIONS

    The following discussion presents the equations of the parameters used to check the form of the probability distribution derived from the histogram technique. The mean, standard deviation, third (skewness), and fourth (kurtosis) normalized central moments of the data were computed. These were computed on the raw input data before preconditioning, if required. The equations for these values are as follows:

Mean,
$$\bar{X} = \frac{1}{N} \sum_{i=1}^{N} x_i$$

Standard deviation,
$$\sigma = \sqrt{\frac{1}{N-1} \sum_{i=1}^{N} (x_i - \bar{X})^2}$$

Skewness,
$$\beta = \frac{\frac{1}{N-1} \sum_{i=1}^{N} (x_i - \bar{X})^3}{\sigma^3}$$

Kurtosis,
$$K = \frac{\frac{1}{N-1} \sum_{i=1}^{N} (x_i - \bar{X})^4}{\sigma^4}$$

    The third and fourth normalized central moments can give a rough idea of the distribution. A Gaussian distribution has a skewness value of 0 and a kurtosis value of 3. A negative skewness value indicates the distribution has an elongated left tail and a positive skewness value indicates an elongated right tail. A distribution is called mesokurtic, platykurtic, or leptokurtic when its kurtosis equals 3, less than 3, or greater than 3, respectively. A platykurtic distribution indicates the data points are less heavily concentrated about the mean, and a leptokurtic distribution indicates more heavily concentrated, as compared to the Gaussian distribution.

    The chi-square goodness-of-fit to a Gaussian distribution was computed because the histogram option was chosen for the probability density function. The method of computing the chi-square value, Y, to test for normality is as follows:

$$Y = \sum_{i=1}^{(K+2)} \frac{(N_i - NP_i)^2}{NP_i}$$

where P_i = probability of being in the "ith" bin if Gaussian

N_i = the number of points in the "ith" bin

N = the total number of points

K = degrees of freedom = (number of bins - 2)

The region of normality acceptance is

$$Y \leq \chi^2_{K;\alpha}$$

where the value of $\chi^2_{K;\alpha}$ is available from Table 5.6-15 of Section 5.6.4 and (α) is the probability of a Type-I error. As an example, suppose $Y = 65$, $K = 50$, and the data is to be tested for normality at the $\alpha = 0.05$ level of significance, then we would accept the data to be normal since $\chi^2_{50;.05} = 67.5$ and $65 < 67.5$.

To test the accuracy of the data acquisition for a specified confidence per-centage, a percentage band for spectral estimation was completed. For example, if a confidence percentage of 98 was specified and the program computed a percentage band of 4.0, this means there is 98 percent certainty that the spectral computations are within 4.0 percent of the true value. The equation for the percentage confidence band is as follows:

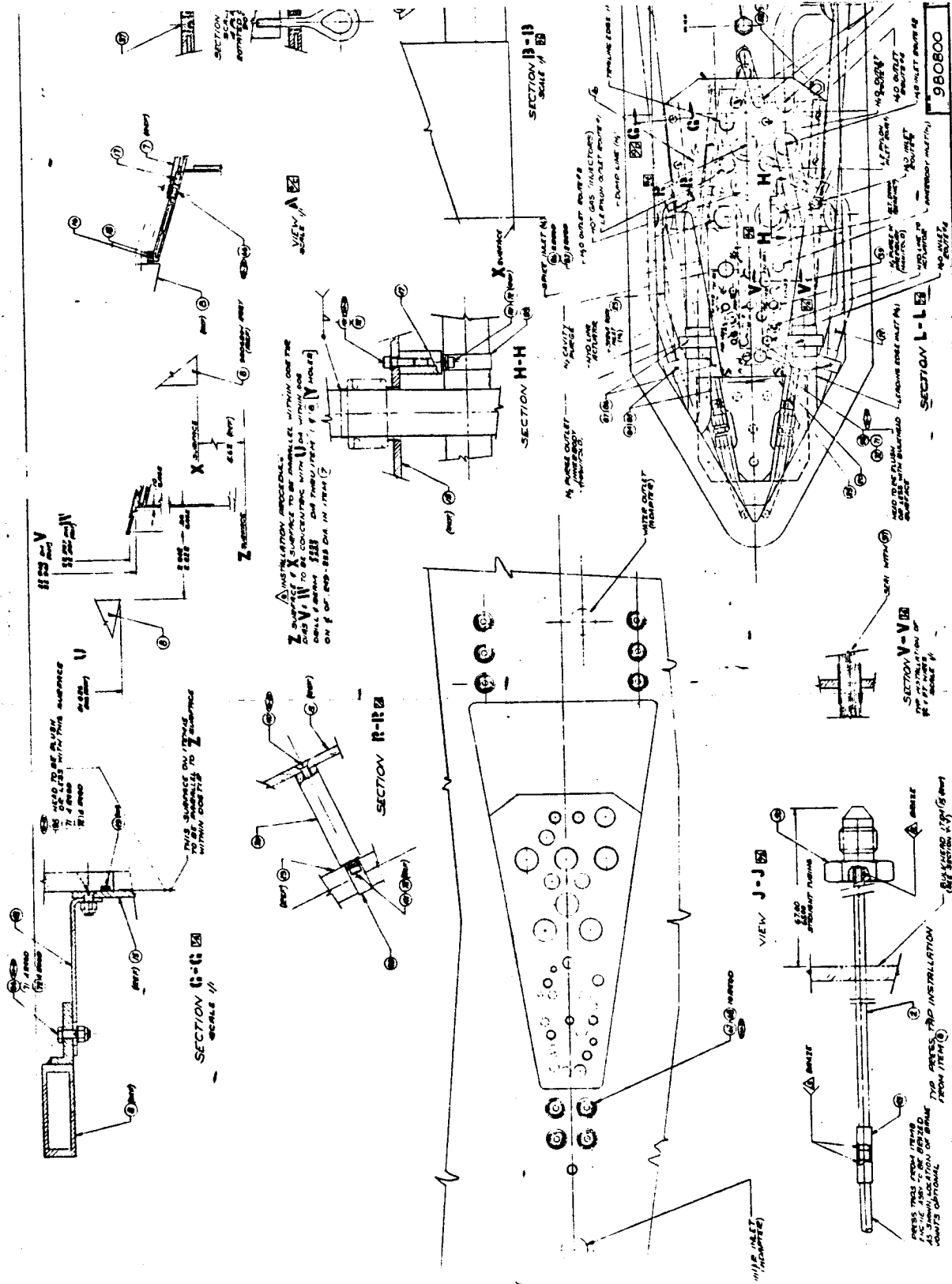$$PCB = \frac{db}{\sqrt{2\left(\frac{N}{m} - \frac{1}{3}\right) - 1}}$$

where N = number of data points

m = maximum lag number

db = decibel spread for specified confidence percentage

The value of PCB was calculated as 6.138 for the tests studied, for a specified confidence percentage of 98.

UNCLASSIFIED

980800

980800